TEAM tAO

1 October 2004

Science

Vol. 306 No. 5693
Pages 1–180 $10

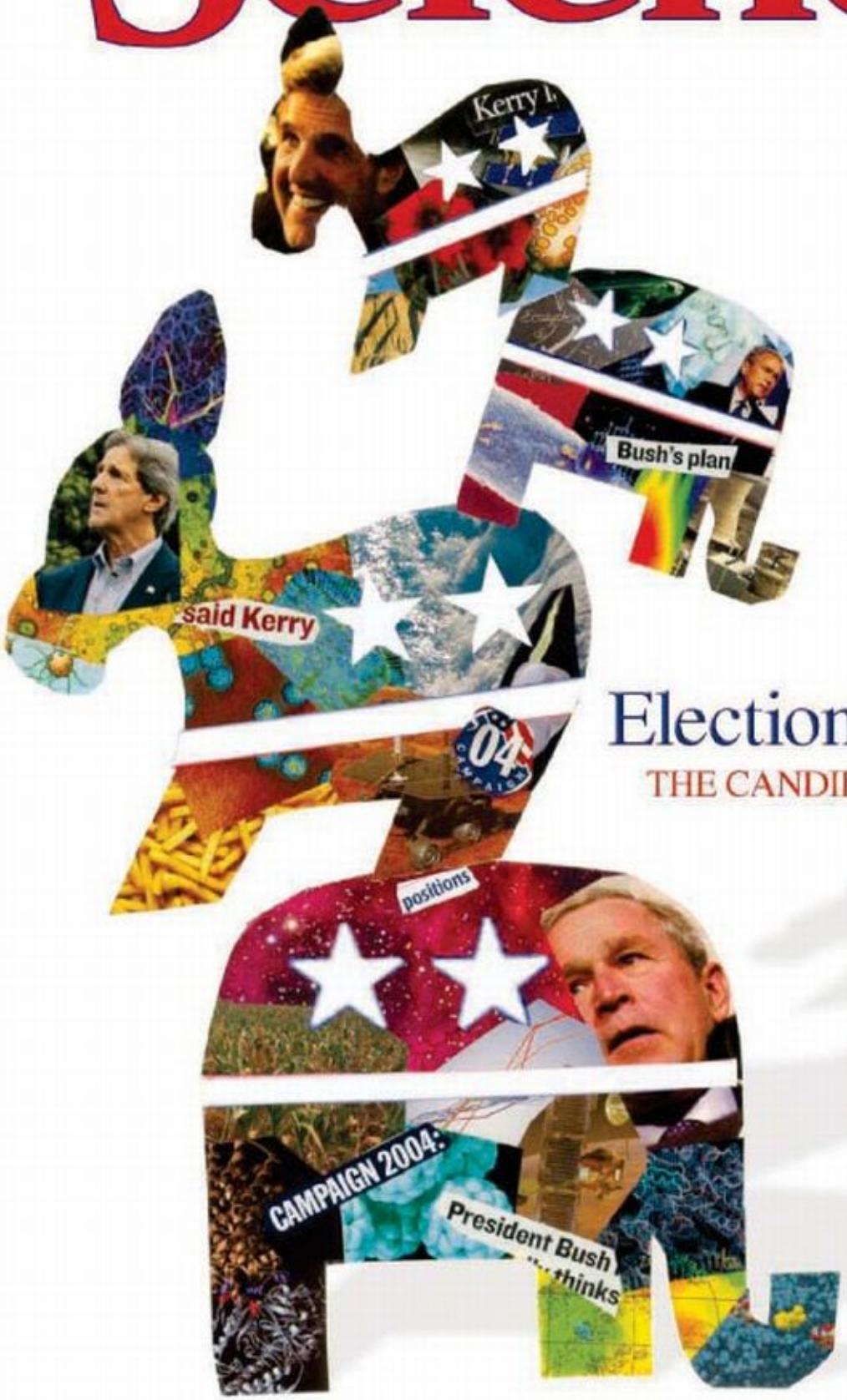

Election 2004

THE CANDIDATES ON SCIENCE

AAAS

Science

COVER Scientific issues have been unusually prominent in this year's presidential campaigns. *Science* asked candidates George W. Bush and John Kerry for their positions on a number of science-related issues. Read their answers on page 46. [Collage: Kelly Buckheit/*Science*]

Volume 306
1 October 2004
Number 5693

DEPARTMENTS

NEWS OF THE WEEK

NEWS FOCUS

40

58

70

2004 PRESIDENTIAL FORUM

LETTERS

BOOKS *ET AL.*

ESSAY

PERSPECTIVES

Contents continued

Review

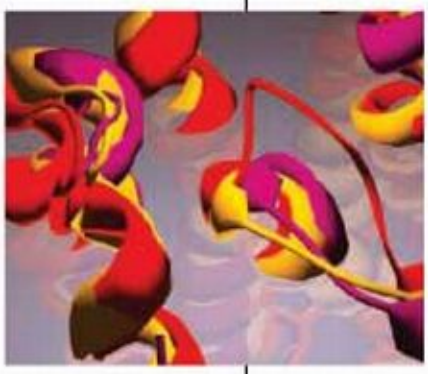

Science Express www.sciencexpress.org

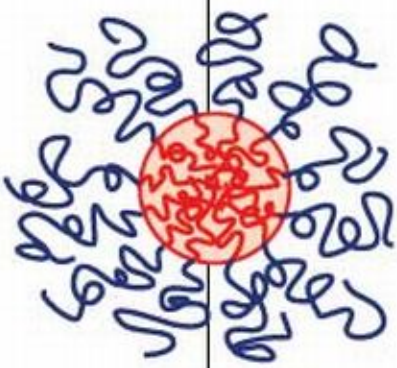

98

Brevia

Research Article

Reports

101

Contents continued

REPORTS CONTINUED

67 &117

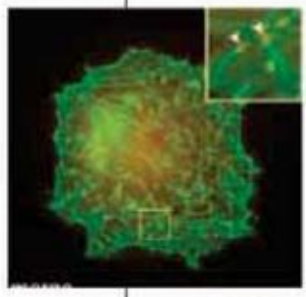

65 &124

AAAS
ADVANCING SCIENCE. SERVING SOCIETY

SCIENCE (ISSN 0036-8075) is published weekly on Friday, except the last week in December, by the American Association for the Advancement of Science, 1200 New York Avenue, NW, Washington, DC 20005. Periodicals Mail postage (publication No. 484462) paid at Washington, DC, and additional mailing offices. Copyright © 2004 by the American Association for the Advancement of Science. The title SCIENCE is a registered trademark of the AAAS. Domestic individual membership and subscription (51 issues): $130 ($74 allocated to subscription). Domestic institutional subscription (51 issues): $550. Foreign postage extra: Mexico, Caribbean (surface mail) $55; other countries (air assist delivery) $85. First class, airmail, student, and emeritus rates on request. Canadian rates with GST available upon request, GST #125488122. Publications Mail Agreement Number 1069624. Printed in the U.S.A.

Change of address: allow 4 weeks, giving old and new addresses and 8-digit account number. Postmaster: Send change of address to Science, P.O. Box 1811, Danbury, CT 06813–1811. Single copy sales: $10.00 per issue prepaid includes surface postage; bulk rates on request. Authorization to photocopy material for internal or personal use under circumstances not falling within the fair use provisions of the Copyright Act is granted by AAAS to libraries and other users registered with the Copyright Clearance Center (CCC) Transactional Reporting Service, provided that $15.00 per article is paid directly to CCC, 222 Rosewood Drive, Danvers, MA 01923. The identification code for Science is 0036-8075/85 $15.00. Science is indexed in the *Reader's Guide to Periodical Literature* and in several specialized indexes.

Contents continued

sciencenow www.sciencenow.org Daily News Coverage

Stem Cells Pick Up the Beat
Embryonic stem cells fix damaged hearts in pigs.

DNA Barcoders Nab New Species
Molecular technique turns up new species of butterflies, birds.

Omega-3s Without That Fishy Odor
Transgenic linseed oil would be first agricultural source of heart-friendly fats.

The international nature of science careers.

science's next wave www.nextwave.org Career Resources for Young Scientists

Global: **International Scientists—Feature Overview and Index** *Edited by R. Arnette*
The October feature discusses various aspects of science's international nature and its impact on careers.

Global/US: **Show Me the Money** *C. Parks*
The Community of Scientists (COS) Web site allows scientists from around the world to find the funding and collaborators needed to be competitive.

Global/Europe: **Young European Scientists Come Together** *T. Vrijenhoek*
Young scientists in Europe have a network of organizations to advance their careers.

Global/US: **Facing Life's Challenges as a Foreign Scientist** *X. Huang*
Hard work, perseverance, and a supportive husband helped this postdoctoral fellow succeed.

Europe: **Research Careers in Spain** *E. Pain*
Numerous resources are available to help young scientists in Spain find job and grant opportunities.

MiSciNet: **A Spiritual Journey** *E. Francisco*
An Osage-Cherokee physicist at NASA credits his traditional teachings for preparing him to be a scientist.

science's sage ke www.sageke.org Science of Aging Knowledge Environment

Perspective: **Ras—The Other Pro-Aging Pathway** *V. D. Longo*
Might Ras play a role in aging in mammals as well as in yeast?

News Focus: **Knife Jugglers** *R. J. Davenport*
Painkillers shift Alzheimer's protein slicer.

News Focus: **Off With Your (Fork)Head** *M. Leslie*
One stress-defusing pathway shuts down another.

Switch blade.

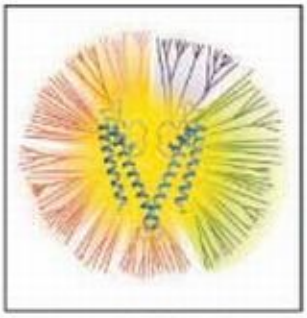

Voltage-gated channel evolutionary tree.

science's stke www.stke.org Signal Transduction Knowledge Environment

Review: **The VGL-Chanome—A Protein Superfamily Specialized for Electrical Signaling and Ionic Homeostasis** *F. H. Yu and W. A. Catterall*
Molecular and evolutionary relations of voltage-gated ion channels and related proteins are reviewed.

Perspective: **Attraction or Repulsion—A Matter of Individual Taste?** *A. Wells and L. Lillien*
EGFR signaling contributes to cell guidance in flies.

Separate individual or institutional subscriptions to these products may be required for full-text access.

The Candidates Speak

Surely it is unnecessary to remind *Science's* readers that we are in the middle of a run-up to a U.S. presidential election. They—you—have a big stake in the outcome, because even more than in 2000, science and technology issues will undergird many of the critical policy decisions of the next administration. Accordingly, as we have done before, *Science*'s editorial and news staffs sat down to think up the most important and challenging questions about science that we could pose to these candidates and their staffs. In mid-June, we sent the questions around to the science policy mavens in each campaign, asking that they respond by mid-August. Senator Kerry met that deadline, barely. President Bush took 3 weeks more, so we let him have an untimed exam and got longer answers.

We are not going to trouble you with a point-by-point comparison of the candidates' views. But a few areas are worth some special attention, starting with the very first question, which was identical to the one asked in 2000. We asked both candidates to choose their science and technology priorities. Four years ago, candidate Bush emphasized education. This year, he emphasized bandwidth, research toward a hydrogen economy, and recruiting science and technology to fight terrorism. Candidate Kerry looked for a balanced research support portfolio, put changing stem cell policy near the top, and promised to elevate the Science Adviser position to its former status as Assistant to the President for Science and Technology.

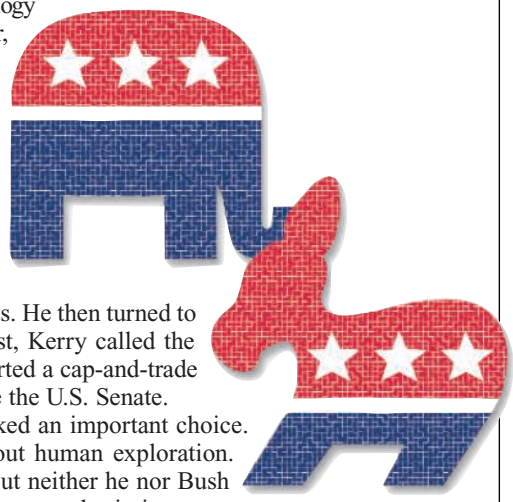

The climate change query produced some interesting differences. Bush quoted sentences from a 2001 National Academy of Sciences report that indicated uncertainty about the effects of anthropogenic sources of global warming in this century, but omitted reference to the recent report from his own administration's task force that accepted the importance of those effects. He then turned to his plans for research on clean coal and hydrogen technology. By contrast, Kerry called the evidence for human involvement in global warming convincing and supported a cap-and-trade system that would resemble that in the McCain-Lieberman bill now before the U.S. Senate.

In their responses on space, both candidates said good things but ducked an important choice. Bush reprised his man-Moon-Mars (3M) project and talked entirely about human exploration. Kerry praised NASA and spoke of both manned and robotic successes. But neither he nor Bush dealt realistically with costs, especially not the price tag for 3M or other manned missions, nor did they realistically approach the challenging question of which kind of space exploration produces the greater scientific yield per dollar invested.

There's an interesting area of disagreement about matters of fact. Bush asserts that he holds firmly to NSDD 189, the 1985 Reagan doctrine declaring that there is no information or knowledge control mechanism short of classification. Kerry claims that instead Bush has created a murky area of "sensitive but not classified" information that is subject to control. It is to be hoped that Bush will turn out to be right on this one, but he will need to convince the Department of Commerce that it has gone "off message" by attempting to assert exactly that kind of control in university contracts.

Where do we find agreement? Well, it's no surprise that both men love the National Institutes of Health budget and support this administration's record of completing its doubling from $13 billion to $27 billion. Both praise the Ocean Commission report and say they will work to follow its recommendations. They both think that foreign students are an asset to the United States and cite our long history of benefiting from such exchanges. Kerry criticizes aspects of the implementation of the visa program, whereas Bush cites surveys that show that the majority of land-grant institutions have suffered no losses in foreign applicants, but their agreement outweighs their differences. And—wonder of wonders!—both support the role of peer review and merit-based competition in allocating federal funds for research. The only difference is in how they label legislative intrusion in the process: Kerry comes right out and calls it "pork."

But in case this analysis makes them look like Tweedledum and Tweedledee, look at their answers carefully. The president and his Democratic challenger have some real differences about core scientific issues: climate change, space, stem cells, and the Endangered Species Act, among others. There's a lot of important stuff here, and it will repay careful reading.

Donald Kennedy
Editor-in-Chief

Published by AAAS

This Week

PAGE 29
Tracing Mars's methane

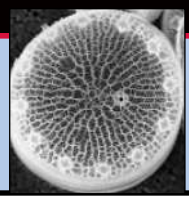

31
Diatoms dissected

EPIDEMIOLOGY

VA Advisers Link Gulf War Illnesses to Neurotoxins

A panel of outside experts chosen by the Department of Veterans Affairs (VA) has concluded that there is a "probable link" between neurotoxins such as sarin gas and the mysterious ailments that struck veterans of the 1990–91 Gulf War. This conclusion—in a draft report obtained by *Science* and scheduled for release later this month—is at odds with other analyses of Gulf War illness, including an August report from the Institute of Medicine (IOM). The VA study also recommends that the VA invest at least $60 million over the next 4 years for additional Gulf War illness research. VA officials declined to comment prior to the report's release on how they might respond.

The VA panel, chaired by former Defense Department official and Vietnam veteran James Binns, was formed in 2002, more than 3 years after Congress passed a law mandating both a new research panel to advise the VA secretary and an expansive IOM review of Gulf War research and treatments. The VA has been under pressure from veterans to de-emphasize the view that stress and trauma were chief drivers of Gulf War illness. "It's clear that something different happened to 1991 Gulf War veterans," says veteran Stephen Robinson, executive director of the National Gulf War Resource Center in Silver Spring, Maryland, and a member of the VA panel.

Exposed? A VA panel says nerve gas in Iraq's Khamisiyah weapons depot, shown here after it was demolished, likely contributed to Gulf War illness.

The authors of the new report argue that neurotoxins are the likeliest explanation for the fatigue, muscle and joint pain, memory loss, and dizziness that has plagued tens of thousands of Gulf War veterans. On the 11-member panel are several veterans and six physician-scientists, including a well-known advocate for this controversial theory: Epidemiologist Robert Haley of the University of Texas Southwestern Medical Center in Dallas. Haley says he was added to the panel after VA Secretary Anthony Principi learned of his views and spent a half-day with him in Texas discussing his work in May of 2001.

But many scientists who study Gulf War cases are unconvinced that low levels of sarin gas, pesticides, or the pyridostigmine bromide pills that troops took to protect them from nerve gas can explain Gulf War illness. For one, they say, it's difficult to determine which troops were exposed to what. Furthermore, many animal and human studies have failed to show that low doses of neurotoxins can cause the kind of problems Gulf War veterans experience (*Science*, 2 February 2001, p. 812).

"I don't know of any serious expert review that has come to these conclusions," says Simon Wessely, director of the King's Centre for Military Health Research in London. Wessely, like many researchers in the field, believes that Gulf War illness arose from a combination of the stress of war, the use of experimental vaccines, and possibly exposures to environmental hazards such as oil-well fires. Because Gulf War ailments are spread evenly across different branches of ▶

FUSION SCIENCE

Europe May Break Out of ITER Partnership

CAMBRIDGE, U.K.—Europe is ready to scrap the planned collaboration on what is supposed to be a global fusion reactor. That's the message from a meeting last week of research ministers from the 25 European Union (E.U.) countries, who set a late-November deadline for deciding whether to press ahead with a French site for the $5 billion International Thermonuclear Experimental Reactor (ITER).

Last month, outgoing E.U. research commissioner Philippe Busquin expressed regret for not having "closed the file" on ITER, whose partners—the E.U., China, Japan, Russia, South Korea, and the United States—have been split for nearly a year over whether to locate the reactor in France or Japan. But in a parting shot, Busquin drafted a letter saying that several ITER partners have a "very strong preference" for the site of Cadarache in southern France and "would support an initiative from the Union to unblock the situation." Last week the ministers appear to have followed his advice, calling on the European Commission to make every effort to negotiate an agreement to build at Cadarache involving "as many partners as possible" and to report back at the council's next meeting on 25–26 November.

The council also ordered the commission to figure out how to fund the project without taking any extra money from E.U. coffers. After the council meeting, French research minister François d'Aubert told reporters that France would double its ITER funding to $1.12 billion, accounting for roughly 20% of the costs. With the E.U. having pledged 40% and Russia and China likely to stake 10% each, that leaves 20% to make up through cost savings or by enlisting new members such as Canada, India, and Switzerland.

The United States and South Korea have voiced support for building ITER at a site in northern Japan. And the E.U.'s solo approach carries increased risk that the success of the project could be compromised. "It would be a tragedy if this leads to an ITER without the United States and Japan," says one European fusion scientist. Worse still, however, would be the possibility of two rival ITERs, one in France and one in Japan—or none at all.

—DANIEL CLERY

CREDIT: DEFENSE DEPARTMENT/AP PHOTO

Published by AAAS

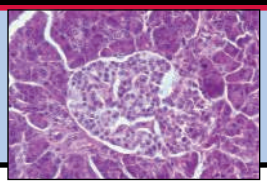

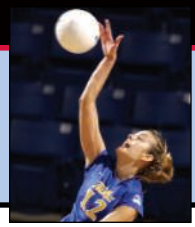

the military, including both the Navy and the Army, Wessely says, the culprits ought to be factors that nearly all troops confronted.

Some experts on Gulf War illness who asked to remain unnamed worry that tying Gulf War illness to neurotoxins overlooks a large number of studies that question the link. For example, a VA-funded study by Larry Davis of the New Mexico VA Health Care System and his colleagues surveyed 1000 Gulf War veterans and 1100 veterans not deployed to the Persian Gulf. The researchers found no evidence of damage to peripheral nerves that distinguished Gulf War veterans from the others.

Haley says the panel considered alternative viewpoints before arriving at its conclusion. Neurobiologist and physician Beatrice Golomb, a panel member from the University of California, San Diego, adds: "There was surprising agreement among the people who put this report together."

But the panel appears to be largely on its own. In August, an IOM report reviewing literature on sarin gas and Gulf War illness concluded that there was "inadequate/insufficient evidence" to link low-dose exposure with persistent neurological symptoms. Still, Lynn Goldman, an epidemiologist at Johns Hopkins University and chair of yet another IOM panel on Gulf War illness, says that it may be too early to rule out any specific cause of this mysterious malady. **–Jennifer Couzin**

CONFLICT OF INTEREST

NIH Proposes Temporary Ban on Paid Consulting

Hoping to allay ongoing controversy about industry consulting by its staff, National Institutes of Health (NIH) officials plan to impose a 1-year ban on all outside paid activities for industry. NIH deputy director Raynard Kington, who announced the proposed moratorium last week, says it will allow NIH to sort out possible ethics lapses and devise a rigorous oversight system. But others worry that the move will further strain valuable ties with companies and make it tougher for NIH to keep top scientists.

The proposed ban comes after months of congressional scrutiny of NIH policies, sparked by a *Los Angeles Times* story last December that reported that some high-ranking NIH scientists had received hundreds of thousands of dollars in payments from industry that posed at least the appearance of a conflict of interest. In June, the House Oversight and Investigations subcommittee announced that some 100 consulting activities reported by drug companies did not show up in NIH's own records (*Science*, 2 July, p. 25). After finding that some of these deals "probably were not appropriately reviewed," NIH has decided it needs a 1-year pause to complete its overall review and make sure new procedures and training are in place, Kington said last week. His memo acknowledges that NIH has found "vulnerabilities in our system."

Kington says NIH will then determine whether to make the ban permanent or allow consulting on "a limited basis." "Clearly, we believe there's value in some of these relationships," Kington says. NIH already plans, however, to permanently ban industry consulting by senior staff members and those who oversee grants.

The moratorium is not a huge shock, say some NIH scientists, because previously approved outside activities were suspended in February for another review. Those consulting arrangements that were reapproved and new ones can continue until the ban takes effect, which probably won't be for a couple of months because NIH first has to propose a new regulation. (NIH says there are 66 active arrangements.) After that, scientists can still advise industry—if they do it for free as part of their job.

Some scientists say the temporary ban will bring welcome clarity, because the rules are confusing now. And scientific exchanges with industry will not end: "Science will move forward," says Robert Desimone, intramural research director for the National Institute of Mental Health, who leaves this month to head the Massachusetts Institute of Technology's McGovern Institute.

Taking a breather. Deputy director Raynard Kington says NIH needs time to address "vulnerabilities" in its ethics system.

But others say the pause—which might end up being closer to 2 years—could be harmful. "You're going to end up losing people from the intramural program," predicts Harold Varmus, president of Memorial Sloan-Kettering Cancer Center in New York City, who as NIH director loosened the rules on consulting in 1995. Several researchers at NIH who consult declined to comment for attribution but suggested that companies may drop their NIH advisers for specific projects and suspend the work while looking elsewhere for advice. This could both jeopardize ongoing research and damage NIH scientists' relationships with the companies, some say.

National Academy of Sciences president Bruce Alberts, who co-chaired a high-level panel earlier this year that advised NIH to continue to permit some industry consulting, says the moratorium is appropriate. However, he warns against a permanent ban, noting that his panel concluded that certain interactions couldn't take place. For example, government employees on official duty are forbidden from signing a confidentiality agreement; companies prefer such agreements so that they can protect shared information. "I think it would be a mistake if this [the ban] were the long-term policy," Alberts says. **–Jocelyn Kaiser**

Parkfield Happens

A scientific event nearly 20 years overdue occurred 28 September near the central California town of Parkfield (population 37) when a magnitude 6.0 earthquake struck. "It was much anticipated but long delayed," says seismologist Ross Stein of the U.S. Geological Survey (USGS) in Menlo Park, California. Attracted by Parkfield's history of quakes every 20 or 30 years, seismologists installed millions of dollars of instruments starting in the 1980s—and then waited. "This is the most well recorded earthquake in history," says USGS's Michael Blanpied.

–Richard A. Kerr

CREDIT: NIH

Published by AAAS

PLANETARY SCIENCE

Heavy Breathing on Mars?

Planetary scientists probing the martian atmosphere through the Mars Express orbiter report that both methane and water tend to be concentrated over the same three equatorial regions of Mars, regions covered by water-enriched soils. The new find further stokes talk of life on Mars, which flared up last March (*Science*, 26 March, p. 1953) when the same researchers first spotted methane on Mars. The gas could be coming from life buried beneath the inhospitable surface. But the association with water raises a new possibility: that researchers are finally seeing wisps of the icy subterranean vault where much of the planet's long-lost water may be stored.

At last week's International Mars Conference in Ischia, Italy, Vittorio Formisano of the Institute of Physics of Interplanetary Space in Rome—the principal investigator on the Planetary Fourier Spectrometer (PFS) instrument on the European Mars Express—refined the picture of methane on Mars. Last spring, he and PFS team members announced the first detection of martian methane at a concentration of about 10 parts per billion.

This time, Formisano could say that the methane is concentrated over the same three equatorial regions—Arabia Terra, Elysium Planum, and Arcadia-Memnonia—where water vapor is concentrated by a factor of 2 to 3 in the lower atmosphere. And those are also three regions, Formisano says, where the U.S. Mars Odyssey orbiter has detected signs of water in the upper meter of martian soil, in the form of ice or hydrated minerals. The coincidence of atmospheric water, methane, and soil water "points to a common source underground," says Formisano. "Then one can speculate as to what that source is."

The methane naturally calls to mind methane-generating bacteria that could live beneath a few kilometers of frozen crust. The accompanying water—a key prerequisite for life—supports that picture. On the other hand, an erupting volcano, a simmering hot spring, or even abiotic reactions between rock and cold ground water could produce methane and water vapor, too.

But some researchers say another source may be more likely still: an exotic mix of methane trapped molecule by molecule in crystalline cages of water ice. Long known on Earth from beneath the deep seabed and within permafrost (*Science*, 13 February, p. 946), such hydrates could form anywhere between 15 meters and as much as several thousand meters beneath the martian surface, according to calculations published in 2000 by Michael Max of Marine Desalination Systems in Washington, D.C., and Stephen Clifford of the Lunar and Planetary Institute in Houston, Texas.

On Earth, hydrate methane usually comes from bacteria decomposing organic matter; on Mars, either life or chemical water-rock reactions could be responsible. Either way, Clifford notes, the martian methane could have been generated and trapped eons ago, as the planet cooled and freezing temperatures crept down through a waterlogged crust. Planetary geologists have seen abundant signs that water shaped the surface of early Mars (*Science*, 6 August, p. 770), and most assume that at least some of that water sank beneath the surface and still resides there. But they've never detected any. Now, they could be seeing it leak out as the methane hydrate slowly decomposes.

Mars too? Methane-trapping water ice, common on Earth, may also be present on Mars, leaking water and methane into the atmosphere.

CREDIT: IAN R. MACDONALD/TEXAS A&M UNIVERSITY, CORPUS CHRISTI

The methane-water coincidence "is a real neat observation," says Clifford, even if "it doesn't uniquely point to life." It does have some hurdles to clear yet, however. The details of the original PFS methane detection have yet to be published, leaving open the possibility that a small part of water vapor's spectral signature has been mistaken for a spectral line of methane. And planetary scientists find it curious that any regional concentration can be recognized at all, because martian weather mixes methane around the planet in a matter of months. Things may get clearer in the next couple of months as PFS data, as well as telescopic observations, come out.

–RICHARD A. KERR

ScienceScope

French Scientists Unhappy Despite Boost in Budget

PARIS—French scientists are disappointed with the government's science spending plan for 2005. But they are not yet protesting the moves. Research minister François d'Aubert last week fulfilled a promise (*Science*, 28 May, p. 1233) by unveiling a plan to channel an additional $1.2 billion a year into public and private research through 2007. The amount includes $400 million for a new national research agency and funding for 150 additional academic scientists next year.

But the planned increases don't fully offset past cuts, critics say. And plans for the new agency "are very vague," says Alain Trautmann, co-director of the cell biology department at the Cochin Institute and a leader of protests that forced the government to backtrack on proposed cuts. For instance, it's not clear whether the agency will focus on basic or applied studies.

The government expects to firm up spending and management plans next month, after the research community presents ideas for reforms due to take hold next year. In the meantime, science groups say they could be back in the streets early next year if the government doesn't address their concerns.

–BARBARA CASASSUS

Seeing Planetary Double

NASA should think twice before moving ahead with two separate missions to find extrasolar planets, says a National Academy of Sciences report requested by the space agency in January and released this week.

NASA initially intended to pursue just one of two methods for detecting distant Earth-sized planets that might harbor life: an infrared interferometer, or a coronagraph for the Terrestrial Planet Finder probe. But in January, NASA decided to do both. The coronagraph would be launched in 2014, followed in 2020 by a joint U.S.-European interferometer.

The possibility of combining data from both missions is intriguing, said the 11-member academy panel led by Wendy Freedman of the Carnegie Observatories in Pasadena, California. But NASA needs to make a stronger scientific case for the coronagraph mission, which it describes as "expensive and challenging." Ultimately, funding both missions could "delay or even preclude" other space science efforts listed in the community's 2000 decadal plan, the panel says. NASA has not yet responded to the report.

–ANDREW LAWLER

Published by AAAS

U.S. SCIENCE BUDGET

NSF, NASA Meet 2005 Request After 'Bonus' From Senate Panel

A Senate spending panel has done some creative accounting to meet the president's request for NASA and the National Science Foundation (NSF) in a tight budget year. But the strategy comes at a price that many scientists may find objectionable, and there is no guarantee that the subterfuge will even hold up when Congress returns after the November elections to complete its work on the overdue 2005 budget.

A bitterly partisan presidential campaign, a massive deficit, and the ongoing war in Iraq have made it harder for legislators to cut the deals normally required to pass the 13-piece federal budget, and the slice that includes NSF and NASA is one of the most contentious. Last week the Senate Appropriations Committee tiptoed through that minefield by declaring $2 billion in the $93 billion bill to be emergency funding and, therefore, exempt from a self-imposed spending cap. Some $800 million of that largesse went to NASA—for getting the shuttle ready to fly again and preparing a mission to rescue the failing Hubble Space Telescope. That raised NASA's budget to $16.4 billion, some $200 million more than the president's request and $1.2 billion above the level approved earlier by its counterpart panel in the House of Representatives.

The emergency label also allowed legislators to meet the president's NSF request for $5.74 billion. That represents a 3% boost over current spending instead of a 2% cut, to $5.47 billion, adopted by the House panel. In another bit of good news, a separate Senate committee last week approved the nomination of acting director Arden Bement, raising hopes that he will be confirmed before the Senate recesses later this month.

Major Research Facilities at NSF

	2005 Request (in millions)	House Panel (in millions)	Senate Panel (in millions)
Continuing			
ALMA	$49.7	$49.7	$49.7
IceCube	$33.4	$51.2	$33.4
EarthScope	$47.3	$47.3	$47.3
New Starts			
NEON	$12.0	$0	$0
Ocean drilling vessel	$40.8	$30.0	$0
RSVP	$30.0	$30.0	$0

SOURCE: HOUSE, SENATE APPROPRIATIONS COMMITTEES

False start. A Senate spending panel doesn't want to fund three new research projects in NSF's 2005 budget request.

The larger Senate figure for NSF includes some unpleasant surprises, however. The most unsettling is the panel's rejection of three new starts in NSF's major facilities account. The panel "saved" a total of $82 million by blocking funding to begin construction of a high-energy physics project called RSVP, a refurbished ocean drilling vessel, and a network of ecological observatories. The House has funded the first two. At the same time, the Senate panel reminded NSF of its promise to request $50 million next year for an Alaska-based research vessel, a home-state project favored by panel chair Ted Stevens (R–AK).

The legislators also cautioned NSF to follow a recent report from the National Academies on how it decides which big new projects to fund (*Science*, 16 January, p. 299). Congress ordered that report after scientists complained about a growing backlog of projects—a situation that, ironically, would recur if the panel's "no new starts" dictum prevails.

NASA gets a $200 million increase over the president's request—but much of it is eaten up by congressional earmarks, projects not backed by the agency. The committee warned the agency not to forget science in its push to return humans to the moon and called for a National Academy of Sciences panel to examine the role of science in the new exploration effort. This action came the same week that a new study by the National Academies warned NASA not to sacrifice solar physics for its new exploration initiative.

–ANDREW LAWLER AND JEFFREY MERVIS

SCIENTIFIC PUBLISHING

Suit Seeks to Ease Trade Embargo Rules

Journals should be free to edit and publish articles by scientists and other authors living in countries under U.S. trade embargoes, says a suit filed this week by a coalition of publishers and authors. Current regulations require U.S. publishers and authors to seek a government license before working with authors in Iran, Cuba, and Sudan; these rules violate trade laws and the freedom of speech, according to the suit, filed 27 September in U.S. federal court in New York City.

The issue has been simmering since October 2003, when the Treasury Department's Office of Foreign Assets Control (OFAC) ruled that U.S. journals needed prior government approval to publish work from embargoed countries (*Science*, 10 October 2003, p. 210). After a heated discussion with publishers, OFAC reversed that ruling 6 months ago but asserted that activities leading to "the substantive or artistic alteration or enhancement" of materials from the embargoed countries were still prohibited without a license. In a 2 April letter to the Institute of Electrical and Electronics Engineers, OFAC Director Richard Newcomb explained that the agency was enforcing the Trading with the Enemy Act and the International Emergency Economic Powers Act.

But OFAC's regulations are illegal, say the Association of American Publishers, Association of American University Presses (AAUP), PEN American Center, and Arcade Publishing. The plaintiffs argue that OFAC has violated 1988 and 1994 revisions to these laws that exempt "information and informational materials" from trade embargoes. OFAC maintains that the 1988 and 1994 revisions do not apply to informational materials "that are not fully created and in existence."

The restrictive regulations "should be stricken from the books because they violate the very statutes that OFAC is purporting to enforce," says Peter Givler, executive director of AAUP. OFAC's rulings have already had "a chilling effect" on the publishing climate, says Givler, citing a recent decision by the University of Alabama Press to suspend plans for publishing archaeology and history books by Cuban scholars.

Publishers were compelled to take the legal route because of OFAC's "double-talk," says Mark Brodsky of the American Institute of Physics. "Sometimes they say editing that involves changing syntax will require a license; when pressure is put on them, they say it's not necessary. Publishing should not be subject to the whims of the bureaucracy."

OFAC spokesperson Molly Millerwise says the agency has no comment on the suit, which asks the government to remove the publishing restrictions.

–YUDHIJIT BHATTACHARJEE

GENETICS

DNA Reveals Diatom's Complexity

Diatoms are an enigma. Neither plant nor animal, they share biochemical features of both. Though simple single-celled algae, they are covered with elegant casings sculpted from silica.

Now a team of 45 biologists has taken a big step toward resolving the paradoxical nature of these odd microbes. They have sequenced the genome of *Thalassiosira pseudonana*, which lives in salt water and is a lab favorite among diatom experts. The work should prove useful to ecologists, geologists, and even biomedical researchers, says Edward Theriot, a diatom systematist at the University of Texas, Austin: "We've just jumped a generation ahead by having this kind of understanding of this genome."

Diatoms date back 180 million years, and remnants of their silica shells make up porous rock called diatomite that is used in industrial filters. Today diatoms occupy vast swaths of ocean and fresh water, where they play a key role in the global carbon cycle. Diatom photosynthesis yields 19 billion tons of organic carbon, about 40% of the marine carbon produced each year; thus, by processing carbon dioxide into solid matter, they represent a key defense against global warming.

Many marine organisms feast on diatoms. When conditions are ripe, the algae can multiply at astonishing rates, creating ocean "blooms" that are sometimes toxic. These blooms can suffocate nearby marine life or make a toxin that harms people who eat infected shellfish. "This is a group of organisms that has amazing importance in global ecology," says Deborah Robertson, an algal physiologist at Clark University in Worcester, Massachusetts.

Since 2002, Daniel Rokhsar, a genomicist at the DOE Joint Genome Institute in Walnut Creek, California, and his colleagues have been unraveling the genome of *T. pseudonana*. They were aided by a technique called optical mapping, in which stretched-out chromosomes are nicked by enzymes and viewed through a light microscope. Those nicked pieces of DNA stay in order and enable the sequencers to assemble almost all the bases in the correct place on the right chromosomes.

The draft genome consists of 34 million bases, Rokhsar, E. Virginia Armbrust, an oceanographer at the University of Washington, Seattle, and their colleagues report on page 79 of this issue. They ultimately found about 11,500 genes along the diatom's chromosomes and along the DNA in its chloroplast and mitochondria.

Analyses of these genes and the proteins they encode confirm that diatoms have had a complex history. Like other early microbes, they apparently acquired new genes by engulfing microbial neighbors. Perhaps the most significant acquisition was an algal cell that provided the diatom with photosynthetic machinery.

Some biologists hypothesize that diatoms branched off from an ancestral nucleated microbe from which plants and animals later arose, a theory supported by the identification of *T. pseudonana* genes in some plant and animal genomes. As diatoms, plants, and animals evolved, each must have shed different genes from this common ancestor. As a result, diatoms were left with what looks like a mix of plant and animal DNA, plus other genes that are remnants of the engulfed algae.

The new data support this complex scenario, says Robertson. Some 182 *T. pseudonana* proteins are related only to red algae proteins; another 865 proteins are found just among plants. About half the proteins encoded by the rest of the diatom's genes are equally similar to counterparts in plants, animals, and red algae.

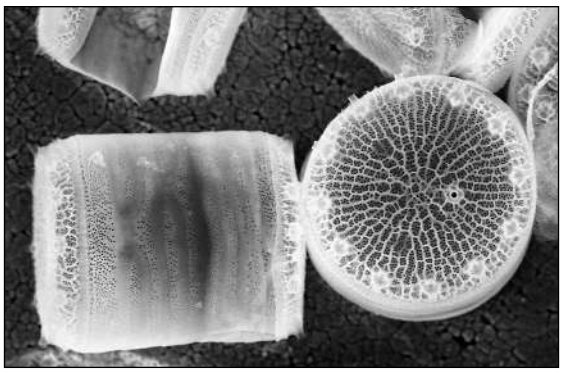

CREDIT: E. V. ARMBRUST *ET AL.*

Aqueous snowflake. The sequence of a diatom should reveal the secrets of its decorative shell.

The newly analyzed genome has also begun to shed light on how a diatom constructs its intricately patterned glass shell. So far, Rokhsar and his colleagues have uncovered a dozen proteins involved in the deposition of the silicon and expect to find more. Such progress could be a boon to materials scientists. "Being able to understand [silica processing] should have a payoff in nanofabrication," says Robertson.

Currently, a mere 100 or so researchers call themselves diatom specialists. With the genome in hand, interest in diatoms is going to expand, Theriot predicts: "It will help put diatoms on everyone's radar."

–ELIZABETH PENNISI

ScienceScope

Experts Probe Flu Death, Call for Poultry Vaccination

A 26-year-old woman in Thailand who died of avian influenza earlier this month probably contracted the disease from her daughter, researchers said this week. But World Health Organization (WHO) scientists are cautiously optimistic that the development is not the start of a major outbreak. Meanwhile, several global health groups are calling for increased vaccination of Southeast Asia's poultry flocks in a bid to corral the dangerous H5N1 virus.

Researchers say the woman, who lived in the Bangkok area, had returned to a rural village in northern Thailand to care for her sick daughter, who probably contracted the virus from local chickens. The daughter was cremated before researchers could collect tissue samples that could confirm her illness. But tissue samples from the mother proved positive for H5N1. The woman's sister has also tested positive for the virus and is in a hospital isolation ward.

Evidence to date suggests a case of "nonsustained, dead-end transmission," says WHO virologist Klaus Stöhr. Similar cases have been documented in the past. But until the WHO collaborating center in Atlanta, Georgia, analyzes the new samples, experts won't know definitively whether the virus has mutated to a more dangerous form. So far, says Stöhr, Thai authorities have detected no increase in respiratory disease among villagers or health workers who cared for the patients.

To keep the virus in check, governments should be vaccinating and not just culling poultry flocks, the United Nations Food and Agriculture Organization and the World Organisation for Animal Health said in a 28 September statement. China and Indonesia already have vaccination programs. But Thailand and other nations do not, in part because poultry exporters fear importing countries will ban products from vaccinated birds, which don't exhibit flu symptoms but can still carry the virus.

–DENNIS NORMILE

Boehlert Has Bypass

Representative Sherwood Boehlert (R–NY) is taking an unexpected break from his duties as chair of the House Science Committee. Boehlert this week underwent triple coronary bypass surgery at the National Naval Medical Center in Bethesda, Maryland, after doctors discovered several blocked arteries. He's expected to be back to work within weeks.

–DAVID MALAKOFF

Published by AAAS

NONPROFIT WORLD

Santa Fe Institute Seeks President

SANTA FE, NEW MEXICO—Barely 15 months into a 5-year term, Robert Eisenstein has stepped down as president of the Santa Fe Institute (SFI) here. His sudden departure last month has reopened debate about how to run the $7 million institute, which has done pioneering work on chaos theory and complex systems.

"The chemistry didn't work," says Robert Denison, a financier and chair of the institute's board of trustees. "It just wasn't a good fit." Denison says that the twin issues of attracting scientific talent and funding were key factors in the board's decision. "I look forward very much to a return to life as a full-time research scientist and educator," says Eisenstein, a physicist and former senior manager at the National Science Foundation who is remaining at SFI as a resident faculty member.

Founded in 1984 by physicists George Cowan, Murray Gell-Mann, and others, SFI bills itself as a "unique environment for visiting and resident scientists." The culture is shaped by a constantly changing cast of characters, the result of a strict no-tenure rule: Resident faculty members receive a 3-year appointment, renewable once, while hundreds of other scientists come for periods ranging from one day to several years. This spring, as three of SFI's core faculty members approached the end of their second terms, two accepted tenured academic jobs: Walter Fontana at Harvard Medical School's systems biology program, and James Crutchfield at a new Center for Computational Science at the University of California, Davis.

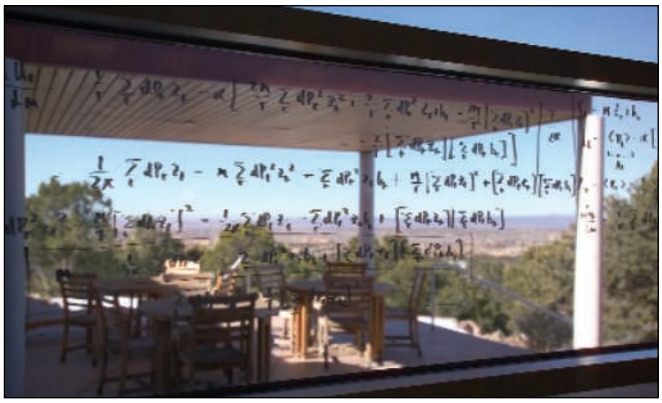

Bright ideas. A gorgeous campus in the mountains is one attraction of the Santa Fe Institute.

The third, J. Doyne Farmer, had his contract extended this summer by a special action of the board of trustees.

The personnel moves created anxiety about the next generation of SFI scientists and whether they would enhance the search for answers to the hard interdisciplinary problems that have attracted people to SFI. "This place runs on people and their ideas," says resident faculty member Ellen Goldberg, an immunologist who stepped down at the end of 2002 after 6 years as president. "As president you try to bring in people familiar with how universities operate but frustrated by their inability to pursue their ideas within traditional academic boundaries."

"Bob took a lot of heat for what happened, even though it was board policy, and [the departing faculty] landed great jobs," says Denison. "I might have acted sooner [to replace them], but Bob felt that he needed to know where we were headed before he could recruit and raise money." Eisenstein's oft-expressed desire to apply SFI's science to societal problems and to inject more science into the local schools, Denison adds, bumped up against faculty members who saw those efforts as a possible distraction from SFI's primary mission to do fundamental research.

Eisenstein plans to work on global sustainability, problems linked to scaling phenomena, and science education. Denison says that he hopes to name an interim president shortly and that SFI has begun an international search for someone who combines scientific achievement with fundraising and organizational skills.

–JEFFREY MERVIS

CANCER RESEARCH

Pioneering Prevention Institute Declares Bankruptcy

A small but influential U.S. research institute known for exploring links between lifestyle and cancer has closed its doors after 35 years. The Institute for Cancer Prevention (IFCP), the only center funded by the National Cancer Institute (NCI) that focused solely on prevention, declared bankruptcy last week and has laid off its roughly 100 employees.

Researchers at the Valhalla, New York–based institute are devastated, and outsiders are lamenting the demise of a group that helped launch the field of cancer prevention—the idea that proper diet and behavior can ward off cancer. "I feel so angry, so unhappy. … Scientists here really put this place on the map," says Karam El-Bayoumy, IFCP's director of research. Meanwhile, some employees want an investigation into what led to the institute's downfall.

Originally called the American Health Foundation, the institute was founded in 1969 by physician Ernst L. Wynder, who 19 years earlier had published a landmark study linking smoking and lung cancer. The foundation's scientists and clinicians built an international reputation for research into everything from tobacco carcinogenesis to the protective effects of green tea. "It really was the flag bearer" for cancer prevention, says oncologist Steven Clinton of Ohio State University in Columbus.

By the time Wynder died in 1999, however, the institute was in financial trouble. To rejuvenate the group, the board hired Donald W. Nixon of the Medical University of South Carolina, who changed its name and expanded clinical research. But its problems grew worse: In January, Nixon informed the board that IFCP had overdrawn funds provided by approximately 15 NCI grants to meet its $18-million-a-year budget. NCI subsequently calculated that IFCP owed it $5.7 million.

"We were caught totally by surprise," says Michael Epstein, chair of IFCP's board and an attorney with Weil, Gotshal & Manges in New York City. IFCP explored a number of possible solutions, Epstein says, including selling the lease on its building or merging with another group willing to take on the debt. But on 21 September, after NCI refused to advance the institute any more money and a biotech company rejected a last-ditch merger offer, IFCP filed for Chapter 11 bankruptcy. A federal judge has since appointed a trustee to liquidate its assets.

Some employees accuse Nixon of mismanagement and question the cost of the institute's Manhattan office. They have asked New York officials to probe several of IFCP's actions, including its alleged failure to make some employee retirement payments over the past year. Nixon could not be reached.

In the meantime, NCI has offered to help researchers move their grants and laboratories to other institutions; at least five of the 15 or so principal investigators are moving 315 kilometers to Pennsylvania State University's medical campus in Hershey. "Hopefully, science will continue to be served," says Epstein, "albeit at other institutions."

–JOCELYN KAISER AND DAVID MALAKOFF

CREDIT: ROBERT BUELTEMAN

Published by AAAS

Will the Edmonton protocol, hailed as a major step toward a cure for type I diabetes, hold up in the long run?

Islet Transplants Face Test of Time

Ellen Berty was driving home from her special-education job when the call came, on the cell phone she'd bought expressly for this purpose. The caller spoke the magical words every person needing a transplant dreams of hearing: "We have a match." In her Mazda convertible, Berty let out a yell of triumph. "I'd won the contest of my life," she recalls thinking on that sunny June day 3 years ago.

Ten hours later, Berty lay sedated in a radiology suite at the National Institutes of Health (NIH) in Bethesda, Maryland, while doctors delicately injected a yellowish green solution into a vein feeding into her liver. The mix held hundreds of thousands of islets, cells from the pancreas of a man who'd died suddenly. These cells were supposed to supply Berty with the critical hormone insulin she'd lacked for 40 years, ever since being diagnosed with type I diabetes at the age of 13.

All smiles, in this case. Ellen Berty and her NIH doctor David Harlan both say her islet transplant was a success. But Harlan worries that not everyone has been so lucky.

CREDIT: CHRIS MADDALONI

Berty's islet-cell transplant is part of a vast global experiment, a test of a therapy that's been hailed as the greatest hope for curing type I diabetes. Five years after physicians in Edmonton began transplanting islets under a new and widely celebrated protocol, the long-term results of this strategy are beginning to emerge. They paint a nuanced and still unfinished picture of a treatment that some doctors concede is riskier than they expected and less effective than they had hoped.

The NIH trial in which Berty enrolled reflects the promise and peril of these transplants. Berty has been one of the lucky ones. She stayed off insulin injections for 2 years after her transplant. Today, she's back on a low dose, but she has relatively few side effects from the immunosuppressive drugs she takes to prevent islet rejection. Like most islet recipients, Berty also has none of the diabetes complications she suffered before.

Still, Berty was NIH's last islet-transplant patient. After treating her and five others, NIH stopped accepting new volunteers, its physicians increasingly anxious that antirejection drugs, which must be taken for life, were spawning problems worse than those the transplanted islets were solving.

Other centers disagreed. They continued testing the procedure, and today more than 300 patients have received islets under the protocol crafted by the Edmonton team. NIH, the Juvenile Diabetes Research Foundation (JDRF), other nonprofit organizations, and several European governments have poured hundreds of millions of dollars into coaxing these transplants to work. But as islet transplants expand and less experienced centers launch islet programs, it's become less clear what "work" really means.

The original goal of islet transplants has been met: Lifelong diabetics receiving new islets have been able to abandon, at least for a time, insulin shots. According to an NIH survey published last month, 22 of 38 islet recipients were still off insulin a year after their transplant. Those numbers sag with time, though, and it's not known how long transplanted islets can thrive, or what's killing them when they fail.

A more pressing question is whether insulin independence is enough. A sizable minority of islet recipients struggle with new health problems, from painful mouth ulcers to anemia to kidney disease, largely attributed to the combination of antirejection drugs prescribed by the Edmonton protocol. And no one knows whether patients given islets actually live longer than they would have without them. A controversial study from some of the NIH scientists who treated Berty hints that the risk of a shortened life span might be real.

Physicians are launching clinical trials to improve the safety and effectiveness of islet transplants, but they're far from offering this experimental therapy to all but the most severely affected diabetes patients. For one, there aren't enough cadaver pancreases to go around. Although many are looking at stem cells as a renewable source of islets, that's still a distant prospect.

Aldo Rossini, director of the diabetes division at the University of Massachusetts Medical School in Worcester, compares the current state of islet transplants to the Wright brothers' first flight. "They flew a couple hundred feet"—a remarkable accomplishment at the time, he notes. Still, says Rossini, "no one could have expected us to fly to California in that plane."

Measures of success

Since 1972, when Paul Lacy, a researcher at Washington University in St. Louis, cured diabetic rats by giving them healthy islets, transplanters have sought to extend that success to humans. The approach seemed obvious: In type I diabetes, the

Published by AAAS

body's immune system mistakenly attacks insulin-producing islet cells in the pancreas, and by the time the symptoms of diabetes surface, most of these islet cells are gone. But in more than 400 human islet transplants beginning in the 1970s, doctors couldn't get transplanted cells to stick. Many suspected that, ironically, the steroid drugs given to prevent islet rejection were also toxic to islet cells.

Then in the summer of 2000, the dreary world of islet transplants changed forever. A team at the University of Alberta in Edmonton, Canada, reported in *The New England Journal of Medicine* that they'd given islets to seven diabetes patients under a new regimen, and after roughly a year, all seven were still off insulin.

Unlike earlier islet transplants, the Edmonton protocol didn't involve steroids. Led by James Shapiro, the Edmonton team combined three antirejection drugs, one of which, sirolimus, had recently begun human testing. It also gave patients islet cells from multiple pancreases.

The group's report instantly became medical legend. "Here," says David Nathan, director of the diabetes center at Massachusetts General Hospital in Boston, "was this absolute miracle."

Research funders quickly responded to Edmonton's success. JDRF, one of the country's wealthiest and most powerful disease advocacy groups, declared islet transplants a top priority, and since 2000 it has poured $225 million into the field. Hospitals in the United States and Europe raced to set up islet-transplant centers, and patients flocked to them in droves. Emory University's 18-month-old islet-transplant program has fielded 5500 inquiries from patients, says surgeon Christian Larsen, its director. Constrained by strict entry criteria and a tight budget, Emory has given transplants to just six.

Like others in the field, Larsen believes that ideal islet-transplant candidates are patients who, despite their best efforts, cannot control their blood sugar. More dangerously, their bodies have lost the ability to sense blood sugar lows, resulting in sudden fainting spells, seizures, and even comas or death. For patients like Berty, who suffered middle-of-the-night seizures and blackouts while driving, the condition is terrifying and profoundly disruptive. It's these patients—maybe 1% of type I diabetics—who islet transplanters welcomed into clinical trials. "Every patient we take on, they're near death's door or in desperate straits," says Shapiro.

Transplanters quickly found, however, that the success of the Edmonton protocol is tough to sustain; the new islets seem to fade over time. Experienced islet-transplant centers like Edmonton, the University of Miami, and the University of Minnesota, Twin Cities, boast insulin independence rates of 80% to 90% a year after transplant, far higher than the rates of many smaller centers. After 3 years, that falls to 60% among Miami's patients, says Camillo Ricordi, scientific director of the Diabetes Research Institute there. Mark Atkinson, a pathologist who studies diabetes at the University of Florida, Gainesville, and research chair of JDRF, recently reviewed unpublished data on patients from Edmonton, 3 to 4 years after their transplants. Between 12% and 25% were insulin independent, he says. Among the original Edmonton seven, only two remain off insulin, says Shapiro.

"Something is not going in the right direction long term," says Ricordi. One possibility, he says, is that the antirejection drugs, although less toxic to islets than steroids, still harm the cells. Some nondiabetic patients taking the drugs after receiving liver, heart, or kidney transplants have developed diabetes, notes David Sutherland, chief of transplantation at the University of Minnesota.

A more fundamental problem may be that the immunosuppressive drugs can't erase the underlying autoimmune response that killed a patient's original islets. "These people don't like islets, no matter whose they are," says Peter Senior, an endocrinologist at the University of Alberta.

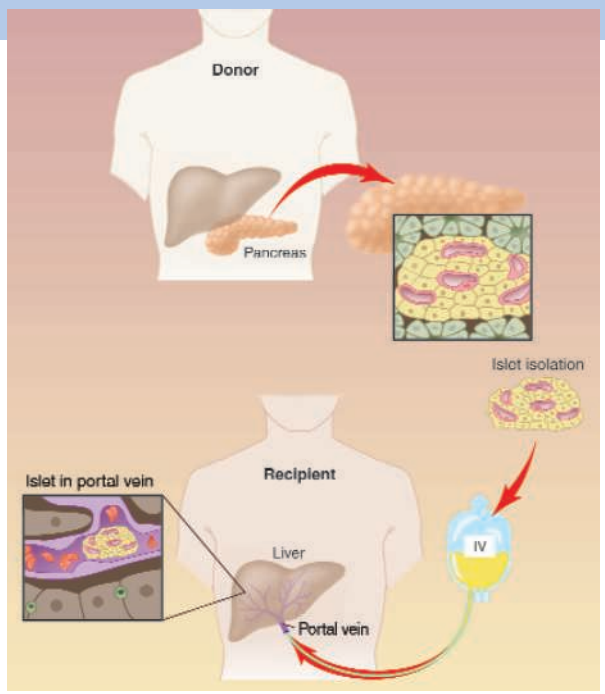

Out and in. After extracting islets from a pancreas, doctors infuse them into a diabetes patient.

Another explanation for islet failure is that patients may be receiving too few islets, even if they get cells from multiple donors. A normal pancreas has roughly 1 million islets, but current techniques allow only about 400,000, at most, to be extracted from a donor pancreas. Moreover, unknown numbers die soon after they're transplanted, forcing the rest to labor unusually hard to supply enough insulin. The islet cells may just "poop out" over time, says Sutherland.

Edmonton found that giving patients islets from as many as three pancreases could sustain insulin production longer. But pancreases are a scarce and costly resource. Fewer than 2000 are donated each year, and most go toward whole-organ pancreas transplants for diabetes. In the United States, they also cost from $15,000 to $25,000 each.

Increasingly, however, transplanters are wondering whether insulin independence, a goal pushed heavily by islet-transplant centers, funders, and many patients, is the only yardstick by which to measure islet-transplant success. Patients like Ellen Berty and others who have gone back on insulin have found that partial islet function can stave off the hypoglycemia they experienced before their transplants. This has doctors hoping that islet transplants might prevent long-term complications of diabetes, even if recipients still need some insulin. "Even if they're not off insulin," says Shapiro, "their problems go away."

Walking a tightrope

But what if the therapy is as bad as the disease? Last month, the risky nature of these transplants was underscored by NIH's first report from its Collaborative Islet Transplant Registry. None of the 86 islet recipients NIH surveyed died from the procedure. But the agency cataloged 20 serious adverse events linked to islet transplants. They include four cases of life-threatening neutropenia, a depletion of white blood cells caused by antirejection drugs. "Islet transplants are still incredibly experimental," says Ricordi.

> "Here was this absolute miracle."
> —David Nathan, Massachusetts General Hospital

Amy Parker learned that the hard way. Parker, who asked that her real name not be used, was diagnosed with type I diabetes as a teenager. As her disease became progressively more unmanageable, she began having seizures from low blood sugar, and blood

CREDIT: K. SUTLIFF/*SCIENCE*

Believer. James Shapiro pioneered the Edmonton protocol, in which more than 300 patients with diabetes have participated.

vessels behind her eyes started to leak. She needed multiple laser eye surgeries to preserve her vision.

In 1999, soon after Edmonton began its revolutionary set of islet transplants for patients like her, she applied. In November and December 2002, Parker underwent two separate islet transplants.

Then, her new ordeal began.

Since receiving the transplants, her insulin requirements have dropped to a quarter of what they once were, and she no longer suffers seizures or hypoglycemia. But every day she experiences "deathly horrible" headaches, a result of the antirejection drugs, she learned. Two summers ago, she began having trouble breathing while on a family vacation in British Columbia. In July, she was switched from the drug sirolimus, a possible culprit, to mycophenolate, another immunosuppressant. If that fails to help her, says Parker, she may drop out of the study and lose her islets.

The experimental nature of islet transplants was further driven home last June at the American Diabetes Association meeting in Orlando, Florida, where the Edmonton team released troubling kidney function data on its first 45 islet-transplant patients. Of the five patients Edmonton has followed for 4 years, two have "quite bad renal outcomes," including one who has required dialysis, says Senior. Overall, a third of the 45 have high levels of a protein in their urine that's normally a harbinger of declining kidney function.

On the other hand, about a fifth of diabetes patients typically develop kidney disease. Says Senior, "These people may well have ended up with kidney failure irrespective of transplant. The question is, are these drugs hastening that?"

Changing course

It's mixed news like this that has dampened enthusiasm among a handful of doctors who once believed islet transplants were ready for patients. One is David Harlan, a diabetes specialist at the National Institute of Diabetes and Digestive and Kidney Diseases (NIDDK) in Bethesda, Maryland, who treated Berty. Like his colleagues around the world, Harlan was enthralled by the Edmonton protocol when it first appeared. In late 2000, he pulled together a transplant team and more than $1 million in NIH funding to launch an islet-transplant program at NIH. From 29 December 2000 through 14 June 2001—the date of Berty's transplant—he and his colleagues performed transplants in six women with severe type I diabetes.

The team quickly grew troubled by what it was seeing. Looked at through the lens of diabetes, the picture was relatively rosy: Four of six patients became insulin independent, and three stayed that way for at least a year and a half. Even those who still needed some insulin no longer suffered the hypoglycemic episodes that had driven them to this experimental trial in the first place.

> "Something is not going in the right direction long term."
> —Camillo Ricordi, University of Miami

But problems abounded. Two patients, including one off insulin, had to discontinue immunosuppressants because of the intolerable side effects, such as deteriorating kidney function, and their bodies rejected the islet cells. Even Ellen Berty, the NIH success story, ran into some trouble. In her first year after the transplant, the antirejection drugs contributed to a severe foot infection and caused mouth ulcers so large that NIH dentists photographed them for use in a textbook. For Harlan, the price NIH islet recipients were paying didn't seem worth it.

"When you expand the experience, you find problems that were not expected," says Antonio Secchi, head of the transplant program at Milan's University Vita-Salute San Raffaele, one of about four major European islet-transplant centers. Two of his center's 10 islet recipients who became insulin independent have since dropped out of the program because of drug side effects.

One central question that preoccupies Harlan is whether islet recipients will live longer than those in comparable health who don't receive transplants. It's too early to answer that question directly, so Harlan turned to data on pancreas transplants. They have been used for years in much the way islet transplants are now, although most are given to diabetes patients who also need kidneys.

Harlan and his colleagues examined data from 124 transplant centers in the United States from 1995 to 2000 and arrived at an unsettling conclusion: Patients receiving a solitary pancreas or a pancreas after a kidney transplant were more likely to die within 4 years than those still on the waiting list.

Published last December in the *Journal of the American Medical Association*, the article touched off a furor. Many transplant surgeons disputed its results. Minnesota's Sutherland and his colleague Rainer Gruessner have reanalyzed the data, and Sutherland says they've arrived at a conclusion opposite to Harlan's. Some patients in Harlan's study, says Sutherland, were on the waiting list of more than one hospital and ended up being counted twice. The study also excluded patients awaiting pancreas transplants who had very poor kidney function; Harlan worried that that might produce misleading results, but Sutherland believes those patients should be included.

Concerns about long-term survival after an islet transplant, however, must be weighed against the improved quality of life that many transplant recipients experience, at least initially. "The psychological benefit of insulin independence is potentially enormous," says Emory's Larsen, "and it's hard to understand for a nondiabetic."

Rita Hart, 46, is off insulin after undergoing three transplants at Miami over 2

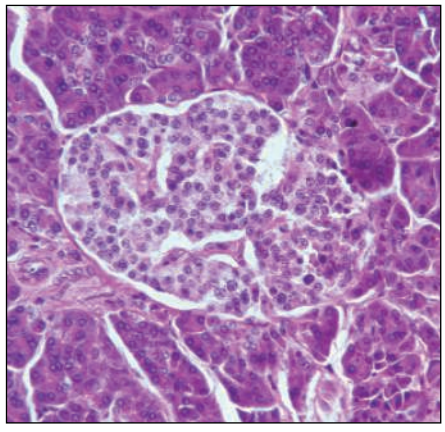

Donation in demand. Islet cells such as these are in short supply for transplants.

CREDITS (TOP TO BOTTOM): COURTESY OF OFFICE OF PUBLIC AFFAIRS/UNIVERSITY OF ALBERTA; MANFRED KAGE/PETER ARNOLD

Published by AAAS

years, the last in July 2003. Before her transplant, diabetes was consuming her life and complications were piling up. "I was losing hope," she says. Now, despite drug side effects that include anemia, she feels vastly more optimistic.

"It's striking how many patients ask for a third transplant," says Senior. "Even with all the side effects and all the downsides, they still think it's a good thing."

And so Edmonton, like many other islet-transplant centers, continues to grow. Today, more than 25 hospitals have performed islet transplants that hew closely to the Edmonton protocol. NIH will soon announce $75 million in awards for a new clinical islet transplantation consortium in which centers will collaborate on islet studies. Although Harlan ended his islet-transplant trial early, the agency believes the treatment is worth pursuing. "This is not a black-and-white issue," says Allen Spiegel, director of NIDDK.

Roadblocks to expansion

New money, however, will go only so far: Islet transplants are extraordinarily expensive, costing up to $200,000 in the United States for one patient in the first year. Anti-rejection drugs add another $30,000 annually after that. At centers like Miami, where most patients remain part of a protocol, the price of success—of supporting patients for years after a transplant—is becoming prohibitive, says Rodolfo Alejandro, an endocrinologist and director of the clinical islet-transplant program at the University of Miami. (Costs in Canada are somewhat lower because there's no charge for organs, and the Alberta health care system agreed in 2001 to pay for transplants for Alberta residents.) Because they're still considered experimental, most United States islet transplants are funded by NIH, JDRF, and sometimes by pharmaceutical companies that manufacture immunosuppressants.

Costs are one roadblock to performing the kind of large, controlled studies that some say are needed before islet transplants can shift from being an experimental therapy to being one approved by the U.S. Food and Drug Administration (FDA). Some islet transplanters, like Alejandro, believe that one option is for FDA to approve the therapy under its existing "orphan drug" category, making it available to essentially the same patients getting islets now—those with uncontrolled diabetes. That way, it could be covered by insurance. A year ago, FDA held a public advisory committee meeting in Gaithersburg, Maryland, and agency officials made clear they want certain issues addressed first. Those include consistency in how islets are processed and a better assessment of the risk-benefit balance.

No matter how FDA rules, major hurdles stand in the way of islet transplants going mainstream. First, the shortage of donor pancreases means scientists must find a renewable source of islets. One popular option would involve using some type of stem cell. This year, JDRF has committed more than $8 million to stem cell research, more than $6 million of it to human embryonic stem cell work. Yet creating islets from stem cells isn't imminent, according to Larsen and other transplanters.

Milder immunosuppressive regimens might come more rapidly. One study that's gearing up at Miami calls for giving islet recipients a dose of bone marrow cells culled from the donor's vertebrae, to try to help patients better tolerate the islet cells.

Current islet recipients, and the many more people with diabetes hoping for a transplant, are eagerly awaiting the day when islet transplants are easier to come by and gentler to receive. But Berty remains upbeat. A book she's written chronicling her experience came out this spring. Its title: *I Used to Have Type 1 Diabetes: Kiss My Islets*.

—JENNIFER COUZIN

Research Community

Science Weathers the Storms

Researchers struggle to keep their work on track in the wake of recent hurricanes

On a small beach in southeastern Florida near Fort Lauderdale, marine biologist Jeanette Wyneken races to collect as many loggerhead sea turtle nests as possible before the full brunt of Hurricane Frances hits. She fills her car with all she can carry and records the GPS coordinates of the nests she must leave behind, hoping that they will still be there when she returns. Her efforts are not entirely selfless, though: She's also guaranteeing that, while the storm wreaks havoc outside, her research on a threatened species can continue in the lab.

Wyneken—like many scientists at southeastern universities and institutions—faced a rare challenge in this season's record string of hurricanes. Many had to battle power outages, flooding, and even police barricades to keep their work on track. Not all succeeded. The hurricanes—Charley, Frances, Ivan, and Jeanne—destroyed sensitive equipment and reagents, set back research, postponed conferences, and forced the extension of grant deadlines. This chain of storms "has been a huge disruption," says University of South Florida oceanographer Frank Muller-Karger, whose St. Petersburg lab had to move its computers into bathrooms to avoid losing data when Charley hit. "It's been an incredibly stressful period."

At Cape Canaveral, even before Frances began pounding the beaches, scientists at the Kennedy Space Center faced some tough choices. "Packing our spacecraft up would set the launch date back at least 2 weeks and cost a couple million dollars," says Neil Gehrels, who heads NASA's Swift gamma ray observing satellite project. But he was loath to take a chance, because "NASA is very cautious with its equipment."

In the end, Gehrels instructed his team to seal the satellite in an airtight metal container and move it to a secure hangar. His prudence proved correct. The space center took a direct hit from Frances, suffering the worst damage since it was established in 1963. Even though the launch date was delayed by the move and subsequent evacuation of personnel, Gehrels says the alternative would have been much worse. "Swift would have taken 5 years to rebuild," he says, "to say nothing of the cost."

Space scuttle. Hurricane Frances shredded the walls of a Kennedy Space Center building used to assemble shuttle parts.

Packing up and evacuating wasn't the preferred option for all southeastern scientists, however. When Hurricane Ivan looked like it

CREDIT: NASA

Storm survivors. Marine biologist Jeanette Wyneken made a risky trek to supply her loggerhead turtles with fresh seawater after Hurricane Frances knocked out power to her lab. Later, she released hatchlings from nests she had saved from the storm, just days before Hurricane Jeanne struck.

CREDIT: WILLIAM M. PLATE/FLORIDA ATLANTIC UNIVERSITY

was on a collision course for New Orleans, Tulane University parasitologist Paul Brindley decided to move his wife and 9-year-old daughter into his lab on the fifth floor of the university's environmental research building. "We thought we'd be safer hunkered down there than at home," he says. Brindley brought beans for his family to eat and air mattresses for them to sleep on and kept his daughter calm by letting her play games on his office computer. Meanwhile, he ventured into his workspace to transfer his schistosomes to liquid nitrogen and plug his freezers into backup generator outlets—just in case.

A backup generator was the first thing to go at the University of Florida, Gainesville, biochemist Arthur Edison discovered when he got a frantic call at 3 a.m. on the morning Frances struck. Edison runs the university's Advanced Magnetic Resonance Imaging and Spectroscopy Facility, which relies on a $2 million system of superconducting magnets to study everything from structural biology to Alzheimer's disease. "The magnets need power to stay cold," he says; otherwise, they can fail in 8 hours. Edison had to wait until morning to check on the magnets because the town was flooded and under curfew. When he entered the building under police escort, he discovered that the entire institute was on the fritz. "The whole place was beeping," he says.

Edison's magnets were fine because they never lost power, but other equipment had failed. He spent several hours plugging powerless machines into working outlets and moving his colleagues' sensitive reagents from dead freezers into working ones. Still, it could have been worse. Remembering how Tropical Storm Allison drowned more than 35,000 lab animals at Baylor College of Medicine in Houston, Texas, in 2001, Edison and others had spent the days before the hurricane sandbagging doors and taping windows shut.

While some were trying to keep water out of their labs, Wyneken was trying to bring it in—hoping to save her loggerhead turtles. Hurricane Frances had knocked out the power to the pumps in her building at Florida Atlantic University in Boca Raton, stopping the flow of fresh seawater to the turtle tanks. Rather than risk using contaminated water from the nearby beach, Wyneken made a 72-kilometer trek up the coast to fill the 50-kilo containers in her truck with water from the Juno Beach Marine Life Center. On the way back, she had to get special permission to cross closed bridges and hiked through a carpet of downed ficus trees.

Many graduate students undertook similar physical risks to keep from losing thesis projects they had spent years working on. When Hurricane Ivan veered toward the Alabama shoreline, Charlyn Partridge, a biology Ph.D. student working at the University of South Alabama in Mobile, ignored her parents' pleas to seek shelter at their home in Louisiana. Instead, she headed straight for the basement of the university's life sciences building. While the Federal Emergency Management Agency set up shop on the first floor, Partridge dissected her pipefish to collect the daily readings she needed for sexual selection studies. "If I had missed a day, I would have lost a month of work and may not have been able to finish my project on time," she says. Partridge acknowledges that she took a risk by going to the lab. "But you need to make sure everything that's important to you is safe," she says. "That also includes the research."

Although no one welcomed the storms, some research actually benefited from them. Hurricane Charley damaged sensors on marine research buoys being used by University of South Florida oceanographer Robert Weisberg, but he left equipment running when Frances hit. "As a result, we got a really nice data set," he says. "And it was totally unplanned." Weisberg says that, although Frances caused some damage, sensors recorded changes in water temperature and current that will eventually be assimilated into models that may help improve hurricane forecasting.

Wyneken is beginning to see a bright side as well. The first eggs she saved on the beach have begun to hatch, and she believes she will be able to collect good data on how young turtles adapt to their environment. "Sometimes you have to do some crazy things for science," she says. "But when you see a whole nest of baby turtles hatching … with their big brown eyes and big floppy feet, it makes all of your efforts and hassles seem worthwhile."

Wyneken's turtles are still going to need some luck. In the coming weeks, she will tag them for further study and release them onto the now-damaged beach where she rescued them. Once they make their way back to the water, they'll contend with predators, starvation, and—as Hurricane Jeanne made clear last week—a storm season that is far from over. **–DAVID GRIMM**

With reporting by Sean Bruich.

Published by AAAS

Dressed for Success: Neandertal Culture Wins Respect

Neandertals made jewelry and must have worn clothing—but were they as sophisticated as modern humans? Researchers gathered at a high-level meeting to find out

GIBRALTAR—One day in 1848, when workers were blasting in a quarry on the Rock of Gibraltar, out of the dust and rubble tumbled a strange-looking human skull. It had a jutting, prognathous face, thick brow ridges, and an elongated brain case. The skull was presented to the Gibraltar Scientific Society, which had no idea what to make of it and put it in storage. Eight years later, miners working in a limestone cave in Germany's Neander Valley came across a similar skull. This time, scientists concluded that it was a sort of primitive human, and so in time "Neandertal" rather than "Gibraltarian" became an epithet for brutish behavior.

But today respect is growing for the Neandertals, whose brains were slightly bigger than those of our own species and who survived more than 100,000 years of sharp fluctuations in climate. Last month, when more than 100 archaeologists and anthropologists gathered here for the third triannual meeting on Neandertals and modern humans,* much of the discussion centered on the Neandertal's abilities and culture.

For example, although Neandertals had always been considered cold hardy, some researchers now conclude that Neandertals must have relied chiefly on their material culture, rather than their cold-adapted biology, to brave the chill of Ice Age Europe. Other researchers made controversial claims that Neandertals were full partners in the cultural innovations that swept through Europe beginning about 45,000 years ago, creating their own original tools and jewelry. Although not everyone at the meeting was willing to go this far, most agreed with anthropologist Jean-Jacques Hublin of the Max Planck Institute of Evolutionary Anthropology in Leipzig, Germany, that "Neandertals were complex hominids doing complex things."

* Perspectives on Human Origins, Gibraltar, 26–29 August 2004.

Feeling the chill

One fact that is not in contention is that Neandertals, who first appeared in Europe and Western Asia about 150,000 years ago and apparently thrived until their extinction about 25,000 years ago, were well adapted to cold northern latitudes. The Neandertal body was chunkier and more muscular than that of modern humans, and their limbs were somewhat shorter—all features thought to help reduce heat loss. In Gibraltar, however, University College London anthropologist Leslie Aiello presented new data that challenge this conventional wisdom. In collaboration with physiologist Peter Wheeler of Liverpool John Moores University, Aiello set out to determine "what it really felt like to be a Neandertal living in Ice Age Europe."

Suited up. Despite their supposedly cold-adapted bodies, Neandertals must have worn clothing at least as warm as a business suit.

CREDIT: KENNETH GARRET

Aiello and Wheeler first tested the hypothesis that the Neandertal's stout body would have kept it significantly warmer. They calculated a parameter called the "lower critical temperature," the limit at which a human must increase its internal heat production (usually by eating more) to maintain a body temperature of 37°C. Using formulas that factor in the thermal conductance of the skin, body surface area, and estimated basal metabolism rate, Aiello and Wheeler compared Neandertals, modern humans, and the tall, slim form of *Homo erectus* found in Africa. To their surprise, the lower critical temperature differed very little among all three: 27.3°C for Neandertals, 28.2°C for modern humans, and 28.5°C for *Homo erectus*. "I find this astounding," Aiello said. "The Neandertal body form will keep it a bit warm, but not enough to live in a very cold environment."

But just how cold was it? Aiello and Wheeler addressed this question with the help of a pioneering research effort known as the "Stage 3 Project," led by Cambridge University geoarchaeologist Tjeerd van Andel. This work has generated a wealth of new data about climatic conditions in Europe between 60,000 and 24,000 years ago, the period of Oxygen Isotope Stage 3 (*Science*, 6 February, p. 759). Because modern humans arrived in Europe around 40,000 years ago, Stage 3 includes the crucial period during which Neandertals and modern humans coexisted.

One of the major achievements of the Stage 3 Project is an estimate of the wind-chill factor—a much better indicator of conditions than temperature alone—at hundreds of sites known to have been occupied by prehistoric humans. The project was able to achieve excellent resolution, creating a Europe-wide grid of 60-kilometer-by-60-kilometer squares and time slices that vary between 3000 and 10,000 years in duration.

Aiello and Wheeler looked at the wind-chill factors for 457 Neandertal and modern human sites. They found that as the last Ice Age approached, a large number of the Neandertal sites would have turned positively frigid. For example, Neandertals living at Kulna Cave in Moravia about 25,000 years ago would have faced winter wind chills of –24°C. Aiello and Wheeler next calculated how much insulation the Neandertals would have needed using a unit of insulation called the "clo." One clo is roughly equal to wearing a modern Western business suit or having 1 centimeter of body hair or 2 centimeters of

Published by AAAS

Tailors' tools? Neandertal bone awls could have been used to pierce skins to make clothing.

body fat. They found that even if Neandertals had worn one clo of insulation, for example in the form of animal skins, toward the latter half of Stage 3, many Neandertal sites would still have been unbearable. Despite their supposed cold-hardiness, Neandertals would have needed a great deal of clothing and shelter to survive in these places, probably calling forth all of their cultural and material resources.

Thus, it is perhaps not surprising that Neandertals usually chose to live in areas where winter wind-chill temperatures were warmer than those occupied by the culturally more sophisticated modern humans. For example, Aiello and Wheeler found that during the period 37,000 to 22,000 years ago, Neandertals faced median winter wind chills of –16°C at their sites, while at sites associated with modern cultures the wind chills ranged from –20°C to –23°C. That suggests that the culturally advanced moderns were even better equipped to fight the cold—and so might have had a competitive edge against the Neandertals during the coming Ice Age. "Neandertals did extremely well for a long time," Aiello concluded. "The only difference was that now they had modern humans to compete with them."

This argument made sense to many researchers at the meeting. Anthropologist Chris Stringer of the Natural History Museum in London, for example, suggests that Neandertal clothes were probably less effective insulators than those sported by modern humans. "There is no evidence of sewing needles from any Neandertal sites," Stringer points out, whereas many modern human sites have such needles.

But some participants argued that Neandertals, at least during the earliest periods of coexistence with modern humans about 40,000 years ago, were just as capable of making clothes as their supposed competitors. "Needles do not appear until much later"—after 25,000 years ago—even at modern human sites, notes archaeologist Francesco d'Errico of the University of Bordeaux in France. "We know from use-wear analysis [of bone and stone tools] that Neandertals were working and scraping animal skins." And some of their bone tools, d'Errico says, could easily have been used to make holes in animal skins, even if they did not have actual needles.

Beads, bones, and brains

Inferences about Neandertal tailoring abilities quickly led to a broader debate about whether Neandertals overall were culturally inferior to modern humans during the short time that the two groups coexisted. At the meeting, d'Errico, along with University of Lisbon archaeologist João Zilhão, sparked fierce debate with arguments to buttress their view that Neandertals and moderns were cultural near-equals.

The debate is tied closely to the chronology of several archaeological "cultures" (*Science*, 2 March 2001, p. 1725). For most of their history, Neandertals made stone flakes, scrapers, and axes collectively known as the Mousterian culture. When modern humans arrived in Europe, they began producing a different culture called the Aurignacian, consisting of more sophisticated stone and bone tools as well as personal ornaments such as beads. The later Aurignacian was also characterized by the beginnings of cave art, and these dramatic developments are sometimes referred to as the "Upper Paleolithic revolution." Right around the time that modern humans arrived, however, the Neandertals underwent a cultural shift, creating beads and tools, called "Châtelperronian," that closely resemble the early Aurignacian. Most archaeologists have assumed that the Neandertals were copying the modern humans through a process of acculturation, but d'Errico, Zilhão, and their co-workers have argued insistently that the Châtelperronian represented an independent cultural achievement.

At Gibraltar, d'Errico and Zilhão continued their attack on the acculturation theory. D'Errico proposed an alternative "multispecies" model for the rise of modern behavior, in which both Neandertals and moderns fully participated in the Upper Paleolithic revolution. In a sweeping review of the archaeological evidence across Europe, d'Errico maintained that modern behavior "appeared at different times and at different places." And he challenged the notion that the Neandertals had simply copied the moderns. His own study of beads from Châtelperronian sites, carried out with postdoc Marian Vanhaeren, showed that Neandertals often made beads from perforated animal teeth, whereas moderns usually made beads from bone and shells and used different perforation techniques. And at Grotte du Renne, a French site occupied first by Neandertals and later by modern humans, d'Errico argued that the Neandertals made sophisticated bone awls earlier and in much greater numbers than their supposedly more "modern" successors.

Zilhão attempted to drive the point home with a review of the radiocarbon dating for sites across Europe. In one of the meeting's most hotly contested talks, he dismissed on technical grounds dates of 40,000 years or earlier at two key central European Aurignacian sites and concluded that there was no reliable evidence for any Aurignacian artifacts before 36,500 years ago. If true, this could mean that the Châtelperronian, which most archaeologists agree can be dated to at least 40,000 years ago, arose in Europe before the arrival of modern humans and that the Neandertals might have launched Europe's Upper Paleolithic revolution all by themselves. "The Châtelperronian comes before the Aurignacian by many millennia," Zilhão concluded.

These arguments received a hostile reaction from some researchers at the meeting. Hublin points out that this time period is right at the limit of radiocarbon dating's capabilities. It makes "no sense" to "ask if the Aurignacian was 36,000 years ago or 38,500 years ago when we have such big margins of error," he says.

Nevertheless, despite the vigorous debates, most researchers at the meeting agreed that the Neandertal's long, successful reign in Eurasia probably means that the cognitive gap between them and modern humans was not as great as many experts once thought. "The Neandertals had big brains, and they must have been using them for something," says Aiello. "The gap is closing, but we haven't fully closed it yet."

–MICHAEL BALTER

CREDITS: COURTESY OF FRANCESCO D'ERRICO

In Volleyball, Crafty Players Serve Up an Aerodynamic Crisis

DAVIS, CALIFORNIA—From 13 to 16 September, researchers from many disciplines discussed sports from curling to skydiving, from table tennis to boxing, at the 5th International Conference on Engineering of Sport.

Ever since Isaac Newton noted that spinning tennis balls follow curving trajectories, scientists and engineers have puzzled over the flight of spherical balls. Now, a new analysis suggests that volleyball is the oddest ball game of all, as the big, light orb regularly enters a curious state in which one half experiences much greater aerodynamic drag than the other does.

Easy does it. Thanks to a volleyball's curious aerodynamics, slower serves produce surprising swerves.

The observation explains why a volleyball can swerve unpredictably by as much as a meter—if it's moving slowly enough. It also puts a new spin on a bit of common wisdom about ball sports, says Ken Bray, a physicist at the University of Bath, U.K. "Everybody always argued that all ball sports are played in this comfortable regime where the drag is constant [with velocity]," Bray says. "But it turns out in volleyball that's not the case."

When a ball moves through the air, a long tangle of swirling air trails behind it. Flapping like a flag in the wind, this "turbulent wake" pulls straight back on the ball and slows it down—the phenomenon known as drag. At low speeds, the wake is large and the drag is high, but if a ball moves faster than a certain speed, the wake suddenly shrinks and the drag plummets. The speed range in which the drag changes rapidly is known as the drag crisis, and balls moving in it can behave unpredictably.

In most sports, the balls hurtle so fast that the drag has bottomed out and the drag crisis never comes into play. But not so for volleyball, reports Thomas Cairns, a mathematician at the University of Tulsa in Oklahoma who coached the women's volleyball team there for 17 years. Cairns and his students videotaped volleyballs launched from a serving machine and then analyzed their trajectories with a computer. In some serves the balls moved with topspin, in which the top of the ball rotates toward the oncoming air and the bottom rotates away from it. When that happens, the top of the ball effectively moves faster through the oncoming air than the bottom half does. Cairns found that the trajectories of some serves made sense only if the top of the ball was moving fast enough relative to the air to avoid the drag crisis, while the bottom half was moving so slowly it dipped into it.

This unusual half-and-half state played havoc with the ball's trajectory and could reverse another key effect of spin: the aerodynamic lift force that can make a ball swerve up or down or side to side. In spite of its name, the lift ordinarily pushes a ball with topspin down, as the spinning ball turns against the turbulent wake like a gear turning against a toothed rail. That means a serve with topspin ordinarily sinks faster than a similar serve with no spin. But Cairns observed a serve with topspin that floated farther than a matching spinless serve. He also saw spinning serves that swerved sideways, but in the direction opposite to the way spinning balls normally curve. Cairns even spotted a few serves that swerved first one way and then the other.

Ultimately, Cairns hopes to figure out how to predict and control those effects. "We'd like to get to the point where you can say to the player, 'Hit it this fast if you want it to do this or that,' " he says. But certain competitive players already seem to take advantage of the strange aerodynamic effects, says Rabindra Mehta, an aerodynamicist at NASA's Ames Research Center in Moffett Field, California. "The men get up there and try to hit the ball as hard as they can," he says. "But if you watch the women, they hit it at about 15 meters per second, which is where this effect comes in."

To Throw Farther, Waste Energy

When throwing, the arm works against itself and wastes energy. But a new mechanical analysis suggests that such seemingly profligate efforts actually enable the limb to fling things farther.

In throwing and other physical activities, the first step forward is often a step back. For example, to jump straight up, a person first crouches toward the ground. "The downward motion is kind of strange when you think about it," says Sam Walcott, a doctoral student in theoretical and applied mechanics at Cornell University in Ithaca, New York. "I'm moving in the direct opposite direction that I want to go."

The body briefly continues to move downward even after the muscles in the legs and torso begin to pull it upward, which means it works against itself. As muscles don't store energy like springs, that "negative work" essentially goes to waste. Similarly, in throwing, the forearm momentarily moves backward even as the upper arm pulls it forward, again squandering energy. Biomechanists aren't sure what purpose this "countermovement" serves.

But Walcott believes that wasting a little energy lets the body use what energy it has left more effectively. Walcott used a computer to study an idealized arm consisting of two straight segments—representing the upper arm and forearm—that hurled a virtual ball. The upper arm could move about a pivot, but only in a plane; the forearm could then move so that it swept out a cone perpendicular to that plane, creating a throwing motion that resembled the whipping action of a baseball player's arm. Torques at the

CREDIT: WALT BEAZLEY/TULSA UNIVERSITY ATHLETIC MEDIA RELATIONS

Published by AAAS

"shoulder" and the "elbow" set the arm in motion. Walcott gave the stick-figure limb a fixed amount of energy to expend and then let the computer search for the arm motion that produced the longest throw.

If the computer program allowed the arm to work against itself, it threw the object farther. The design of the arm doesn't allow it to chuck the object at any old angle and speed, Walcott explains, but "doing this negative work somehow allows us to get closer" to the optimal angle and speed.

It's an interesting argument, says Michele LeBlanc, a biomechanist at California Lutheran University in Thousand Oaks, but the abstract analysis probably isn't the entire explanation of countermovement. The details of how specific muscles, bones, and sinews interact will also play a role, she says. Jill McNitt-Gray, a biomechanist at the University of Southern California in Los Angeles, says that the precise function of countermovement will probably vary even from person to person: "You and I can jump together, and how you get your vertical impulse and how I get my vertical impulse might be different."

Pulling Straight to the End of the Pool

For decades, competitive freestyle swimmers have been taught to make an S-shaped path when pulling their hands through the water. But measurements and calculations now show that to generate the maximum thrust, swimmers should pull their hands straight back through the water, reports a mechanical engineer whose research was inspired by his previous study of turtles.

Swimmers have been purposely doing the "S-pull" since the early 1970s, when famed swimming coach James ("Doc") Counsilman used underwater cameras to film elite swimmers and found that they were moving their hand first out to the side and then back under their bodies. By moving side to side, hands acted like little airplane wings or propeller blades, Counsilman argued, generating hydrodynamic lift that pulled the swimmer through the water. That lift would supplement the force generated by simply pushing against the water with the palms. In recent years, researchers have questioned just how large and important the lift forces are, but the S-pull has remained a standard technique among competitive swimmers.

However, the S-pull may not be the best pull for all races and circumstances, says Shinichiro Ito of Japan's National Defense Academy in Yokosuka. Using measurements of the lift and drag coefficients of manikin hands and a computer model of a swimmer, he found that the S-pull makes the most efficient use of energy, as it maximizes the ratio of lift to drag. It does not, however, generate the most thrust. Instead, Ito found, a straight "I-pull" yields more pure power.

Ito had already observed something similar in his study of freshwater turtles. When paddling about leisurely, turtles wave their feet in flourishes, doing a reptilian version of the S-pull. When frightened, however, terrified terrapins pull their feet straight back to swim away as fast as possible. Analysis showed that for turtles, the sinuous movement was more efficient, Ito says, but the straight movement produced greater thrust.

Other familiar creatures also provide living examples of the advantages of the I-pull. Underwater video shows that Australian swimming sensation Ian Thorpe snaps his elbow and pulls his hand straight through the water, Ito says. Other swimmers are following the nine-time Olympic medalist's lead, says Yuji Ohgi, a professor of physical education at Keio University in Fujisawa, Japan. "At the Sydney Olympics [in 2000], only Ian Thorpe had the I-shaped pull," he says. But now, "many, many Australian swimmers do it."

Thorpedo away! Olympic champion Ian Thorpe pulls his hands straight through the water.

Switching from S-pull to I-pull isn't easy, says Ohgi, who is also a swimmer. Good swimmers generate power by rolling from one side of their bodies to the other, he says, and that makes their hands move side to side almost automatically. "The I-shaped pull is rather more difficult than the S-shaped pull because of the rolling motion" of the body, Ohgi says. Still, to shave every fraction of a second from their times, more swimmers are tackling the challenging technique and learning to swim like a frightened turtle.

–ADRIAN CHO

Snapshots From the Meeting

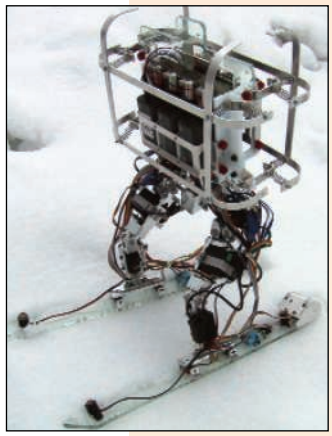

R2D2 meets K2. A robot standing 45 centimeters tall and weighing 3 kilograms swishes down a 10-meter artificial ski slope much like a human skier, report engineer Takeshi Yoneyama of Kanazawa University in Japan and colleagues. The mechanical downhiller isn't completely lifelike, because it doesn't generate nearly as much force with its legs as humans do. Still, the robot has already provided insights into why skiers move their joints the way they do.

A swell new wetsuit. A high-tech wetsuit automatically adjusts to keep divers warmer in cold water, reports engineer Alec Jessiman of Midé Technology Corp. in Medford, Massachusetts. As water flows in and out of a conventional wetsuit, it carries away a diver's body heat. But when temperatures dip, the suit made of SmartSkin absorbs water and swells to fill in the gaps between diver and suit. That shuts off the flow within minutes and reduces heat loss by as much as 70%.

The camber of least resistance. The tops of the wheels of racing wheelchairs are tilted toward each other to make them more stable. But such "camber" also reduces the amount of rolling friction, reports Nick Hamilton, a sports engineer at the University of Sheffield, U.K. Hamilton figured that the friction must be least when the wheels are perpendicular to the ground. To his surprise, his measurements showed that the friction was smallest when the wheels leaned by 8 to 14 degrees, presumably because the tires deform to reduce the amount of contact with the ground.

–A.C.

CREDITS: (TOP TO BOTTOM) T. YONEYAMA/KANAZAWA UNIVERSITY; ASSOCIATED PRESS

Published by AAAS

Politicians are fond of touting research and innovation as drivers for economic prosperity, keys to good health and environmental preservation, and pillars of national defense. Traditionally, these topics are included mainly to provide applause lines in stump speeches. But this year they have become campaign issues, too.

The two major party candidates for U.S. president, incumbent Republican George W. Bush and his Democratic challenger, Senator John Kerry, and their representatives have sparred repeatedly over issues ranging from embryonic stem cell research to global warming. But that discourse, played out across several months and thousands of miles, may have been hard for the average voter or international reader to follow. So as it has done in past elections, *Science* has consolidated the debate by inviting each candidate to lay out his views on a dozen important issues. Their unedited answers follow.

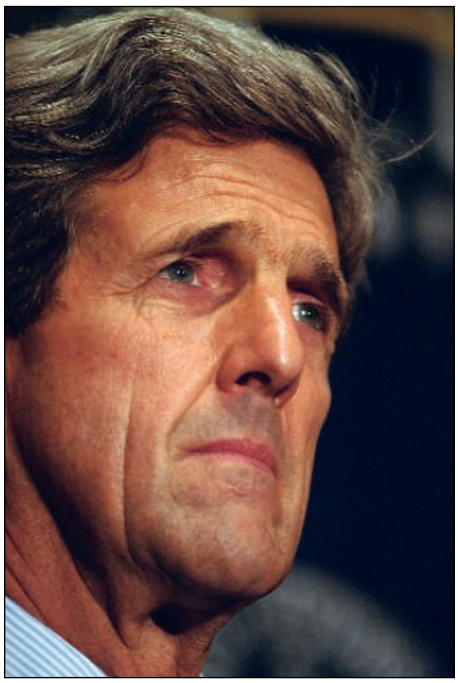

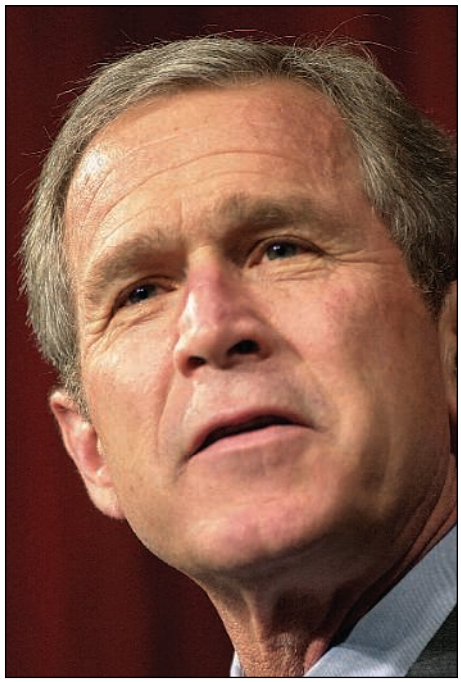

Bush and Kerry Offer Their Views on Science

Science: ***What are your top three priorities in science and technology?***

BUSH: America's economy leads the world because our system of private enterprise rewards innovation. Entrepreneurs, scientists, and skilled workers create and apply the technologies that are changing our world. I believe that our government must work to help create a new generation of American innovation and an atmosphere where innovation continues to thrive.

• *Ensure every American has access to affordable broadband by 2007.* Broadband is a critical infrastructure that empowers our nation's economy, improves Americans' quality of life, and offers life-enhancing applications such as e-learning and telemedicine. We must keep the Internet tax-free, reduce burdensome regulations, and promote innovative technologies such as wireless and broadband over power lines.

• *Perform next-generation hydrogen research.* I have dedicated $1.7 billion over 5 years to develop hydrogen fuel cells and related technologies. The 2005 budget includes $228 million for the Hydrogen Fuel Initiative, an increase of $69 million, or 43%, over 2004 funding, to develop the technologies to produce, store, and distribute hydrogen for use in fuel-cell vehicles, electricity generation, and other applications. My 2005 budget proposes tax incentives totaling $4.1 billion through 2009 to spur the use of clean renewable energy and energy-efficient technologies.

• *Recruit science and technology to combat terrorism.* Terrorists use technology to their advantage, and we must maintain overpowering technical leadership to negate their efforts. Fortunately, the relevant technologies are often "dual use," so countering bioterrorism, for example, will also help defeat naturally occurring infectious diseases such as SARS.

KERRY: First, I will restore and sustain the preeminence of American science and technology. This means supporting a strong, well-balanced federal program of basic and applied research across biological, physical, engineering, mathematical, and other disciplines. My administration will ensure that research advances connect directly to practical inventions to maintain economic leadership, create good jobs, improve health, and protect the environment while meeting our energy needs. I will lift the ban on federal funding of research on stem cell lines created after August 2001. I will support federal research partnerships and create a fiscal and regulatory environment that encourages investment in innovation.

Second, John Edwards and I will work to ensure that Americans are prepared for the jobs of the future, jobs that depend increasingly on a grasp of science, engineering, and mathematics. It's critical that all women and men of all ethnic backgrounds are encouraged to enter these fields or to appreciate their significance in their own careers. Our educational system must develop new tools that can convey complex information while sustaining the essential excitement of scientific discovery.

Third, I will ensure that all decisions made by my administration will be informed by the best possible science and technology advice. I will bring science back into the White House. I will restore the position of Assistant to the President for Science and Technology and ensure that objective scientific advice, including criticism, is fully considered at the White House and federal agencies.

CREDITS (LEFT TO RIGHT): DAN HERRICK/ZUMA/CORBIS ; STEFAN ZAKLIN/ GETTY IMAGES

Published by AAAS

CLIMATE CHANGE

Science: ***Is human activity increasing global temperatures? If so, should the United States set specific goals with respect to limiting or reducing greenhouse gas emissions by the end of the decade?***

KERRY: The scientific evidence is clear that global warming is already happening and rising levels of global warming pollution are making the problem worse. For years in the Senate, I worked with our allies to fight for a balanced global warming treaty. President Bush rejected the Kyoto Protocol, stubbornly walking away from the negotiating table altogether and eroding our relations with global allies. John Edwards and I will take the United States back to the negotiating table, rebuild relations with other nations, and work with them to include the United States—as well as developing nations—in the solution.

BUSH: In 2001, I asked the National Academy of Sciences to do a top-to-bottom review of the most current scientific thinking on climate change. The nation's most respected scientific body found that key uncertainties remain concerning the underlying causes and nature of climate change. As the NAS stated, "Because there is considerable uncertainty in current understanding of how the climate system varies naturally and reacts to emissions of greenhouse gases and aerosols, current estimates of the magnitude of future warming should be regarded as tentative and subject to future adjustments upward or downward." The NAS found: "Because of the large and still uncertain level of natural variability inherent in the climate record and the uncertainties in the time histories of the various forcing agents (and particularly aerosols), a causal linkage between the buildup of greenhouse gases in the atmosphere and the observed climate changes during the 20th century cannot be unequivocally established."

Based on the NAS study, I launched a comprehensive, long-term policy agenda that focuses on building the most innovative, efficient technologies that will reduce greenhouse gas emissions while allowing the economy to grow. Through research and development into next-generation hydrogen and clean coal technologies, my plan sets a goal to reduce greenhouse gas intensity by 18% over the next decade. This approach has the virtue of addressing the greenhouse gas buildup regardless of its relation to global temperatures and, at the same time, preserving a strong economy.

To implement this agenda, my fiscal year (FY) 2005 budget seeks nearly $2 billion in funding for climate change science conducted by 13 federal agencies, up from $1.7 billion in 2002. These federal agencies are implementing the administration's 10-year strategic plan for the U.S. Climate Change Science Program that was released in July 2003 and praised by the NAS in February 2004 as articulating "a guiding vision" and "appropriately ambitious and broad in scope."

I have also established the Climate Change Technology Program to focus on technology to reduce greenhouse gas emissions via renewable energy, fossil energy, and nuclear energy efficiency improvements and carbon sequestration. My FY 2005 budget proposes $5.8 billion for climate change activities, including nearly $3 billion for research on advanced energy technologies (e.g., hydrogen-powered vehicles and power plants, clean coal, fusion power, and carbon capture and storage methods). Both the Climate Change Science and Technology Programs are strengthened by our strong international collaborations.

Science: ***Cap-and-trade programs for greenhouse gas emissions are starting up in other countries. Do you favor such a program for the United States?***

BUSH: [No response.]

KERRY: As John Edwards and I work to rejoin the international community on global warming, we will work at home to take concrete steps to reduce greenhouse gas emissions. Our environmental and energy plans tap the ingenuity of American industry to reduce pollution while creating new jobs manufacturing cleaner technologies. The cap-and-trade system was pioneered in America, where it reduced acid rain pollution at a small fraction of the expected costs. John Edwards and I support a similar approach to global warming, setting concrete limits to reverse the growth in global warming pollution but letting industry find the best path for getting there.

CLONING

Science: ***Should U.S. government–funded scientists be allowed to do somatic cell nuclear transfer (research cloning), creating early preimplantation human embryos for research purposes?***

BUSH: I believe all human cloning is

STEM CELL RESEARCH

Science: ***Should U.S. government–funded scientists have access to human embryonic stem cell lines generated after August 2001? Should they be able to create new lines?***

BUSH: My administration is the first to allow federal funding for human embryonic stem cell research. However, I put in place reasonable ethical requirements for scientists who want to use taxpayer dollars. I believe that scientific discovery and ethical principles can go hand in hand and that we should not use taxpayer money to encourage or endorse the additional destruction of living, human embryos.

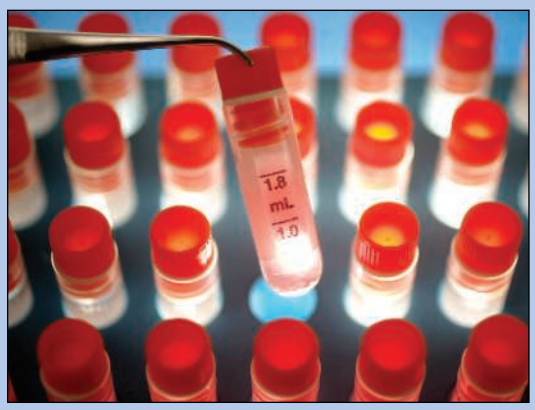

I remain committed to fully exploring the promise and potential of stem cell research without violating ethical principles and while maintaining respect for all human life. And I have dramatically increased funding for all forms of stem cell research. In addition, NIH is creating a new National Embryonic Stem Cell Bank, which is important for consolidation, reducing costs, and maintaining uniform quality control over the cells.

KERRY: Yes. As president, I will lift the current ban on federal funding of research on stem cell lines created after August 2001. Right now, more than 100 million Americans suffer from illnesses that one day could be wiped away with stem cell therapy, including cancer, Parkinson's, diabetes, and other debilitating diseases. We must make funding for this research and other important scientific work a priority in our universities and our medical community—all while we ensure strict ethical oversight. And we must secure more funding for it at agencies like the National Institutes of Health and the National Science Foundation.

CREDIT: PETER MACDIARMID/REUTERS/CORBIS

Published by AAAS

wrong, and a total ban on human cloning is necessary to ensure the protection of human life as the frontiers of science expand. Anything short of a comprehensive ban would be impossible to enforce and would permit human embryos to be created, developed, and destroyed solely for research purposes. I strongly support a comprehensive law against all human cloning.

KERRY: I'm proud to support bipartisan legislation by Senator Orrin Hatch that would make human cloning illegal. This bipartisan legislation includes support for somatic cell nuclear transfer, which would provide greater access to stem cells to conduct the important research we need. We all have loved ones who suffer from diseases that could be cured or ameliorated by this research, including cancer, Parkinson's, diabetes, spinal cord injury, and Alzheimer's. This is not a partisan issue. We should not put ideological shackles on the ability of America's doctors to bring them those urgently needed cures.

PUBLIC HEALTH

Science: ***Should there be any restrictions on using foreign aid for abortions or counseling on birth control methods?***

KERRY: As a senator, I have repeatedly voted against efforts to impose the global gag rule, and as president, I will continue to fight these attempts to silence foreign nongovernmental organizations.

BUSH: My administration is cultivating a culture of life. I believe that taxpayer funds should not be used to pay for abortions or to advocate or actively promote abortion abroad. United States' funding will not be available to international groups that perform abortions, counsel abortion as a family-planning option, or lobby foreign governments on abortion policy. This means that the U.S. government will not use taxpayer dollars to try to legalize abortion in countries in Latin America, Africa, and Muslim countries in which the people are strongly opposed to abortion and believe in the protection of unborn children.

Science: ***Does the U.S. Department of Agriculture's mission to promote U.S. agricultural products, that is, to eat more, get in the way of efforts to combat the emergent obesity problem?***

BUSH: I believe we must address the growing epidemic of obesity and poor personal fitness in America. I do not believe the USDA's mission to promote agricultural products undermines broader efforts to combat the emergent obesity problem. Americans are being encouraged to eat healthier, more nutritious foods like fruits and vegetables and to abstain from consuming excessive amounts of food high in fat and calories. There are important steps individuals can take in their everyday lives to greatly reduce the risk of obesity. I created the Steps to a HealthierU.S. Initiative to coordinate the resources and expertise of federal agencies to encourage Americans, especially children, to make simple improvements in physical activity and make healthy choices. My 2005 budget calls for $125 million, an increase of $81 million, for the Steps to a Healthier U.S. program, which funds innovative programs that use proven methods to reduce the burden of obesity, diabetes, and asthma-related complications in local communities.

In launching the HealthierU.S. Initiative, I challenged the President's Council on Physical Fitness and Sports to retool to better serve youth. The council created the new "President's Challenge" awards program that draws wide support and is widely available.

KERRY: Promoting greater consumption of healthy foods, including fruits and vegetables, does not get in the way of the obesity problem. We must combat this epidemic by instilling healthier lifestyles in our children, including encouraging exercise and better eating

SPACE POLICY

Science: ***Can we afford to send astronauts back to the moon and on to Mars? Should that be the cornerstone of U.S. space policy? If so, what parts of the current program should be scaled back or eliminated to make room for it?***

KERRY: Today, thanks to decades of public investment in space exploration activities, a rotating international team of astronauts is living and working in space on the International Space Station, a dozen Americans have walked on the Moon, we have rovers exploring the surface of Mars, and an armada of spacecraft continues to explore our solar system. NASA is an invaluable asset to the American people and must receive adequate resources to continue its important mission of exploration.

However, there is little to be gained from a space initiative that throws out lofty goals but fails to support those goals with realistic funding. I am committed to increasing funding for NASA and space exploration, because it not only makes critical contributions to our economy, but also expands our understanding of the world we live in.

CREDIT: NASA

BUSH: My administration firmly believes that the benefits of space technology are far-reaching and affect the lives of every American. Space exploration has yielded advances in communications, weather forecasting, medicine, electronics, and countless other fields. For example, image-processing technologies used in life-saving computed tomography (CAT) scanners and magnetic resonance imaging (MRI) trace their origins to technologies engineers use in space.

In January of this year, we committed the United States to a long-term human and robotic program to explore the solar system, starting with a return to the Moon, to ultimately enable future exploration of Mars and other destinations. It will be affordable and sustainable, while maintaining the highest levels of safety. Return missions to the Moon will give astronauts the opportunity to develop new technology and to harness the Moon's resources to allow manned exploration of more challenging environments. Furthermore, an extended human presence on the Moon could reduce the costs of further exploration, since lunar-based spacecraft could escape the Moon's lower gravity using less energy at less cost than Earth-based vehicles.

The program commits the nation to a fiscally responsible long-term program to explore space through the use of robotic missions and human exploration. This new vision is a measured one that will be executed on the basis of available resources, accumulated experience, and technology readiness.

Published by AAAS

CREDIT: MARK WILSON/GETTY IMAGES

habits. This is not only a public health issue, but it's an economic one. Treating illnesses related to obesity makes up about 9% of national health spending annually. It's time for our country to get in front of the problem by expanding our national public health system to prevent the onset of obesity and to stop costly illnesses before they destroy lives.

SECURITY ISSUES

Science: ***Do you fully support the Reagan-era directive (NSDD 189) that establishes a clear line between classified and unclassified research?***

KERRY: Yes. Our security depends on the strongest possible protection of classified material. An effective system requires that the rules are clearly understood, respected, and competently managed. New technologies and new threats from terrorists require expanding the reach of classification. The Bush administration has created a murky area of "sensitive, but not classified" that could both weaken security and undermine the communication essential for productive research. I will replace the new Bush administration rules after carefully considering proposals already made by the National Academy of Sciences and giving full protection to our nation's secrets and national security.

BUSH: The key to maintaining U.S. technological preeminence is to encourage open and collaborative basic research. The linkage between the free exchange of ideas and scientific innovation, prosperity, and U.S. national security is particularly evident as our armed forces depend less and less on internal research and development for the innovations they need to maintain the military superiority of the United States. In the context of the broad-based review of our technology transfer controls that began in 2001, my administration is reviewing and updating as appropriate the export-control policies that affect basic research in the United States. Our new security environment has necessitated new regulations on the dissemination of "critical infrastructure information," such as the location of hazardous materials. In the meantime, the policy on the transfer of scientific, technical, and engineering information set forth in NSDD 189 has remained and will remain in effect, and I will ensure that President Reagan's policy continues to be followed.

ENVIRONMENTAL STEWARDSHIP

Science: ***Do you support the recommendation of the U.S. Oceans Commission to create a high-level oceans policy panel led by a senior White House appointee and to double federal spending on marine research over 5 years?***

BUSH: I appointed the U.S. Commission on Ocean Policy (the Oceans Commission) in 2001 to review a broad range of issues ranging from stewardship of marine resources and pollution prevention to enhancing and supporting marine science, commerce, and transportation, while also giving equal consideration to environmental, technical, feasibility, economic, and scientific factors.

The Oceans Commission's formal submission this fall will inform future budget and policy decisions to sustain healthy oceans for the future. Already, I am moving forward on some of the commission's preliminary recommendations. In June, I submitted to Congress an "Organic Act" to enhance, among other things, the ability of the National Oceanic and Atmospheric Administration to assess and predict changes in ocean, coastal, Great Lakes, and atmospheric ecosystems.

KERRY: I worked to pass the legislation in 2000 that created the U.S. Oceans Commission, and I will draw on their expertise and findings in implementing my environmental plan. John Edwards and I have a four-point plan to protect our oceans. First, we will implement tough new protections to monitor beaches and to notify the public of any risks. Second, we will crack down on polluters releasing toxic substances into our waters. Third, we will work to reduce threats from runoff pollution that contribute to beach closings. Finally, we will provide communities with the tools they need to protect their coasts.

Science: ***Does the Endangered Species Act need to be reworked? If so, how should it be improved?***

KERRY: John Edwards and I support protecting wildlife and the important goals of the Endangered Species Act. We will implement the act in a cooperative manner that extends the benefits of wildlife and habitat protection to public and private lands. With adequate funding and a cooperative approach that works for both wildlife and property owners, John Edwards and I will continue America's strong legacy of protecting wildlife.

BUSH: The Endangered Species Act (ESA) serves a noble purpose, which Americans overwhelmingly support. For example, ESA led to the recovery of the Gray Wolf, which is why my administration was able to remove it from the list of threatened and endangered species. But even with occasional successes, ESA has been undermined by a flood of litigation, preventing the Fish and Wildlife Service from protecting new species and recovering plants and animals already listed as threatened or endangered. In my view, courts will not save species; focused, results-based conservation programs will. My administration is providing federal grants on a competitive basis to individuals and groups engaged in voluntary conservation efforts on private lands that benefit imperiled species. And with the help of more than $40 billion for wetlands and conservation programs as part of the 2002 Farm Bill, we are providing thousands of acres of new habitat for species and wildlife. I look forward to working with Congress to build on these efforts in modernizing ESA for future generations.

ITER

Science: ***By siding with Japan, the United States has contributed to the current stalemate over where to build the International Thermonuclear Experimental Reactor (ITER). Would you shift support to Europe as***

Published by AAAS

VISAS

Science: ***With regard to visa policy, many scientists feel that the pendulum has swung so far toward protecting our borders that the free exchange of ideas is being eroded. Does the government need to remove some of the barriers to entry for those who have a legitimate scientific or educational purpose for coming to the United States?***

BUSH: My administration values the contributions that foreign scientists and students make to our nation's scientific enterprise, while recognizing the importance of safeguarding our security. We will continue to welcome international students and scientists while implementing balanced measures to protect our homeland.

The science, university, and technology communities have been affected by the stricter visa requirements put into place following the terrorist attacks of September 11, 2001. The administration is actively working to improve many visa, immigration, and security processes impacting international guests and visitors. We are making progress. For example, we have shortened dramatically the process time for visa applications of scientists and students pursuing scientific areas of study. This program has been revised following a recent policy review to shorten processing time.

KERRY: We can balance science and security. In the wake of 9/11, America took important steps to improve security for visa applicants to the United States. However, we can improve our visa system to process visa applications for legitimate scientists and students more quickly while still screening individuals that pose a genuine security risk. With more resources and better procedures, we do not need to face a trade-off between scientific exchange and national security.

a way to move this project forward? At what point would you withdraw U.S. support for the project?

KERRY: Our energy plan will tap America's initiative and ingenuity to strengthen our national security, to grow our economy, and to protect our environment. I support a strategically balanced U.S. fusion program that includes participation in ITER to supplement a strong domestic fusion science and technology portfolio. As president, my first priority internationally on this and other energy issues will be to engage other nations to find areas of cooperation and common ground.

BUSH: I remain committed to building the ITER project, and based on recommendations from the Department of Energy, I believe Japan is the best location for ITER. My administration will continue to collaborate with all ITER participants, including our European partners, in realizing the promise of fusion energy through ITER. This project is one of the four "transformational technology" pillars of my climate change strategy, which focuses on building the emissions-free technologies of the future. From an inexhaustible and entirely clean fuel source, a fusion plant could generate huge amounts of electricity to power megacities and to produce hydrogen for transportation needs with no emissions of greenhouse gases. The results of ITER will advance the effort to produce clean, safe, renewable, and commercially available fusion energy by the middle of this century.

ENERGY POLICY

Science: ***Worldwide energy demand is rising at the same time oil production is expected to peak soon and to begin declining. But burning more coal will greatly increase carbon emissions. How would your energy research and development (R&D) priorities address these problems?***

BUSH: I believe America's energy future must include coal—the key challenge is developing technologies to make it burn cleaner. My Clear Skies legislation, which is the most aggressive presidential initiative in history to reduce power plant emissions, will create a $50 billion market for clean coal technologies. Through Clear Skies, we will cut sulfur dioxide, nitrogen oxides, and mercury by 70%, while maintaining America's most domestically secure, affordable, and reliable energy source. Additionally, as a key part of my comprehensive national energy policy, I am investing more than $2 billion over 10 years in the clean coal technologies that will transform America's energy economy, including support for FutureGen, an international, public-private initiative to build the world's first coal-based power plant that can produce both electricity and hydrogen with virtually no emissions of air pollutants or greenhouse gases.

KERRY: Our energy plan will increase and enhance domestic energy sources and provide incentives to help Americans use energy more cleanly and efficiently while creating 500,000 new jobs. The United States can develop and deploy clean energy technologies that will make us more efficient and allow us to capitalize on domestic and renewable sources of energy. John Edwards and I believe that we need clear benchmarks by which to measure the emissions performance of existing and new uses of coal. Our administration will provide a flexible package of incentives to construct state-of-the-art advanced coal plants, including Integrated Gasification Combined-Cycle (IGCC) coal-fueled power plants. In addition, we will invest in research and development into advanced fossil and renewable fuel technologies and fund research into advanced greenhouse gas mitigation and sequestration technologies.

MANAGING SCIENCE

Science: ***Do you support the doubling of the National Science Foundation budget over the next 5 years?***

KERRY: I have consistently supported major increases in the NSF programs, which provide the foundation for all mission-oriented research. The NSF budget will have a high priority in my administration and will be doubled. The timing of the doubling will depend on how quickly we can recover from the enormous budget deficits created by the Bush administration. I will not subject NSF to the uncertainties faced by NIH—following a bi-

CREDIT: ORBAN THIERRY/CORBIS SYGMA

Published by AAAS

partisan plan, its budget doubled from 1998 to 2003, but the Bush administration stopped the growth abruptly and plans to reduce NIH spending in the coming 5 years.

BUSH: My 2005 budget provides the highest amount ever requested for NSF and represents a 30% increase over FY 2001. The administration has requested $5.7 billion in FY 2005. Although NSF represents less than 5% of the total federal budget for research and development, it accounts for about 14% of all federal support for basic research and 40% of non–life science basic research at U.S. academic institutions. NSF's broad support for basic research, particularly at U.S. academic institutions, not only provides a central source for discovery in many fields but also encourages and supports development of the next generation of scientists and engineers. Moreover, in fulfilling its mission, NSF has used its funding efficiently and effectively.

Science: ***After a 5-year doubling, the budget of the National Institutes of Health is now expected to rise by less than the rate of inflation for biomedical research. What budget increase would you recommend for NIH in 2006 and beyond?***

BUSH: I have demonstrated my commitment to biomedical research by completing a 5-year doubling of the NIH budget to more than $27 billion from a level of $13 billion. NIH entered the postdoubling period far stronger and better positioned to improve health through advances in research. The NIH now trains 1500 more scientists per year and issues 10,000 more research grants than it did in 1998. New insights into human biology and behavior are bringing us closer to prevention strategies and treatments for many of the most dreaded diseases and conditions.

The FY 2005 program level for NIH is $28.8 billion, an increase of $764 million (2.7%) over FY 2004, which is greater than the Office of Management and Budget's estimated rate of inflation. We have not yet fully assessed the NIH's needs for 2006, but I recognize the importance of this agency's mission.

KERRY: I supported doubling of the NIH budget, beginning in 1998, and will continue to support sustained growth. NIH has a spectacular record in improving human health. Its work around the country has opened exciting new avenues of research—including stem cell research—that promise even more spectacular advances in coming decades. I will support consistent, sustained growth to expand NIH biomedical research, to invest in health promotion and disease prevention, and to strengthen the ties between NIH and other R&D agencies.

Science: ***How would you reduce the possibility of financial conflicts of interest arising from government scientists who collaborated with industry?***

KERRY: Full disclosure and effective, continuous monitoring are essential for any effective strategy for avoiding conflict of interest in corporations, universities, and federal agencies. The senior positions in federal R&D agencies are very demanding and require the overriding commitment of the individual. A modest amount of preapproved, fully disclosed outside activities may be beneficial to the government and the public, as well as industry and the individual. But supplementary income should never exceed some reasonable fraction of the federal salary and should never lead to the reality or the appearance of conflict of interest that could undermine the integrity of agency procedures.

BUSH: There are regulations in place to deal with this problem, and I fully support their enforcement. There are strict checks in

CREATIONISM

Science: ***Should "intelligent design" or other scientific critiques of evolutionary theory be taught in public schools?***

KERRY: I believe that ideology should not trump science in the context of educating our children. Still, public school curriculum is a matter subject to local control. Communities must decide which sound, scientific theories are appropriate for the classroom.

BUSH: The federal government has no control over local curricula, and it is not the federal government's role to tell states and local boards of education what they should teach in the classroom. Of course, scientific critiques of any theory should be a normal part of the science curriculum.

CREDITS (TOP TO BOTTOM): JIM YOUNG/REUTERS/CORBIS; BETTMANN/CORBIS

Published by AAAS

place to ensure that scientists are complying with their obligations, and my administration welcomes suggestions from all interested parties as to any additional steps that may need to be taken.

Science: ***Is the United States losing its edge in attracting the best and brightest of foreign students?***

BUSH: Many developed countries continue to be concerned about losing their best and brightest students to the United States. Because of our substantial investment in university-based research and the relatively higher status accorded to junior researchers, the United States remains the most attractive nation in the world for young people beginning their research careers. The United States benefits substantially from foreign students.

Student exchanges enhance global understanding and increase goodwill toward the United States after students return to their home countries. Many world leaders attended U.S. universities for parts of their education, and foreign students make substantial contributions to scientific research. The United States remains the world's leading producer of and a net exporter of high-technology products and ranks among the global leaders in R&D spending, according to *Science and Engineering (S&E) Indicators 2004*, a biennial report that I receive from the National Science Board (NSB). Indeed, U.S. preeminence in science is not an accident; it is due fundamentally to our openness to scientific exchange, which has enabled us over the generations to benefit from the best scientific expertise in the world. So I am sensitive to the need to attract foreign students and to the obstacles—or perceived obstacles—they may face in our changed security environment.

There have been some difficulties as we adjusted our visa application process after the terrorist attacks of September 11, 2001. My administration has worked to streamline this process while improving security. For example, 64% of institutions recently surveyed by the National Association of State Universities and Land-Grant Colleges reported that applications from foreign undergraduate students have either increased in number or stayed constant, while 52% reported increased or unchanged numbers of graduate student applications. In short, we are working hard to ensure that this nation and its institutions of higher learning will continue to attract the world's brightest young people.

KERRY: U.S. science and engineering have a long history of benefiting from the talents of immigrants—particularly foreign students. In the wake of 9/11, America took important steps to improve security for visa applicants to the United States. But the Bush administration has implemented the system in a way that makes it difficult or impossible for foreign scholars to attend international meetings or visit home. With more resources and better procedures, we do not need to face a tradeoff between scientific exchange and national security.

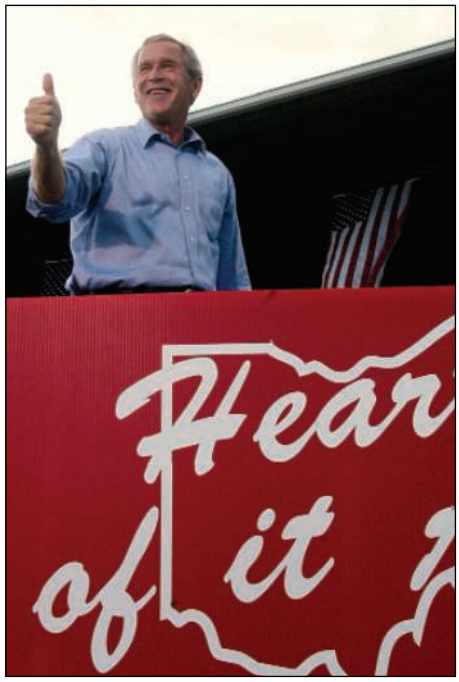

Science: ***Should Congress be allowed to fund research programs that have not undergone competitive peer review?***

KERRY: Competitive peer review is at the heart of our highly successful federally supported R&D programs. I am one of the many members of Congress who have strongly criticized "pork-barrel" awards in appropriations bills. There are better ways to help build R&D capabilities in communities and institutions with low levels of R&D funding, such as NSF's Experimental Program to Stimulate Competitive Research (EPSCoR), the Historically Black Colleges and Universities Program, and support for science and math teacher training. We must also remember that competition in science and technology must meet increasingly stiff international standards.

BUSH: Competitive peer review is the cornerstone of the scientific establishment. It is a scientifically rigorous process employed by funding agencies to allocate federal support for innovative research. Peer-review criteria for federal programs are clearly established prior to submission of proposals, and the panel of experts is selected to ensure fair evaluation. It is also routinely used by scientific and technological journals to ensure evaluation of quality, objectivity, and integrity of data for publication.

It is also the responsibility of the federal government to ensure that the people's investments in federally sponsored research are well managed and wisely used, which is the focus of my management agenda. In order to ensure that our R&D dollars are invested as effectively as possible, my administration has been expanding the use of transparent investment criteria to help us make decisions on where investments are likely to get us the best returns for our country. Our efforts include applying specific criteria that programs or projects must meet to be started or continued, clear milestones for gauging progress, and improved metrics for assessing results.

EPSCoR, started by NSF and now within seven federal agencies, and NIH's Institutional Development Award (IDeA) Program are excellent examples of successful, competitive, peer-reviewed research programs targeted toward improving our nation's science and technology capability. The program funds research activities of talented researchers at universities and nonprofit organizations in states and territories that historically have not received significant federal R&D funding. The merit-based program enables researchers, institutions, and states to improve their research capabilities and quality and to compete more effectively for non-EPSCoR research funds and works.

CREDITS (LEFT TO RIGHT): AFP/GETTY IMAGES; JIM BOURG/REUTERS/CORBIS

Published by AAAS

LETTERS

Letters to the Editor

Letters (~300 words) discuss material published in *Science* in the previous 6 months or issues of general interest. They can be submitted through the Web (www.submit2science.org) or by regular mail (1200 New York Ave., NW, Washington, DC 20005, USA). Letters are not acknowledged upon receipt, nor are authors generally consulted before publication. Whether published in full or in part, letters are subject to editing for clarity and space.

Retraction

IN THE REPORT "SYNAPTIC CHANGES IN LAYER 2/3 underlying map plasticity of developing barrel cortex" (*1*), we concluded that functional and anatomical changes in layer 2/3 underlie different forms of cortical map plasticity. It was pointed out to us by a reader that the anatomical analysis contains errors. Although these errors did not affect the main conclusions, we reanalyzed the data set. Re-analysis confirmed that whisker stimulation evokes a cortical response, which spreads preferentially to neighboring, nondeprived cortical columns as originally reported. However, the reported difference between the axonal fields in control and deprived animals was not statistically significant. Further, the deprivation-induced decrease in unitary EPSP amplitude was also not statistically significant. Thus, major conclusions of the Report are no longer supported, and we retract the Report. We apologize for any confusion that we may have caused to the readers of *Science*.

CARL C. H. PETERSEN,[1] MICHAEL BRECHT,[2] THOMAS T. G. HAHN,[3] BERT SAKMANN[3]

[1]The Laboratory of Sensory Processing, Brain and Mind Institute, Ecole Polytechnique Fédérale de Lausanne (EPFL), Lausanne CH-1015, Switzerland. [2]Department of Neuroscience, Erasmus University, Dr. Molewaterplein 50, NL-3015 Rotterdam, Netherlands. [3]Department of Cell Physiology, Max-Planck-Institute for Medical Research, Jahnstrasse 29, Heidelberg D-69120, Germany.

Reference

1. C. C. H. Petersen, M. Brecht, T. T. G. Hahn, B. Sakmann, *Science* **304**, 739 (2004).

GALEX and UV Observations

IN HIS ARTICLE "ULTRAVIOLET ASTRONOMERS face loss of vision" (News Focus, 25 June, p. 1899), Govert Schilling makes the important point that we will soon lose our view of the ultraviolet (UV) sky unless we preserve or replace the few existing UV space missions. However, for the Galaxy Evolution Explorer (GALEX), the future now looks brighter than the fall 2005 end date stated in the article. GALEX received the top ranking in the April 2004 Senior Review of Astronomy and Physics Mission Operations and Data Analysis Programs (*1*). NASA accepted the recommendation for "completion of the prime mission in FY05 and FY06, with an extended mission covering… FY07-FY08" [(*1*), p. 4]. GALEX is healthy and carries no consumables, so we hope it will be capable of observing well beyond 2008.

Schilling's article discusses the importance of UV observations. Emphasizing this, the NASA Review lists three areas in which GALEX surveys are particularly significant to the astrophysics community. The first is synergy with FUSE and HST, UV missions that can follow up on sources identified by GALEX. Second, the wide-area GALEX legacy database of the 135- to 280-nm UV sky promises to be "one of the most important data sets in astrophysics in this decade" [(*1*), p. 4]. Third, the GALEX Guest Investigator (GI) program will broaden GALEX scientific impact well beyond the primary science of star formation history in galaxies.

Finally, we wish to qualify Schilling's caveat about the dearth of glorious UV images. The wealth of GALEX images are both beautiful and scientifically compelling (*2*). The GALEX images trace star formation in a profound variety of physical settings, as well as many otherwise invisible physical processes important in understanding galaxy formation and evolution in the local and early universe.

PETER G. FRIEDMAN AND D. CHRISTOPHER MARTIN

California Institute of Technology, MS 405-47, 1200 East California Boulevard, Pasadena, CA 91125, USA.

References

1. See http://spacescience.nasa.gov/admin/divisions/sz/SenRev04.pdf.
2. See samples at www.galex.caltech.edu/imagegallery.html.

The GALEX observation of M31 is a mosaic of 10 GALEX images with FUV and NUV displayed in blue and red, respectively. The image shows blue regions of young, hot, high-mass stars tracing out the spiral arms where star formation is occurring and the central orange-white "bulge" of old, cooler stars formed long ago. The star-forming arms of M31 are unusual in being quite circular rather than the usual spiral shape. Many other regions of star formation can be seen far outside the main body of the galaxy. The image shows several smaller companion galaxies. These include M32, a dwarf elliptical galaxy directly below the M31 central bulge and just outside the spiral arms, and M110, which is above and to the right of the M31 center. M110 has an unusual FUV bright core in an otherwise "red" old star halo.

Clinical Trials or Exploitation?

THE CHANGING LANDSCAPE OF RESEARCH and the market pressures are causing a shift of medical experiments by U.S. entities overseas, where bureaucracy is less rigorous, patients are more eager to enroll, and costs are significantly lower. Ethical concerns about international trials and the protection of subjects have been heightened (*1*, *2*). Nonetheless, little has been done to prevent underprivileged communities from being left out of clinical and scientific benefits after having served as test subjects. This happens in 33% of the studies conducted overseas (*3*); after a successful trial, the sponsor does not market the product locally. In the United States, patients tested for a new product continue to receive it either through the market or by applying to special programs. Sponsors should be required to market the new drug in the country where the trial was carried out, and to do so considering local economy, health care coverage, and purchasing power. This calls for a more direct involvement of local institutions. This would allow such institutions to not only protect individual patient rights, but also gain expertise and become more competitive.

We understand the economic and practical barriers faced by U.S. sponsors, as much as we acknowledge their need to maintain profits. Nonetheless, we see an urgent need for international consensus on ethical guidelines for entities conducting clinical experiments overseas. Such guidelines must cover all phases of a trial, from the design to the follow-up, through the review process, but they cannot be mere recommendations, as seen so far. Compliance with these rules must become a prior binding condition for the approval of any study proposal. This would constitute an important step taken against scientific capitalism, ethical relativism, and, in general, toward a fairer world.

IGNAZIO R. MARINO AND CLAUDIA CIRILLO
Department of Surgery, Jefferson Medical College, 1025 Walnut Street, Philadelphia, PA 19107, USA.

References and Notes

1. The National Bioethics Advisory Commission (NBAC), *Ethical and Policy Issues in International Research* (NBAC, Bethesda, MD, 2001).
2. World Medical Association (WMA), "Declaration of Helsinki: Ethical Principles for Medical Research Involving Human Subjects," adopted in June 1964; last note of clarification in 2002.
3. P. Lurie, S. M. Wolfe, Letter to the National Bioethics Advisory Commission regarding their report on the challenges of conducting research in developing countries (Public Citizen Health Research Group Publication No. 1545), 13 Nov. 2000 (available at www.citizen.org/publications/release.cfm?ID=6746).

Climate Change and Malaria

SIR DAVID A. KING'S CLAIM THAT "CLIMATE change is the most severe problem that we are facing today—more serious even than the threat of terrorism" ("Climate change science: adapt, mitigate, or ignore?", Policy Forum, 9 Jan., p. 176) is based, in part, on UK government-sponsored impacts analyses (*1*, *2*) that estimate that by the 2080s, because "of continued warming, millions more people around the world may in future be exposed to the risk of hunger, drought, flooding, and debilitating diseases such as malaria. Poor people in developing countries are likely to be most vulnerable" (p. 176). But the very studies underlying the latter quote, and which King cites, show that, for the most part, many more millions would be at risk in the absence of climate change (*2*). For instance, the population at risk of malaria (PAR-M) in the absence of climate change is projected to double between 1990 and the 2080s, to 8,820 million (*2*). However, unmitigated climate change would, by the 2080s, further increase PAR-M by another 257 to 323 million (*2*).

Thus, by the 2080s, halting further climate change would, at best, reduce total PAR-M by 3.5% [=100 × 323/(323 + 8,820)] (*3*). On the other hand, reducing carbon dioxide emissions with the goal of eventually stabilizing carbon dioxide at 550 ppm would reduce total PAR-M by 2.8% (*2*) at a cost to developed nations, according to King, of 1% of GDP in 2050 (p. 177), or about $280 billion in today's terms (*4*). But malaria's current annual death toll of about 1 million could be halved at an annual cost of $1.25 billion or less, according to the World Health Organization, through a combination of measures such as residual home spraying with insecticides, insecticide-treated bednets, improved case management, and more comprehensive antenatal care (*5*). Clearly, implementing such measures now would provide greater malaria benefits over the next few decades than would climate stabilization at any level. It would also reduce vulnerability to malaria from all causes—man-made or natural—now and in the future (*3*). Similarly, reducing present-day vulnerabilities to the other risk factors mentioned by King (i.e., hunger, water shortage, and flooding) could well provide larger benefits at lower costs over

Published by AAAS

the next few decades than would climate change mitigation efforts that go beyond so-called "no-regret" actions, that is, actions that are worth undertaking on their own merits unrelated to any climate change–related concerns (e.g., elimination of subsidies for fossil fuel usage or land clearance) (*3*).

The World Bank estimates that with additional annual expenditures of $40 to $60 billion, the United Nation's Millennium Development Goals to advance sustainable development could be reached by 2015 (*6*, *7*). Comparing these goals (e.g., at least halving poverty, hunger, illiteracy, child and maternal mortality, and the proportions of populations lacking safe water and sanitation) (*6*) against what can be expected from halting further climate change (*2*) indicates that no matter how serious climate change is compared to terrorism, it pales by comparison with the more mundane problems poor people in developing countries face today and over the next few decades. Even advancing halfway toward those goals would provide greater benefits for environmental and human well-being from now through the 2080s, and do so more economically than would heroic mitigation efforts (*2*, *6*). Thus, it would be far more beneficial, and cost-effective, at least for the next several decades, to reduce vulnerabilities to current problems, especially if they might be exacerbated by climate change (e.g., hunger, malaria, drought, and flooding) (*3*). Even with a lagtime of 50 years to account for the inertia of the climate and energy system, the aforementioned analyses suggest we may have at least a quarter century window (2080s minus 50 years) before deciding on the depth and extent of mitigation. Meanwhile, we should focus on improving mitigation and adaptation technologies and our knowledge of climate change science, economics, and responses. This way we can advance sustainable development and solve the problems of today while furthering our ability to solve the problems of the day after tomorrow.

INDUR M. GOKLANY*

Office of Policy Analysis, U.S. Department of the Interior, 1849 C Street, NW, Washington, DC 20240, USA. E-mail: igoklany@ios.doi.gov

*Views expressed here are the author's and not necessarily those of any unit of the federal government.

References

1. M. L. Parry *et al.*, *Global Environ. Change* **9**, S1 (1999).
2. N. W. Arnell *et al.*, *Clim. Change* **53**, 413 (2002).
3. I. M. Goklany, *Energy Environ.* **14**, 797 (2003).
4. World Bank, *World Development Indicators* (World Bank, Washington, DC, 2004).
5. World Health Organization, *World Health Report 1999* (WHO, Geneva, 1999).
6. World Bank, "The Costs of Attaining the Millennium Development Goals," available at www.worldbank.org/html/extdr/mdgassessment.pdf (accessed 25 June 2004).
7. United Nations, "UN Millennium Development Goals," available at www.un.org/millenniumgoals/ (accessed 8 July 2004).

Response

THERE IS NO REAL CHOICE BETWEEN ACTION ON climate change and action on poverty, disease, hunger, and other millennium development goals. These are part of the same sustainable development agenda. Climate change is already affecting developing countries, and it is the poorest regions of the world—such as Africa and Southeast Asia—that are most at risk. The many people who have died and the millions now homeless through the monsoon flooding in Bangladesh will bear witness to that. This kind of event can be expected to become more frequent and more extreme as global warming accelerates, exacerbated by rising sea levels.

To meet the millennium development goals, serious investment is needed in areas such as public health and infrastructure for water and energy. The British government under Prime Minister Tony Blair's leadership is strongly committed to that. The total UK official development assistance (ODA) will rise to almost £6.5 billion by 2007/08, which will mean that our ODA will have risen from 0.26% of Gross National Income (GNI) in 1997 to 0.47% in 2007/08.

At the same time, the clock is ticking as concentrations of greenhouse gases mount in the atmosphere. At well over 370 ppm, we are already at 50% above preindustrial levels, unlikely to have been seen on Earth for around 20 million years. Global action is needed now if we are to retain the chance to stabilize emissions at a level to avoid even more dangerous climate change than that to which we are already committed. The work of the Intergovernmental Panel on Climate Change, representing the overwhelming majority of world scientific opinion, including in the United States, has shown that we are now on track to seeing average global temperatures rise by 1.5° to 5.8°C this century as a result of human activities—burning of fossil fuels and deforestation. Failure to act will result in a price, both human and economic, that will be paid across the world for generations to come. Once CO_2 is released into the atmosphere, it will remain there for centuries.

That is why real climate action is needed now at a global level. As Tony Blair has announced, during our G8 Presidency, we wish to deliver real progress on both climate change and African development.

SIR DAVID A. KING

Chief Scientific Adviser to Her Majesty's Government and Head of the Office of Science and Technology, 1 Victoria Street, London SW1H 0ET, UK.

A Bit of History About Edwin A. Link

I WAS INTERESTED TO READ THE NEWS FOCUS discussion regarding the fiscal and educational challenges being undertaken by many U.S. marine laboratories, including the Scripps Institution of Oceanography (SIO), Harbor Branch Oceanographic Institution (HBOI) and Woods Hole Oceanographic Institution (WHOI) ("Saving Scripps," D. Malakoff, 9 July, p. 166). It is important that the contributions of the pioneering engineers and scientists who helped found these institutions not be overlooked, though.

For example, the photo caption accompanying the sidebar on p. 167 notes that the Harbor Branch submersibles were named after Seward Johnson Sr., but neglects to mention that they were also named after the late Edwin A. Link (1904–81), the engineer and inventor who designed the Johnson-Sea-Link (JSL) submersibles, as well as many other novel marine engineering devices (e.g., the submersible decompression chamber and the first pressurized diver lockout small submersible). Link and Johnson worked hand in hand from their respective engineering and financial backgrounds during the founding and initial operation of HBOI, and the name of the submersibles reflects the importance of their dual contributions.

The Link Foundation, established by Ed Link and his wife, Marion, continues to provide vital financial support to Harbor Branch, including sponsorship of their Summer Internship program, which this year celebrates its 30th year of launching the careers of future marine scientists and ocean engineers.

RICHARD W. MURRAY*

Department of Earth Sciences, Boston University, 685 Commonwealth Avenue, Boston, MA 02215, USA.

*The author is Special Advisor to the Link Foundation and grandnephew of Ed Link.

CORRECTIONS AND CLARIFICATIONS

News Focus: "Telescopes break new ground in quest for cosmic rays" by D. Clery (3 Sept., p. 1393). The location given for the Whipple telescope was incorrect. The Fred Lawrence Whipple Observatory is on Mount Hopkins, Arizona, not Kitt Peak.

Reports: "Foundering lithosphere imaged beneath the southern Sierra Nevada, California, USA," by O. S. Boyd *et al.* (30 July, p. 660). There were errors in temperatures reported in the Fig. 3 caption. The correct sentence is "Compositions defined in the text that best match the seismic observations are garnet pyroxenite (red diamond) at 1000°C, spinel peridotite (red circle) at 1200°C, and garnet peridotite (red triangle) at 1000°C." Also, the source of the fellowship listed in the acknowledgments in reference 30 was incorrect. It should have been the Cooperative Institute for Research in Environmental Sciences.

BIOETHICS

Thinking About Caring About Animals

David Magnus

The company Genetics Savings and Clone recently began taking orders from people who are so enamored of their cats that they are willing to spend $50,000 to have them cloned. Millions of people in the United States consider their pet dog or cat to be a member of their family, and with the development of that relationship has come a commitment to provide health care that is beyond the reach of most humans. Feline kidney-transplant programs are now available. At the same time, industrial agriculture treats animals as merely part of the production process and attempts to find ways to cram an ever-increasing number of animals into as little space as possible. Most of us who have deep emotional attachments to some nonhuman animal spend little time thinking of the source of the hamburger or chicken we eat or the leather products we happily wear. Yet these practices typically result in the abject misery of large numbers of animals. This incongruity lies at the heart of *Animal Rights*, a collection of essays edited by Cass Sunstein and Martha Nussbaum.

The editors, professors at the University of Chicago Law School, have gathered a well-balanced collection that explores the legal and philosophical underpinnings of rational approaches to how we ought to think about animals. The authors cover several different overlapping debates in their contributions. Although nearly everyone agrees in principle that it is wrong to cause an animal to suffer unless there is a compensatory benefit, there is a great deal of disagreement over how far that prohibition extends as well as what it is based on. Should we think primarily in terms of animal welfare or animal rights? That is, should we simply aim at limiting needless suffering, or are nonhuman animals entitled to the same basic rights and respect as humans are? If animals have rights, how far do those rights extend and are there limits to which sorts of animals have them?

Animal Rights
Current Debates and New Directions
Cass R. Sunstein and Martha C. Nussbaum, Eds.

Oxford University Press, New York, 2004. 350 pp. $29.95. ISBN 0-19-515217-4.

The reviewer is at the Stanford Center for Biomedical Ethics, 701 Welch Road, Suite 1105, Palo Alto, CA 94305, USA. E-mail: dmagnus@stanford.edu

Several of the authors explore various legal rights that animals might possess, including the right to bring lawsuits. Should animals be thought of as property, or is that an example of prejudice analogous to the ownership of slaves in earlier times?

The differences that separate many of the contributors to this collection are vast and as difficult to bridge as those found in any divisive social issue. Several of the contributors see the recognition of animal rights as simply the final step in an evolutionary process by which we have come to recognize new groups as equal (in important respects) to the rest of us. Different racial and ethnic groups and women were all once regarded as inferior. Some day, these authors claim, we will see our failure to recognize animal rights as a similar failing. How could such a bold claim be defended?

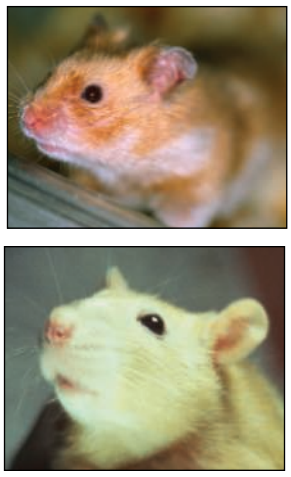

Unequal treatment under U.S. law.

One major train of argument notes that we attribute full moral status to infants and retarded individuals. Yet at least some nonhuman animals seem to have the capacity to engage in thought and social interactions at a level comparable to infants. A small number may have the capacity to be self-aware. How can we consistently deny such rights to one group of sentient beings while insisting on them for another? In response, Richard Posner and others claim that this argument rests on a false premise, namely that rights are based upon cognitive abilities. They point to the fact that newborn infants are recognized as parts of the human community with all the rights that entails. Their lack of cognitive ability may be relevant to some rights (e.g., the right to make decisions for themselves), but the most fundamental rights that persons possess are held regardless of cognitive ability.

Some of the book's most interesting material deals with current regulatory issues regarding animal welfare. Most legislation in the United States reflects the inconsistent (and possibly incoherent) views that most of us seem to hold with respect to animals. As philosopher James Rachels asks in his very clearly written chapter, what is the basis for distinguishing which animals are excluded from the various laws that have been enacted to protect animal welfare? The original U.S. Animal Welfare Act (1966), which applies only to warm-blooded animals, excluded from consideration agricultural animals or horses (other than those being used for research purposes). That exemption ensures that the treatment of many (maybe most) animals is not governed by this legal requirement that we consider even their basic welfare or treat them with minimal decency. Problems arise when one seeks a philosophical basis for this differential treatment. It is unlikely that the distinction between protected and unprotected species could in any way be defended on the basis of the characteristics of the animals themselves. Rachels also objects to other exclusions that have been introduced through subsequent interpretations of the original law and Jesse Helms's 2002 amendment to it. The latter redefined "animal" so as to exclude rats, mice, and birds from protection, which had the effect of removing 90% of the animals used in experimentation from the regulations. It is difficult to find ethical justification for protecting hamsters and guinea pigs but not mice.

There are undoubtedly several reasons why we are so inconsistent in our attitudes toward animals. For the enormous number of agricultural animals we raise, our practices largely reflect how little people think about the origins of our food. In the United States, we are unusually disconnected from our food sources. The disquiet many of us feel when we learn more about the terrible suffering that takes place in industrial agriculture makes us feel guilty. But giving up our culinary habits is hard, and ignorance is bliss.

In the end, as philosopher Richard Rorty and judge Posner argue, there may be no rational basis for our attitudes toward animals. Why do we cry over the killing of baby seals or the endangerment of the koalas, yet feel little over the suffering of pigs (who are probably much more intelligent)? Why do we offer far greater protection to guinea pigs than to mice? Our judgments probably rest on aesthetics as much as on any rational basis. Who we choose to allow into our community is at least partly a function of which animals we see as aesthetically pleasing or as similar enough to us for us to identify with them. If this is so, our behavior and attitudes are ultimately expressions of sentiment, and no ra-

CREDITS: (TOP) ANDY CRUMP, TDR, WHO/SCIENCE PHOTO LIBRARY; (BOTTOM) MARIO BEAUREGARD/CORBIS

Published by AAAS

tional moral framework is likely to capture such a complex and culturally laden construct. Perhaps that explains why so many of us love our dogs and still enjoy a good steak. This collection of essays provides a fine introduction to a number of difficult and controversial questions. It is particularly strong in its treatment of the philosophical and legal issues that surround animal rights.

HISTORY OF SCIENCE

On the Power to Create

Iwan Rhys Morus

Promethean Ambitions
Alchemy and the Quest to Perfect Nature
by William R. Newman

University of Chicago Press, Chicago, 2004. 349 pp. $30, £21. ISBN 0-226-57712-0.

We live in a world that is increasingly obsessed by both the possibilities and the dangers of breaking the boundary between the natural and the artificial. Scarcely a week goes by without newspaper headlines being dominated by fresh claims and counterclaims about human cloning or genetically modified foods. Depending on one's perspective, the potentialities of future science represent either progress and the possibility of eliminating poverty and disease or a moral and scientific quagmire. One of the very few things about which all sides in these debates might agree is that this is a particularly modern problem. The very fact that we are even talking about such utopian (or dystopian) possibilities is a sign of the unprecedented success (or failure) of modern science. *Frankenstein*, after all, was fiction—what we are now talking about is the real thing. William R. Newman's *Promethean Ambitions* reminds us that, in this respect at least, there is nothing new under the sun.

Talk about the distinction between the natural and the artificial does indeed have a very long history, as have a range of efforts to redefine that boundary. Since the ancient Greeks, if not earlier, philosophers have debated the difference between the real and the unreal (between nature and culture, we might say), and others have tried to redefine those boundaries.

Newman, a historian of science at Indiana University, chooses the fascinating topic of alchemy as his case study in the long history of human efforts to breach the barriers between nature and human artifice. Traditionally, the goal of alchemy had always been to perfect nature, to convert everyday mundane materials into something of incomparably higher value. We think of alchemists as searching for the philosophers' stone that would deliver the secret of turning base metals into gold. As such, alchemy had its connections with other human activities that claimed to be able to intervene in the natural order of things, activities such as medicine, magic, and even art. Newman relates a handful of ancient Greek fables concerning the power of the artist to improve upon nature to remind us that debates about the possibilities of alchemy took place against a far broader context of discussions about humans' capacities to mimic or even transcend the natural order. From the early Christian and medieval periods onward, debates about just how far human interventions in the natural order could be expected to succeed had obvious theological consequences. According to one tradition that Newman traces back to medieval Arabic scholars, the capacity to transmutate substances belonged only to God, a view that made alchemy tantamount to heresy. Indeed, as Newman notes, from the late 13th century onward religious orders issued a series of proclamations against the practice of alchemy by their members.

Alchemist with Homunculus in Vessel **by David Ryckaert III (17th century).** In the lower right corner there is a barely perceptible child playing with a bladder, a conventional symbol of folly.

CREDIT: REISS-ENGELHORN-MUSEEN, MANNHEIM

This left supporters of alchemy in something of a double bind. On the one hand, they were condemned as charlatans claiming powers that they simply did not have. On the other, they stood accused as blasphemers, usurping powers reserved for God, and were often suspected of dallying with demons. As is well known by now, alchemy played an important role during the period we no longer call the Scientific Revolution. To many proponents of the New Sciences such as Paracelsus, Robert Boyle, and even Isaac Newton, alchemy seemed a highly promising avenue of research, combining as it did the direct investigation of nature with the search for lost secrets of the ancients. Maybe it was through alchemy that science inherited its dangerous edge, open to accusations of both charlatanry and impiety in just the same way. Newman's example of the homunculus—the artificial man—is suggestive in this respect. The possibility of artificial life could be a number of things to medieval and early modern commentators: it could be fraud, it could be heresy, or it could be the highest example of man's newfound powers over the natural world. What Newman does make clear is that none of these debates were conducted in black and white.

I am not sure to what extent I would want to follow Newman in linking contemporary debates about the moral pitfalls of tinkering with nature with the long history of alchemy. He is certainly correct that we would do well to remember these older debates in all their complexity. They are an important corrective to facile moral posturing on both sides of the contemporary argument, if nothing else. Neither will it do to dismiss alchemy with the remark that it was only make believe. After all, its proponents (and more than a few of its opponents) were just as convinced of its efficacy as we are today about the power of genetic engineering. The problem in the end is one of different economies. Alchemy, in its most recent form at least, was practiced within the context of a culture of courtly patronage. Genetic engineering is a global industry. However suggestive and seductive the similarities between the debates may be, they cannot overcome these differences in place and scale. Nonetheless, I certainly did not allow such qualms to distract me from enjoying Newman's thought-provoking book. Alchemy is a fascinating topic in its own right and *Promethean Ambitions* does full justice to it.

The reviewer is in the School of Anthropological Studies, Queen's University, Belfast, BT7 1NN, UK. E-mail: i.morus@qub.ac.uk

This year's essay series highlights the benefits that scientists, science, and technology have brought to society throughout history.

What Kind of Science Is Experimental Physics?

H. Otto Sibum

In 1923, the German theoretical physicist Felix Auerbach told his readers that experimental physicists, unlike botanists or geologists, do not observe nature but rather artificially create physical phenomena in their laboratories. He made what would today be regarded as a contentious claim (*1*):

> X-rays are not a 'natural phenomenon', until Röntgen there weren't such, they have been invented by him (this expression is more appropriate than the conventional 'discovered'); and in case it turns out that there will be such rays in nature, this does not change the issue essentially.

Reflections like this on the artificial technological character of experiment—or, more precisely, the kind of scientific experience gained through the use of human devices—is not just an important expression of Auerbach's time. It is an integral part of a long historical debate, going back at least to the 17th century, about the epistemological status of experiment and experience. In this essay, I concentrate on the mid-18th to the early 20th century, a time period in which a "third man" was sought to bridge the divide between theorists and practitioners, between science and the mechanical arts. The consequent emergence of a new scientific persona—the experimentalist—was coupled to the establishment of experimental physics as an academic discipline.

Reproduction of a historical experiment from the 18th century. The light phenomena produced through mechanical friction in a vacuum tube were considered a model of the Aurora Borealis.

Since the early modern period, scholarly opinions on "the art of experiment" ranged from denying that it had any epistemological value to the 19th-century conviction that this form of inquiry was the only way to make sense of natural causes. A key issue in these controversies was that the physical manipulation of objects was seen as not belonging to the scholarly tradition, in which a clear distinction between doing and knowing still predominated. In 1764, the philosopher Christian Wolff argued (*2*):

> In such circumstances, a third man would be needed, who could in himself unite science and art, in order to correct the *theorists*' infirmities and to combat the prejudice of the lovers of the arts, as if they could be therein complete without the *theory*, and leave [theory] to the idle heads good-for-nothing in the world.... Hence ... [the engineer] compared himself to a bat, tolerated among neither birds nor quadrupeds, and he complained that he was hated by the practitioners of art as well as despised by the *theorists*, for he wanted by his nature to be celebrated as a remarkable man by both, and to share fame in the learned world with the latter and happiness at court with the former.

In establishing experimental physics within academia, experimentalists were experiencing the advantages and disadvantages of the third man's position. Like bats, they were difficult to classify. Did their studies of nature, practiced with head and hand, lead to a specific form of knowledge? And did this knowledge qualify as science? How one answered this question depended on one's stance toward the implicit distinction made in those days between experimental knowledge and science, or knowledge in general and scientific knowledge in particular. Furthermore, the dominant understanding of scientific knowledge as universal, autonomous, and permanent was intimately linked with the hegemony of the written text in the scholars' form of life. Hence, from the mid-18th century onward, several generations of experimental natural philosophers were required to free the art of experiment from its epistemological stigma and to position their knowledge within academia.

The main challenge to traditional text-based scholarship was that experimentalists' had to develop and study instruments to investigate nature's effects.

The new fields of electricity and magnetism within experimental physics were particularly challenging, because nearly all phenomena connected with these fields were observable only with the assistance of instruments or apparatus. Artificially created illuminations in an electrified vacuum tube were regarded as models of the Aurora Borealis. But experimenters did not only equate artificially created phenomena with macroscopic phenomena. In the late 18th century, the Italian physicist Alessandro Volta succeeded in detecting and explaining microphysical phenomena. He constructed a model of the electric fish, today known as the first electric battery, which for the first time demonstrated the existence of an electric current. At the end of the 18th century, different knowledge claims based on experiences made in those artificially created local settings often led to controversies about the true meaning and scope of these experiences.

Despite the immense practical achievements in creating "new physical truth," this conflict persisted into the 19th century. Artisans, merchants, engineers, instrument makers, and scholars participated in a complex historical process of molding the physical sciences based on experimentation. Artisanal knowledge became essential for the experimental sciences, but this expert knowledge resided outside of academia. The material interests of the state in promoting industry and the military enabled experimentalists to pursue their research and finally forced traditional academia to establish scientific laboratories (*3*).

The term "Handwerksgelehrte," coined in Germany in the second half of the 19th century, captures the amalgamation of the experimentalists movement with the traditional academic elite. What had previously been regarded as separate knowledge traditions—experimentalists and bookish scholars—now merged into a distinct community of experimental scientists in which ways of acting and ways of knowing had equal epistemological status (*4*). By the end of the 19th century, lab-

H. Otto Sibum is at the Max Planck Institute for the History of Science, Wilhelmstrasse 44, 10117 Berlin, Germany. E-mail: sibum@mpiwg-berlin.mpg.de

Published by AAAS

oratories had been established in most universities in Europe and North America.

The teaching of physics also changed during this time. Chairs for experimental physics were set up, and a new scientific methodology emerged. Hermann von Helmholtz and James Clerk Maxwell promoted an understanding of induction that stressed the similarities between the intellectual work of the experimental physicist and that of the artist. Both continuously reminded their audiences that experimental physics differed from traditional scholarship. Maxwell followed his general conviction "that the facts are things which must be felt, they cannot be learned from any description of them" (*5*). Similarly, Helmholtz told the Naturforscherversammlung in Innsbruck in 1869 (*6*):

> Besides the kind of knowledge that books and lectures provide, the researcher in the natural sciences needs the kind of personal acquaintance that only rich, attentive sensory experience can give him. His senses must be sharpened.... His hand must be exercised that it can easily perform the work of a blacksmith, locksmith, joiner, draftsman, or violinist.

This plea represents the gradual change in the epistemological status of sensuous experience in science. Helmholtz, Maxwell, and others placed sensuous experience center stage in the process of generating scientific knowledge and of bridging the divide between theorists and practitioners.

From the mid-18th to the early 20th century, the establishment of experimental physics as an academic discipline challenged the still-dominant epistemological divide between knowing and doing.

And yet, reflections about the epistemological status of experimental physics in general and sensuous experience in particular continued. Not only the new Handwerksgelehrte, but even laypersons forcefully argued for a mediation between knowing and doing, theory and experience. The German tanner Joseph Dietzgen, for example, announced in 1869 that the third man's problem had not been fully resolved (*7*). To him, the tension resulted from a conflict between two philosophical traditions about the sources of knowledge: the idealist regards the source of knowledge in reason only, the materialist in the sensually perceived world. But he saw a way out of this contradiction (*7*):

> The mediation of this contradiction requires the insight that both sources of knowledge are intimately connected with each other... Therefore even the lowest art of experiment which acts on the basis of experienced rules, is only gradually different from that scientific practice which is based on mere theoretical principles.

By the end of the 19th century, the increasing number of techniques to investigate microphysical objects, such as x-rays and electrons, changed the experiential basis of physics and evoked various reflections about these sources of knowledge. Particularly the artificial technological character of experimental physics was discussed (*1*):

> Experimental physics does not—as the term already suggests—practice observation of nature like other natural sciences, it deploys artificial experiments which are performed just for a specific purpose. Strictly speaking, physics with regard to its method is not a natural science like astronomy, geology, botany, etc.; it does not deal with natural phenomena but artificial phenomena produced by intentional acts of the researcher; in this sense we can speak of physics as a technical science.

By 1900, more than 90% of German physicists practiced precisely this technical science. But the physics community was still not speaking with one voice, and several different stances about the epistemological status of experiment and sensuous experience in generating knowledge continued to exist. The experimental physicist Otto Wiener suggested that instrument-based physical research should be regarded as an evolutionary process of the extension of the human senses. Generalizations were derived from sensuous experience. Consequently, elements of theory were to be understood as "condensed experience."

Auerbach took a very similar stance in describing the practice of theoretical physics: for him, the source of scientific knowledge was always experience, the latter not to be regarded as the test of a theory but as the materials to build up the theory. The implied claim—he argued—that theoretical physics constructs its general fundament from experience might make it appear as if physicists are arguing in a circle. How could one derive the facts of experience from a general schema and at the same time gain this schema by orientating one's self toward experience?

To persuade his audience, he refers to the most striking invention of 19th century electrical engineering: the dynamo. First built by Siemens, it starts to produce current immediately when turned by hand, because a trace of magnetism inherent in iron produces weak electric currents, which feed the same machine. In a similar way, theoretical physicists want to gain as much knowledge about nature as possible from a minimum of experience. Of course with some practice they could build theoretical physics directly from the condensed experience stored in the mind, with the foresight that a retrospective check against experience will not contradict the theoretical claim; but if contradictions occur, they would have to restructure their abstract building or eventually replace it by another one (*8*).

Auerbach distinguished this practice of theorizing from another kind of theoretical physics, which promotes the idea that the general can be derived exclusively from the researcher's mind [(*8*), p. 2]:

> They construct an ideal world, declare their satisfaction, if the real world matches the ideal. But in case of contradictions these theorists would go that far and declare the real world as false because it does not match with the ideal.

In doing so, he clearly commented on a tendency among some theoretical physicists, who held that experience and reason would remain divided in two separate domains (*9*):

> Experience remains, of course, the sole criterion of physical utility of a mathematical construction. But the creative principle resides in mathematics. In a certain sense, therefore, I hold it true that pure thought can grasp reality, as the ancients dreamed.

By the turn of the 20th century, the art of experiment had been developed to the most powerful art of knowing within science. In Germany, experimental physicists regarded the artificial technological character of experimentation as the extension of the human senses, opening up new realms of experience. This changing experiential basis even induced an increasing self-reflexivity in physics, which shaped the formation of different types of theoretical physics.

References and Notes

1. F. Auerbach, *Entwicklungsgeschichte der modernen Physik* (Springer, Berlin, 1923).
2. B. F. de Belidor, *Architectura Hydaulica* (Klett, Augsburg, 1764), introduction by C. Wolff.
3. M. N. Wise, *Bourgeois Berlin and Laboratory Science*, in preparation.
4. H. O. Sibum, *Sci. Context* **16**, 89 (2003).
5. H. O. Sibum, *Cambridge Rev.* **116**, 25 (1995).
6. H. Helmholtz, *Über die Ziele und Fortschritte der Naturwissenschaft* (Friedrich Vieweg und Sohn, Braunschweig, 1871).
7. J. Dietzgen, *Das Wesen der menschlichen Kopfarbeit dargestellt von einem Handwerker. Eine abermalige Kritik der reinen und praktischen Vernunft* (Otto Meißner, Hamburg, 1869).
8. F. Auerbach, *Die Methoden der theoretischen Physik* (Akademische Verlagsanstalt, Leipzig, 1925).
9. A. Einstein, in *Ideas and Opinions*, based on *Mein Weltbild*, Carl Seelig, Ed., and other sources. New translations and revisions by Sonja Bargmann (Bonanza Books, New York, 1954), pp. 270–276.

STRUCTURAL BIOLOGY

Evolution of RNA Architecture

Eric Westhof and Christian Massire

The discovery of catalytic RNAs (ribozymes) by Altman (*1*) and Cech (*2*) in the early 1980s entirely changed our views of the RNA molecule. This breakthrough led to a remarkable increase in knowledge about the folding of RNA molecules and their activity. Currently, tiny RNA molecules—microRNAs (*3*) and small interfering RNAs (*4*)—are transforming our thinking about how gene expression is regulated. In addition, the high-resolution crystal structures of the bacterial ribosome subunits (*5*, *6*) have boosted by orders of magnitude the database of possible RNA structures and motifs. Also appearing are exciting crystal structures of self-splicing group I introns (*7*, *8*). On page 104 of this issue, Krasilnikov *et al*. (*9*) promote our understanding of RNA structure still further. They report the crystal structure of the specificity (S) domain of ribonuclease P (RNase P) from the bacterium *Thermus thermophilus*.

The ribozyme RNase P is a ribonucleoprotein particle that induces maturation of the 5′ end of transfer RNAs (tRNAs). RNase P is present in bacteria, archaea, and eukaryotes, and elements of its RNA component are highly conserved. There are two types of bacterial RNase P based on sequence alignments of the RNA component: type A (from *Escherichia coli* and *T. thermophilus*) and type B (from *Bacillus subtilis*) (*10*). Type B RNase P RNA sequences, derived from the ancestral type A form, are found exclusively in select branches of the largest group of Gram-positive bacteria, which includes pathogens such as *B. anthracis*. Biochemical and biophysical data show that RNase P RNA is composed of two independent domains: the catalytic domain and the S domain (*11*). The S domain recognizes and binds to the pre-tRNA substrate through the highly conserved thymine loop of pre-tRNAs. Despite the invariant structure of the pre-tRNA substrate, the RNA components of type A and type B RNase P show characteristic differences in their secondary structure (see the figure).

E. Westhof is at the Institut de Biologie Moléculaire et Cellulaire du CNRS, Université Louis Pasteur, F-67084 Strasbourg, France. E-mail: e.westhof@ibmc.u-strasbg.fr C. Massire is at Ibis Therapeutics, Carlsbad, CA 92008, USA. E-mail: cmassire@isisph.com

What Krasilnikov *et al*. (*9*) address is how to build a similar recognition interface for a rather invariant substrate (pre-tRNA) from RNase P RNA secondary structures that are only partly conserved. First, the investigators solved the crystal structure to 2.9 Å of the S domain of the type A RNase P RNA from *T. thermophilus*. Then, they directly compared the secondary and tertiary structures of this molecule to those of the type B RNA S domain of *B. subtilis*, whose crystal structure they solved to 3.15 Å last year (*12*). Their study offers structural insights into how evolution has tinkered with the elegant architecture of RNA.

RNA folding can be viewed as hierarchical, with preformed helical domains associating into helical bundles leading to compact tertiary structures driven by interactions between RNA-RNA anchor modules. From the two crystal structures of Krasilnikov *et al*., we can actually see how the P13/P14 stem that is unique to type A RNA and the P10.1 stem that is unique to type B RNA form independently folded units that can be added to or removed from the common core with minimal alterations to the fold (see the figure). Indeed, the type B P10.1 stem is inserted in the well-defined P10/P11 core in place of a single bulged-out nucleotide. Similarly, P13/P14 is deleted with noticeable alterations in the conformation of only two adjacent nucleotides. It is surprising how minimally the intricate fold of the internal L11/12 loop is perturbed by the insertion of and the connections to the stacked P13/P14 helices. The key is the presence of modules with 5′ and 3′ ends within close proximity to one another. This occurs naturally in the module formed by the coaxially stacked P13 and P14 stems and in the P10.1 module, which includes a five-nucleotide loop on its 3′ end that acts like a miniature stem-loop cap. Further, the insertion of the P10.1 element in P11 allows for the formation of most of the tertiary–non-Watson-Crick pairs of P11 as found in type A RNase P RNA. The modular RNA architecture is apparent because in the case of both type A and type B RNase P RNA, a coaxial stack of base

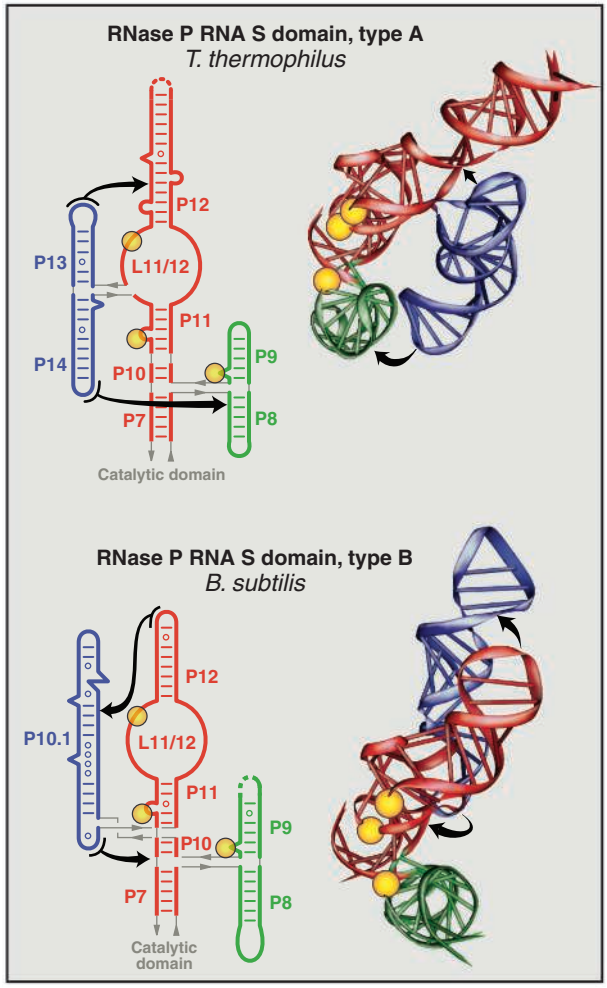

A snapshot of ribozyme evolution. The secondary structure and tertiary fold of the S domain of type A (from *T. thermophilus*) and type B (from *B. subtilis*) RNase P RNA. The main interaction points of the pre-tRNA substrate with the S domain are indicated in yellow. Krasilnikov *et al.* (*9*) compared the conserved parts of the central component P11 and L11/12 of the tRNA recognition region for type A and B RNA and found the root-mean-square deviation to be about 1.6 Å indicating that the core region is conserved even though the secondary structure differs. The principal RNA-RNA contacts are indicated by gray arrows (which point from the adenines to the shallow/minor grooves of the contacted helices). The common orientation is along the P8-P9 coaxial stack of helices. Coordinates are from (*9*, *12*).

CREDIT: KATHARINE SUTLIFF/*SCIENCE*

pairs (P13/P14, P10.1, P8/P9) is grafted onto a similar core.

Surprisingly, the crystal structure of the ribosome as well as of other RNAs demonstrate a recurring motif: that is, long-range RNA-RNA anchors mediated by adenine bases that make contact with the shallow minor grooves of two stacked base pairs of RNA helices (*14*). RNA has a remarkable propensity for contributing two contiguous adenines to such A-minor interactions. Sometimes the consecutive adenines belong to GNAA tetraloops, but other RNA motifs also are able to fold with two adenines poised for binding to the shallow/minor groove of a helicoidal region. The proper conformation of these adenines is generally ensured by other local interactions involving one edge of the adenines, leaving the other edges free for further long-range interactions.

The four RNA-RNA contacts (indicated by arrows in the figure) are all mediated by A-minor interactions. Strikingly, the anchoring of the subdomains is via A-minor anchoring motifs between different peripheral domains, even though they are embedded within very different structural contexts. In type A RNA, adenines in the heptaloop L13 and the tetraloop L14 contact stacked base pairs in P12 and at the base of P8, respectively (*9*). But in type B RNA, adenines in the apical loop of P12 contact a special motif in P10.1, and a single-stranded region organizes itself in a loop with two adenines contacting the stack between P7 and P10 (*12*). Thus, with A-minor anchoring motifs, nonhomologous peripheral elements can form different and mutually exclusive long-range contacts to promote an identical functional purpose: the stabilization of the helical stems that build the recognition core (helices P7 to P11) that correctly positions the substrate. There is increasing awareness of the structural importance of peripheral RNA domains in the evolution and function of RNAs. For example, peripheral domains of the small hammerhead ribozyme identified in sequence alignments affect its catalytic activity (*13*).

RNA structural bioinformatics is based on comparative analysis, which searches for coordinated events in sequence evolution to infer spatial relationships. The structural knowledge gained by comparing sequences of homologous RNAs is unequaled: All of the long-range contacts discussed above have been identified by comparative analysis (*15*, *16*). Yet the exquisite atomic views of such contacts would not have been possible without crystallography. Furthermore, the two crystal structures offer definite clues about conserved residues (especially bulges or unpaired regions) that were clearly seen as conserved in sequence alignments but whose role was unclear. The next challenge resides in the integration of the rich and complex three-dimensional information gained by crystallography with the ever-increasing number of sequence databases. The implication is that systematic comparisons between crystal structures and aligned sequences should tease apart the key molecular connections that maintain biologically functional RNAs. The goal is to derive the rules of molecular evolution that govern the RNA world, which forms the origin of our DNA-based modern life.

References

1. C. Guerrier-Takada *et al.*, *Cell* **35**, 849 (1983).
2. K. Kruger *et al.*, *Cell* **31**, 147 (1982).
3. D. P. Bartel, *Cell* **116**, 281 (2004).
4. Y. Dorsett, T. Tuschl, *Nature Rev. Drug Discov.* **3**, 318 (2004).
5. B. T. Wimberly *et al.*, *Nature* **407**, 327 (2000).
6. N. Ban *et al.*, *Science* **289**, 905 (2000).
7. P. L. Adams *et al.*, *Nature* **430**, 45 (2004).
8. F. Guo *et al.*, *Mol. Cell*, in press.
9. A. S. Krasilnikov *et al.*, *Science* **305**, 104 (2004).
10. B. D. James *et al.*, *Cell* **52**, 19 (1988).
11. A. Loria, T. Pan, *RNA* **2**, 551 (1996).
12. A. S. Krasilnikov *et al.*, *Nature* **421**, 760 (2003).
13. A. Khvorova *et al.*, *Nature Struct. Biol.* **10**, 708 (2003).
14. P. Nissen *et al.*, *Proc. Natl. Acad. Sci. U.S.A.* **98**, 4899 (2001).
15. J. L. Chen *et al.*, *EMBO J.* **17**, 1515 (1998).
16. C. Massire *et al.*, *J. Mol. Biol.* **279**, 773 (1998).

APPLIED PHYSICS

Boosting Magnetoresistance in Molecular Devices

Christoph Strunk

Advances in nanoelectronics continue to push forward the miniaturization of devices and the improvement of their speed and functionality. Of particular importance are the fields of molecular electronics and spintronics. By studying electronic transport at molecular scales—for example, through individual carbon nanotubes (*1*), C_{60} molecules (*2*), and single organic molecules (*3*)—researchers try to reach the ultimate size limits for devices. In spintronics, the spin rather than the charge is used to store and process classical as well as quantum information (*4*).

On page 86 of this issue, Pasupathy *et al.* (*5*) succeed in merging these two fields. They explore molecular quantum dots consisting of single C_{60} molecules, which are sandwiched between two ferromagnetic nickel electrodes (see the figure). These new spintronic devices combine two fundamental electron-electron interaction effects of condensed matter physics: the Kondo effect and ferromagnetism. At first sight, these effects seem to exclude each other, but they have now been integrated in one device. Once a controlled assembly of such devices is achieved, they may even outperform more conventional magnetoelectronic devices.

Previous experiments have shown that a quantum dot trapping an unpaired electron can display the Kondo effect, which is one of the most prominent many-body effects in condensed matter physics (*6*, *7*). If the tunneling barriers defining the quantum dot are sufficiently transparent, the wave function of the single electron can leak out of the dot and hybridize with the delocalized electrons in the contacts. The Coulomb repulsion on the dot leads to an antiferromagnetic exchange

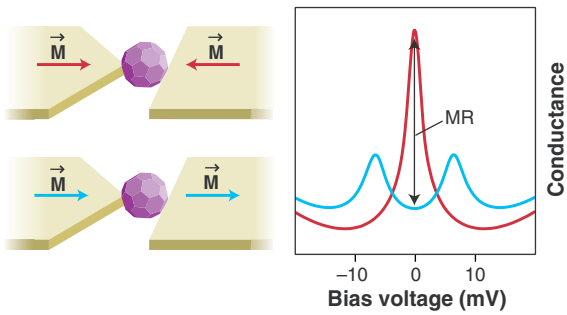

Merging the Kondo effect and ferromagnetism. (Left) Artist's view of the C_{60} quantum dot between ferromagnetic nickel electrodes. The different shapes of the electrodes enable a controlled transition between parallel and antiparallel alignment of the magnetization, $\vec{\mathbf{M}}$. **(Right)** Differential conductance versus bias voltage of the device for the parallel (blue) and antiparallel state (red). For parallel alignment, the Kondo resonance is split by the exchange fields of the two electrodes. For antiparallel alignment, the exchange fields of the two electrodes cancel each other, and Kondo resonance is restored at zero-bias voltage. This leads to a large magnetoconductance MR, which exceeds the usual tunneling magnetoconductance (arrow).

CREDIT: PRESTON HUEY/*SCIENCE*

The author is in the Department of Experimental and Applied Physics, University of Regensburg, Universitätsstrasse 31, D-93040 Regensburg, Germany. E-mail: christoph.strunk@physik.uni-r.de

coupling between the electron spin on the dot and the neighboring electron spins in the electrodes. The corresponding coupling energy can be expressed as a characteristic temperature, the Kondo temperature T_K. Below this temperature, the spin on the dot is screened by the formation of a cloud of electrons on the electrodes, having a spin polarization antiparallel to the spin on the dot. The formation of the screening cloud enhances the density of states in the electrodes and leads to a high-conductance state. The hallmark of the Kondo effect is a pronounced peak in the differential conductance with width k_BT_K (where k_B is the Boltzmann constant), which gradually disappears at temperatures above T_K. In the presence of a magnetic field, this peak shows a Zeeman splitting.

Until recently, the prospects for using the Kondo effect in quantum dots in applications were poor because it required temperatures below 1 K. The use of molecules as quantum dots has pushed the Kondo temperature up to 30 K (*8*, *9*). However, at this high T_K, very large external magnetic fields are required to split the Kondo resonance, again precluding applications in magnetoelectronics.

The situation is changed completely by the experiment of Pasupathy *et al.* (*5*). The use of ferromagnetic electrodes puts the antiferromagnetic Kondo interaction in competition with the ferromagnetic spin alignment by the ferromagnet's exchange field. The exchange field is responsible for the spontaneous spin polarization of the ferromagnet and acts also on the single spin trapped on the quantum dot. It has an effect similar to that of an external magnetic field. However, the corresponding Zeeman energy is given by the Curie temperature, T_C, which is 20 to 30 times larger than T_K. The exchange field is much larger than laboratory-scale magnetic fields.

Moreover, in devices with symmetric coupling, the exchange fields of the two electrodes cancel each other if their magnetization is antiparallel. Hence, a huge effective magnetic field can be controlled by the tiny external magnetic fields required to switch the magnetization of the two electrodes. By virtue of the ferromagnetic hysteresis, the molecular device turns out to be a bistable switch, which can be controlled precisely in the same way as more conventional magnetoelectronic devices—with the advantage that the magnetoresistance is enhanced by the Kondo resonance and much larger than the usual tunneling magnetoresistance (see the figure).

The main drawback of the new devices is that so far, their fabrication relies on chance. Only 30 out of 1000 devices show the Kondo effect. This is typical for the current state of molecular electronics. The control of the electronic transport properties of molecular devices requires a positioning of the device components with an accuracy far better than 1 nm. The assembly of carbon nanotube field-effect transistors has been demonstrated using DNA templates (*10*), but does not yet allow a sufficient level of precision. Here is much scope for future developments. Nevertheless, the experiment of Pasupathy *et al*. is an important proof of principle and will fuel progress in fundamental physics, sample fabrication, and device applications.

References

1. S. J. Tans, A. R. M. Verschueren, C. Dekker, *Nature* **393**, 49 (1998).
2. C. Joachim, J. K. Gimzewski, R. Schittler, C. Chavy, *Phys. Rev. Lett.* **74**, 2102 (1995).
3. J. Reichert *et al.*, *Phys. Rev. Lett.* **88**, 176804 (2002).
4. S. A. Wolf *et al.*, *Science* **294**, 1488 (2001).
5. A. N. Pasupathy *et al.*, *Science* **306**, 86 (2004).
6. D. Goldhaber-Gordon *et al.*, *Nature* **391**, 156 (1998).
7. S. M. Cronenwett, T. H. Oosterkamp, L. P. Kouwenhoven, *Science* **281**, 540 (1998).
8. J. Park *et al.*, *Nature* **417**, 722 (2002).
9. W. Liang *et al.*, *Nature* **417**, 725 (2002).
10. K. Keren *et al.*, *Science* **302**, 1380 (2003).

GEOPHYSICS

Are Earth's Core and Mantle on Speaking Terms?

Cin-Ty Aeolus Lee

Earth's interior is divided into a central core made of an iron-nickel alloy and a rocky mantle made of silicate and oxide minerals. Earth scientists often ignore the core in their treatments of the chemical and dynamic evolution of the mantle after core-mantle segregation. However, there has been growing debate on whether there may be significant chemical interaction between the core and the mantle. On page 91 of this issue, Humayun *et al*. (*1*) present data that suggest that the lower mantle may be enriched in iron compared to the upper mantle, and that this iron enrichment may indeed be due to core-mantle interaction.

If the lower mantle is enriched in iron through chemical reactions between the lower mantle and the liquid outer part of the Earth's core (*2*), then the dynamics of the core and mantle must be coupled. The iron enrichment will also influence the physical properties of the lower mantle (such as its density, elasticity, and electrical conductivity). However, direct evidence for an iron-rich lower mantle is lacking. Moreover, even if the lower mantle is enriched in iron, other explanations are plausible. For example, the mantle may retain a primordial compositional stratification. Alternatively, subduction of oceanic crust or deep-sea marine sediments, some of which may be enriched in iron and manganese, may cause the enrichment.

It is widely believed that volcanic hotspots are the surface manifestations of plumes rising up from the lower mantle or core-mantle boundary. Earth scientists therefore use hotspot volcanoes as windows into Earth's deep interior. Humayun *et al*. (*1*) report the Fe/Mn ratios of basaltic lavas associated with a well-known hotspot, Hawaii. They show that the Hawaiian lavas have higher Fe/Mn ratios than basalts from mid-ocean ridges; the latter only tap the upper mantle (see the figure, inset).

The authors argue that the partitioning of iron and manganese between melts and the mantle is roughly equal, and that the Fe/Mn ratio of a melt should therefore closely reflect the Fe/Mn ratio of the melt source region. They thus suggest that the high Fe/Mn ratios of the Hawaiian lavas reflect a lower mantle enriched in iron, possibly due to long-term chemical interaction between the core and the mantle.

If this interpretation is correct, then the results provide the second observational evidence for a core component to the Hawaiian mantle source. The first evidence came from anomalously high concentrations of the isotope ^{186}Os in Hawaiian lavas (*3*), which were attributed to a Hawaiian mantle source that has incorporated small amounts of outer-core material. The latter is hypothesized to have elevated ^{186}Os due to its high Pt/Os ratio and radioactive decay of ^{190}Pt to ^{186}Os (*3*). Others have argued that the ^{186}Os anomalies are more likely to result from incorporation of subducted Fe-Mn–rich marine sediments (*4*, *5*), which also have high Pt/Os ratios. However, such sediments have low Fe/Mn ratios, which is inconsistent with the high Fe/Mn ratios of Hawaiian lavas reported by Humayun *et al*. (*1*).

Why were the consistently high Fe/Mn ratios in Hawaiian lavas not recognized earlier, given that iron and manganese have been routinely measured for decades? Humayun *et al*. suggest that the existing database of iron and manganese in Hawaiian lavas and mid-ocean ridge basalts

The author is in the Department of Earth Science, Rice University, Houston, TX 77005, USA. E-mail: ctlee@rice.edu

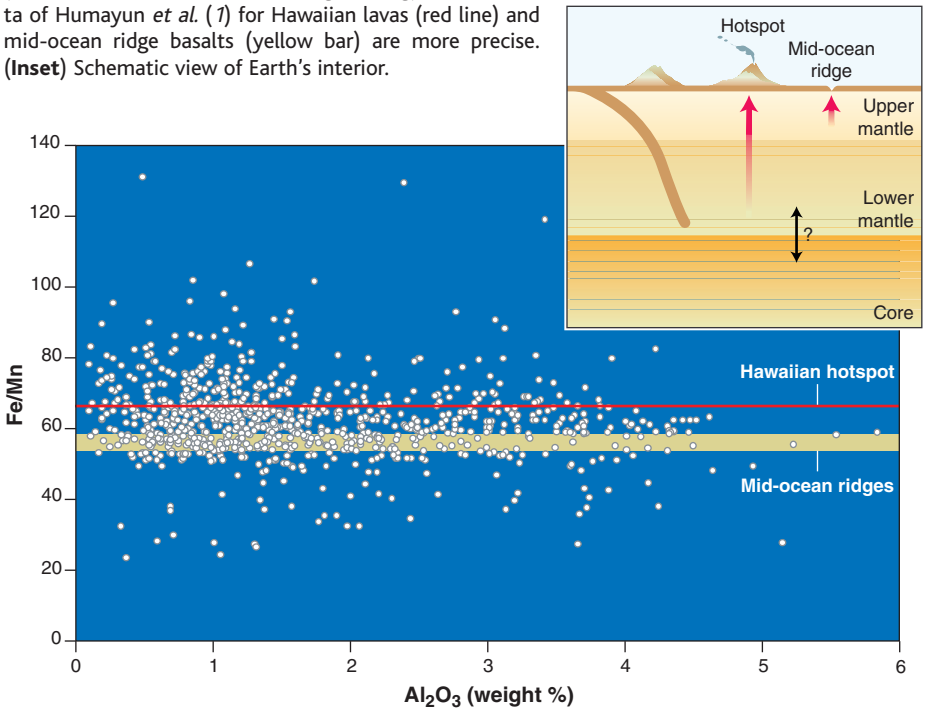

A window into Earth's interior? Literature data of Fe/Mn ratios in fresh mantle rocks (open circles) (*6*) are plotted against their Al_2O_3 content, which is a proxy for the degree of melt extraction (the Al_2O_3 content decreases during melting). The new data of Humayun *et al.* (*1*) for Hawaiian lavas (red line) and mid-ocean ridge basalts (yellow bar) are more precise. (**Inset**) Schematic view of Earth's interior.

[figure S2 in (*1*)] may be affected by interlaboratory biases, which obscure systematic differences between lavas. They show that a more precise and internally consistent database reveals systematic differences between the Fe/Mn ratios of Hawaiian lavas and mid-ocean ridge basalts.

In light of a more precise and internally consistent dataset on basalts, it may be worth revisiting whether there are intrinsic variations in Fe/Mn ratios in the upper mantle that may not necessarily be associated with iron enrichment due to core-mantle interaction. For example, a compilation of Fe/Mn data in upper-mantle samples (see the figure) shows that the Fe/Mn ratio of the upper mantle is roughly 60 ± 20 (2 standard deviations), corresponding to a total variation of ~60%. The difference between the Fe/Mn ratios of Hawaiian lavas and mid-ocean ridge basalts measured by Humayun *et al*. is less than 15%, well within the scatter seen in upper-mantle samples (see the figure).

It is not entirely clear whether the large scatter in the mantle samples is real or a result of interlaboratory bias. If it is real, the implication is that high-Fe/Mn regions exist in the upper mantle that could yield high-Fe/Mn magmas upon melting. In fact, previously melted mantle may well develop high Fe/Mn ratios because such mantle would be richer in olivine (an abundant mineral in the upper mantle), which preferentially incorporates iron over manganese [figure 3A in (*1*)]. Remelting of previously melted mantle could therefore give rise to high Fe/Mn magmas.

If the lower mantle is indeed iron-rich, our understanding of mantle circulation and Earth's bulk composition may need to be revised. It is thus necessary to explore alternative explanations for high Fe/Mn ratios in magmas. To do so, a combination of petrology and high-precision measurements of iron and manganese in mantle rocks is crucial. It may also be worth considering other first-series transition elements (such as Cr, V, Co, and Ni), because the abundance patterns of these elements imparted by partial melting differ from those imparted by core-mantle interaction. Regardless of the outcome of these studies, the work of Humayun *et al*. may rekindle an interest in first-series transition metals in the geosciences.

References

1. M. Humayun, L. Qin, M. D. Norman, *Science* **306**, 91 (2004).
2. E. Garnero, *Science* **304**, 834 (2004).
3. A. D. Brandon *et al.*, *Science* **280**, 1570 (1998).
4. G. Ravizza, J. Blusztajn, H. M. Prichard, *Earth Planet. Sci. Lett.* **188**, 369 (2001).
5. A. Schersten *et al.*, *Nature* **427**, 234 (2004).
6. W. F. McDonough, S.-S. Sun, *Chem. Geol.* **120**, 223 (1995).

VIROLOGY

Src Launches Vaccinia

Alan Hall

Contrary to popular belief, pathogens have evolved not with the sole purpose of killing their hosts, but rather to multiply and spread efficiently under the pressure of natural selection. Our need to develop smart new therapeutic strategies to deal with bacterial and viral infections has stimulated serious efforts to understand the intimate relationship between host and pathogen. An unexpected spinoff from this work has been fresh insight into the molecular mechanisms underlying mammalian cell biology, particularly the organization and control of the actin and microtubule cytoskeletons. Bacteria and viruses have both exploited the unique properties of these dynamic, filamentous structures to facilitate their own life cycles. The report by Newsome *et al*. (*1*) on page 124 of this issue describes a mechanism by which vaccinia virus commandeers a host cell tyrosine kinase called Src to allow a smooth switch from microtubule-driven intracellular transport to actin-driven extracellular extrusion.

Enhanced online at www.sciencemag.org/cgi/content/full/306/5693/65

The author is in the MRC Laboratory for Molecular Cell Biology & Cell Biology Unit, University College, London WC1E 6BT, UK. E-mail: alan.hall@ucl.ac.uk

Vaccinia virus is one of humanity's best friends: It has lent its name to the most successful strategy yet for preventing infection and is responsible for eradicating smallpox from our planet. This virus is surrounded by an envelope and its DNA encodes close to 200 genes. After entering the cell, the viral core attaches to microtubules and moves to the perinuclear region of the host cell where the virus then replicates its DNA (*2*). A complex series of maturation steps leads to a viral core particle surrounded by two concentric membranes—this intracellular enveloped virus (IEV) then must make its way to the plasma membrane; for release. It has been estimated that because of its large size, this process would take more than 10 hours by diffusion. In fact, it takes the vaccinia virus less than a minute because the virus hitches a ride on kinesin, a host motor protein that normally transports cargo (protein complexes or vesicles) along microtubules to the cell periphery (see the figure, step 1). The viral A36R protein, which is the focus of the Newsome *et al*. report, plays a key role in this process. This protein is present

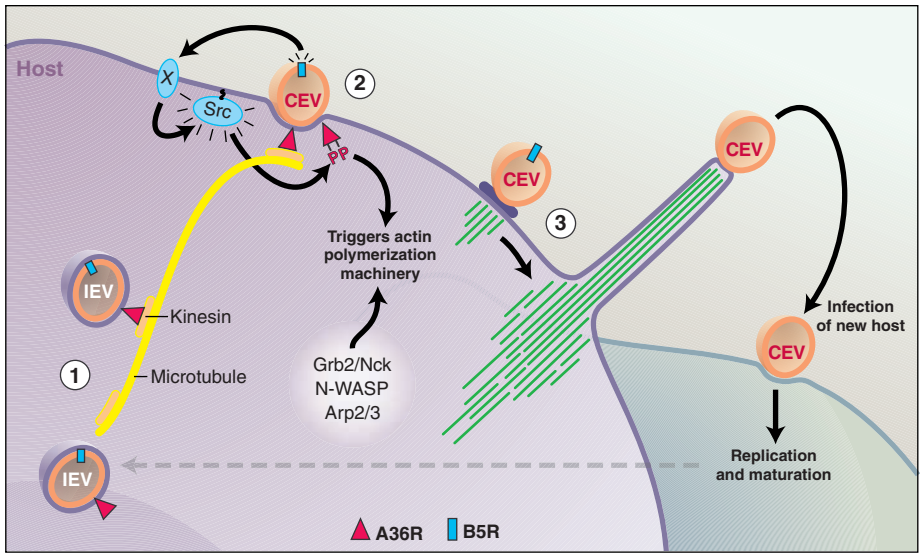

Switching modes of transport. Vaccinia virus uses Src, a host cell tyrosine kinase, to switch from microtubule-dependent intracellular transport to actin-dependent extracellular extrusion. Step 1: IEV particles, formed in the perinuclear region, interact with kinesin through the viral A36R protein, allowing microtubule-dependent transport (yellow line) to the cell periphery. Step 2: After fusion with the plasma membrane, an infectious CEV is released but remains associated with the extracellular surface of the host. A second viral protein, B5R, interacts with an unknown host cell surface protein (X) to activate the cellular tyrosine kinase Src. Src, in turn, phosphorylates A36R at two sites (PP), triggering its dissociation from kinesin. This leads to recruitment of the host cell's actin polymerization machinery, including two adapter proteins, Nck and Grb2, the scaffold protein N-WASP, and the Arp2/3 nucleation complex. Step 3: Polymerization of actin monomers into filaments (green) drives the formation of a fingerlike protrusion, which launches the CEV of vaccinia virus away from the host cell, facilitating cell-to-cell spread of viral progeny.

on the outer membrane of the IEV, and its amino terminus physically interacts with the kinesin light chain (*3*).

At the cell periphery, the IEV fuses with the plasma membrane to release a cell-associated enveloped virus (CEV). Apparently, this strategy ensures efficient cell-to-cell dissemination of viral progeny. The CEV induces rapid actin polymerization in the host cell just underneath its attachment site. As the viral particle sits at the tip of the fingerlike membrane extension of actin filaments, it is launched away from the host cell (see the figure, step 3). How does this happen? The surprise is that the same viral protein required for IEV transport along microtubules, A36R, is also required for actin polymerization (*4*). The vaccinia-induced filamentous actin structure resembles the actin tail that invasive bacteria such as *Listeria* induce to enable them to move around within the cytoplasm. Both involve recruitment of the host cell's Arp2/3 complex. The trigger for recruiting this actin nucleation machine, however, is different for the vaccinia CEV, which requires tyrosine phosphorylation of A36R (at residues 112 and 132) by the host cell tyrosine kinase, Src (*5*). In fact, the biochemistry here bears a remarkable resemblance to that used by enteropathogenic *Escherichia coli* (EPEC), which does not enter cells but induces actin filament assembly underneath its attachment site to generate a protruding actin pedestal. This event is also triggered by activation of host Src-like tyrosine kinases (*6*).

To understand how A36R participates in both microtubule transport and actin-based motility, Newsome *et al*. generated a phospho-specific antibody. With this antibody, they discovered that A36R is phosphorylated only at the plasma membrane, not when it is associated with kinesin-IEV complexes being transported along microtubules. Furthermore, viruses containing a mutant form of A36R that cannot be phosphorylated were transported to the cell periphery, but, as previously shown by this group, were unable to induce actin filament formation. These observations led the authors to propose that A36R acts as a switch: In its nonphosphorylated state it couples IEVs to kinesin to allow their transport to the periphery, but when phosphorylated at the plasma membrane it triggers kinesin dissociation and recruitment of the actin polymerization machinery (see the figure, step 2).

Strong evidence that this is indeed the case has come from experiments using Src inhibitors and cells lacking Src-family kinases. In both cases, kinesin remains associated with viral particles at the plasma membrane. One fly in the ointment here is that the association of A36R with kinesin in vitro is not inhibited by tyrosine phosphorylation. The authors speculate that phosphorylation of A36R might increase its affinity for another viral protein, A33R, whose binding site overlaps with that for kinesin, but as yet there appears to be no direct evidence for this (*1*, *3*). The switch in function does, however, suggest that tyrosine phosphorylation generates some interesting structural changes in A36R, as well as new binding sites for proteins containing SH2 (Src homology 2) domains.

The crucial importance of host cell Src to the viral life cycle raises an obvious question: How is Src activated? It is well established that the viral protein, B5R, located on the CEV surface is essential for actin assembly. This led Newsome *et al*. to speculate that B5R might be capable of acting at the extracellular surface of the host cell to generate an outside-in signal that activates Src. To explore this idea, they constructed recombinant viruses in which the surface-exposed tail of B5R, which consists of four short consensus repeat (SCR) domains, had been mutated. A mutation that disrupts SCR4 prevented viral-induced Src activation, whereas a virus in which SCRs 1, 2, and 3 had been deleted, but leaving SCR4 intact, was still able to activate Src. It appears that SCR4 on the B5R protein is capable of interacting with the host cell to activate Src (see the figure, step 2). The analogy with EPEC and pedestal formation is striking; in this case a bacterially encoded protein (intimin) also promotes Arp2/3-dependent actin polymerization through activation of Src (*6*). However, there is at least one significant difference: EPEC encodes its own intimin receptor, which it first delivers into the host plasma membrane. The SCR domain of vaccinia B5R seems to participate in protein-protein interactions; the next task will be to find a host-encoded surface receptor for B5R. In this respect, it would be interesting to know whether soluble SCR4 can activate Src when added to cells. Why bacteria and viruses use these different strategies to accomplish similar goals is not clear—perhaps it affords pathogens more control over the host's response.

What do these observations tell us about mammalian cell biology? Vaccinia virus shows many similarities to transport vesicles. Indeed, the paper by Newsome *et al*. suggests that these studies may provide important insights into mechanisms of intracellular, microtubule-driven transport. Although the concept that kinesinlike motors recognize cargo-associated receptor proteins is not new, there are few examples where the regulation of this interaction is understood at the molecular level. Kinesin itself interacts with a large number of proteins, and although many are likely to act as receptors for specific cargoes, these have been identified in only a few cases. One recent example is p120catenin, a protein that interacts with

CREDIT: KATHARINE SUTLIFF/*SCIENCE*

members of the cadherin protein family and is thought to regulate the assembly of cell-cell adherens junctions. It now appears that p120catenin also links vesicles containing N-cadherin to kinesin, thereby promoting their rapid delivery to the cell surface (*7*). However, even here it is not clear whether p120catenin interacts directly with kinesin and how this interaction is regulated. After reaching the cell periphery, N-cadherin must dissociate from the motor to be incorporated into the plasma membrane. What initiates motor detachment is not known, although Chen *et al*. (*7*) note that p120catenin is a Src substrate and they speculate that Src activation may be a signal for kinesin detachment. In light of the findings of Newsome *et al*., this sounds like a good hypothesis.

References

1. T. P. Newsome, N. Scaplehorn, M. Way, *Science* **306**, 124 (2004); published online 5 August 2004 (10.1126/science.1101509).
2. G. L. Smith *et al*., *Annu. Rev. Microbiol.* **57**, 323 (2003).
3. B. M. Ward, B. Moss, *J. Virol.* **78**, 2486 (2004).
4. C. M. Sanderson *et al*., *J. Gen. Virol.* **79**, 1415 (1998).
5. F. Frischknecht *et al*., *Nature* **401**, 926 (1999).
6. N. Phillips *et al*., *Nature Cell Biol.* **6**, 618 (2004).
7. X. Chen *et al*., *J. Cell Biol.* **163**, 547 (2003).

CELL BIOLOGY

Chemical Genetics Hits "Reality"

David S. Bellows and Mike Tyers

The pharmaceutical industry and television networks have traditionally taken a similar approach toward product development: Start with a bankable star and attempt to build a show around a single personality. In both cases, this target-based discovery strategy has produced a few long-running blockbusters and a large number of expensive flops. Recently, television production companies have taken a more unbiased approach with so-called "reality" programs that rely on a small cast carefully selected from a huge pool of applicants. The producers limit their search to interesting personalities that will produce the desired effect in the artificial environment they have developed. The drug discovery equivalent of reality-based programs is the forward chemical genetic screen, in which cells or extracts are tested against a library of small molecules and then are examined for a specific phenotype (*1*). Following this trend, Verma *et al*. (*2*) report on page 117 of this issue their forward chemical genetic screen that identifies small molecules capable of disrupting the cell's protein degradation machinery.

Forward chemical genetic screening is analogous to the classical genetics strategy of mutagenesis: A small molecule mimics a genetic mutation by altering the function of one or more gene products (*3*). As with forward genetic screens, the difficulty lies in identifying the target that is altered by the small molecule to give the observed phenotype. Drug targets have historically been identified through biochemical isolation and affinity purification using traceable compound derivatives or compounds bound to solid-phase matrices (*4*). However, these methods work best when the target is abundant and the compound binds its target with high affinity, stringent criteria that are rarely met. Verma *et al*. have taken a different approach—they have used several in vitro reconstituted components of a complex cellular pathway to winnow down the list of potential protein targets.

In eukaryotic cells, the ubiquitin-proteasome system (UPS) is the primary mechanism for degrading unwanted or misfolded intracellular proteins (*5*). Proteins are marked for degradation by addition of a polymer of ubiquitin, a 76–amino acid protein. Ubiquitin monomers are attached sequentially, first to the target protein and then to each other, via isopeptide bonds on lysine residues through the action of a cascade of enzymes called E1, E2, and E3. The E3 enzymes, also known as ubiquitin ligases, determine substrate specificity. Polyubiquitinated proteins are then targeted to the proteasome, a large multisubunit complex with a central proteolytic core (see the figure). Regulatory protein caps at each end of the proteasome act in part as polyubiquitin receptors and ensure that only polyubiquitinated proteins are degraded. The ubiquitin chain is then removed from tagged proteins, which are unfolded and fed into the proteasome core where they are degraded to short polypeptides.

By regulating the stability of cyclins and other cell cycle proteins at key transition points, the UPS ensures progression of cells through the cell cycle (*6*). Verma *et al*. exploit this requirement for proteolysis in the cell cycle by screening for small molecules that block the UPS and mitosis. Cyclin B, an essential activating subunit of the cyclin-dependent kinase Cdk1, must be degraded by the proteasome to enable the completion of mitosis. The E3 ligase that adds ubiquitin molecules to cyclin B—called the anaphase-promoting complex/cyclosome (APC/C)—is inactive during interphase and requires entry into mitosis for its activation. The APC/C identifies its protein targets through recognition of short sequence motifs called the destruction box and the KEN box (*7*). Thus, stabilization of cyclin B acts as a positive readout (called a reporter) for small mole-

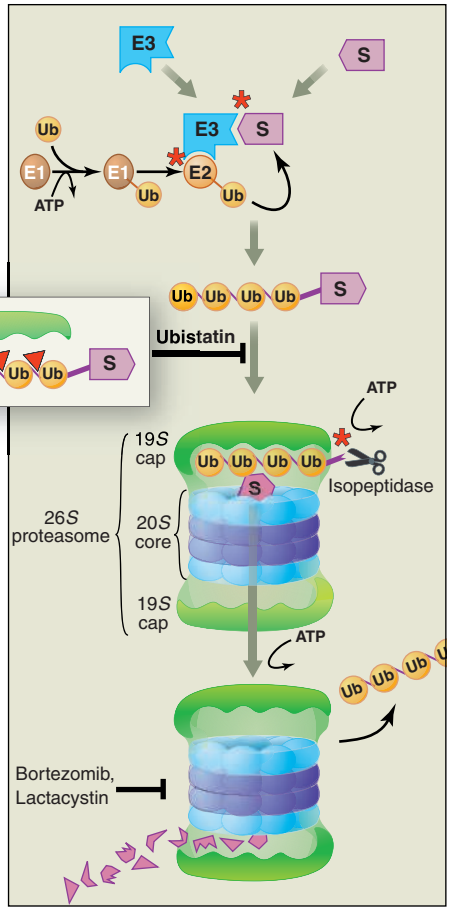

Protein degradation, a therapeutic target. The ubiquitin-proteasome system of protein degradation. A protein substrate (S) is recruited to an E3 ubiquitin ligase that is charged with ubiquitin by E1 and E2 enzymes. The substrate is polyubiquitinated by the E3 ligase in iterative catalytic cycles. The polyubiquitinated substrate is recruited to the proteasome, a large complex composed of a catalytic 20*S* core and two regulatory 19*S* caps. (**Inset**) Small-molecule inhibitors called ubistatins (red triangles) interfere with this step. The substrate is then deubiquitinated, unfolded, and translocated to the 20*S* core for proteolytic degradation. Traditional proteasome inhibitors such as Bortezomib or lactacystin inhibit the protease catalytic sites of the proteasomal core. Other protein-protein interaction interfaces potentially amenable to small-molecule interdiction are marked by red cogs.

The authors are at the Samuel Lunenfeld Research Institute, Mount Sinai Hospital, Toronto, Ontario M5G 1X5, Canada. E-mail: tyers@mshri.on.ca

cules that inhibit mitotic entry, anaphase, or the UPS. Verma *et al*. designed a reporter system consisting of the destruction box domain of the frog cyclin B1 fused to luciferase, an enzyme that generates a luminescent signal. The authors screened 109,113 small molecules against interphase extracts from frog oocytes for sustained luminescence when the extracts were stimulated to enter mitosis. They identified 22 candidate inhibitors of proteolysis. Sixteen of the compounds no longer inhibited luciferase degradation when added to prestimulated extracts, suggesting that their mode of action may be to inhibit either mitotic entry or APC/C activation. The six remaining compounds were candidates for inhibitors of cyclin B1 degradation itself. Three of the compounds also blocked the degradation of β-catenin, a protein that is ubiquitinated by a different E3 ligase, indicating that they may be general inhibitors of ubiquitin-dependent proteolysis. Importantly, the three compounds that blocked the degradation of cyclin B and β-catenin did not affect either cyclin B ubiquitination or the proteolytic activity of the proteasome core, suggesting that these small molecules blocked an unknown target.

To define the mechanism of inhibition, Verma *et al*. used a reconstituted UPS system consisting of purified proteasomes and ubiquitinated Sic1 (UbSic1), a well-characterized proteasomal substrate that is degraded at the G_1- to S-phase transition of the cell cycle in budding yeast (*8*). Addition of a proteasome inhibitor together with ubistatin A or B did not result in the accumulation of deubiquitinated UbSic1. This suggested to the authors that ubistatins appear to act at or upstream of the isopeptidase that removes polyubiquitin before the targeted proteins enter the proteasome core. Indeed, both ubistatins bound directly to polyubiquitin chains as assessed by mobility shift and nuclear magnetic resonance experiments, and blocked binding of polyubiquitin to ubiquitin receptor proteins. In a further validation of substrate specificity, ubistatin A failed to block in vitro proteolysis of ornithine decarboxylase, a ubiquitin-independent proteasome substrate. Finally, microinjection of ubistatin A into mammalian cells inhibited the degradation of a synthetic UPS substrate. Together, these experiments demonstrate the power of screening in multiple model systems where the target pathway is highly conserved.

Verma *et al*. were able to adopt a rational candidate strategy to determine the mechanism of inhibition because their screen was built around a well-characterized cellular pathway. Despite the elegance of this particular example, target identification remains the Achilles' heel of chemical phenotype screening. Recently, whole-genome reagents, such as the systematic gene deletion mutants of budding yeast and systematic RNA interference knockdown libraries, have spurred the development of genomic techniques for identifying the targets of small-molecule inhibitors (*9*). The advent of techniques for rapid identification of small-molecule targets should encourage a renaissance in forward chemical genetic screening.

The Verma *et al*. study also raises two important general points. Because the function of the UPS is essential to the cell, it would seem an unlikely therapeutic target. However, this pathway is under scrutiny by those developing chemotherapeutics because general UPS inhibitors appear to selectively kill transformed tumor cells, such as the blood cells involved in multiple myeloma and acute myelogenous leukemia (*10*). For example, Bortezomib, a proteasome inhibitor that blocks the protease active site, was recently approved for treating multiple myeloma patients. In addition, proteasome inhibitors appear to function as selective chemosensitizers or radiosensitizers in a variety of tumor cells (*10*). The mechanism of the enhanced sensitivity of tumor cells to proteasome inhibition is the subject of speculation. Inhibition of the proteasome may subtly alter cell cycle, checkpoint, or apoptotic networks that rely on UPS-mediated steps. The susceptibility of cancer cells to proteasome inhibition suggests that an attack aimed at several networks simultaneously may be a viable strategy to combat multigenic diseases (*11*). Finally, the ubistatins reinforce the notion that it is indeed possible to disrupt protein-protein interactions with small molecules (*12*). Several other steps in the UPS may also be susceptible to modulation by small molecules (see the figure). In all, this research reveals new opportunities for developing therapeutics that have targets beyond enzyme active sites, and gets at the very heart of biological specificity, the regulation of protein interactions (*13*).

References

1. M. Bredel, E. Jacoby, *Nature Rev. Genet.* **5**, 262 (2004).
2. R. Verma *et al*., *Science* **306**, 117 (2004).
3. L. H. Hartwell *et al*., *Science* **278**, 1064 (1997).
4. T. U. Mayer, *Trends Cell Biol.* **13**, 270 (2003).
5. A. Hershko, A. Ciechanover, *Ann. Rev. Biochem.* **67**, 425 (1998).
6. R. W. King *et al*., *Science* **274**, 1652 (1996).
7. J. M. Peters, *Mol. Cell* **9**, 931 (2002).
8. R. Verma *et al*., *Cell* **118**, 99 (2004).
9. X. S. Zheng *et al*., *Chem. Biol.* **11**, 609 (2004).
10. J. Adams, *Nature Rev. Cancer* **4**, 349 (2004).
11. J. R. Sharom *et al*., *Curr. Opin. Chem. Biol.* **8**, 81 (2004).
12. M. R. Arkin, J. A. Wells, *Nature Rev. Drug Discov.* **3**, 301 (2004).
13. T. Pawson, P. Nash, *Science* **300**, 445 (2003).

CLIMATE

A Stellar View on Solar Variations and Climate

Peter Foukal, Gerald North, Tom Wigley

The global warming observed over the past century has been attributed to both natural and human forcings (*1*). One of the natural forcings may be variations in solar activity, which appear to be correlated with climate change (*2*). Climate models have used reconstructions of solar irradiance to reproduce important aspects of past global warming (*3*). However, recent studies of Sun-like stars call for a reevaluation of the influence of solar activity variations on climate.

Analyses of space-borne solar radiometry since 1978 [for example, (*4*)] confirm that the Sun brightens during periods of high activity, when bright magnetic structures more than compensate for the dimming caused by sunspots. However, over an 11-year sunspot cycle, the irradiance varies by only about 0.08%—probably too little for a meaningful influence on climate. The question, then, is whether the sunspot cycle is superimposed on irradiance variations of similar or greater magnitude that take place over periods longer than 11 years.

The apparent identification of a solar component in past climate variations in recent model studies (see the figure) rests on the assumption that such variations over longer periods exist. The solar forcing used in these models includes both the sunspot cycle and a more speculative long-term component. The amplitude of this second component is roughly five times that of the magnetic modulation during sunspot cycles. It is based on evidence for luminosity variations in Sun-like stars (*5*) and on a hypothesized long-term relationship between the Sun's magnetic field and its luminosity (*6*). However, the scientific basis for this component is much less robust than for the sunspot-cycle component.

Stellar observations (*5*) have suggested that Sun-like stars have low-activity phases

P. Foukal is at Heliophysics Inc., Nahant, MA 01908, USA. G. North is in the Department of Atmospheric Sciences, Texas A&M University, College Station, TX 77843, USA. T. Wigley is at the National Center for Atmospheric Research, Boulder, CO 80307, USA. E-mail: pfoukal@world.std.com

during which the magnetic activity is even lower than during minima in the sunspot cycle. Extrapolation of the Sun's radiometrically observed irradiance to this low-activity level suggests that solar irradiance in the 17th century may have been 0.25% lower than today (*7*, *8*). Reconstructions of irradiance variations based directly (*7*) or indirectly (*8*) on the stellar evidence have been used in numerous climate studies, some of which form the basis of the Intergovernmental Panel on Climate Change's conclusions on the relative roles of different external climate forcings (*1*).

Additional evidence for large multidecadal solar luminosity variations came from photometric studies of Sun-like stars, some of which exhibited cyclic variations 3 to 5 times those observed radiometrically in the Sun (*9*). This finding suggested that similarly large luminosity variations may have occurred on the Sun in the recent past. However, concerns were soon raised as to whether the stars studied in (*9*) and in (*5*) were truly Sun-like—that is, with very similar mass, age, and chemical composition to the Sun—because the high-dispersion data required for such identification are relatively difficult to obtain.

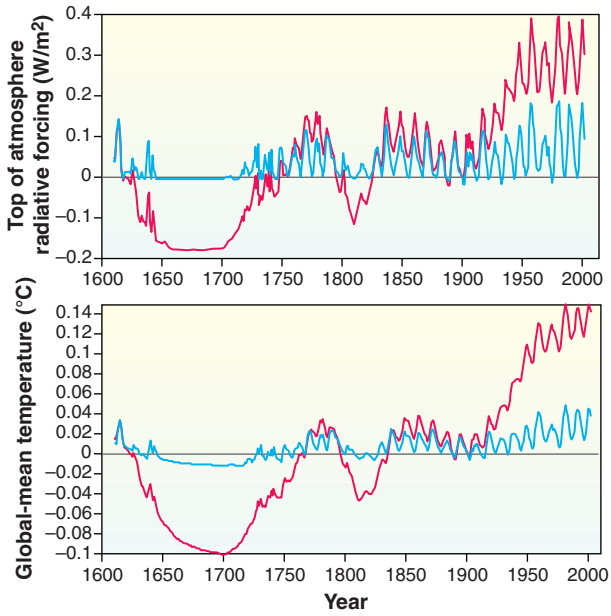

Apparent magnitude of solar forcings. (**Top**) Top-of-atmosphere solar forcing (red) from (*7*), showing the sunspot cycle component separately (blue). (**Bottom**) Global-mean temperature responses to the forcings shown in the top panel, calculated with the MAGICC climate model using best estimate parameters (*19*). Forcings and responses are zeroed in 1900. The temperature response to the speculative long-term component is much larger than to the sunspot-cycle component alone.

Of the stars considered to date, only 18 Scorpii (HR6060) seems to be a sufficiently close solar analog for comparison with the Sun's present irradiance behavior (*10*). Furthermore, if the model of Lean *et al*. (*7*) correctly describes the Sun's past activity, it requires disappearance of the prominent photospheric magnetic network as recently as the 1920s (*11*). This magnetic network was discovered in the early 1890s, and its area has exhibited no significant changes since at least 1915. The model is therefore unlikely to be correct.

Recent results raise further concerns about the scientific basis of the irradiance reconstructions used in recent climate models. First, the bimodal distribution of stellar magnetic activity cited in (*5*) as evidence for low-activity phases in Sun-like stars is not found when more homogeneous samples of stars are studied in more detail (*12*, *13*). Second, wide-band photometry of 18 solar analogs (*14*) shows no evidence of luminosity variations greater than 0.05%. The data so far do not support the earlier conclusion that the Sun's irradiance variability of 0.08% is lower than that of similar stars. Searches for large-amplitude multidecadal variations in solar output have also been unsuccessful (*15*).

A further claim that the 11-year sunspot cycle might be superimposed on substantial long-term variations comes from variations in the interplanetary magnetic field (IMF) identified in the "aa" index, a daily and half-daily index of geomagnetic activity that dates back to 1868 (*6*, *16*). The IMF is a measure of changes in the "open" magnetic flux of the Sun. These changes have, in turn, a statistical relationship with solar irradiance variations. The aa index increased gradually between 1900 and about 1955, possibly indicating a decadal-timescale increase in irradiance. However, both the data calibration and the connection to irradiance variations (*17*) have been questioned. Furthermore, the statistical relationship between the IMF and irradiance is significant only on the monthly time scale, not on the interannual time scale. Any relationship on longer time scales must therefore remain speculative.

The reason for the apparent constancy of the Sun's luminosity, despite its vigorous convection, is probably the enormous thermal inertia of atmospheric layers below the shallow photosphere. Without this inertia, the large irradiance fluctuations caused by spots and faculae would be rapidly canceled by compensating temperature variations outside these localized structures (*15*).

Lean *et al*. recently accepted (*17*) that the long-term irradiance variations used in climate models in the past decade may be a factor of ~5 larger than can be justified. The full impact of this changed outlook on attempts to explain past climate variations and estimates of climate sensitivity to external forcing remains to be seen.

Some recent climate models incorporate the possible effects of solar ultraviolet (UV) flux variations on climate via their effect on stratospheric ozone, which might influence the propagation of planetary waves and hence the latitudinal heat distribution in the troposphere. However, the correlation between 20th-century global temperature changes and a reconstruction of UV flux is relatively low (*18*). It is therefore unclear whether UV effects can add significantly to the strength of the direct solar irradiance changes usually considered in climate modeling. Other studies suggesting that solar plasma and field outputs (including cosmic ray influences) might affect climate remain speculative.

The absence of convincing evidence does not rule out long-term luminosity variations of the Sun. It does, however, emphasize the need for more reproducible solar radiometry, more accurate photometry, and studies of larger samples of Sun-like stars. New technologies—including cryogenic radiometers, thermal imagers, and automated photometric telescopes—are now available to provide these advances. It should then be possible to move beyond modeling based on speculative irradiance changes toward a more physically based understanding of Sun-climate relations.

References and Notes

1. J. T. Houghton *et al.*, Eds., *Climate Change 2001: The Scientific Basis* (Cambridge Univ. Press, Cambridge, 2001).
2. T. Crowley, *Science* **289**, 270 (2000).
3. P. A. Stott *et al.*, *Clim. Dyn.* **17**, 1 (2001).
4. C. Fröhlich, J. Lean, *Geophys. Res. Lett.* **25**, 4377 (1998).
5. S. Baliunas, R. Jastrow, *Nature* **348**, 520 (1990).
6. M. Lockwood, R. Stamper, M. N. Wild, *Nature* **399**, 437 (1999).
7. J. Lean, J. Beer, R. Bradley, *Geophys. Res. Lett.* **22**, 3195 (1995).
8. D. Hoyt, K. Schatten, *J. Geophys. Res.* **98**, 18895 (1993).
9. G. W. Lockwood *et al.*, *Nature* **360**, 653 (1992).
10. G. F Porto de Mello, L. da Silva, *Astrophys. J.* **482**, L89 (1997).
11. P. Foukal, L. Milano, *Geophys. Res. Lett.* **28**, 883 (2001).
12. M. Giampapa *et al.*, in preparation.
13. J. Hall, G. W. Lockwood, *Astrophys. J.*, in press.
14. G. Henry, in preparation.
15. P. Foukal, *Eos* **84**, 205 (2003).
16. M. Lockwood, R. Stamper, *Geophys. Res. Lett.* **26**, 2461 (1999).
17. J. Lean, Y. Wang, N. Sheeley, *Geophys. Res. Lett.* **29**, 2224 (2002).
18. P. Foukal, *Geophys. Res. Lett.* **29**, 2089 (2002).
19. T. M. L. Wigley, S. C. B. Raper, *Science* **293**, 451 (2001).

20. We thank M. Giampapa, J. Hall, and G. Henry for permission to cite and discuss their results prior to publication. We also thank J. Eddy, C. Fröhlich, J. Leibacher, and M. Schlesinger for helpful comments. P.F.'s work on this article was supported by NSF grant ATM 0303557 and NASA grant NNG04GN41G, both to Heliophysics, Inc.

Assessing the Causes of Late Pleistocene Extinctions on the Continents

Anthony D. Barnosky,[1]* Paul L. Koch,[2] Robert S. Feranec,[1] Scott L. Wing,[3] Alan B. Shabel[1]

One of the great debates about extinction is whether humans or climatic change caused the demise of the Pleistocene megafauna. Evidence from paleontology, climatology, archaeology, and ecology now supports the idea that humans contributed to extinction on some continents, but human hunting was not solely responsible for the pattern of extinction everywhere. Instead, evidence suggests that the intersection of human impacts with pronounced climatic change drove the precise timing and geography of extinction in the Northern Hemisphere. The story from the Southern Hemisphere is still unfolding. New evidence from Australia supports the view that humans helped cause extinctions there, but the correlation with climate is weak or contested. Firmer chronologies, more realistic ecological models, and regional paleoecological insights still are needed to understand details of the worldwide extinction pattern and the population dynamics of the species involved.

Fifty thousand years ago, continents were populated with more than 150 genera of megafauna (animals >44 kg) (*1*–*4*). By 10,000 years ago, at least 97 of those genera were gone (Fig. 1, Table 1, and table S1) (*5*). Prevailing explanations include human impacts (*1*, *2*, *6*–*8*), environmental changes (*1*, *2*, *9*–*11*), and a combination of both (*1*, *3*, *4*, *12*–*14*). If humans caused the extinctions, it will profoundly influence our thinking about what is "natural" (*15*), how ecosystems respond to different scales and kinds of environmental change (*16*), how long extinctions take (*17*), and conservation of species and ecosystems (*2*, *18*, *19*).

Anthropogenic extinction models, including overkill (*20*), blitzkrieg (rapid overkill) (*21*), and sitzkrieg (fire, habitat fragmentation, and the introduction of exotic species and diseases) (*6*), have been considered plausible because large animals were preferentially affected (*1*, *2*, *5*, *22*, *23*). Species with low reproductive rates, with which large body size correlates, were hit hardest (*24*, *25*). Almost all of the slow-breeding survivors in Australia, Eurasia, the Americas, and Madagascar are nocturnal, arboreal, alpine, and/or deep-forest dwellers, which is consistent with overkill models of extinction but hard to explain by environmental change alone (*24*). Survival of large, open-country, slow-breeding animals in Africa is an exception to this pattern that must factor into extinction explanations.

On islands, humans cause extinctions through multiple, synergistic effects, including predation and sitzkrieg (*1*, *2*, *6*, *26*). Only rarely have island megafauna been demonstrated to go extinct because of environmental change without human involvement (*27*–*29*). Incontrovertible impacts of humans on islands have been cited as a potent argument that prehistoric humans also caused extinctions on continents (*1*, *2*, *6*), but extrapolation of extinction mechanisms from islands to continents is often disputed (*4*, *26*). Here, we focus on the continents, where causes of extinction remain controversial (*8*, *19*, *30*–*32*).

The perspective from Eurasia and Africa has been that humans exerted at most a minor influence on Pleistocene extinctions, whereas in Australia, North America, and South America, a primary role for humans has been strongly argued (*1*–*3*). How consistent with that perspective is recent evidence from simulations, chronology, archaeology, paleontology, climatology, and ecology?

Simulations

Most simulations (table S2) (*5*) treat prey as a single species with life history parameters [initial biomass, population growth rate (r), and carrying capacity (K)] that are varied, either to simulate effects on particular species [such as mammoth (*33*) or moa (*34*, *35*)] or to understand values that render prey vulnerable to extinction (*20*, *21*, *36*, *37*). Either human population dynamics are modeled with parameters that respond to prey population size (*20*, *21*), or human population densities are varied independently in sensitivity tests (*34*–*37*). Hunting efficiency is varied too.

Results differ depending on the input parameters (*5*). Overkill occurs consistently in single-prey simulations with coupled human-prey population dynamics, but stability analyses suggest this may be a mathematically inevitable outcome (*38*). Simulations with uncoupled human and prey population dynamics produced blitzkrieg for New Zealand moas (*34*, *35*), but other simulations counterintuitively found that overkill was less likely for large, slow-breeding prey (*36*, *37*), perhaps because the models feature low human population densities and assume hunting efficiency drops as prey become rare.

Simulations of humans foraging on multiple prey (as opposed to one prey species) yield the crucial idea that overkill of slow-breeding prey is more likely when hunter populations become large, because hunters are subsidized by eating rapidly breeding prey or gathered foods when preferred slow-breeding prey becomes scarce (*38*, *39*). The most comprehensive simulation (*8*) involves predation by North American immigrants on 41 species of large animals and a single, undifferentiated secondary resource (plants and small game). Assuming that hunters nonselectively took prey as it was encountered, overkill resulted for a range of hunting efficiencies, geography of invasion, and competitive interactions (*5*). The best model correctly predicted the fate of 34 of 41 species, with final human population densities of ~28 people per 100 km^2 receiving ~30% of their calories from large animals. The median time to extinction was 895 years (*40*). The rules of this simulation did not allow prey species to disperse outside geographic ranges estimated from fossil data (*41*), whereas humans were allowed to disperse anywhere. Such assumptions are consistent with climatic or other environmental limits to the ranges of large mammals and show how climate could modulate an extinction driven primarily by human hunting.

Logical next steps would be to apply sensitivity tests to assumptions about geographic ranges, carrying capacity, and rules of

[1]Department of Integrative Biology and Museums of Paleontology and Vertebrate Zoology, University of California, Berkeley, CA 94720, USA. [2]Department of Earth Sciences, University of California, Santa Cruz, CA 95064, USA. [3]Department of Paleobiology, National Museum of Natural History, Smithsonian Institution, Washington, DC 20560, USA.

*To whom correspondence should be addressed. E-mail: barnosky@socrates.berkeley.edu

dispersal and to allow realistic, selective foraging by humans. Assumptions about prey naiveté influence outcomes of single-prey simulations (*4*, *37*) and need to be explored for multiple-prey simulations [e.g., (*8*, *39*)]. It will be important to learn if realistic models can simulate the survival of megafauna in Africa or the magnitude of extinction in Australia, a continent where some question whether human populations were ever large or technologically sophisticated enough to drive overkill (*4*).

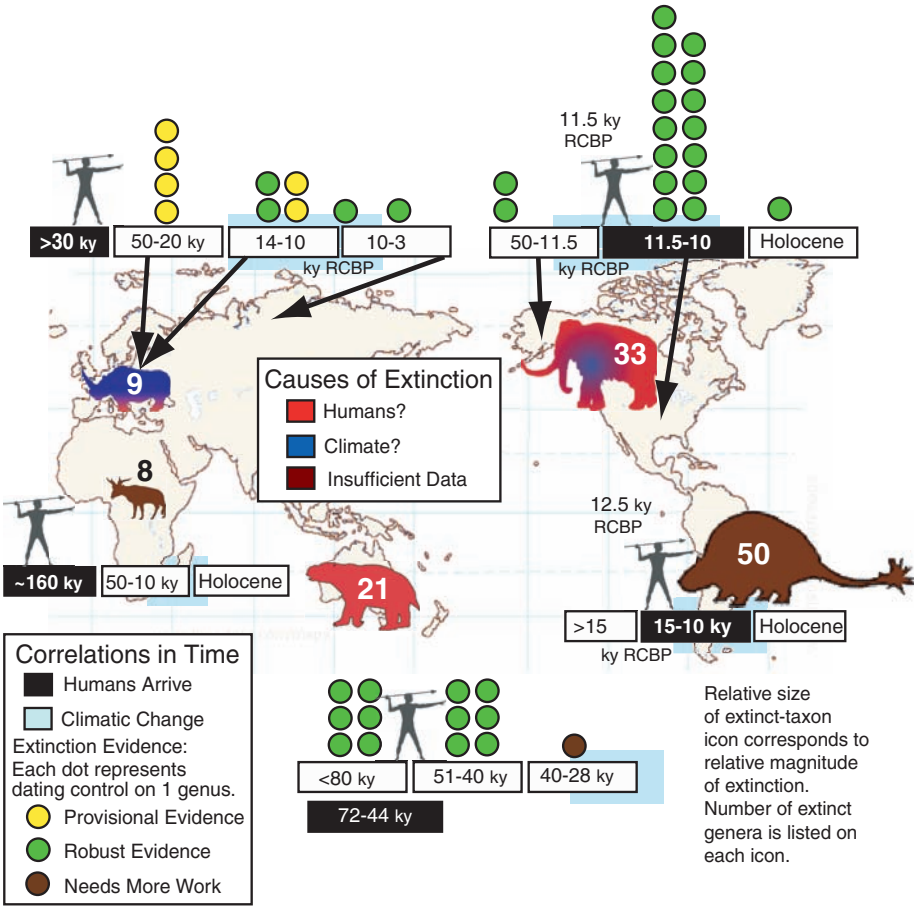

Fig. 1. Summary of the numbers of megafaunal genera that went extinct on each continent (Table 1), the strength of the extinction chronology, and a comparison of the timing of extinction with the timing of human arrival and late Pleistocene climatic change. Extinction timing for individual genera was judged as robust or provisional based on previous publications that evaluated quality of dates. Sources are as follows: Europe (*3*, *14*, *47*), Siberia (*48*), North America (*11*, *29*, *46*, *57*), and Australia (*4*, *7*). For humans, the date is the earliest generally accepted arrival of *Homo sapiens sapiens*; pre-*sapiens* hominins were present in Eurasia and Africa much earlier.

Chronology

Recent work has confirmed two salient points for northern high- and mid-latitudes:

1) In northern Europe, Siberia, and Alaska, extinction occurred in two pulses coincident with climatic change (Fig. 2C), with the loss of warm-adapted animals from 45 to 20 thousand radiocarbon years before present (ky RCBP) and cold-adapted animals from 12 to 9 ky RCBP (*5*). The pulsed demise of the megafauna in Eurasia also coincides with first the spread and then increases in population sizes of *Homo sapiens sapiens* (*42*), who had a more diverse suite of tools and broader diets (*14*, *43*) than the pre-*sapiens* hominins. Pre-*sapiens* hominins hunted megafauna in Europe for at least 400,000 years (*44*) without inducing extinctions, but may have lived at densities too low to have a pronounced impact on prey populations (*43*). Some species survived in northern Eurasia into the mid-Holocene (*5*); these late survivors were in areas where human populations were never large.

2) In central North America, the arrival of Clovis-style hunters, extinction of megafauna, and marked climatic change all cluster between 11.5 and 10 ky RCBP (*31*, *45*). Published accounts suggest that at least 15 species became extinct near the start of or during the Younger Dryas climate event, perhaps within the short "Clovis window" between 11.4 and 10.8 ky RCBP (*19*, *31*, *46*). A close correspondence of extinction with both human arrival and climatic change is well supported.

Thus, in mid-latitudes of the Northern Hemisphere, extinction was most pronounced where climatic change and new (North America) or potentially increased (Eurasia) human impacts hit simultaneously. In the far north, the geographically complex chronology of extinction suggests that an interplay between human impacts and climatic change governed extinction dynamics. For some species [such as mammoths (*29*, *47*–*49*) and giant Irish deer (*50*)], Siberia and certain islands apparently offered refugia in regions that lacked large human populations. In other areas and for other species [such as horses and mammoths in mainland Alaska (*11*)], extinction occurred with climatic change even in the absence of significant human populations.

In the Southern Hemisphere, the story is still unfolding, with new information from Australia playing a key role. Australia's main extinction pulse was earlier than in the Northern Hemisphere, came after humans arrived, and seems not to match any major regional or global climatic change. However, the chronology is much less secure than for Eurasia and North America. The most comprehensive Australian analyses indicate that of the 21 extinct genera of megafauna, 12 persisted to at least 80 ky BP, and at least 6 persisted to between 51 and 40 ky BP (*7*, *37*). Humans arrived somewhere between 71.5 and 44.2 ky BP (*5*, *37*). Both human arrival and megafaunal extinction seem to predate regionally evident Late Glacial Maximum climatic change (*7*) (Fig. 2B). It is disputed whether megafauna lingered as recently as 28 ky BP in sites such as Cuddie Springs (*4*, *51*, *52*) and whether ocean-based climatic records are reliable proxies for environmental change on the Australian continent (*4*, *5*).

In South America, generally accepted dates place humans in coastal Chile and Patagonia at 12.9 to 12.5 ky RCBP (*53*–*55*), and sites younger than 10 ky RCBP are common (*56*). The megafauna went extinct in the late Pleistocene, probably after humans arrived and as climate changed, but until more comprehensive analyses are undertaken, little else can be said with certainty.

Supporters of overkill have long argued that extinctions in Africa (*5*) and central Eurasia were milder (Fig. 1, Table 1, and table S1) because humans coevolved with megafauna there for hundreds of thousands of years, whereas they were an invasive species in the Americas and Australia. That would explain the magnitude of extinction in the Americas and Australia, but it offers no insights as to why any extinctions took place in Africa, or why Eurasia experienced a 36% loss of its megafauna.

Solving those problems will require a better understanding of the extinction chronology, background extinction rates, timing and details of climatic change, and patterns of human population growth and resource use.

Archaeology and Paleontology

On all of the involved continents, archaeological remains and extinct megafauna have been found in association (*5*). Debate continues on two unresolved questions:

1) What constitutes evidence that humans hunted megafauna? In Africa and Eurasia, acceptable evidence includes cut marks and breakage of fossil bones. In contrast, cut marks and breakage alone are seldom regarded as strong evidence in North America (*57*, *58*). New insights are possible by applying uniform criteria across continents to recognize kill sites, but such comparisons have not yet been done.

2) Are there too few kill sites to support overkill models? Until recently, it was not possible to determine if the number of kill sites (however one defines them) was consistent with a given overkill model, because we could not quantify the proportion of kill sites relative to all fossil occurrences of extinct taxa. With electronic databases (*41*, *57*), estimating these proportions is now feasible for North America. Under certain assumptions (*5*), the data suggest that on that continent (i) kill sites are very frequent for mammoths; (ii) at least one taxon (*Platygonus*, the peccary) is found at fewer kill sites than expected; and (iii) most taxa are too rare in the fossil record to reliably judge their kill-site frequency (table S3).

Table 1. Numbers of mammalian megafaunal genera affected by Pleistocene extinction. Numbers are based on our vetting of the primary literature (*5*), including but not restricted to (*1*–*4*) and (*7*). Column A gives the number of genera on a given continent that went extinct globally; column B, the number of extinct genera that survived on another continent; column C, the number of Pleistocene genera on the continent that were still alive historically; and column D, the percent of megafaunal genera that went extinct on each continent (columns A + B divided by columns A + B + C).

Continent	A	B	C	D
Africa	5	3	36	18
Australia*	14	–	2	88
Eurasia†	5	4	16	36
North America	28	5	13	72
South America	49	1	10	83

*Australia also has seven extinct (and no surviving) genera of megafaunal reptiles and birds. †Our use of "Eurasia" encompasses only northern Asia (part of the Palaearctic Region), because insufficient data exist to include southern Asia (the Oriental Region).

Climatic Change and Ecological Effects

Climatic change is known to affect animals, often by triggering vegetation changes (*5*). The question is whether late Pleistocene climatic changes were unusual enough to trigger unusual ecological response. Three ecological models with general explanatory power have been applied to the Pleistocene extinctions debate: the proboscideans-as-keystone species model (*2*, *5*, *59*), co-evolutionary disequilibrium (*5*, *10*), and the mosaic-nutrient model (*5*, *60*). One prediction of the keystone-species model is that proboscideans should be the first to disappear in the fossil record, but in Eurasia (*47*, *48*, *61*), Alaska (*11*), and probably central North America (*31*, *62*, *63*), they were among the last to go. The co-evolutionary disequilibrium and mosaic-nutrient models require that the changes in climate and ecosystem structure at the time of extinction were unusual relative to earlier conditions in the Pleistocene. This is underscored by recent work demonstrating that megafaunal extinction did not characterize earlier glacial-interglacial transitions in Europe (*3*, *14*), Australia (*5*, *64*), or North America (*5*, *65*, *66*).

Paleoclimate records do not support a unique late Pleistocene transition. Global-scale oxygen-isotope records indicate that the most recent deglaciation was neither more rapid nor of greater magnitude than other shifts in the past 700,000 years (Fig. 2A). At a regional scale, climatic shifts around North and South America, Eurasia, and Africa at the time of extinction, although large, were not unusual (Fig. 2, B and C). If the extinction in Australia occurred before 40 ky BP, it would have occurred when ocean records were relatively placid (Fig. 2B).

Long pollen records from areas with megafaunal remains are few, but they allow a first approximation of how the magnitude of floral change compares to the timing of extinction in various regions. The comparison requires converting published pollen records to a standardized scale (Fig. 3). In

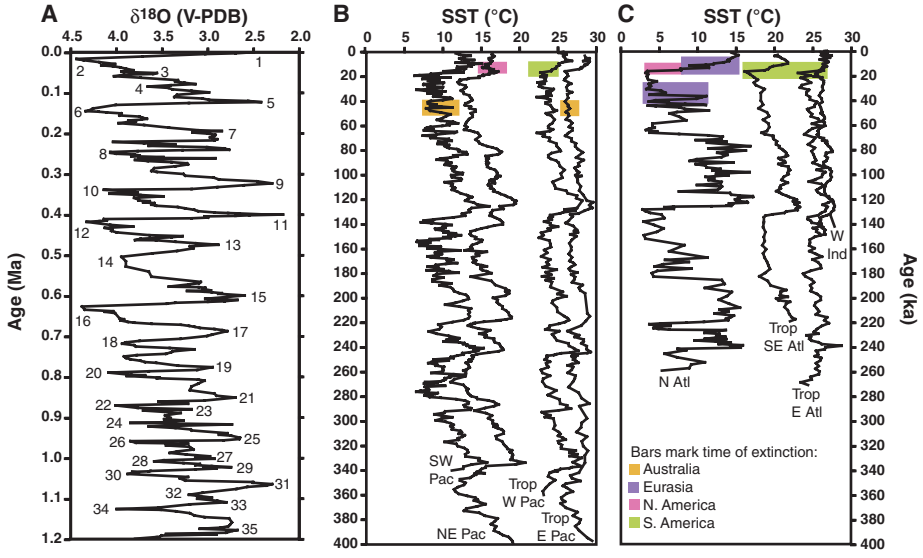

Fig. 2. (**A**) Oxygen isotope data from benthic foraminifera at North Atlantic Deep-Sea Drilling Program site 607 (*81*, *82*). The isotopic signal ($\delta^{18}O$) in benthic foraminifera largely reflects variations in continental ice volume, with a smaller effect due to changes in ocean bottom temperatures. Numbers refer to marine isotope stages (*81*, *82*). Most well-constrained extinctions and drops in abundance occurred in stages 2 and 3. V-PDB, Vienna–Pee Dee Belemnite. (**B** and **C**) Sea-surface temperature (SST) records from the (B) Pacific and (C) Atlantic and Indian oceans, respectively. Colored bars indicate the time of extinction on nearby continents. The core label, latitude, longitude, type of SST estimate, and source are as follows: northeast Pacific (NE Pac), Ocean Drilling Program (ODP) 1020, 41.00°N, 126.43°W, alkenone (*83*); tropical east Pacific (Trop E Pac), TR 163-9, 2.26°N, 90.95°W, Mg/Ca (*84*); tropical west Pacific (Trop W Pac), ODP 806B, 1.32°N, 159.36°E, Mg/Ca (*84*); southwest Pacific (SW Pac), MD 97-2120, 45.53°S, 174.93°E, Mg/Ca (*85*); west Indian (W Ind), MD 85674, 3.18°N, 50.43°E, alkenone (*86*); north Atlantic (N Atl), K 708-1, 50.00°N, 23.73°W, foraminiferal transfer function (average of data reported for August and February) (*87*); tropical east Atlantic (Trop E Atl), GeoB 1112, 5.77°S, 10.75°W, Mg/Ca (*88*); and tropical southeast Atlantic (Trop SE Atl), GeoB 10285, 20.10°S, 9.19°E, alkenone (*89*). All ages in this figure are in calendar years (ky BP), not ^{14}C years (ky RCBP), using age models in primary publications, except for core K 708-1, where ^{14}C ages reported in (*87*) were converted to calendar years with CALIB 98 (*90*) from 0 to 22,000 ^{14}C years and with data from (*91*) for 22,000 to 45,000 ^{14}C years.

some areas, vegetation change coincides with extinction (Fig. 3, E, G, and L), but in others it does not (Fig. 3, D, F, H, and M). Elsewhere, the last phases of extinction correlate with vegetation change but the initial extinctions may not (Fig. 3, I and J). In still other regions, extinctions are not well enough dated to compare with vegetation change (Fig. 3, A to C, K, and N). Particularly interesting is northeastern Australia (Fig. 3O), where the extinction may coincide with a rapid transition to full glacial biomes unlike any seen in 150,000 years, including the prior full glacial period around 130 ky BP; this might support an environmental component to extinction at that location.

A generalized ecological model that has just begun to receive attention is that of state-changes in ecosystems, either when certain thresholds are crossed (*67*) or because of intrinsic nonlinear dynamics (*68*). Future work could gainfully explore whether the nature of climatic change in certain areas is consistent with threshold effects, as well as whether ecological systems exhibit dynamical properties that indicate a susceptibility to collapse.

Current State of the Evidence

How far has the debate about Pleistocene extinction on continents progressed in the last 40 years? The case for humans contributing to extinction is now much stronger than it was in the early days, with support from recent work on chronology, simulations, paleoclimatology, paleontology, and archaeology. Yet it is an oversimplification to say that an abrupt wave of hunting-

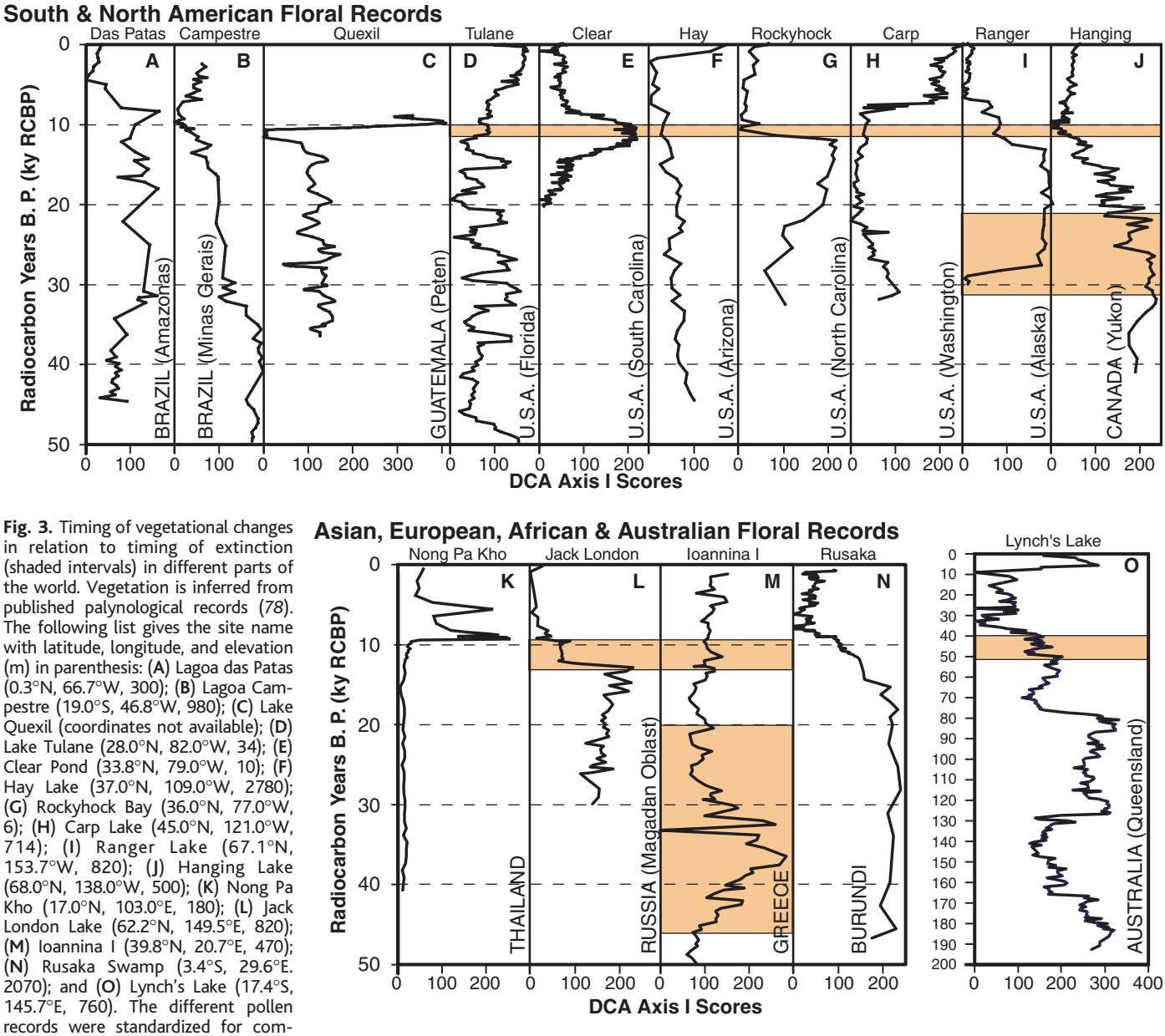

Fig. 3. Timing of vegetational changes in relation to timing of extinction (shaded intervals) in different parts of the world. Vegetation is inferred from published palynological records (*78*). The following list gives the site name with latitude, longitude, and elevation (m) in parenthesis: (**A**) Lagoa das Patas (0.3°N, 66.7°W, 300); (**B**) Lagoa Campestre (19.0°S, 46.8°W, 980); (**C**) Lake Quexil (coordinates not available); (**D**) Lake Tulane (28.0°N, 82.0°W, 34); (**E**) Clear Pond (33.8°N, 79.0°W, 10); (**F**) Hay Lake (37.0°N, 109.0°W, 2780); (**G**) Rockyhock Bay (36.0°N, 77.0°W, 6); (**H**) Carp Lake (45.0°N, 121.0°W, 714); (**I**) Ranger Lake (67.1°N, 153.7°W, 820); (**J**) Hanging Lake (68.0°N, 138.0°W, 500); (**K**) Nong Pa Kho (17.0°N, 103.0°E, 180); (**L**) Jack London Lake (62.2°N, 149.5°E, 820); (**M**) Ioannina I (39.8°N, 20.7°E, 470); (**N**) Rusaka Swamp (3.4°S, 29.6°E. 2070); and (**O**) Lynch's Lake (17.4°S, 145.7°E, 760). The different pollen records were standardized for comparison by Detrended Correspondence Analysis (DCA); the DCA Axis I score is used to depict when pollen abundances shift, which in turn reflects changes in surrounding vegetation. The standardization proceeded by downloading the taxon abundance matrix for each core from (*78*), removing the aquatic taxa (e.g., floating and emergent aquatics and algae), and calculating the percent abundance for each terrestrial sporomorph type in each sample. Each matrix was independently subjected to DCA with the software package MVSP 3.12a (*92*). Taxon abundances were unweighted and 26 segments were used in four detrending cycles. The score of each sample on the first axis of the DCA (which for these analyses expresses 20 to 40% of the total variation in the data set) is used to quantify its floral composition in relation to the other samples from the same core. The age of each sample is from the published age model (*78*) for each site.

induced extinctions swept continents right after first human contact. Instead, the evidence shows that blitzkrieg *sensu stricto* can be firmly rejected in western Europe, Siberia, Alaska, and probably Australia and central North America. Without late Pleistocene climatic change, it is likely that species such as horses in Alaska and mammoths and giant Irish deer in central Eurasia would have survived longer, despite the presence of humans. The recent information now points toward humans precipitating the extinction, but also to an instrumental role for late Pleistocene climatic change in controlling its timing, geographic details, and perhaps magnitude. The mechanism for climatic effects is likely to be found in detailed species-by-species analyses (*19*), rather than in one of the three existing global ecological models (*10*, *59*, *60*), none of which is fully consistent with observations.

Data density and quality are still uneven. The Eurasian record is increasingly good and reveals that late Pleistocene climatic change contributed to extinction by driving range adjustments in large mammals. An idea that needs further testing is that the arrival and population expansion of *Homo sapiens sapiens* began to fragment megafaunal ranges by 30,000 years ago, ultimately restricting megafauna to inviable populations in far northern refugia by the end of the Pleistocene. Australian evidence suggests that megafaunal extinction followed human arrival, and that both probably preceded significant global or regional South Pacific climatic change, which is consistent with a role for humans. However, the timing of key events still cannot be bracketed within error bars less than ~10,000 years, the youngest records of extinct megafauna are controversial, and local environmental changes may differ from the global or regional pattern (*4*, *5*). In South America, published data on extinction chronology is accumulating but awaits critical analysis. In Africa, better temporal resolution is needed to assess how the timing of the few extinctions matches local environmental changes and human impacts.

In contrast, robust dating verifies simultaneous climatic change and first human contact in the conterminous United States, where extinctions were particularly rapid and pronounced. Support for human impacts includes (i) indisputable hunting of two extinct species, (ii) clustering of extinctions within 1,500 years (and perhaps less) of first contact with Clovis hunters, (iii) widespread distribution of Clovis hunters, (iv) simulations, and (v) more pronounced extinction than in mid-Pleistocene glacial-interglacial transitions. On a broader North American scale, the demise of megafaunal species without significant human presence in Alaska is consistent with some role for climate (*11*).

General Implications

The data show that the late Pleistocene extinction event was spread over more than 50,000 years globally; was the accumulation of diachronous, shorter-term pulses that took place on a regional basis; and was amplified by the interaction of both biotic (humans as invasive species) and abiotic (climatic) drivers.

A significant implication for conservation biology is that the coupling of marked climatic change with direct human impacts on fauna is especially pernicious. Both effects are under way today at unprecedented rates. Data generated in the Pleistocene extinctions debate are now robust enough to support earlier contentions (*15*) that the modern global ecosystem is unique in having vast populations of one species (humans) and a depauperate array of megafauna. The net effect, through loss of many herbivores, carnivores, and scavengers, has been simplification and loss of redundancy in food webs (*69*). This has implications for the stability of global ecosystems.

Productive Future Directions

The accumulated evidence suggests it is time to move beyond casting the Pleistocene extinction debate as a dichotomy of humans versus climate and instead to untangle the complex impacts that both had on megafauna. From the archaeological perspective, we need to know when human population sizes on each continent became large enough to affect vulnerable fauna. Kill-site and dating criteria must be standardized between continents. To understand the effects of environmental changes, much remains to be done in determining how changes in particular climatic parameters would have impacted population sizes of affected species. Particularly promising in this regard are advances in the study of fungal spores from megafaunal dung in lake sediments (*70*) and the use of ancient DNA to model population-level change (*71*–*74*). Improvements in the chronology of extinction and paleoclimatic reconstructions for South America and Africa are especially needed, as is a more detailed understanding of whether the last glacial-interglacial transition was different from earlier ones in pertinent ways. Rigorous, ecologically based models of range contraction and extinction must be formulated through linkage of work that has proceeded largely independently in paleoecology and ecology, especially in such areas as food-web dynamics, keystone species, and ecosystem state-change. Some problems were intractable when the Pleistocene extinctions debate began but can now be addressed through new dating techniques (*7*, *75*, *76*); through the assembly and analysis of paleoecological, paleoclimatic, and archaeological databases (*41*, *77*, *78*); and through isotopic studies to reconstruct details of both the paleoclimate and paleoecology (*79*, *80*).

References and Notes

1. P. S. Martin, R. G. Klein, Eds., *Quaternary Extinctions: A Prehistoric Revolution* (Univ. of Arizona Press, Tucson, 1984).
2. R. D. E. MacPhee, Ed., *Extinctions in Near Time: Causes, Contexts, and Consequences* (Kluwer/Plenum, New York, 1999).
3. A. J. Stuart, *Biol. Rev. Camb. Philos. Soc.* **66**, 453 (1991).
4. S. Wroe, J. Field, R. Fullagar, L. S. Jermin, *Alcheringa* **28**, 291 (2004).
5. Materials and methods are available as supporting material on *Science* Online.
6. J. M. Diamond, *J. Archaeol. Sci.* **16**, 167 (1989).
7. R. G. Roberts *et al.*, *Science* **292**, 1888 (2001).
8. J. Alroy, *Science* **292**, 1893 (2001).
9. R. D. Guthrie, *Carnegie Mus. Nat. Hist. Spec. Publ.* **8**, 482 (1984).
10. R. W. Graham, E. L. Lundelius Jr., in (*1*), pp. 223–249.
11. R. D. Guthrie, *Nature* **426**, 169 (2003).
12. A. D. Barnosky, in *Mass Extinctions: Processes and Evidence*, S. K. Donovan, Ed. (Belhaven, London, 1989), pp. 235–254.
13. P. S. Martin, H. E. Wright Jr., Eds., *Pleistocene Extinctions: The Search for a Cause* (Proceedings of the VII Congress of the International Association for Quaternary Research, Yale Univ. Press, New Haven, CT, 1967), vol. 6.
14. A. J. Stuart, in (*2*), pp. 257–270.
15. P. S. Martin, C. R. Szuter, *Conserv. Biol.* **13**, 36 (1999).
16. A. D. Barnosky, E. A. Hadly, C. J. Bell, *J. Mammal.* **84**, 354 (2003).
17. H. M. Regan, R. Lupia, A. N. Drinnan, M. A. Burgman, *Am. Nat.* **157**, 1 (2001).
18. J. B. Callicott, *J. Biosci.* **27**, 409 (2002).
19. D. K. Grayson, D. J. Meltzer, *J. Archaeol. Sci.* **30**, 585 (2003).
20. S. L. Whittington, B. Dyke, in (*1*), pp. 451–465.
21. J. E. Mosimann, P. S. Martin, *Am. Sci.* **63**, 304 (1975).
22. J. Alroy, in (*2*), pp. 105–143.
23. S. K. Lyons, F. A. Smith, J. H. Brown, *Evol. Ecol. Res.* **6**, 339 (2004).
24. C. N. Johnson, *Proc. R. Soc. London Ser. B* **269**, 2221 (2002).
25. N. G. Jablonski, M. J. Whitfort, N. Roberts-Smith, Q. Q. Xu, *J. Hum. Evol.* **41**, 131 (2000).
26. D. K. Grayson, *J. World Prehist.* **15**, 1 (2001).
27. A. D. Barnosky, *Science* **228**, 340 (1985).
28. A. D. Barnosky, *Quat. Res.* **25**, 128 (1986).
29. R. D. Guthrie, *Nature* **429**, 746 (2004).
30. D. K. Grayson, *Science* **294**, 1459 (2001).
31. S. J. Fiedel, G. Haynes, *J. Archaeol. Sci.* **31**, 121 (2004).
32. D. K. Grayson, D. J. Meltzer, *J. Archaeol. Sci.* **31**, 133 (2004).
33. M. I. Budyko, *Sov. Geogr. Rev. Transl.* **8**, 783 (1967).
34. A. Anderson, *J. Archaeol. Sci.* **16**, 137 (1989).
35. R. N. Holdaway, C. Jacomb, *Science* **287**, 2250 (2000).
36. D. Choquenot, D. M. J. S. Bowman, *Global Ecol. Biogeogr. Lett.* **7**, 167 (1998).
37. B. W. Brook, D. M. J. S. Bowman, *Proc. Natl. Acad. Sci. U.S.A.* **99**, 14624 (2002).
38. G. E. Belovsky, *J. Anthropol. Archaeol.* **7**, 329 (1988).
39. B. Winterhalder, F. Lu, *Conserv. Biol.* **11**, 1354 (1997).
40. J. Alroy, *Science* **294**, 1461 (2001).
41. FAUNMAP Working Group, *Ill. Mus. Sci. Pap.* **25**, 1 (1994).
42. O. Bar-Yosef, *Annu. Rev. Anthropol.* **31**, 363 (2002).
43. S. L. Kuhn, M. C. Stiner, in *Hunter-Gatherers: An Interdisciplinary Perspective*, C. Panter-Brick, R. H. Layton, P. Rowley-Conwy, Eds. (Cambridge Univ. Press, Cambridge, 2001), pp. 99–142.
44. H. Thieme, *Nature*, **385**, 807 (1997).

45. J. Kutzbach *et al.*, *Quat. Sci. Rev.* **17**, 473 (1998).
46. D. K. Grayson, in *Handbook of North American Indians: Environment, Origins, and Population* (Smithsonian Institution Press, Washington, DC, in press), vol. 3.
47. A. J. Stuart, L. D. Sulerzhitsky, L. A. Orlova, Y. V. Kuzmin, A. M. Lister, *Quat. Sci. Rev.* **21**, 1559 (2002).
48. R. D. E. MacPhee *et al.*, *J. Archaeol. Sci.* **29**, 1017 (2002).
49. S. L. Vartanyan, V. E. Garutt, A. V. Sher, *Nature* **362**, 337 (1993).
50. S. Gonzalez, A. C. Kitchener, A. M. Lister, *Nature* **405**, 753 (2000).
51. J. R. Dodson, R. Fullagar, J. Furby, R. Jones, I. P. Prosser, *Archaeol. Oceania* **28**, 94 (1993).
52. J. Field, R. Fullagar, G. Lord, *Antiquity* **75**, 696 (2001).
53. T. F. Lynch, *Am. Antiq.* **55**, 12 (1990).
54. D. J. Meltzer *et al.*, *Am. Antiq.* **62**, 659 (1997).
55. M. T. Alberdi, L. Miotti, J. L. Prado, *J. Archaeol. Sci.* **28**, 411 (2001).
56. T. D. Dillehay, *The Settlement of the Americas: A New Prehistory* (Basic Books, New York, 2000).
57. D. K. Grayson, D. J. Meltzer, *J. World Prehist.* **16**, 313 (2002).
58. G. Haynes, *The Early Settlement of North America: The Clovis Era* (Cambridge Univ. Press, Cambridge, 2002).
59. N. Owen-Smith, *Paleobiology* **13**, 351 (1987).
60. R. D. Guthrie, in (*1*), pp. 259–298.
61. S. L. Vartanyan, K. A. Arslanov, T. V. Tertychnaya, S. B. Chernov, *Radiocarbon* **37**, 1 (1995).
62. R. W. Graham, T. W. Stafford, E. Lundelius, H. A. Semken, J. Southen, paper presented at the 67th Annual Meeting of the Society of American Archaeology, Denver, CO, 20 to 24 March, 2002.
63. D. K. Grayson, *J. World Prehist.* **5**, 193 (1991).
64. K. C. Moriarty, M. T. McCulloch, R. T. Wells, M. C. McDowell, *Palaeogeogr. Palaeoclimatol. Palaeoecol.* **159**, 113 (2000).
65. A. D. Barnosky *et al.*, *Proc. Natl. Acad. Sci. U.S.A.* **101**, 9297 (2004).
66. A. D. Barnosky, Ed., *Biodiversity Response to Climate Change in the Middle Pleistocene: The Porcupine Cave Fauna from Colorado* (Univ. of California Press, Berkeley, 2004).
67. M. Scheffer, S. R. Carpenter, J. A. Foley, C. Folke, B. Walker, *Nature* **113**, 591 (2001).
68. M. A. Forster, *Oikos* **103**, 235 (2003).
69. R. V. Solé, J. M. Montoya, *Proc. R. Soc. London Ser. B* **268**, 2039 (2001).
70. D. A. Burney, G. S. Robinson, L. P. Burney, *Proc. Natl. Acad. Sci. U.S.A.* **100**, 10800 (2003).
71. I. Barnes, P. Matheus, B. Shapiro, D. Jensen, A. Cooper, *Science* **295**, 2267 (2002).
72. E. A. Hadly, M. H. Kohn, J. A. Leonard, R. K. Wayne, *Proc. Natl. Acad. Sci. U.S.A.* **95**, 6893 (1998).
73. E. A. Hadly, M. Tuinen, Y. Chan, K. Heiman, *J. Mammal.* **84**, 403 (2003).
74. E. A. Hadly *et al.*, *PLoS Biol.* **2**, e290, in press; published online 7 September 2004 (10.1371/journal.pbio.0020290).
75. T. W. Stafford Jr. *et al.*, *Geology* **27**, 903 (1999).
76. E. Bard, F. Rostek, G. Ménot-Combes, *Science* **303**, 178 (2004).
77. D. G. Anderson, M. K. Faught, *A North American Paleoindian Database* (www.anthro.fsu.edu/research/paleo/paleoind.html) [cited January 2004].
78. Contributors to the Modern and Fossil Pollen Data Bank, International Geosphere–Biosphere Program Past Global Changes (IGBP PAGES)/World Data Center for Paleoclimatology, National Oceanic and Atmospheric Administration/National Geophysical Data Center Paleoclimatology Program, available at www.ngdc.noaa.gov/paleo/pollen.html (2004).
79. P. L. Koch, *Annu. Rev. Earth Planet. Sci.* **26**, 573 (1998).
80. M. J. Kohn, T. E. Cerling, in *Phosphates: Geochemical, Geobiological and Materials Importance*, M. J. Kohn, J. Rakovan, J. M. Hughes, Eds. (Reviews in Mineralogy and Geochemistry, Mineralogical Society of America, Washington, DC, 2002), vol. 48, pp. 455–488.
81. W. F. Ruddiman, M. E. Raymo, D. G. Martinson, B. M. Clement, J. Backman, *Paleoceanography* **4**, 353 (1989).
82. M. E. Raymo, W. F. Ruddiman, J. Backman, B. M. Clement, D. G. Martinson, *Paleoceanography* **4**, 413 (1989).
83. T. D. Herbert *et al.*, *Science* **293**, 71 (2001).
84. D. W. Lea, D. K. Pak, H. J. Spero, *Science* **289**, 1719 (2000).
85. K. Pahnke, R. Zahn, H. Elderfield, M. Schulz, *Science* **301**, 948 (2003).
86. E. Bard, F. Rostek, C. Sonzogni, *Nature* **385**, 707 (1997).
87. J. Imbrie *et al.*, *Paleoceanography* **7**, 701 (1992).
88. D. Nuernberg, A. Mueller, R. R. Schneider, *Paleoceanography* **15**, 124 (2000).
89. R. R. Schneider, P. J. Mueller, G. Ruhland, *Paleoceanography* **10**, 197 (1995).
90. M. Stuiver *et al.*, *Radiocarbon* **40**, 1041 (1998).
91. J. W. Beck *et al.*, *Science* **292**, 2453 (2001).
92. Kovach Computing Services, Multi-Variate Statistical Package, available at www.kovcomp.co.uk.

93. We thank the NSF for funding aspects of this research; contributors to the European, North American, Latin American, and Indo-Pacific pollen databases for making their data available online; D. K. Grayson, P. Martin, and five anonymous reviewers for comments on earlier versions of the manuscript, and students and faculty who contributed to the lively discussions on these issues in seminars at the University of California Berkeley and Santa Cruz campuses. This is contribution no. 1863 from the University of California Museum of Paleontology.

Supporting Online Material

www.sciencemag.org/cgi/content/full/306/5693/70/DC1
Materials and Methods
SOM Text
Tables S1 to S3
References and Notes

Curving and Frustrating Flatland

Kyusoon Shin,* Hongqi Xiang,* Sung In Moon, Taehyung Kim, Thomas J. McCarthy, Thomas P. Russell†

Molecular conformations and assemblies are strongly influenced by their environment. Constraints imposed by bounding surfaces can break the symmetry of a structure, causing marked departures from classical equilibrium behavior. This opens new pathways for materials with unique structures. Diblock copolymers, formed by two chemically different polymers joined together at one end, self-organize into periodic domains that are receiving much attention as nanostructured materials for device applications (*1*, *2*). In the bulk, i.e., without external constraints, the morphology of a block copolymer is dictated by the interactions between segments comprising the copolymer, the volume fraction of the blocks, and the area occupied by each block at the interface between the domains. Placing the copolymer between hard, flat surfaces spatially confines the morphology. If the copolymer period and the wall-separation distance are incommensurate, stretching or compression of the copolymer molecules will occur, altering the fundamental repeat period (*3*). If the confining geometry is nonplanar, as with a cylindrical pore geometry, then both commensurability and imposed curvature influence the morphology (*4*). When the diameter of the confining cylinder is large in comparison to the copolymer period, morphologies identical to those observed under planar confinement are found (*5*). When the cylinder diameter is small and incommensurate with the copolymer period, the imposed curvature produces unusual morphologies, expanding the repertoire of nanoscopic structures attainable with these versatile molecules.

Melts of symmetric diblock copolymers of styrene (PS) and butadiene (PBD) with molecular weights of 28,900 [PS-*b*-PBD (I)] and 18,400 [PS-*b*-PBD (II)] with polydispersities of 1.02 and 1.03, respectively, were drawn into nanoporous alumina membranes by capillary action (*5*, *6*). We used a weak base to dissolve the alumina and produce free-standing nanoscopic rods of copolymers. PS and PBD are highly immiscible, and PBD, having a low surface energy, strongly segregates to the high-surface-energy alumina interface.

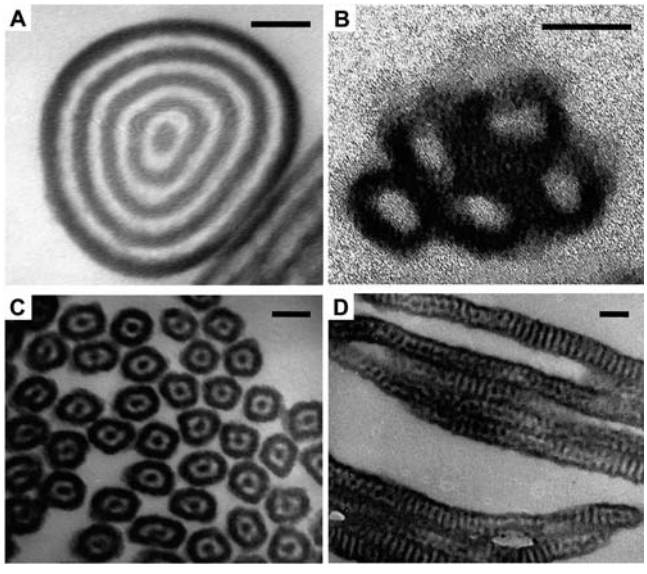

Fig. 1. (A to D) TEM images of PS-*b*-PBD nanorods from a nanoporous alumina membrane. The pore diameters d and lamellar repeating periods L_0 are (A) 190 and 23.5 nm, (B) 45 and 23.5 nm, and both (C) and (D), 45 and 17.6 nm, respectively. (A), (B), and (C) are cross-sections cut normal to the rod axis, and (D) is a cross-section parallel to the rod axis. Scale bars, 50 nm.

The morphologies of these copolymers in the bulk are lamellar with repeat periods L_0 of 23.5 and 17.6 nm, respectively. Figure 1A is a transmission electron microscopy (TEM) image of PS-*b*-PBD (I) confined to pores with diameters d of ~190 nm ($d/L_0 \sim 8.1$), commensurate with L_0. As expected from simulations and theory (*7*–*9*) and as shown elsewhere (*5*), eight concentric alternating cylinders of PS and PBD can be seen. The lower surface-energy PBD domain (dark regions) is located at the cylinder walls. Figure 1B is a TEM image of PS-*b*-PBD (I) in 45-nm pores ($d/L_0 \sim 1.9$), and only a central core of PS, surrounded by a layer of PBD, appears. This structure requires a substantial deformation of the block copolymer chains, but because of the strong immiscibility of PS and PBD and the low interfacial energy of PBD, a lamellar morphology persists.

TEM images of PS-*b*-PBD (II) in 45-nm diameter pores ($d/L_0 \sim 2.6$, highly incommensurate) are shown normal to and along the pore axes (Fig. 1, C and D, respectively). Here, d and L_0 are incommensurate. With planar surfaces, a compressed lamellar morphology would be seen (*3*). However, in a cylindrical geometry, the high degree of curvature imposed on the planar lamellar morphology causes a frustration of chain packing at the interface, resulting in a fundamental change in the morphology. Normal to the rod axis, concentric layers are observed with PBD located in the centers and at the outer walls of the rods. Along the rods, a stacked PS lamellar structure is seen, with a central spine and outer edges of PBD. Thus, a transition from a lamellar to a stacked-disc or toroidal-type structure occurs. This morphology, forced on the block copolymer by curvature and incommensurability, is not accessible by other means.

References and Notes

1. M. Park, C. Harrison, P. M. Chaikin, R. A. Register, D. H. Adamson, *Science* **276**, 1401 (1997).
2. T. Thurn-Albrecht *et al.*, *Science* **290**, 2126 (2000).
3. P. Lambooy *et al.*, *Phys. Rev. Lett.* **72**, 2899 (1994).
4. S. P. Gido, E. L. Thomas, *Macromolecules* **27**, 849 (1994).
5. H. Xiang *et al.*, *Macromolecules* **37**, 5660 (2004).
6. S. I. Moon, T. J. McCarthy, *Macromolecules* **36**, 4253 (2003).
7. G. J. A. Sevink, A. V. Zvelindovsky, J. G. E. M. Fraaije, H. P. Huinink, *J. Chem. Phys.* **115**, 8226 (2001).
8. X.-H. He, M. Song, H.-J. Liang, C.-Y. Pan, *J. Chem. Phys.* **114**, 10510 (2001).
9. R. B. Thompson, V. V. Ginsburg, M. W. Matsen, A. C. Balazs, *Science* **292**, 2469 (2001).
10. Supported by the National Science Foundation, through a Nanoscience Interdisciplinary Research Team, the Materials Research Science and Engineering Center at the University of Massachusetts–Amherst, the U.S. Department of Energy, and the Hyperstructured Organic Materials Research Center at Seoul National University.

Supporting Online Material
www.sciencemag.org/cgi/content/full/306/5693/76/DC1
Materials and Methods
Figs. S1 to S3
References and Notes

10 May 2004; accepted 4 August 2004

Department of Polymer Science and Engineering, Silvio O. Conte National Center for Polymer Research, University of Massachusetts, Amherst, MA 01003, USA.

*These authors contributed equally to this work.
†To whom correspondence should be addressed. E-mail: russell@mail.pse.umass.edu

Maintained Cardiac Pumping in Anoxic Crucian Carp

Jonathan A. W. Stecyk,[1]* Kåre-Olav Stensløkken,[2] Anthony P. Farrell,[1] Göran E. Nilsson[2]

Humans, like most vertebrates, die within minutes when deprived of molecular oxygen (anoxia), in part because of cardiac failure. In contrast, freshwater turtles (genera *Chrysemys* and *Trachemys*) have the ability to survive anoxia for months at low temperatures, but to do so, they drastically suppress cardiac activity and autonomic cardiovascular control (*1*, *2*). Although the crucian carp (*Carassius carassius*) shares this anoxia tolerance, we show here that this fish can retain normal cardiac performance and autonomic cardiovascular regulation for at least 5 days of anoxia at 8°C. In contrast, its cousin the common carp (*Cyprinus carpio*) survives only 24 hours of severe hypoxia, even though cardiac activity is strongly depressed (*3*).

Prolonged anoxic survival requires balancing energy supply and demand, as well as coping with the acidosis associated with anaerobic end-product accumulation. Therefore, anoxic freshwater turtles reduce metabolism by 90%, precluding an up-regulation of glycolysis (*4*), and they buffer lactic acid accumulation with their bone and shell (*5*). Correspondingly, cardiac output ($\dot{Q}$) is reduced by 92% (*1*), and autonomic cardiovascular control is blunted (*2*). Conversely, anoxic crucian carp remain active, up-regulate glycolysis to maintain their adenosine triphosphate supply, and avoid acidosis by converting lactate into ethanol (*6*). Thus, we hypothesized that their cardiovascular status and control might be maintained during anoxia. We examined this hypothesis by measuring $\dot{Q}$, heart rate (f_H), stroke volume (V_S), ventral aortic blood pressure (P_{VA}), and respiration rate (f_R) and by calculating peripheral vascular resistance (R) and cardiac power output (PO) of crucian carp during 5 days of anoxia at 8 ± 1°C (*7*).

After an initial adjustment period, $\dot{Q}$, f_H, V_S, PO, and f_R all returned to pre-anoxic levels throughout days 2 to 5 of anoxia, whereas P_{VA} and R decreased significantly ($P < 0.05$) by 30% and 40%, respectively, indicating vasodilation (Fig. 1). Furthermore, autonomic controls remained intact during anoxia. Cardiac inhibitory cholinergic and excitatory β-adrenergic tones were revealed by respective increases and decreases in both f_H and $\dot{Q}$ after injections of the pharmacological inhibitors of these control processes (*7*) (fig. S1, A and C). Tonic α-adrenergic vasoconstriction was revealed by decreased P_{VA} and R after pharmacological α-adrenergic blockade (*7*) (fig. S1, B and D).

These responses point to an unusual tolerance of a vertebrate heart and autonomic nervous system to prolonged anoxia. Other anoxic hearts either fail immediately, show strongly suppressed activity (turtle and common carp) (*1*, *3*), or lack autonomic control (hagfish) (*8*). The crucian carp's maintained $\dot{Q}$, reduced R, and conserved autonomic control may permit the rapid distribution of glucose from its unusually large liver glycogen store (*6*) to metabolically active tissues and the transport of waste lactate to the muscle, the sole site of ethanol production (*6*). Sustained $\dot{Q}$ will also allow for ethanol shuttling to the gills for excretion. Using Fick's Principle, we estimate a 23% to 85% loss of ethanol from venous blood with each passage through the gills (*7*). Because ethanol is freely diffusible across the gill epithelia, ethanol excretion is likely perfusion-limited. Therefore, by maintaining $\dot{Q}$ during anoxia, the crucian carp may prevent ethanol accumulation and even intoxication in tissues.

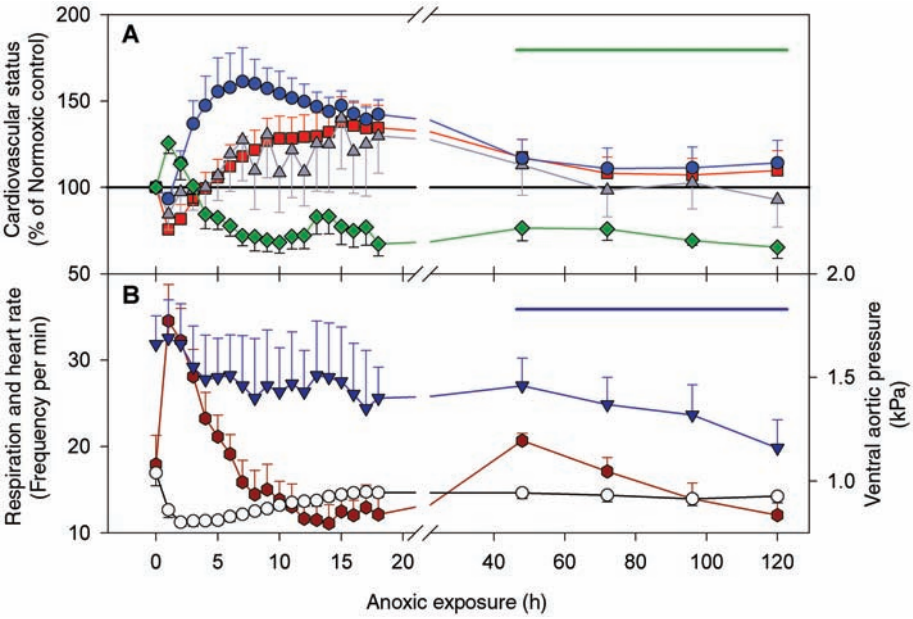

Fig. 1. Cardiorespiratory status of anoxic crucian carp. (**A**) Stroke volume (blue circles), cardiac output (red squares), cardiac power output (gray triangles), and peripheral resistance (green diamonds) after the indicated period of anoxia. (**B**) Respiration rate (red hexagons), ventral aortic pressure (blue triangles), and heart rate (white circles). Significant differences ($P < 0.05$; repeated measures analysis of variance, Friedman for percentages; Student-Newman-Keuls posttests) between time zero (normoxic) and hours 48, 72, 96, and 120 for peripheral resistance and ventral aortic blood pressure are indicated by the horizontal, stand-alone blue and green lines, respectively. Values are means ± SEM; n = 6 to 18 fish.

References and Notes

1. J. M. T. Hicks, A. P. Farrell, *J. Exp. Biol.* **203**, 3765 (2000).
2. J. M. T. Hicks, A. P. Farrell, *J. Exp. Biol.* **203**, 3775 (2000).
3. J. A. W. Stecyk, A. P. Farrell, *J. Exp. Biol.* **205**, 759 (2002).
4. D. C. Jackson, *J. Appl. Physiol.* **24**, 503 (1968).
5. D. C. Jackson, *J. Physiol.* **543**, 731 (2002).
6. G. E. Nilsson, *News Physiol. Sci.* **16**, 217 (2001).
7. Materials and methods are available as supporting material on *Science* Online.
8. M. Axelsson, A. P. Farrell, S. Nilsson, *J. Exp. Biol.* **151**, 297 (1990).
9. Supported by the Natural Sciences and Engineering Research Council of Canada (J.A.W.S. and A.P.F.), the Research Council of Norway (G.E.N.), and a Company of Biologists Travelling Fellowship (J.A.W.S.).

Supporting Online Material
www.sciencemag.org/cgi/content/full/306/5693/77/DC1
Materials and Methods
Fig. S1

26 May 2004; accepted 5 August 2004

[1]Department of Biological Sciences, Simon Fraser University, 8888 University Drive, Burnaby V5A 1S6, Canada. [2]Physiology Programme, Department of Molecular Biosciences, University of Oslo, Post Office Box 1041, N-0316, Oslo, Norway.

*To whom correspondence should be addressed. E-mail: jstecyk@interchange.ubc.ca

The Genome of the Diatom *Thalassiosira Pseudonana*: Ecology, Evolution, and Metabolism

E. Virginia Armbrust,[1]* John A. Berges,[2] Chris Bowler,[3,4] Beverley R. Green,[5] Diego Martinez,[6] Nicholas H. Putnam,[6] Shiguo Zhou,[7] Andrew E. Allen,[8,4] Kirk E. Apt,[9] Michael Bechner,[7] Mark A. Brzezinski,[10] Balbir K. Chaal,[5] Anthony Chiovitti,[11] Aubrey K. Davis,[12] Mark S. Demarest,[10] J. Chris Detter,[6] Tijana Glavina,[6] David Goodstein,[6] Masood Z. Hadi,[13] Uffe Hellsten,[6] Mark Hildebrand,[12] Bethany D. Jenkins,[14] Jerzy Jurka,[15] Vladimir V. Kapitonov,[15] Nils Kröger,[16] Winnie W. Y. Lau,[1] Todd W. Lane,[17] Frank W. Larimer,[18,6] J. Casey Lippmeier,[9,19] Susan Lucas,[6] Mónica Medina,[6] Anton Montsant,[3,4] Miroslav Obornik,[5]† Micaela Schnitzler Parker,[1] Brian Palenik,[12] Gregory J. Pazour,[20] Paul M. Richardson,[6] Tatiana A. Rynearson,[1] Mak A. Saito,[21] David C. Schwartz,[7] Kimberlee Thamatrakoln,[12] Klaus Valentin,[22] Assaf Vardi,[4] Frances P. Wilkerson,[23] Daniel S. Rokhsar[6,24]*

Diatoms are unicellular algae with plastids acquired by secondary endosymbiosis. They are responsible for ~20% of global carbon fixation. We report the 34 million–base pair draft nuclear genome of the marine diatom *Thalassiosira pseudonana* and its 129 thousand–base pair plastid and 44 thousand–base pair mitochondrial genomes. Sequence and optical restriction mapping revealed 24 diploid nuclear chromosomes. We identified novel genes for silicic acid transport and formation of silica-based cell walls, high-affinity iron uptake, biosynthetic enzymes for several types of polyunsaturated fatty acids, use of a range of nitrogenous compounds, and a complete urea cycle, all attributes that allow diatoms to prosper in aquatic environments.

Diatoms are unicellular, photosynthetic, eukaryotic algae found throughout the world's oceans and freshwater systems. They form the base of short, energy-efficient food webs that support large-scale coastal fisheries. Photosynthesis by marine diatoms generates as much as 40% of the 45 to 50 billion metric tons of organic carbon produced each year in the sea (*1*), and their role in global carbon cycling is predicted to be comparable to that of all terrestrial rain forests combined (*2*, *3*). Over geological time, diatoms may have influenced global climate by changing the flux of atmospheric carbon dioxide into the oceans (*4*).

A defining feature of diatoms is their ornately patterned silicified cell wall, or frustule, which displays species-specific nanostructures of such fine detail that diatoms have long been used to test the resolution of optical microscopes. Recent attention has focused on biosynthesis of these nanostructures as a paradigm for future silica nanotechnology (*5*). The long history (more than 180 million years) and dominance of diatoms in the oceans is reflected by their contributions to vast deposits of diatomite, most cherts, and a considerable fraction of current petroleum reserves (*6*).

As photosynthetic heterokonts, diatoms reflect a fundamentally different evolutionary history from the higher plants that dominate photosynthesis on land. Higher plants and green, red, and glaucophyte algae are derived from a primary endosymbiotic event in which a nonphotosynthetic eukaryote acquired a chloroplast by engulfing (or being invaded by) a prokaryotic cyanobacterium. In contrast, dominant bloom-forming eukaryotic phytoplankton in the ocean, such as diatoms and haptophytes, were derived by secondary endosymbiosis whereby a nonphotosynthetic eukaryote acquired a chloroplast by engulfing a photosynthetic eukaryote, probably a red algal endosymbiont (Fig. 1). Each endosymbiotic event led to new combinations of genes derived from the hosts and endosymbionts (*7*).

Before this project, relatively few diatom genes had been sequenced, few chromosome numbers were known, and genetic maps did not exist (*8*). The ecological and evolutionary importance of diatoms motivated our sequencing and analysis of the nuclear, plastid, and mitochondrial genomes of the marine centric diatom *Thalassiosira pseudonana*.

Whole-Genome Sequencing and Architecture

The *T. pseudonana* genome was sequenced by using a whole-genome shotgun approach, with 14-fold sequence coverage (*9*) (table S1). Genomic DNA was isolated from a clonal culture produced by repeated mitotic divisions of a single diploid founder cell. Finished quality circular mitochondrial and plastid genomes were derived from the whole-genome shotgun data and from organelle-enriched DNA. This whole-genome shotgun project has been deposited at DNA Data Bank

[1]School of Oceanography, University of Washington, Seattle, WA 98195, USA. [2]Department of Biological Sciences, University of Wisconsin–Milwaukee, Milwaukee, WI 53201, USA. [3]Laboratory of Molecular Plant Biology, Stazione Zoologica, Villa Comunale, I 80121 Naples, Italy. Organismes Photosynthétiques et Environnement, Département de Biologie, [4] Ecole Normale Supérieure, 75230 Paris, France. [5]Department of Botany, University of British Columbia, Vancouver, B.C., Canada, V6T 1Z4. [6]Department of Energy Joint Genome Institute, Walnut Creek, CA, 94598, USA. [7]Departments of Genetics and Chemistry, University of Wisconsin–Madison, Madison, WI 53706, USA. [8]Department of Geosciences, Princeton University, Princeton, NJ 08540, USA. [9]Martek Biosciences Corp, 6480 Dobbin Road, Columbia, MD 21045, USA. [10]Department of Ecology, Evolution, and Marine Biology and Marine Science Institute, University of California, Santa Barbara, CA 93106, USA. [11]School of Botany, University of Melbourne, Victoria 3010, Australia. [12]Scripps Institution of Oceanography, University of California San Diego, La Jolla, CA 92093, USA. [13]Lockheed Martin Corporation, Sandia National Laboratory, Post Office Box 969, MS-9951, Livermore, CA 94551, USA. [14]Ocean Sciences Department, University of California Santa Cruz, Santa Cruz, CA 95064, USA. [15]Genetic Information Research Institute, Mountain View, CA 94043, USA. [16]Lehrstuhl Biochemie I, Universität Regensburg, D-93053, Regensburg, Germany. [17]Biosystems Research Department, Sandia National Laboratories, Livermore, CA 94551–0969. [18]Genome Analysis Group, Oak Ridge National Laboratory, Oak Ridge, TN 37831, USA. [19]Department of Biological Sciences, University of Hull, Hull HU6 7RX, UK. [20]Program in Molecular Medicine, University of Massachusetts Medical School, Worcester, MA 01605, USA. [21]Department of Marine Chemistry and Geochemistry, Woods Hole Oceanographic Institution, Woods Hole, MA 02543, USA. [22]Alfred Wegener Institute, 27570 Bremerhaven, Germany. [23]Romberg Tiburon Center, San Francisco State University, Tiburon, CA 94920, USA. [24]Center for Integrative Genomics, University of California at Berkeley, Berkeley, CA, USA

*To whom correspondence should be addressed. E-mail: armbrust@ocean.washington.edu (E.V.A.), dsrokhsar@lbl.gov (D.S.R.)

†Present address: Institute of Parasitology, Academy of Sciences of the Czech Republic, Branisovska 31, 370 05 Ceske Budejovice, Czech Republic.

of Japan (DDBJ)/European Molecular Biology Laboratory (EMBL)/GenBank under the project accession AAFD00000000. The version described in this paper is the first version, AAFD01000000.

Sequence polymorphisms between nuclear chromosome copies were easily detected as discrepancies between aligning reads supported by two or more reads for each of two alternate sequences. This analysis showed that 0.75% of the nucleotides in the nuclear genome are polymorphic (fig. S1), which is comparable to levels seen previously in marine animals (*10*, *11*). Only two haplotypes were observed, consistent with descent from a single diploid founder.

Twenty-four pairs of nuclear chromosomes ranging in size from 0.34 to 3.3 Mb were characterized by optical restriction site (*Nhe I*) mapping, for a total of 34.5 Mb. Over 90% of the sequence can be assigned to individual chromosomes, including a 350-kb cluster of ~35 copies of ribosomal DNA repeats (Fig. 2). Nine chromosome pairs can be separated into their respective haplotypes on the basis of restriction site polymorphisms, and seven of these pairs can be further distinguished from one another by insertions or inverted duplications ranging from tens of kilobases to a megabase in size. Surprisingly, DNA sequence and optical maps indicate that chromosome 23 is nearly identical to a comparably sized segment of chromosome 21. Chromosome 23 was likely created by an extremely recent duplication whose divergence is less than the haplotypic variation in the genome, possibly since the isolation of this laboratory strain. The plastid genome appears in the optical map as concatemers of similar restriction patterns, which suggests that several variants of the plastid genome are present. The mitochondrial genome at ~44 kbp is too small for accurate optical mapping.

A majority of interspersed repeats in the nuclear genome are relics of transposable elements that constitute as much as 2% of the genome (table S2). Among the most common transposable elements are long-terminal repeat retrotransposons, including *Copia* (*Copia1-9_TP*) and *gypsy*; both categories of diatom retrotransposons appear to self-prime reverse transcription in a manner not previously observed (fig. S2). A potentially novel superfamily of nonautonomous transposable elements was observed that is derived from *gypsy* but that encodes only integrase and is flanked by terminal inverted repeats (TE1_TP). The presence of multiple autonomous transposons suggests that transposon tagging may hold future promise for generating diatom mutants (*12*).

Overview of Gene and Protein Features

A total of 11,242 protein-coding genes are predicted in the diatom nuclear genome (*9*), along with 144 plastid-encoded and 40 mitochondrial-encoded genes (fig. S3 and Table 1). Of the total predicted nuclear proteins, 5916 are supported by homology (score > 200, E-value < 1 e-20) with public database proteins, 7007 have recognizable Interpro domains, and 6799 can be assigned to a eukaryotic cluster of orthologous groups (fig. S4). The unusual assortment of Interpro protein domains (Table 2) provides insights into regulatory mechanisms underlying gene expression, intracellular signaling, and transport that can now be tested experimentally.

The major categories of transcription factor in *T. pseudonana* are of the heat-shock family, which is relatively rare in other eukaryotes. Transcription factors containing homeobox and Rel homology regions (RHR) are also well represented, although the latter lack the MADS-box domains found in higher plants. The importance of chromatin-level control of gene expression can be inferred from identification of many putative proteins with characteristic domains such as bromodomains, chromodomains, histone deacetylases, SET, high mobility group (HMG), and regulator of chromosome condensation 1 domains (RCC1) (Table 2). Regulation by RNA processing is also suggested by the high proportion of gene models encoding RNA processing proteins with DEAD box helicase domains (Table 2 and fig. S4).

Unlike many other eukaryotes, the diatom does not appear to rely heavily on receptor kinases or leucine-rich repeat (LRR)–containing receptors, because neither of the large categories of proteins containing kinase domains or LRRs (Table 2) possess obvious transmembrane domains. Furthermore, no G protein–coupled receptors (GPCR) were found, which suggests that the major class of diatom receptor awaits discovery.

From the high numbers of kinase-encoding domains in the genome (Table 2), phospho-relay-based signal transduction systems appear to be commonly used in *T. pseudonana*. Of these, bacterial two-component histidine kinase–based signaling represents an important subclass, because sensor and response regulator domains were detected in a range of configurations. The most notable examples are a phytochrome with sensor and kinase domains that apparently functions as a light-regulated histidine kinase and members of a prokaryotic nitrate/nitrite sensing system (NifR3, NarL) (*13*) with a receiver domain and a DNA binding output domain, which would be the first example of such a nitrogen-sensing system in eukaryotes. The lack of obvious Hpt proteins suggests that diatoms employ novel relay systems.

The diatom contains a dramatically reduced number of major facilitator family (MFS) transporters relative to other eukaryotes (Table 2). A relatively high proportion of the identified transporters are similar to ones known to confer multidrug resistance or to transport excess metals out of cells or into vacuoles, which indicates that diatoms likely avoid toxicity by exporting potential toxins out of the cytoplasm.

Establishment of Secondary Endosymbiosis

The secondary endosymbiosis hypothesis (Fig. 1) [reviewed in (*7*)] predicts different possible origins for nuclear-encoded diatom genes: nuclear or mitochondrial genomes of the secondary heterotrophic host, and nuclear, plastid, or mitochondrial genomes of the red algal endosymbiont. To infer gene origins in the modern diatom, we compared its proteome with that of two extant photosynthetic eukaryotes (the green plant *Arabidopsis thaliana* and the red alga *Cyanidioschyzon merolae*) and one heterotrophic eukaryote (*Mus musculus*).

Almost half the diatom proteins have similar alignment scores to their closest homologs in plant, red algal, and animal genomes (Fig. 3 and fig. S5), underscoring the evolutionarily ancient divergence of Plantae (red algae, green algae, and plants), Opisthokonta (animals/fungi), and the unknown secondary host that gave rise to the heterokont (diatom) lineage. Interestingly, 806 diatom proteins align with mouse

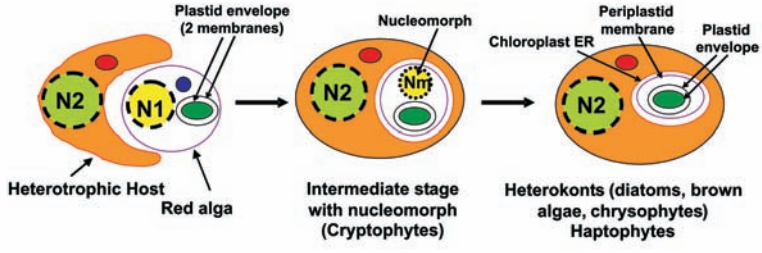

Fig. 1. Origin of chloroplasts by secondary endosymbiosis involving a red algal endosymbiont. The endosymbiont nucleus (N1) disappeared after the transfer of many genes to the host nucleus (N2), except in cryptophyte algae, which have a relict nucleus [nucleomorph (Nm)] between the plastid and the two new membranes derived from the red algal plasma membrane (periplastid membrane) and the endomembrane system of the host (chloroplast ER). Not shown are ribosomes attached to the outer surface of the chloroplast ER or the continuity of chloroplast ER with the rest of the ER system. Nuclear-encoded plastid proteins are translated on these ribosomes and must therefore cross four membranes. The red algal mitochondrion (small blue circle) was also lost.

proteins but not with green plant or red alga proteins (score ≥ 100 with BLOSUM62 matrix, or E-value < 1e-5) (Fig. 3A). The most straightforward interpretation is that these ''animal-like'' genes were derived from the heterotrophic secondary host, although scenarios involving gene loss in the plant/red algal lineage cannot be ruled out. Many could encode components of the flagellar apparatus and basal bodies, as has recently been shown for proteins shared by animals and the green alga *Chlamydomonas* but not shared with *A. thaliana* (*14*). Contrary to expectation, 182 diatom proteins have matches only to red algal proteins, whereas 865 align only with plant proteins. This is probably because the *A. thaliana* proteome is more than four times as large as the *Cyanidioschyzon merolae* proteome (Table 2). A similar comparison that included the cyanobacterium *Nostoc* sp. PCC 7120 emphasizes the large number of proteins shared by all groups of photosynthetic eukaryotes (Fig. 3B and fig. S5), many of which are likely involved in chloroplast functions.

The assemblage of genes identified in our modern diatom representative reflects large-scale transfers of genes between genomes during establishment of the endosymbiosis (*7*, *15*). In addition to *C. merolae*, we compared proteins encoded by the nucleomorph genome (remnant red algal symbiont nucleus) of the cryptophyte *Guillardia theta* (*16*) with the *T. pseudonana* nuclear-encoded proteome. Six nuclear diatom genes are most closely related to nucleomorph genes [*dhm*, *cbbX*, *cpn60* (*groEL*), *ftsZ*, *hcf136*, and *hli*]. Four of these genes are also found on red algal plastid genomes (*cbbX*, *cpn60*, *ftsZ*, and *hli*), thus demonstrating successive stages in gene transfer from red algal plastid to red algal nucleus (nucleomorph) to heterokont host nucleus.

In contrast to the situation in higher plants (*17*) and dinoflagellates (*18*), no evidence was found for recent large-scale transfers of *T. pseudonana* plastid or mitochondrial DNA to the nuclear genome. However, closely related copies of the *psbW* gene (*psb28*), which encodes a photosystem II protein, were found on both plastid and nuclear genomes, suggesting at least one

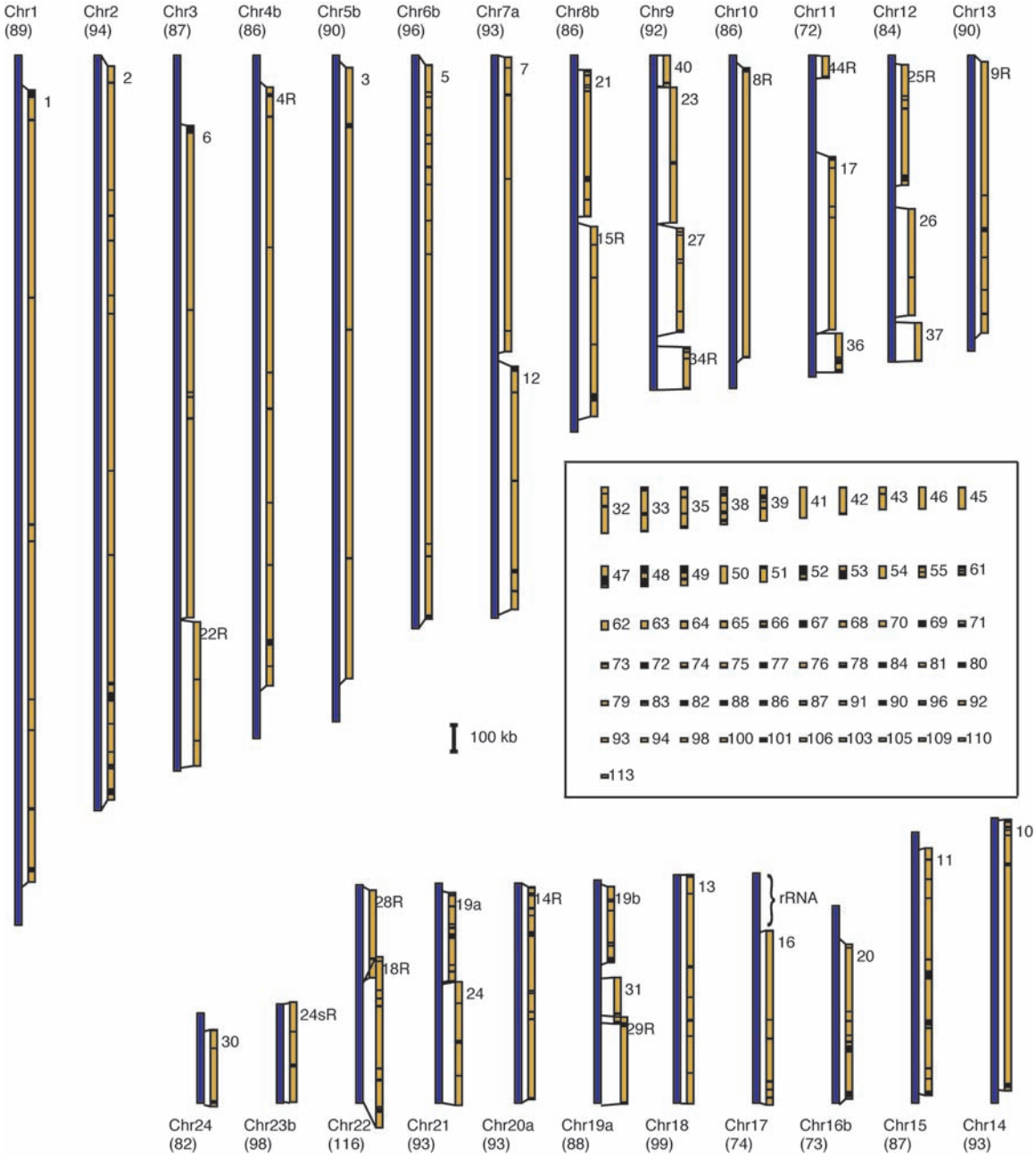

Fig. 2. Schematic representation of 24 chromosomes in *T. pseudonana*, including 9 chromosomes with two distinguishable haplotypes (indicated with an "a" or "b" after the chromosome number). Blue lines represent optical maps of chromosomes, and gold-colored lines represent whole-genome scaffold sequences with gaps shown as horizontal black lines. All sequences are shown to scale except that small gaps are shown with a minimum line width so that all gaps are visible. Scaffolds are labeled by their number and are represented 5′ to 3′ down the page. Numbers in parentheses indicate the percentage of each chromosome's length spanned by mapped scaffolds. A letter "R" after a scaffold indicates reverse complementation. Scaffolds assigned to the map based on comparison between the map and in silico scaffold digests are positioned adjacent to the matching segment of the map. Lines connect the ends of each placed scaffold with the end points of the aligning segment of the map. Scaffolds that cannot be unambiguously placed on the map are shown in the box.

plastid-to-nucleus transfer ''in progress.'' Only a plastid copy of the *psbW* gene is found in *C. merolae*, which supports the recent nature of this transfer. No red algal mitochondrial genes could be detected in *T. pseudonana* (E-value < 1e-5), and phylogenetic analysis of multiple mitochondrial genes supported the inclusion of diatom and red algal sequences in separate clades (fig. S6). Both results are consistent with the hypothesis that red algal mitochondria were lost by the ancestral heterokont, with only the heterotrophic host mitochondria retained (Fig. 1).

Table 1. General features of *T. pseudonana* genomes.

Feature	Value
Nuclear genome	
Size (bp)	34.5 million
Chromosome number	24
Chromosome size range (bp)	360,000 to 3,300,000
G + C content (overall %)	47
G + C content (coding %)	48
Transposable elements (overall %)	2
Protein-coding genes	11,242
Average gene size (bp)	992
Average number introns per gene	1.4
Gene density (bp per gene)	3,500
tRNAs	131 (includes at least 1 per codon)
Plastid genome	
Size (bp)	128,813
G + C content (overall %)	31
Protein-coding genes	144
Gene density (bp per gene)	775
tRNAs	33
Mitochondrial genome	
Size (bp)	43,827
G + C content (overall %)	30.5
Protein-coding genes	40
Gene density (bp per gene)	1137.5
tRNAs	22

Establishment of a stable secondary endosymbiosis required evolution of a protein import system to allow cytoplasmically synthesized proteins to traverse the two additional membranes that surround the plastid (Fig. 1). An N-terminal signal peptide sequence directs proteins across the endoplasmic reticulum (ER) membrane, which is continuous with the outermost plastid membrane in most heterokonts (*19*), but the mechanism of transit across the next three membranes remains unclear. A majority of putative plastid transit sequences examined (57/67) have a Phe at the +1 position (after the predicted signal cleavage site), frequently followed by a Pro at position +3, +4, +5, or +7 (fig. S7 and table S3). The first 17 to 18 positions are enriched in Ser, Thr, and Arg and have few negatively charged amino acids, similar to transit sequences of higher plants (*20*) but unlike those of the alveolate parasite *Plasmodium falciparum* (*21*). Tic 110 (with limited similarity to *C. merolae* Tic 110) was the only identified member of the Tic and Toc proteins that make up the chloroplast protein translocation system in plants (*22*), which suggests that novel changes to the import system have occurred. Homologs of plant stromal-processing and thylakoid-processing peptidases were identified, as were components of the Sec, Tat, and SRP thylakoid translocation-insertion machinery, which suggests that once proteins arrive

Table 2. Protein domains (based on Interpro matches) in *T. pseudonana* and comparison with four other eukaryotes. Estimated proteome size is given in parentheses under the name of each organism.

Interpro ID	*T. pseudonana* (11,242)		*C. merolae* (6,229)		*A. thaliana* (26,187)		*N. crassa* (10,082)		*M. musculus* (27,098)		Interpro name
	Proteins	Rank	Proteins	Rank	Proteins	Rank	Proteins	Rank	Proteins	Rank	
Ten most abundant domains in T. pseudonana											
IPR000719	202	1	71	4	1055	1	122	4	594	4	Protein kinase 1
IPR002290	136	2	61	5	228	2	101	7	351	6	Serine/threonine protein kinase 1
IPR003593	135	3	86	2	314	10	93	8	136	31	AAA ATPase
IPR001680	116	4	81	3	267	12	121	5	325	8	G protein beta WD-40 repeats
IPR001245	111	5	52	8	43	163	90	10	250	7	Tyrosine protein kinase
IPR001440	105	6	27	21	137	33	37	25	165	29	TPR repeat
IPR002110	101	7	10	32	156	38	49	19	292	17	Ankyrin
IPR001410	97	8	57	6	153	28	74	13	119	44	DEAD/DEAH box helicase
IPR001611	96	9	10	32	544	4	14	44	257	19	Leucine-rich repeat
IPR001650	95	10	56	7	147	40	71	14	107	62	Helicase, C terminal
Additional abundant domains in T. pseudonana											
IPR003590	32	41	2	>50	0	–	2	>50	0	–	Leucine-rich repeat ribonuclease
IPR002341	75	16	4	>50	23	>200	2	>50	36	>200	HSF/ETS DNA binding
IPR000232	65	20	3	>50	24	>200	3	>50	5	>200	Heat shock factor
IPR006671	51	27	7	>50	51	117	9	49	41	182	Cyclin, N terminus
IPR000595	39	35	1	>50	29	>200	4	>50	0	–	Cyclic nucleotide binding
IPR006663	62	21	14	>50	78	72	14	44	52	111	Thioredoxin domain 2
IPR006662	50	29	9	>50	78	82	10	48	45	163	Thioredoxin
IPR000408	39	36	12	>50	52	134	13	45	46	157	Regulator of chromosome condensation (RCC)
IPR005123	43	31	3	>50	114	46	10	48	0	–	20G-Fe (II) oxygenase
IPR007090	58	26	1	>50	332	11	0	–	0	–	Leucine-rich repeat, plant
Underrepresented domains in T. pseudonana											
IPR001810	2	>50	6	>50	648	4	36	26	82	81	Cyclin-like F-box
IPR007087	13	>50	17	36	182	28	90	10	730	4	Zn-finger, C2H2 type
IPR004827	10	>50	5	>50	74	93	24	34	62	116	Basic-leucine zipper (bZIP)
IPR007114	32	39	12	>50	87	71	117	6	95	67	MFS (transporter)

in the plastid stroma, machinery derived from the cyanobacterial ancestor directs them to their final destination.

Metabolic Adaptations to Life in Aquatic Environments

The frustule: Life in a glass house. The most distinctive aspect of diatoms is the frustule, which consists of hydrated silicon dioxide (silica) and a small amount of organic material. The strength of the frustule is hypothesized to help protect diatoms from being crushed during predation (*23*). The frustule is composed of two unequally sized halves connected by a series of overlapping siliceous girdle bands (*24*). Replication of the frustule during mitotic divisions creates two differently sized daughter cells, one of which is smaller than the parent cell. Cell size is ultimately restored through sexual reproduction (*24*). In generating and maintaining their frustules, diatoms control biogenic cycling of silicic acid in the ocean to such an extent that every atom of silicon entering the oceans is incorporated into diatom frustules about 40 times before its burial in sea-floor sediments (*25*).

Silicon biochemistry is largely uncharacterized in any organism. We identified three genes that encode transporters for active uptake of silicic acid (*26*). Silica precipitates within a silica deposition vesicle (SDV) in a process controlled by long-chain polyamines and a family of Lys- and Ser-rich phosphoproteins (silaffins) that are embedded within the forming silica frustule (*27*). Five silaffins were identified on the basis of genome sequence and N-terminal sequences of biosilica-associated *T. pseudonana* proteins (*28*). No matches were found to the silaffin gene *sil-1* of the diatom *Cylindrotheca fusiformis* or to silicateins that initiate silica precipitation in sponges (*29*). Long-chain polyamine biosynthesis presumably requires spermidine and spermine synthase–like enzymes (Fig. 4), and *T. pseudonana* has at least four times as many copies of genes encoding these enzymes as any other organism sequenced to date.

Dissolution of the frustule in water is minimized because it is surrounded by an organic casing that includes glycoproteins with high levels of rhamnose and xylose, two sugars rarely found in other eukaryotic glycans. Based on the presence of highly conserved calcium-binding domains (*30*), four new frustulins (casing glycoproteins) were identified, but no pleuralins, which are associated with terminal girdle bands in *C. fusiformis* (*31*). Consistent with a high content of hydroxylated amino acids found in the organic casing (*32*), one of the more abundant gene families in *T. pseudonana* encodes prolyl-4 hydroxylases.

Staying afloat. Diatoms must compensate for their dense silica frustule to maintain position within the illuminated portion of the water column. Some diatoms, including members of *Thalassiosira*, apparently increase drag and thus decrease sinking rates by extruding chitin fibers from pores in the frustule (*24*). These fibers can represent as much as 40% of total cell biomass and 20% of total cellular nitrogen (*33*). Enzymes for chitin biosynthesis and at least 22 putative chitinases were identified. This suggests that chitin fiber length may be dynamic and perhaps regulated at different life-cycle stages or in response to a balance between a need for flotation and a need for enhanced nutrient delivery; a reduction in chitin fiber length will decrease the thickness of the boundary layer around a cell, thus enhancing nutrient flux to the cell surface. The multiple chitinases could also play roles in defense against fungal infection. Identification of a chitooligosaccharide N-deacetylase indicates that *T. pseudonana* also generates chitin-based oligosaccharides.

Nitrogen metabolism/urea cycle. The genome encodes multiple transporters for nitrate and ammonium, the primary inorganic nitrogen sources for diatoms, and a single copy of a plastid-localized nitrite transporter (Fig. 4). The presence of multiple transporters for essential inorganic nutrients (nitrate, ammonium, phosphate, sulfate, silicic acid) likely reflects differential regulation and/or substrate affinities. We also found evidence for uptake and use of organic forms of nitrogen and for catabolism of amino acids (e.g., transaminases and glutamate dehydrogenase) and purines (e.g., uricase and allantoicase), which indicates that *T. pseudonana* uses multiple forms of nitrogen.

Identification of enzymes necessary for a complete urea cycle was unanticipated, because this pathway has not previously been described in a eukaryotic photoautotroph. Unlike other organisms with a urea cycle, diatoms are unlikely to excrete ''waste'' urea because they posses an active urease and can grow on urea as a sole nitrogen source. In *T. pseudonana*, the enzyme that catalyzes the first step of the urea cycle [carbamoyl phosphate synthase (CPS III)] appears to be targeted to mitochondria (table S4), as in other organisms with a urea cycle. Higher plants possess a plastid-localized version of CPS that uses glutamine rather than NH_4^+ and is required for the first step of pyrimidine biosynthesis. The diatom has lost this form of CPS but has a second CPS III–type gene without any organellar targeting sequence, which suggests that pyrimidine biosynthesis occurs in the cytoplasm of diatoms as in heterotrophs, rather than in plastids as in higher plants/green algae (Fig. 4). This observation raises the intriguing question of how pyrimidines are transported across the four plastid membranes.

The urea cycle appears to be fully integrated into diatom metabolism in ways not previously suspected. Two intermediates of the urea cycle, arginine and ornithine, feed into other pathways present in the diatom. Ornithine is used to make spermine and spermidine, the polyamines required for diverse functions in all eukaryotes (*34*), and probably also long-chain polyamines required for silica precipitation during frustule formation. Ornithine can also be converted directly to proline by ornithine cyclodeaminase. The genome encodes many proline-rich proteins and proteins containing proline-binding motifs. Arginine is used for the synthesis of the signaling molecule nitric oxide through nitric oxide synthase, which in higher plants plays a role in pathogen defense. We also find evidence for generation of the energy-storage molecule, creatine phosphate, by a urea cycle branch pathway originating from arginine (Fig. 4) that is absent from *A. thaliana*, *C. reinhardtii*, and *C. merolae*. Urea can also serve as an osmolyte, although this seems less likely in *T. pseudonana* because enzymes involved in synthesis of the more common osmolytes, betaine and mannose, as well as two plant-like halotolerance proteins, were identified.

Carbon fixation. Despite the global importance of diatom carbon fixation, considerable debate still surrounds how diatoms concentrate and deliver CO_2 to the active site of the carbon-fixation enzyme Rubisco. Reinfelder and colleagues have championed the hypothesis that diatoms rely on a

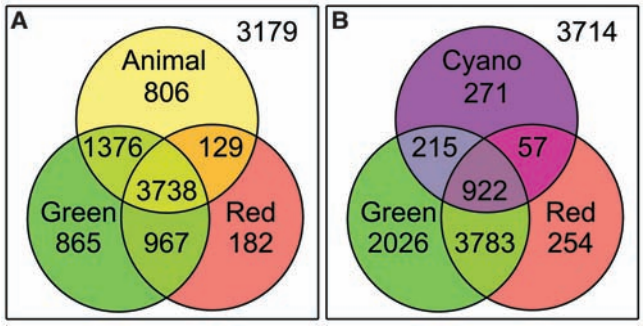

Fig. 3. Diatom proteins with homologs (BLAST scores ≥ 100) in other organisms. (**A**) Venn diagram of the distribution of *T. pseudonana* proteins with homology to proteins from *A. thaliana* (green), *C. merolae* (red) or *M. musculus* (animal). (**B**) Same as (A), but with *Nostoc* sp. PCC 7120 instead of *M. musculus*. Number outside the circles indicates the number of *T. pseudonana* proteins with no homology to the examined proteomes.

carbonic-anhydrase–dependent C4-like carbon-concentrating mechanism (*35*). We identified complete cytoplasmically localized glycolytic and gluconeogenic pathways, as well as additional enzymes necessary for interconversions and production of C4 compounds (Fig. 4). However, we found no evidence for plastid localization of decarboxylating enzymes required for delivery of CO_2 to Rubisco. The multiple carbonic anhydrases identified here catalyze interconversions between CO_2 and bicarbonate, but all appear to localize to the cytoplasm rather than the plastid as in C3 plants and green algae. This in silico analysis should help guide future experimentation.

Energy stores. Diatoms accumulate fixed carbon primarily as chrysolaminaran (1,3-β-D-glucan) during nutrient-replete conditions. This carbohydrate is metabolized rapidly during dark periods, and both an endo- and an exo-1,3-β-D-glucanase were identified. In addition, putative sugar transporters were identified, which would enable uptake of reduced carbon from the environment.

As in metazoans, longer-term storage of reduced carbon in diatoms involves lipids (*36*), which have the additional advantage of enhancing buoyancy. All plastid-containing organisms examined to date, including *P. falciparum* and now *T. pseudonana,* carry out de novo biosynthesis of fatty acids within the plastid via a type II fatty acyl synthase, followed by export of fatty acids to the cytoplasm (*37*). At least 25% of the fatty acids synthesized by *T. pseudonana* are polyunsaturated (*38*), including the nutritionally important eicosapentaenoic (EPA) and docosahexaenoic (DHA) acids. We identified a complete pathway for polyunsaturated fatty acid biosynthesis, such as several microsomal elongases and desaturases (including a putative Δ4 desaturase) that successively modify simpler fatty acids. Additional lipid-related components identified include a deduced sterol biosynthetic pathway that should produce cholesterol, cholestanol, and epibrassicasterol (Fig. 4) and a C-24(28) sterol reductase, presumably involved in the synthesis of 24-methylene sterols.

Two pathways for β oxidation of fatty acids are present in *T. pseudonana*. One pathway is localized to mitochondria, because a full set of the required enzymes possess predicted mitochondrial transit peptides (Fig. 4 and table S4). The second pathway appears to be localized to peroxisomes because it includes an acyl-CoA oxidase that is restricted to peroxisomes in other organisms (*39*, *40*), and potential peroxisomal targeting motifs (*40*) were found for enzymes known to be specific for β oxidation of polyunsaturated fatty acids, including a 2, 4-dienoyl-CoA reductase and a Δ3, 5-Δ2, 4-dienoyl-CoA isomerase. The peroxisomal pathway is expected to generate

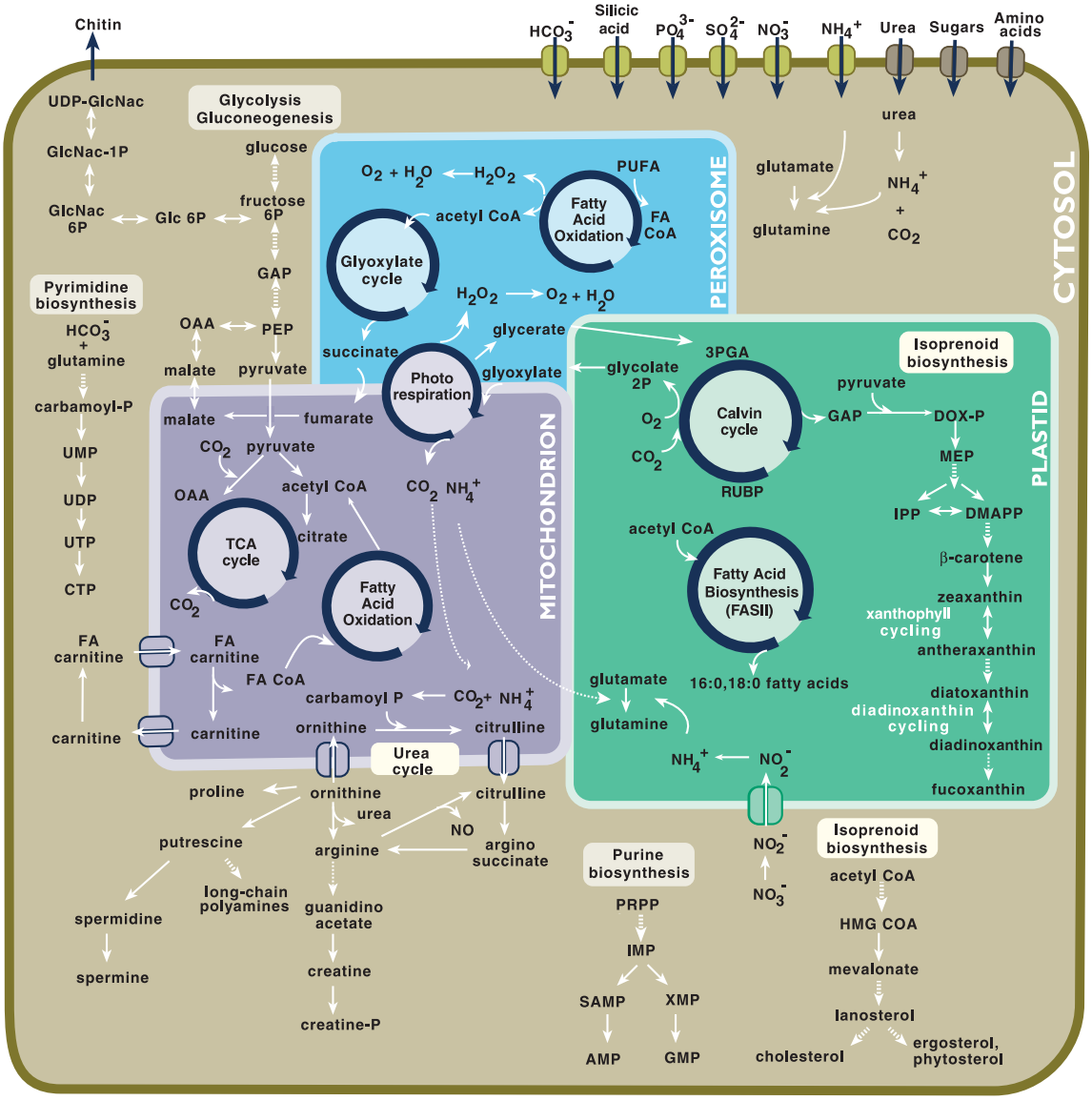

Fig. 4. Novel combinations of metabolic pathways and key components of nutrient transport in *T. pseudonana*. Metabolic steps are represented by arrows. Solid arrows indicate direct steps in a pathway, dashed arrows indicate that known multiple steps in a pathway are not shown, and dotted arrows represent hypothesized steps. Transporters or pathways localized to mitochondrion and plastid are supported by identification of targeting presequences. Pathways localized to peroxisome are based primarily on similar localization in other organisms. Transporters of unknown localization are shown in the outer membrane.

substantial quantities of H_2O_2, and a gene for catalase/peroxidase was found, although its protein localization could not be predicted. As with higher plants, peroxisomal pathway products in *T. pseudonana* presumably feed into the glyoxylate cycle and ultimately into gluconeogenesis for carbohydrate production (Fig. 4). Thus, diatoms appear to use stored lipids for both metabolic intermediates and generation of adenosine 5′-triphosphate (ATP), which likely explains how diatoms can withstand long periods of darkness and begin growing rapidly upon a return to the light.

Light harvesting, photoprotection, and photoperception. Diatoms commonly dominate in well-mixed water columns where they must cope with dramatic changes in intensity and spectral quality of light over relatively short time frames. Our in silico analyses indicate that diatoms likely perceive blue and red light, but not green light. We identified putative homologs of cryptochromes, which function as blue-light photoreceptors in other eukaryotes (*41*), and phytochrome, which is consistent with an earlier report hypothesizing that diatoms can perceive red/far-red light (*42*). No obvious matches to phototropins or rhodopsins (putative blue and green receptors) were identified. The absence of a detectable green light receptor was a surprise because green light persists to the greatest depth in coastal waters, whereas red light and blue light are both absorbed at relatively shallow depths. This combination of photoreceptors may help diatoms perceive their proximity to the surface and/or detect red chlorophyll fluorescence from neighboring cells (*43*).

The light-harvesting complex (LHC) family in *T. pseudonana* includes at least 30 fucoxanthin-chlorophyll *a/c* proteins that absorb light and transfer it to photosynthetic reaction centers. No relicts of red algal phycobiliprotein genes were detected. No evidence was found for the PsbS protein essential for operation of the photoprotective xanthophyll cycle in higher plants (*44*). This is unexpected because the major mechanism for dissipation of excess light energy in diatoms is an augmented xanthophyll cycle that involves the interconversion of diadinoxanthin and diatoxanthin in addition to the well-known violaxanthin-zeaxanthin interconversion found in higher plants (Fig. 4). No genes were found for other photoprotective members of the LHC superfamily (e.g., Elips, Seps) except for two small Hli proteins hypothesized to protect against damage from reactive oxygen species in cyanobacteria.

Damage from reactive oxygen species generated during photosynthesis could also be minimized by the two Fe-type and two Mn-type superoxide dismutases (SODs). Similar to *P. falciparum*, no obvious match to a Cu/Zn-type SOD was found, nor was a match found for a Ni-containing SOD recently discovered in marine cyanobacteria (*45*). Components of several pathways associated with use of the antioxidants glutathione, ascorbate, and alpha-tocopherol were also identified.

Iron uptake. Productivity of major regions of the modern surface ocean is limited by low iron levels (*46*). Diatoms frequently dominate phytoplankton blooms created during large-scale iron fertilization experiments, which emphasizes their important role in the marine carbon cycle (*47*, *48*). We identified components of a high-affinity iron-uptake system (*49*) composed of at least two putative ferric reductases that contain the required heme and cofactor binding sites necessary for activity. In addition, a multicopper oxidase and two iron permeases were identified that together could deliver Fe^{3+} to cells by reduction to ferrous iron. Diatoms may also use iron transport proteins found in cyanobacteria, and they possess genes that appear to encode key enzymes necessary for the synthesis of enterobactin, an iron-scavenging siderophore. Genes for metallothioneins and for phytochelatin synthases, which play important roles in metal homeostasis and detoxification, were also identified.

Conclusions

Sequence and optical mapping of the *T. pseudonana* genome showed that it is diploid with 24 chromosome pairs, data that could not be obtained by conventional cytological techniques. Analysis of predicted coding sequences demonstrated that it possesses a full complement of transporters for the acquisition of inorganic nutrients and a wide range of metabolic pathways, as expected for a highly successful photoautotroph. Its origin by secondary endosymbiosis is supported by evidence for gene transfer from the nucleus of the red algal endosymbiont and by the presence of ER signal sequences on chloroplast-targeted proteins.

About half the genes in the diatom cannot be assigned functions on the basis of similarity to genes in other organisms, in part because diatoms have distinctive features that cannot be understood by appeal to model systems. Diatoms are unusual in the way they metabolize silicon to form their characteristically ornate silica frustule; protein transport into plastids is a more complicated system than is currently understood; the way CO_2 is delivered to RubisCo remains unclear; the high proportion of polyunsaturated fatty acids produced and their oxidation to feed intermediate metabolism is unusual among eukaryotes; even the receptors required to integrate environmental signals remain unknown. The presence of the enzymatic complement of the urea cycle is unexpected, because there was no reason to suspect its presence; there is no current information about metabolic fluxes through the pathway. The unusual assortment of protein domains may reflect novel mechanisms of gene regulation.

The genomic information provided by this project suggests starting points for a number of experimental investigations of the biology of these globally important organisms and their interaction with the marine environment in which they thrive. The use of genome sequence to infer ocean ecology provides a powerful approach to exploring ecosystem structure.

References and Notes

1. D. M. Nelson, P. Tréguer, M. A. Brzezinski, A. Leynaert, B. Quéguiner, *Global Biogeochem. Cycles* **9**, 359 (1995).
2. C. B. Field, M. J. Behrenfeld, J. T. Randerson, P. G. Falkowski, *Science* **281**, 237 (1998).
3. D. G. Mann, *Phycologia* **38**, 437 (1999).
4. M. A. Brzezinski *et al.*, *Geophys. Res. Lett.* **29**, 10.1029/2001GL014349 (2002).
5. J. Parkinson, R. Gordon, *Trends Biotechnol.* **17**, 190 (1999).
6. J. S. S. Damste *et al.*, *Science* **304**, 584 (2004).
7. P. G. Falkowski *et al.*, *Science* **305**, 354 (2004).
8. A. Falciatore, C. Bowler, *Annu. Rev. Plant Biol.* **53**, 109 (2002).
9. Materials and methods are available as supporting material on *Science* Online.
10. P. Dehal *et al.*, *Science* **298**, 2157 (2002).
11. S. Aparicio *et al.*, *Science* **297**, 1301 (2002).
12. V. Walbot, *Curr. Opin. Plant Biol.* **3**, 103 (2000).
13. V. Stewart, P. J. Bledsoe, *J. Bacteriol.* **185**, 2104 (2003).
14. J. B. Li *et al.*, *Cell* **117**, 541 (2004).
15. J. M. Archibald, M. B. Rogers, M. Toop, K.-I. Ishida, P. J. Keeling, *Proc. Natl. Acad. Sci. U.S.A* **100**, 7678 (2003).
16. S. Douglas *et al.*, *Nature* **410**, 1091 (2001).
17. W. Martin, *Proc. Natl. Acad. Sci. U.S.A.* **100**, 8612 (2003).
18. J. D. Hackett *et al.*, *Curr. Biol.* **14**, 213 (2004).
19. P. G. Kroth, *Int. Rev. Cytol.* **221**, 191 (2002).
20. X.-P. Zhang, E. Glaser, *Trends Plant Sci.* **7**, 14 (2002).
21. B. J. Foth *et al.*, *Science* **299**, 705 (2003).
22. K. Cline, in *Light-Harvesting Antennas in Photosynthesis*, vol.13, *Advances in Photosynthesis and Respiration*, B. R. Green, W. W. Parson, Eds. (Kluwer Academic Publishers, Dordrecht, Netherlands, 2003), pp. 353–372.
23. C. E. Hamm *et al.*, *Nature* **421**, 841 (2003).
24. F. E. Round, R. M. Crawford, D. G. Mann, *The Diatoms: Biology and Morphology of the Genera* (Cambridge Univ. Press, Cambridge, 1990).
25. P. Tréguer *et al.*, *Science* **268**, 375 (1995).
26. M. Hildebrand, B. E. Volcani, W. Gassmann, J. L. Schroeder, *Nature* **385**, 688 (1997).
27. M. Sumper, N. Kröger, *J. Mater. Chem.* **14**, 2059 (2004).
28. N. Poulsen, N. Kröger, *J. Biol. Chem.*, in press.
29. K. Shimizu, J. Cha, G. D. Stucky, D. E. Morse, *Proc. Natl. Acad. Sci. U.S.A.* **96**, 361 (1998).
30. N. Kröger, C. Bergsdorf, M. Sumper, *EMBO J.* **13**, 4676 (1994).
31. N. Kröger, R. Wetherbee, *Protist* **151**, 263 (2000).
32. B. E. Volcani, in *Silicon and Siliceous Structures in Biological Systems*, R. Simpson, B. E. Volcani, Eds. (Springer, New York, 1981), pp. 157–200.
33. J. McLachlan, A. G. McInnes, M. Falk, *Can. J. Bot.* **43**, 707 (1965).
34. P. Coffino, *Proc. Natl. Acad. Sci. U.S.A.* **97**, 4421 (2000).
35. J. R. Reinfelder, A. M. L. Kraepiel, F. M. M. Morel, *Nature* **407**, 996 (2000).
36. G. A. Dunstan, J. K. Volkman, S. M. Barrett, C. D. Garland, *J. Appl. Phycol.* **5**, 71 (1993).
37. R. F. Waller *et al.*, *Proc. Natl. Acad. Sci. U.S.A.* **95**, 12352 (1998).
38. G. A. Dunstan, J. K. Volkman, S. M. Barrett, J. M. Leroi, S. W. Jeffrey, *Phytochemistry* **35**, 155 (1994).
39. M. Fulda, J. Shockey, M. Werber, F. P. Wolter, E. Heinz, *Plant J.* **32**, 93 (2002).
40. A. T. J. Klein, M. van den Berg, G. Bottger, H. F. Tabak, B. Distel, *J. Biol. Chem.* **277**, 25011 (2002).

41. M. Yanovsky, S. Kay, *Nature Rev. Mol. Cell Biol.* **4**, 265 (2003).
42. C. Leblanc, A. Falciatore, C. Bowler, *Plant Mol. Biol.* **40**, 1031 (1999).
43. M. Ragni, M. Ribera, *J. Plankton Res.* **26**, 433 (2004).
44. X.-P. Li *et al.*, *Nature* **403**, 391 (2000).
45. B. Palenik *et al.*, *Nature* **424**, 1037 (2003).
46. J. K. Moore, S. C. Doney, D. M. Glover, I. Y. Fung, *Deep-Sea Res. II* **49**, 463 (2002).
47. P. W. Boyd *et al.*, *Nature* **407**, 695 (2000).
48. K. H. Coale *et al.*, *Science* **304**, 408 (2004).
49. N. J. Robinson, C. M. Procter, E. L. Connolly, M. L. Guerinot, *Nature* **397**, 694 (1999).
50. This work was performed under the auspices of the U.S. Department of Energy's (DOE) Office of Science, Biological, and Environmental Research Program and by the University of California, Lawrence Livermore National Laboratory under Contract No. W-7405-Eng-48, Lawrence Berkeley National Laboratory under contract No. DE-AC03-76SF00098, and Los Alamos National Laboratory under contract No. W-7405-ENG-36.; and DOE (DE-FG03-02ER63471 to E.V.A.), European Union Margens (QLRT-2001-01226 to C.B.), the CNRS Atip program (2JE144 to C.B.), and the U.S. Environmental Protection Agency (R827107-01-0, Basic to B.P., M.H.).

Supporting Online Material
www.sciencemag.org/cgi/content/full/306/5693/79/DC1
Materials and Methods
Figs. S1 to S7
Tables S1 to S4
References

7 June 2004; accepted 17 August 2004

REPORTS

The Kondo Effect in the Presence of Ferromagnetism

Abhay N. Pasupathy,[1] Radoslaw C. Bialczak,[1] Jan Martinek,[2] Jacob E. Grose,[1] Luke A. K. Donev,[1] Paul L. McEuen,[1] Daniel C. Ralph[1]*

We measured Kondo-assisted tunneling via C_{60} molecules in contact with ferromagnetic nickel electrodes. Kondo correlations persisted despite the presence of ferromagnetism, but the Kondo peak in the differential conductance was split by an amount that decreased (even to zero) as the moments in the two electrodes were turned from parallel to antiparallel alignment. The splitting is too large to be explained by a local magnetic field. However, the voltage, temperature, and magnetic field dependence of the signals agree with predictions for an exchange splitting of the Kondo resonance. The Kondo effect leads to negative values of magnetoresistance, with magnitudes much larger than the Julliere estimate.

Measurements on individual quantum dots have in recent years provided a detailed understanding of the Kondo effect (*1–7*): the coupling between a localized spin and conduction electrons that serves as a fundamental model for understanding correlated-electron physics (*8*). Itinerant-electron ferromagnetism is an alternative correlated-electron state that can arise from Coulomb interactions between electrons. These two states ordinarily compete with each other; in heavy fermion systems, a phase transition is thought to exist between the Kondo and magnetic ground states (*9*). Calculations for the consequences of coupling between a Kondo-regime quantum dot and ferromagnetic electrodes have produced conflicting predictions (*10–14*). Experimentally, Kondo physics has not previously been studied in quantum dots with magnetic electrodes, despite work with both normal-metal (*1–6*) and superconducting (*7*) systems, because of difficulty in achieving sufficiently strong coupling between the dot and magnetic materials. We demonstrate here that C_{60} molecules can be strongly coupled to nickel (Ni) electrodes so as to exhibit the Kondo effect. Ferromagnetism can suppress Kondo-assisted tunneling, but Kondo correlations are still present within the ferromagnetic electrodes, and in particular situations the strong-coupling limit of the Kondo effect can still be achieved.

First, we compare measurements made using (magnetic) Ni and (nonmagnetic) gold (Au) electrodes, building on studies of single-electron transistors made using C_{60} (*15*) and previous measurements of Kondo-assisted tunneling using C_{60} in contact with Au electrodes (*6*). Our devices are made by using electron-beam lithography and liftoff to create electrodes that are 30 nm high and 50 nm wide at their narrowest point. After cleaning the electrodes in an oxygen plasma (0.25 W/cm^2 for 2 min), we deposit 50 μl of a dilute solution (≈100 μM) of C_{60} in toluene over a 30-mm^2 area of the chip and allow the solvent to evaporate. We cool the chip to 1.5 K and then use an electromigration procedure (*16*) to create a nanometer-scale break in the wire. One or more molecules of C_{60} can bridge this gap. For C_{60} with nonmagnetic Au electrodes, some samples show featureless tunnel conduction or conventional high-resistance Coulomb blockade characteristics (*15*), but in approximately 20% of 100 junctions the differential conductance [$G(V) \equiv dI/dV \equiv 1/R(V)$] curves display a peak at $V = 0$ (Fig. 1A) (*6*) (V, voltage; I, current; R, resistance). This peak can be split by applying a magnetic field B, with an average g factor ≈ 2. These features are signatures of the Kondo effect in a spin-1/2 quantum dot (*1–6*). The Kondo signals were absent in a set of 40 control samples that underwent the same fabrication procedure, but without the C_{60} deposition.

For magnetic Ni electrodes, the shapes of the two electrodes were designed to give them different magnetic anisotropies, so that they undergo magnetic reversal at different values of B(*17*). We have experimented with several combinations of shapes and have had good success with the pattern shown in Fig. 1B. The magnetic properties of test electrodes were checked in the absence of any molecules, by measuring the magnetoresistance of tunnel junctions created by electromigration (Fig. 1C). The curves display hysteretic switching features familiar from previous studies of magnetic tunnel junctions (*18*), demonstrating that we can control the relative orientation of the magnetic moments in the two electrodes between parallel (P) and approximately antiparallel (AP) alignment. We can compare the magnitude of the junction magnetoresistance (JMR) to the Julliere estimate (*19*): JMR $\equiv (R_{AP} - R_P)/R_P = 2P^2/(1 - P^2)$, where R_P is the resistance when the magnetizations are parallel, R_{AP} is the resistance when the magnetizations are antiparallel, and P is the tunneling spin polarization. Using $P = 0.31$ measured for thin films of Ni with aluminum oxide tunnel

[1]Laboratory of Atomic and Solid State Physics, Cornell University, Ithaca, NY 14853, USA. [2]Institut für Theoretische Festkörperphysik, Universität Karlsruhe, 76128 Karlsruhe, Germany; Institute for Materials Research, Tohoku University, Sendai 980–8577, Japan; and Institute of Molecular Physics, Polish Academy of Sciences, 60–179 Poznań, Poland.

*To whom correspondence should be addressed. E-mail: ralph@ccmr.cornell.edu

barriers (*20*), the Julliere estimate is JMR = 21%. The sample shown in Fig. 1C has JMR = 19%, and for other samples we find values in the range from 10 to 19%.

After we performed electromigration on Ni samples with C_{60} adsorbed on them, about 5% of the devices exhibited simple high-resistance Coulomb blockade characteristics (*15*); and in approximately 3% of 1200 total devices, we observed $G(V)$ versus V curves similar to those in Fig. 2, A and C. Instead of having a single peak in $G(V)$ centered at $V = 0$ as observed for Kondo tunneling with Au electrodes, when the moments of the Ni electrodes were aligned parallel by a small applied field, we observed two peaks in $G(V)$, approximately symmetric about $V = 0$ and with similar amplitudes and widths, situated atop a background that can be asymmetric in V. These characteristics are different from Coulomb blockade conductance peaks (*21*).

The split peaks in Figure 2 display a strong dependence on the relative orientation of the magnetic moments in the two electrodes. Figure 2B shows a color scale plot of $G(V,B)$ for sample 1 as a function of B (y axis) and V (x axis), recorded at 1.5 K. B is swept from negative to positive values. When $B < -10$ mT, there are two peaks in $G(V)$ with a splitting $\Delta V_P = 16$ mV that displays only a weak dependence on B. At $B = -10$ mT, there is an abrupt switch, at which point the splitting is reduced to $\Delta V_{AP} = 7.6$ mV. In the range -10 mT $< B < 200$ mT, the splitting between the peaks gradually increases. At $B = 200$ mT, there is a second abrupt switching event, and the $G(V)$ curves for larger positive fields are the same as at large negative fields. When the sweep direction for B is reversed, the $G(V,B)$ plots exhibit magnetic hysteresis, with the switching fields reversed about $B = 0$. We can therefore associate these changes with the relative orientation of the moments in the two magnetic electrodes. For negative B in Fig. 2B, the moments are parallel and the peak splitting is large. At $B = -10$ mT, one moment reverses to give an approximately antiparallel configuration with a smaller splitting. On further increasing B, the other moment rotates gradually, and then at $B = 200$ mT the second moment reverses to restore the P configuration.

Figure 2, C and D, shows a similar progression as a function of B for sample 2. Again there is a large splitting, $\Delta V_P = 18$ mV, for parallel moments in the electrodes, but in the AP configuration the splitting is reduced sufficiently that only one peak in $G(V)$ is resolvable. The lack of splitting for the AP case indicates that the strong-coupling Kondo effect is possible even in the presence of ferromagnetic electrodes.

The splittings between the conductance peaks are too large to be associated with Zeeman splitting of the Kondo resonance in a local magnetic field. Assuming a g factor of 2, a splitting $\Delta V_P = 16$ mV corresponds to a magnetic field of 70 T. An upper limit on the local magnetic field that can be generated by the magnetic electrodes in the small gap is given by their magnetization, 0.6 T for Ni.

The magnetic field dependence of our split peaks is in excellent agreement with some recent predictions that the interaction of a quantum dot with spin-polarized electrodes can produce a splitting of the Kondo resonance (*12–14*). In this model, the conductance of a single-level quantum dot is determined by the tunneling spin polarizations P_L, P_R and the couplings Γ_L, Γ_R between the dot and the left and right electrodes. We will assume that polarizations are $P_L = P_R = P = 0.31$ (as for a Ni junction) for the P orientation and $P_L = -P_R = P$ for the AP orientation. Because of quantum charge fluctuations, the

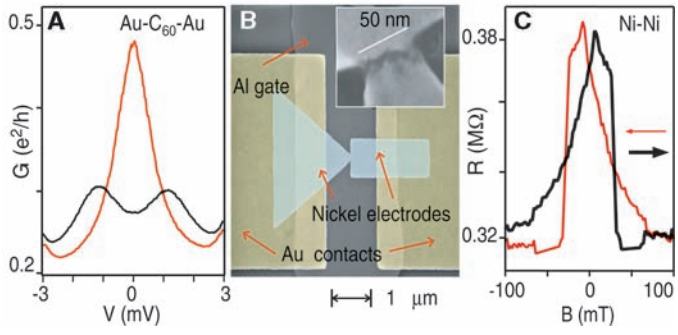

Fig. 1. (**A**) Kondo signal for C_{60} with Au electrodes at $T = 1.5$ K. At $B = 0$ (red line), there is a zero-bias peak in $G(V)$ that becomes split for $B = 10$ T (black line). (**B**) Scanning electron micrograph of a Ni break junction. The magnetic field is applied in the horizontal direction. (**Inset**) Close-up of the junction region after electromigration. (**C**) Tunneling magnetoresistance near $V = 0$ at $T = 4.2$ K of a Ni contact after electromigration, with no C_{60} molecule present.

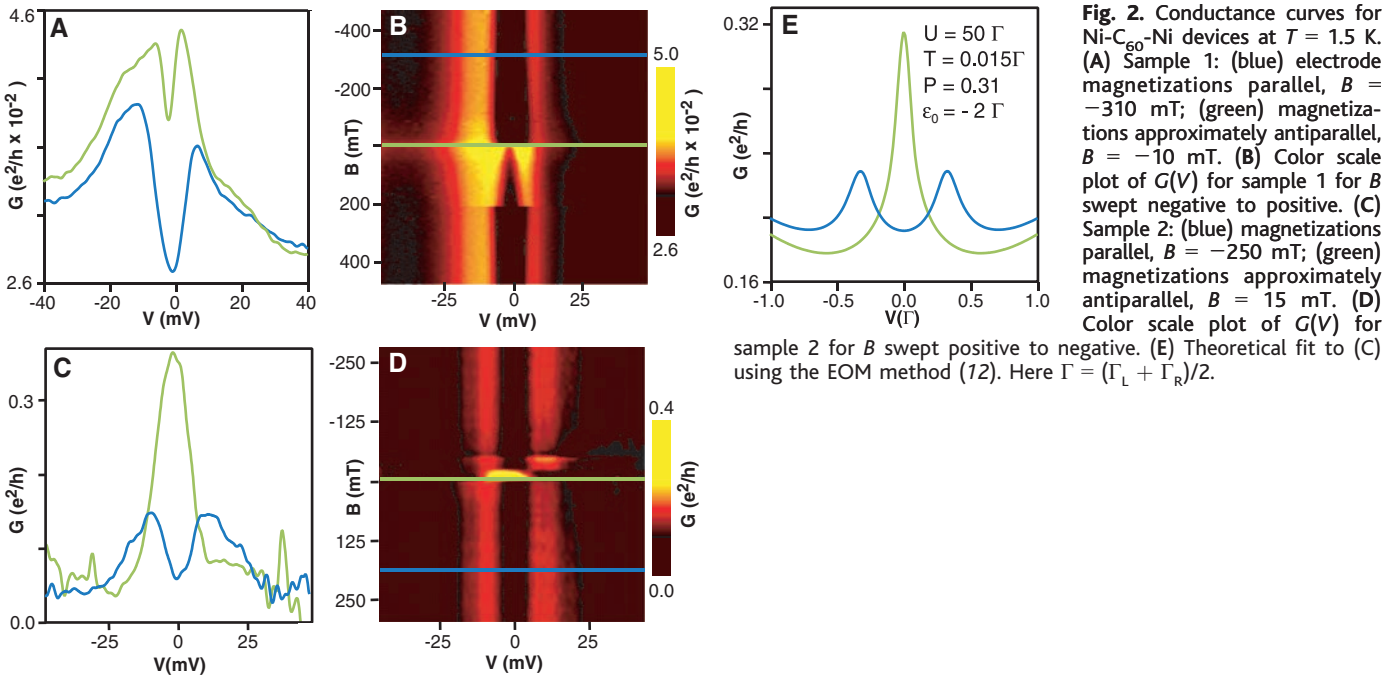

Fig. 2. Conductance curves for Ni-C_{60}-Ni devices at $T = 1.5$ K. (**A**) Sample 1: (blue) electrode magnetizations parallel, $B = -310$ mT; (green) magnetizations approximately antiparallel, $B = -10$ mT. (**B**) Color scale plot of $G(V)$ for sample 1 for B swept negative to positive. (**C**) Sample 2: (blue) magnetizations parallel, $B = -250$ mT; (green) magnetizations approximately antiparallel, $B = 15$ mT. (**D**) Color scale plot of $G(V)$ for sample 2 for B swept positive to negative. (**E**) Theoretical fit to (C) using the EOM method (*12*). Here $\Gamma = (\Gamma_L + \Gamma_R)/2$.

spin asymmetry in the coupling to the electrodes produces a spin-dependent renormalization of the dot's levels ε_σ (bare value ε_0), breaking the spin degeneracy: $\varepsilon_\uparrow \neq \varepsilon_\downarrow$. This results in a splitting of the $G(V)$ curve which (in the general case when an external field B is applied) has the value (*13*)

$$e\Delta V = 2\,|\,g\mu_B B + a\sum_{r=L,R} P_r\Gamma_r\,| \qquad (1)$$

Here μ_B is the Bohr magneton and a is a constant of order unity whose magnitude and sign depend on the charging energy U, ε_0, and the detailed band structure (*22*). If the magnetizations are AP and the dot has equal couplings to both electrodes $\Gamma_L = \Gamma_R$, the exchange interactions from the two electrodes are compensated. In this situation, the strong-coupling Kondo effect is restored despite the spin polarization in the leads, and the splitting is predicted to be reduced to zero near $B = 0$ (Fig. 2E). However, when one takes into account that typically $\Gamma_L \neq \Gamma_R$, then the low-B peak splittings in the P and AP orientations should be (assuming $\Gamma_L > \Gamma_R$)

$$e\Delta V_P = 2aP(\Gamma_L + \Gamma_R) \qquad (2)$$

$$e\Delta V_{AP} = 2aP(\Gamma_L - \Gamma_R) \qquad (3)$$

These results are consistent with our measurements of larger splittings for parallel moments and smaller but generally nonzero splittings in the AP case (*23*).

For sample 1, Fig. 2B and Eqs. 2 and 3 together provide an estimate for the tunnel coupling ratio $\Gamma_L/\Gamma_R = (\Delta V_P + \Delta V_{AP})/(\Delta V_P - \Delta V_{AP}) \approx 3$. If we pick a typical value of $aP \approx 0.15$ (*12–14*) we can estimate $\Gamma_L \approx 45$ meV and $\Gamma_R \approx 15$ meV. For sample 2, for which no splitting was resolved in the AP state, we can set the limit $\Gamma_L/\Gamma_R < 2$, with $\Gamma_L, \Gamma_R \approx 30$ meV. These numbers will change according to the value of aP assumed, according to Eq. 1. To obtain other estimates of device parameters, we have performed theoretical fits of $G(V)$ using the equations-of-motion (EOM) technique (*12*). A plot for sample 2 in the parallel (solid) and antiparallel (dashed) magnetization orientations is shown in Fig. 2E. The parameters used are $\Gamma = 30$ meV, $\varepsilon_0 = -60$ meV, and $U = 1.5$ eV. The fits are relatively insensitive to changes in U by up to an order of magnitude. Γ and ε_0 are determined to about a factor of 2 once P_L, P_R are set. Values of the same order of magnitude are extracted for sample 1.

Further confirmation that the split peaks in $G(V)$ are associated with Kondo physics comes from their dependence on temperature (T) and B. In order to measure changes at cryogenic temperatures and laboratory magnetic fields, one must focus on samples with narrow-in-V conductance peaks, associated with small Kondo temperatures (T_K) (Fig. 3). Theory indicates that the T dependence of the peak conductance around T_K should be approximately logarithmic even when the Kondo resonance is split (*24*). This is what we observe, for both parallel (Fig. 3A, sample 3) and antiparallel (Fig. 3B, sample 4) alignment of the electrode moments.

In Fig. 3C, we show how an applied magnetic field affects the $G(V)$ versus V curves for sample 4, which has a particularly narrow peak width (0.3 meV). For all values of B displayed, the electrode moments are approximately parallel. The extracted peak positions are plotted in Fig. 3D. The peak spacing increases approximately linearly with $|B|$ with a g factor of 1.8 ± 0.3. Assuming that the tunneling polarization of Ni is positive (*20*), this would imply that the sign of a in Eq. 1 is positive (*22*). There is a residual zero-field splitting of $\Delta V_P = 0.14 \pm 0.06$ mV.

We have shown that coupling to the magnetic electrodes produces a large local exchange field on the quantum dot (greater than 50 T) that can be modulated by using a small external magnetic field (<100 mT) to control the relative orientation of the moments in the electrodes. We find that this amplification can dramatically enhance the JMR, in agreement with theoretical predictions (*12*). As a magnetic field is used to turn the electrode moments from parallel to antiparallel alignment, the zero-bias JMR is −38% for sample 1 (Fig. 4A) and −80% for sample 2 (Fig. 4B). The sign of the JMR is negative, opposite to the typical behavior in magnetic tunnel junctions, and the magnitude is much larger than the Julliere value of 21%. This happens because the Kondo resonance occurs closer to the Fermi energy for the antiparallel magnetization orientation, thus enhancing its conductance (*12*). A different mechanism for negative values of JMR has been discussed previously in connection with sequential electron tunneling via localized charge states (*25*), but the magnitude of this effect is smaller than the Kondo mechanism we report.

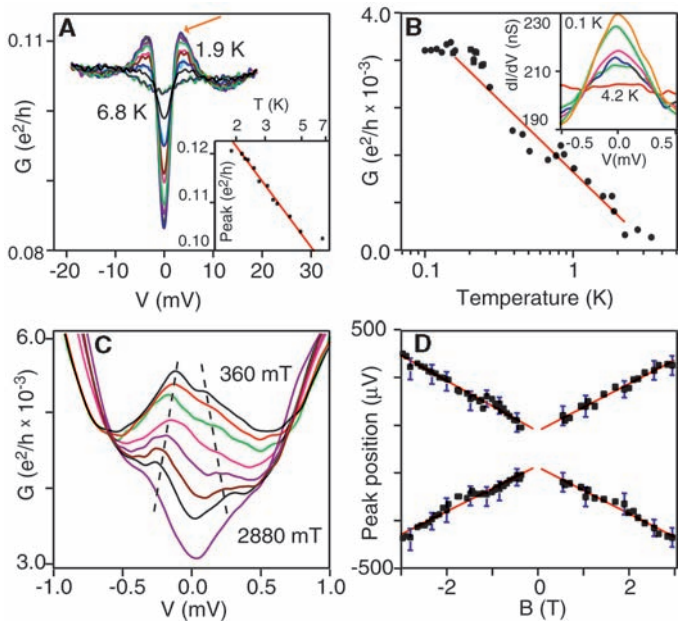

Fig. 3. (**A**) T dependence of $G(V)$ for Ni-C_{60}-Ni sample 3 with electrode moments parallel, B = 250 mT. (**Inset**) Peak conductance (red arrow) versus T for these curves. (**B**) Fitted height above background for Kondo peak versus T for Ni-C_{60}-Ni sample 4 with electrode moments approximately antiparallel, B = 10 mT. (**C**) $G(V)$ for sample 4 at 100 mK, at equally spaced values of B for which the electrode moments are parallel. (**D**) Peak positions extracted from (C). Typical error bars are shown.

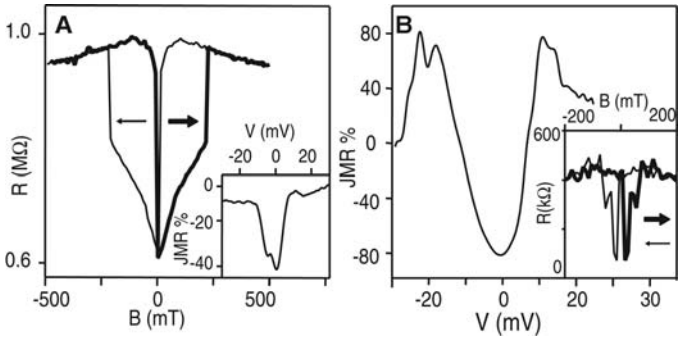

Fig. 4. $V = 0$ magnetoresistance at T = 1.5 K and the JMR as a function of V for two Ni-C_{60}-Ni samples. (**A**) Sample 1. (**B**) Sample 2.

References and Notes

1. D. Goldhaber-Gordon *et al.*, *Nature* **391**, 156 (1998).
2. S. M. Cronenwett, T. H. Oosterkamp, L. P. Kouwenhoven, *Science* **281**, 540 (1998).
3. J. Nygard, D. H. Cobden, P. E. Lindelof, *Nature* **408**, 342 (2000).
4. J. Park *et al.*, *Nature* **417**, 722 (2002).
5. W. Liang *et al.*, *Nature* **417**, 725 (2002).
6. L. H. Yu, D. Natelson, *Nano Lett.* **4**, 79 (2004).
7. M. R. Buitelaar, T. Nussbaumer, C. Schonenberger, *Phys. Rev. Lett.* **89**, 256801 (2002).
8. A. C. Hewson, *The Kondo Problem to Heavy Fermions* (Cambridge Univ. Press, Cambridge, 1993).

9. In the Kondo ground state, the localized spin is screened by the conduction electrons, suppressing magnetic interactions. In the magnetic ground state, spin degeneracy is broken, which suppresses spin fluctuations and Kondo correlations (*26*).
10. N. Sergueev *et al.*, *Phys. Rev. B* **65**, 165303 (2002).
11. P. Zhang, Q.-K. Xue, Y. Wang, X. C. Xie, *Phys. Rev. Lett.* **89**, 286803 (2002).
12. J. Martinek *et al.*, *Phys. Rev. Lett.* **91**, 127203 (2003).
13. J. Martinek *et al.*, *Phys. Rev. Lett.* **91**, 247202 (2003).
14. M.-S. Choi, D. Sanchez, R. Lopez, *Phys. Rev. Lett.* **92**, 056601 (2004).
15. H. Park *et al.*, *Nature* **407**, 57 (2000).
16. H. Park *et al.*, *Appl. Phys. Lett.* **75**, 301 (1999).
17. R. P. Cowburn, *J. Phys. D* **33**, R1 (2000).
18. E. Y. Tsymbal, O. N. Mryasov, P. R. LeClair, *J. Phys. Cond. Mat.* **15**, R109 (2003).
19. M. Julliere, *Phys. Lett. A* **54**, 225 (1955).
20. D. J. Monsma, S. S. P. Parkin, *Appl. Phys. Lett.* **77**, 720 (2000).
21. Coulomb blockade conductance peaks are not generally symmetric in V nor do they have similar heights for positive and negative bias, because the capacitances and resistances to the two electrodes are different in general (*27*).
22. J. Martinek *et al.*, http://arxiv.org/abs/cond-mat/0406323 (2004).
23. In addition to the Kondo signals, tunneling through the independent electron resonances should be expected to produce peaks in $G(V)$ centered at the Coulomb blockade energy thresholds, with widths on the order of Γ. However, we do not usually resolve these Coulomb blockade peaks in the Kondo samples. Estimates of Γ as large as many tens of milli–electron volts suggest that they would be difficult to observe. Nevertheless, we do expect that electron tunneling through these broad single-electron resonances contributes to the asymmetric conductance background underlying the Kondo signals.
24. J. Paaske, A. Rosch, P. Wölfle, *Phys. Rev. B* **69**, 155330 (2003).
25. E. Y. Tsymbal, A. Sokolov, I. F. Sabirianov, B. Doudin, *Phys. Rev. Lett.* **90**, 186602 (2003).
26. S. Doniach, *Phys. B* **91**, 231 (1977).
27. E. Bonet, M. M. Deshmukh, D. C. Ralph, *Phys. Rev. B* **65**, 045317 (2002).
28. We thank F. Kuemmeth for experimental help and J. Barnaś, L. Borda, P. Bruno, R. Bulla, J. von Delft, L. Glazman, H. Imamura, J. König, S. Maekawa, J. Petta, A. Rosch, G. Schön, M. Sindel, J. Stankowski, M. Vojta, and Y. Utsumi for discussions. This work was supported by NSF through the Cornell Center for Materials Research (grant DMR-0079992) and use of the Cornell NanoScale Facility; by the Defense Advanced Research Projects Agency/Office of Naval Research (grant N00173-03-1-G011); by the Army Research Office (grant DAAD19-01-1-0541); and by the Deutsche Forschungsgemeinshaft under the Center for Functional Nanostructures, "Spintronics" Research and Training Network of the European Community (EC) (grant RTN2-2001-00440), project PBZ/KBN/044/P03/2001 and EC contract G5MA-CT-2002-04049.

28 June 2004; accepted 11 August 2004

Extinct ^{244}Pu in Ancient Zircons

Grenville Turner,[1]* T. Mark Harrison,[2,3] Greg Holland,[1] Stephen J. Mojzsis,[4] Jamie Gilmour[1]

We have found evidence, in the form of fissiogenic xenon isotopes, for in situ decay of ^{244}Pu in individual 4.1- to 4.2-billion-year-old zircons from the Jack Hills region of Western Australia. Because of its short half-life, 82 million years, ^{244}Pu was extinct within 600 million years of Earth's formation. Detrital zircons are the only known relics to have survived from this period, and a study of their Pu geochemistry will allow us to date ancient metamorphic events and determine the terrestrial Pu/U ratio for comparison with the solar ratio.

The isotope ^{244}Pu is one of the longest lived of the so-called extinct isotopes that were present in the early solar system and that recorded nucleosynthetic processes immediately preceding its formation. This nuclide is produced solely in the r process, and its half-life is sufficiently long that it is expected to have been well-mixed locally within the galaxy in the sense that, on an 82-million-year (My) time scale, distances over which ^{244}Pu is dispersed are greater than the mean distance between supernovae in star-forming regions (*1*). On this basis, the equilibrium ratio of ^{244}Pu/^{238}U is expected to be equal to the ratio of the respective half-lives, i.e., 82/4450 = 0.018, multiplied by a number of order unity (related to the production rate of heavy precursors). A well-constrained initial value, combined with other key isotope abundance ratios (^{107}Pd, ^{129}I, ^{182}Hf, ^{235}U, ^{238}U, and ^{232}Th) would provide raw data with which to improve our understanding of the details of the r process and the timing of local nucleosynthetic events before the formation of the solar system (*1–5*).

Also, ^{244}Pu has a key role in understanding Earth evolution. Models of volatile transport within and from the mantle and of the origin and evolution of the atmosphere are influenced by inferences made from noble gas studies (*6–11*). A key parameter in these models is the Pu/U ratio, which determines the relative ingrowth of ^{136}Xe (from ^{244}Pu and ^{238}U fission) and ^{4}He (from U and Th decay) and hence quantifies the link between the Xe flux from the deep mantle source and that of He. Several attempts have been made to determine the overall ^{244}Pu/^{238}U ratio for the solar system (*12*, *13*) and to use ^{244}Pu as an early solar system chronometer (*14–16*); however, the solar value of ^{244}Pu/^{238}U is still uncertain within a factor of two, probably lying between 0.004 and 0.008. The discovery of terrestrial zircons with formation intervals between 4.0×10^9 and 4.4×10^9 years ago (Ga) offers an alternative way to resolve the issue. ^{238}U decay is the dominant source of fissiogenic xenon produced after 3.8 Ga, whereas ^{244}Pu decay dominates before 4.4 Ga. Between 4.0 and 4.4 Ga, contributions from ^{244}Pu and ^{238}U are expected to be comparable, and Pu/U can in principle be obtained directly from xenon analyses on samples with closure ages in this time interval. The ^{131}Xe/^{136}Xe ratio is particularly sensitive, varying between 0.085 for the spontaneous fission of ^{238}U and 0.246 for ^{244}Pu fission. A previous attempt to apply this method to large numbers of coeval zircons from

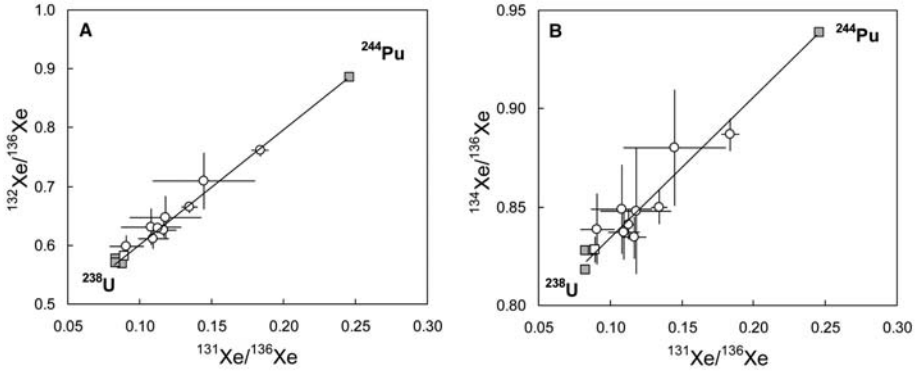

Fig. 1. After corrections for atmospheric Xe (fig. S4), the correlations of (**A**) ^{132}Xe/^{136}Xe with ^{131}Xe/^{136}Xe and of (**B**) ^{134}Xe/^{136}Xe with ^{131}Xe/^{136}Xe indicate that the remaining Xe is a two-component mixture produced by the spontaneous fission of ^{238}U and ^{244}Pu (solid squares). The highest ^{131}Xe/^{136}Xe ratio corresponds to a ^{244}Pu/^{238}U ratio of 0.0066 ± 0.0010 (calculated at 4560 Ma). Open circles are Jack Hills detrital zircons; open square is a 3.6-Gy-old zircon.

[1]Department of Earth Sciences, University of Manchester, Manchester M13 9PL, UK. [2]Research School of Earth Sciences, Australian National University, Canberra, ACT 0200, Australia. [3]Department of Earth and Space Sciences and Institute of Geophysics and Planetary Physics, University of California, Los Angeles, CA 90095, USA. [4]Department of Geological Sciences, Center for Astrobiology, University of Colorado, Boulder, CO 80309–0399, USA.

*To whom correspondence should be addressed. E-mail: grenville.turner@man.ac.uk

3.8-Gy-old igneous rocks from West Greenland was essentially frustrated by the overwhelming contribution from ^{238}U fission (*17*).

Detrital zircons from Early Archean metasediments in the Jack Hills region of Western Australia have U-Pb ages as old as 4.4 Gy (*18–21*). These minute grains, typically 50 to 200 μm in size and weighing only a few micrograms, are the only known relics of Earth's earliest crust. Because the ancient zircons are detrital and of unknown provenance, it is essential that measurements of xenon isotopes are carried out on individual zircons. The amount of xenon present in a single zircon is very small, around 10^{-15} cm^3 at standard temperature and pressure for a 2-μg zircon initially containing 200 parts per million (ppm) uranium. This is comparable to blank levels and sensitivities of conventional noble gas mass spectrometers. We have developed a sensitive mass spectrometer based on laser resonance ionization (*22*). The instrument, RELAX (refrigerator-enhanced laser analyzer for xenon), can analyze samples of only a few thousand atoms, some two orders of magnitude smaller than conventional noble gas mass spectrometers. We analyzed xenon, released by laser-stepped heating, from eight zircon grains from Jack Hills with ages between 4.12 and 4.22 Gy and one of circa (ca.) 3.6 Gy (*23*). Unambiguous evidence for the presence of fissiogenic xenon was obtained for all extractions (figs. S1 to S4). On the basis of the amount of ^{130}Xe in the spectra, the contribution from atmospheric ^{136}Xe was typically a few hundred atoms and largely or wholly instrumental blank. The contribution of atmospheric ^{136}Xe in those analyses releasing the most gas was less than 1 part in 300 (fig. S4). The actual fission compositions were calculated by subtracting these minor amounts of atmospheric xenon on the basis of the amount of ^{130}Xe.

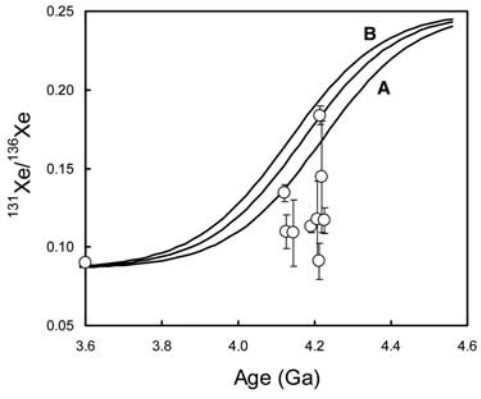

Fig. 2. A comparison of the measured $^{131}Xe/^{136}Xe$ ratios in zircons with the calculated dependence on closure age and Pu/U ratio for xenon produced by the spontaneous fission of ^{244}Pu and ^{238}U. Meteorite analyses suggest that the solar system's initial $^{244}Pu/^{238}U$ ratio at 4560 Ma is in the interval from 0.004 (curve A) to 0.008 (curve B). $^{131}Xe/^{136}Xe$ ratios for two zircons with concordant U-Pb ages lie within the predicted range. Data lying below the theoretical curves are from zircons with discordant U-Pb ages, probably as a result of xenon loss during early metamorphism.

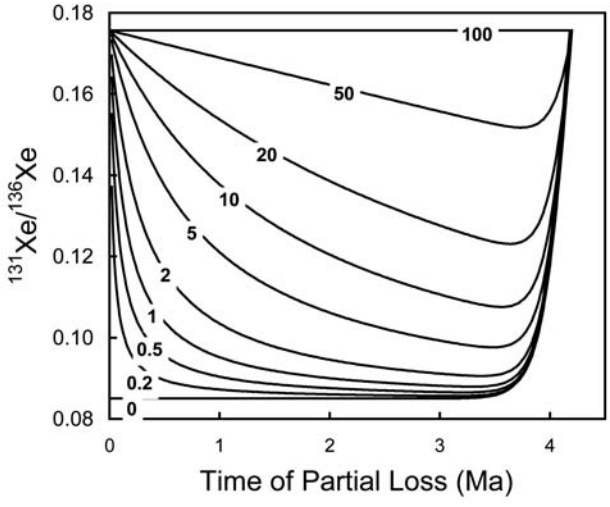

Fig. 3. Theoretical curves for the dependence of $^{131}Xe/^{136}Xe$ on time of partial Xe loss due to a postcrystallization event. The curves assume a crystallization age of 4200 Ma and initial $^{244}Pu/^{238}U$ = 0.006. The numbers on the curves indicate the percentage of xenon retained by the zircon after the loss event. The $^{131}Xe/^{136}Xe$ ratio is most sensitive to loss around 3600 Ma, when ^{244}Pu has fully decayed and maximum time is available for the subsequent buildup of xenon from ^{238}U fission.

The mass spectrum of the ca. 3600-My-old zircon was, as expected, that of ^{238}U fission and, within uncertainty, showed no contribution from fission of ^{244}Pu. The spectra of xenon released from the older zircons demonstrated the presence of varying proportions of ^{244}Pu fission (Fig. 1). The fissiogenic $^{131}Xe/^{136}Xe$, $^{132}Xe/^{136}Xe$, and $^{134}Xe/^{136}Xe$ ratios lie on mixing lines connecting ^{238}U and ^{244}Pu fission xenon. The highest $^{131}Xe/^{136}Xe$ ratio, 0.184 ± 0.006 at 4215 Ma, is obtained for a zircon (sample ANU07 8,2) with concordant $^{206}Pb/^{238}U$ and $^{207}Pb/^{235}Pb$ ages and corresponds to an initial Pu/U ratio of 0.0066 ± 0.0010, intermediate between the extreme meteorite estimates. A second zircon (Cu10 6,1) with U/Pb ages differing by 40 My (i.e., 99% concordant) has an inferred Pu/U ratio of 0.0038 ± 0.006. The remaining zircons have more discordant U/Pb ages (97% to 24%) and $^{131}Xe/^{136}Xe$ ratios below the values anticipated from the meteorite Pu/U estimates (Fig. 2). The inferred Pu/U ratios are 0.002 or less (Table 1). This could be the result of preferential loss of the earlier-formed Pu xenon or the result of chemical fractionation of Pu and U during or before the formation of the zircons.

Correlation between the Pu/U ratios and Pb/U discordance (Table 1) is most readily explained by xenon loss. In recent stepped heating experiments on 3.8-Gy-old zircons from West Greenland, fission Xe was released at temperatures above 1400°C (*17*), probably reflecting the disproportionation of

Table 1. Xenon ratios for major gas releases. Isotope ratios are raw data uncorrected for air contribution. Concordance was defined as 100% minus the percent difference of $^{206}Pb/^{238}U$ and $^{207}Pb/^{206}Pb$ ages. Cu 10 6,1 and ANU07 8,2 are grains with Pu/U ≥ 0.004. Numbers in parentheses are errors in the most significant figures.

Zircon	Age concordance (Ma)		^{136}Xe (atoms)	$^{130}Xe/^{136}Xe$	$^{131}Xe/^{136}Xe$	$^{132}Xe/^{136}Xe$	$^{134}Xe/^{136}Xe$	Pu/U (range)
Cu10 5,9	3600		298,000	0.001 (1)	0.097 (2)	0.589 (5)	0.829 (6)	
Cu10 9,8	4191 (9)	97%	176,000	0.000 (1)	0.110 (2)	0.626 (6)	0.841 (7)	0.0009 – 0.0012
Cu3 6,8	4125 (9)	95%	62,000	0.000 (2)	0.109 (5)	0.611 (10)	0.837 (12)	0.0008 – 0.0025
Cu10 6,1	4122 (7)	99%	152,000	0.000 (1)	0.137 (3)	0.667 (7)	0.850 (8)	0.0033 – 0.0044
FC30 9.3	4140 (13)	97%	43,600	0.009 (4)	0.153 (9)	0.677 (17)	0.855 (19)	<0.0029
ANU07 8,2	4215 (4)	100%	257,000	0.009 (1)	0.226 (3)	0.804 (7)	0.892 (7)	0.0056 – 0.0077
			55,000	0.077 (5)	0.524 (15)	1.101 (22)	0.930 (18)	0.0007 – 0.0061
FC12 5,6	4218 (8)	24%	191,000	0.003 (1)	0.131 (4)	0.641 (8)	0.837 (9)	0.0007 – 0.0013
ANU09 14,5	4212 (16)	97%	144,000	0.000 (2)	0.091 (6)	0.599 (13)	0.839 (17)	<0.0005
			63,000	0.000 (3)	0.117 (13)	0.646 (24)	0.848 (29)	<0.0023

zircon into baddelyite and silica. Comparison of U-Xe and U-Pb ages (*24*) suggests that Xe is at least as strongly retained as Pb. Nevertheless, Pb loss associated with metamictization is commonly observed in zircons (*25*), and, given the antiquity and complex history of the ancient detrital zircons, it is likely that loss of Xe will also have occurred in a portion of our samples.

We have developed a two-stage model to show how the $^{131}Xe/^{136}Xe$ ratios are affected by Xe loss during diffusion or recrystallization events and provide an illustration for zircons with a crystallization age of 4.2 Gy and initial Pu/U = 0.006 (Fig. 3). Early events cause the loss of predominantly Pu-fission xenon, and the subsequent buildup is dominated by xenon from U. In consequence, the present-day $^{131}Xe/^{136}Xe$ ratio is lowered, reaching a minimum for loss occurring around 3.5 to 3.8 Ga. As the time of Xe loss approaches the present, the short time available for U fission ingrowth relative to the amount of Pu xenon results in measured $^{131}Xe/^{136}Xe$ ratios that approach the value they would have if no loss had occurred. The $^{131}Xe/^{136}Xe$ ratio is thus most sensitive to Xe loss during Archean events. This suggests that the low $^{131}Xe/^{136}Xe$ ratios in the discordant Jack Hills zircons may be the result of events before the formation of the Jack Hills metasediments. To be more definitive requires an additional relationship between the time of Xe loss and the degree of loss. Such a relationship can in principle be provided by the simultaneous determination of U-Xe ages.

We have detected Xe with an isotopic composition characteristic of the spontaneous fission of ^{244}Pu in individual 4.1- to 4.2-Gy-old detrital zircons. The initial Pu/U ratios, at 4.56 Ga, implied by our analyses range from essentially zero to 0.0066 between individual zircons. This is probably the result of Xe loss during subsequent metamorphic processes, e.g., those associated with formation of the host metasediments. Combining the present procedures with U-Xe dating methods has the potential to date these early metamorphic processes. The highest implied Pu/U ratio is within the range of estimates from meteorites, but, in order to quantify a global Pu/U ratio for the early Earth, future work will require an improved understanding of the geochemical behavior of Pu relative to U and the rare earth elements in zircon crystallization.

References and Notes

1. B. S. Meyer, D. D. Clayton, *Space Sci. Rev.* **92**, 332 (2000).
2. D. D. Clayton, *Astrophys. J.* **268**, 381 (1983).
3. G. J. Wasserburg, M. Busso, R. Gallino, *Astrophys. J.* **466**, L109 (1996).
4. S. Goriely, M. Arnould, *Astron. Astrophys.* **379**, 1133 (2001).
5. A. G. W. Cameron, F.-K. Thielemann, J. J. Cowan, *Phys. Rep.* **227**, 283 (1993).
6. T. Staudacher, C. J. Allegre, *Earth Planet. Sci. Lett.* **60**, 389 (1986).
7. C. J. Allegre *et al.*, *Nature* **303**, 762 (1983).
8. C. J. Allegre *et al.*, *Earth Planet. Sci. Lett.* **81**, 127 (1986).
9. R. K. O'Nions, I. N. Tolstikhin, *Earth Planet. Sci. Lett.* **124**, 131 (1994).
10. D. Porcelli, G. J. Wasserburg, *Geochim. Cosmochim. Acta* **59**, 4921 (1995).
11. J. Kunz, T. Staudacher, C. J. Allegre, *Science* **280**, 877 (1998).
12. G. B. Hudson, B. M. Kennedy, F. P. Podosek, C. M. Hohenberg, *Proc. Lunar Planet. Sci. Conf.* **19**, 547 (1989).
13. G. W. Lugmair, K. Marti, *Earth Planet. Sci. Lett.* **35**, 273 (1977).
14. F. Shukolyukov, F. Begemann, *Geochim. Cosmochim. Acta* **60**, 2453 (1996).
15. Y. N. Miura, K. Nagao, N. Sugiura, T. Fujitani, P. H. Warren, *Geochim. Cosmochim. Acta* **62**, 2369 (1998).
16. P. Pellas, C. Fieni, M. Trieloff, E. K. Jessberger, *Geochim. Cosmochim. Acta* **61**, 3477 (1997).
17. M. Honda, A. P. Nutman, V. C. Bennett, *Earth Planet. Sci. Lett.* **207**, 69 (2003).
18. D. O. Froude *et al.*, *Nature* **304**, 616 (1983).
19. S. A. Wilde, J. W. Valley, W. H. Peck, C. M. Graham, *Nature* **409**, 175 (2001).
20. S. J. Mojzsis, T. M. Harrison, R. T. Pidgeon, *Nature* **409**, 178 (2001).
21. T. M. Harrison, S. J. Mojzsis, *Geochim. Cosmochim. Acta* **67**, A135 (2003).
22. J. D. Gilmour, I. C. Lyon, W. A. Johnston, G. Turner, *Rev. Sci. Inst.* **65**, 617 (1994).
23. Materials and methods are available as supporting material on *Science* Online.
24. Yu. A. Shukolyukov, A. P. Meshik, D. P. Krylov, O. V. Pravdivtseva, in *Noble Gas Geochemistry and Cosmochemistry*, J. Matsuda, Ed. (Terra Science, Tokyo, 1994), p. 125.
25. T. E. Krogh, *Geochim. Cosmochim. Acta* **46**, 637 (1982).

26. This work was supported by grants from Particle Physics and Astronomy Research Council (G.H.), the Australian Research Council, NSF Division of Earth Sciences Infrastructure and Facilities program (T.M.H.) and NASA Exobiology Program (S.J.M.). Technical help from A. Busfield and R. Mohapatra in the RELAX laboratory is gratefully appreciated.

Supporting Online Material

www.sciencemag.org/cgi/content/full/306/5693/89/DC1
Materials and Methods
Figs. S1 to S4

2 June 2004; accepted 13 August 2004

Geochemical Evidence for Excess Iron in the Mantle Beneath Hawaii

Munir Humayun,[1,2]* Liping Qin,[1] Marc D. Norman[3]

Chemical interaction of Earth's mantle with the liquid outer core should influence the mantle's iron content. Osmium isotope ratios in Hawaiian lavas indicate a mass flux of ≤1% core to the mantle, which is the immediate source of these lavas. We present precise measurements of the Fe/Mn ratio for Hawaiian lavas, revealing an increase of 1 to 2% in the mole fraction of iron in the mantle beneath Hawaii. This corresponds to a density anomaly of about 0.5%, about the same magnitude observed in seismic tomography models of the Pacific superswell region. These data also rule out a role for Mn-rich sediments as the source of the Hawaiian Os isotope signal.

On the basis of geophysical evidence, some mantle plumes are argued to arise from the core-mantle boundary (CMB). Chemical interaction between the core and the mantle at the CMB may involve physical entrainment of differentiated outer core (*1*), disequilibrium chemical reactions (*2*), equilibrium chemical reactions (*3*, *4*), isotopic exchange (*5*), or exsolution of a light element component during inner core growth (*4*, *6*), each of which may impart distinct isotopic and chemical signatures to the adjacent mantle. Assuming that the effects of chemical interaction are localized to mantle adjacent to the CMB, plumes arising from the CMB may entrain mantle that has experienced core-mantle interaction and advect such chemical signatures to the surface where they may be detected in the chemistry of erupted lavas. Osmium isotopic composition of Hawaiian picrites has provided the best indication for the entrainment of differentiated outer core material in the source of the Hawaiian plume, implying a mass flux ≤1% by weight (*1*). The absence of unradiogenic $^{182}W/^{184}W$ in the Hawaiian picrites, however, has been taken as evidence against core-mantle interaction (*7*). It has also been used to support the suggestion that the observed Re-Pt-Os isotope systematics (*1*) can be explained by the recycling of surficial Mn sediments (with high Pt/Os and Pt/Re ratios) into the source of the Hawaiian plume (*7*, *8*). Evidence of Mn enrichment was not found in Gorgona Island komatiites, which exhibited coupled ^{186}Os-^{187}Os isotope variations (*9*).

Iron, the dominant constituent of the core, is probably the most important element with a geochemical cycle that can be affected by exchange across the CMB. The Fe flux is of primary concern in geodynamic models, because it influences the density of the mantle (*10*–*12*). The constant molar 100 Mg/Mg+Fe (Mg#) is 89 ± 2 (1σ) of

[1]Department of the Geophysical Sciences, 5734 South Ellis Avenue, Chicago, IL 60637, USA. [2]National High Magnetic Field Laboratory and Department of Geological Sciences, Florida State University, Tallahassee, FL 32310, USA. [3]Research School of Earth Sciences, Australian National University, Canberra ACT 0200, Australia.

*To whom correspondence should be addressed. E-mail: humayun@magnet.fsu.edu

primitive mantle xenoliths, which implies that the upper mantle contains 6.26 ± 0.63% (1σ) Fe as FeO dissolved in minerals (*13*). From seismic tomography and mineral physics constraints, the lower mantle is inferred to possibly contain 10 to 20% higher Fe (*10*–*12*). The inferred excess Fe may be primordial (*4*), the result of recycling of Fe-rich crust (*10*), or the result of Fe exchange across the CMB (*11*). Notably, the present uncertainties (10%, 1σ) assigned to upper mantle Fe abundances are comparable to the expected excess Fe in lower mantle derived plumes. Geochemical evidence for excess Fe in mantle-derived melts has been further limited by chemical fractionation of Fe from Mg and other elements during partial melting and fractionation (*14*). Here, we present a refined method that uses Fe/Mn ratios to determine excess Fe abundances in the sources of mantle-derived magmas.

Because most of the Fe in the mantle is Fe^{+2} (FeO) and all of the Mn is Mn^{+2} (MnO), Fe and Mn share the same charge and have a similar ionic radius, the two properties that most influence the partitioning behavior of elements in magmatic processes. During partial melting and fractional crystallization, the abundance of Mn^{+2} follows that of Fe^{+2}, so the Fe/Mn ratio should remain approximately constant. The coherence of the Fe and Mn geochemical cycles in the mantle is not followed by sedimentary processes or by core-mantle interaction, because Fe or Mn occurs in other valence states. A global suite of mantle peridotites yields Fe/Mn = 60 ± 10 (1σ) (*13*), whereas a similar comparison of basalts yields Fe/Mn = 59 ± 9 (1σ) (*15*). The scatter of existing measurements of the Fe/Mn ratio in basalts from a single tectonic setting conceals the variations predicted by geophysical models. Because a substantial part of this scatter may be due to analytical artifacts (*15*), a new technique based on inductively coupled plasma mass spectrometry (ICP-MS) has been developed for the precise (±0.5%) determination of the Fe/Mn ratio of fresh basalts (*16*).

Our measurements resolve Hawaiian picrites from mid-ocean ridge basalts (MORBs) or Icelandic picrites (Fig. 1A). Unlike radiogenic isotope ratios, the Fe/Mn ratio may be affected by the degree of partial melting, the residual mantle mineralogy, and the extent of olivine fractionation or accumulation experienced by the lavas. Given that olivine has a higher Fe/Mn ratio, olivine removal from the melt should decrease the Fe/Mn ratio of erupted lava, whereas olivine accumulation should increase the Fe/Mn ratio. One test of the precision of the data is to observe Fe/Mn variations associated with olivine fractionation (Fig. 1B; data are plotted individually for each volcano). Using estimates of the MgO content of primary magma (magma composition before crystal fractionation or accumulation) (*17*), we determined the primary magma Fe/Mn ratio (Table 1). The excess Fe/Mn in Hawaiian picrites relative to MORB is not the result of olivine accumulation, given that Icelandic picrites with the same MgO range as Hawaiian picrites show Fe/Mn similar to MORBs, and three Kilauea basalts also exhibit an Fe/Mn > 65. Furthermore, Fig. 1 shows that the high Fe/Mn ratio is characteristic of picrites and basalts from Loihi, Kilauea, Mauna Kea, Mauna Loa, Hualalai, Kohala, and Koolau (i.e., the entire Hawaiian plume).

Explanations of the radiogenic $^{186}Os/^{188}Os$ ratios in terms of recycling of Mn-rich sediments (*7*, *8*) imply that Fe/Mn ≤ 40, substantially lower than the mantle value of 60. Mixing models involving Mn-sediment

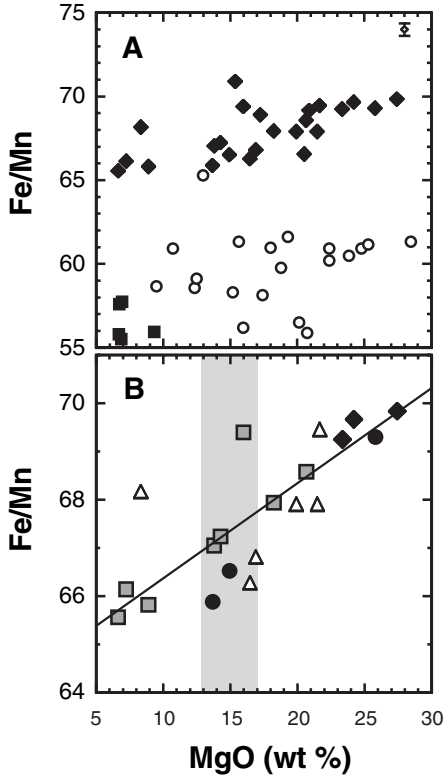

Fig. 1. (**A**) Fe/Mn determined by ICP-MS versus MgO for Hawaiian lavas (diamonds), Icelandic picrites (circles), and MORB glasses (squares). A representative error bar (2σ) (open diamond) is shown in the upper right-hand corner. (**B**) An expansion of the scale for the Hawaiian lavas, showing suites for which three or more samples from the same volcano were analyzed: Kilauea (squares), Loihi (diamonds), Mauna Loa (triangles), and Hualalai (circles). Each suite forms an olivine fractionation or accumulation trend; Kil 1-7 and MLKAH-4 deviate from the trends for no apparent reason. The shaded field depicts the range of estimated primitive melt MgO contents for the Hawaiian picrites (*17*).

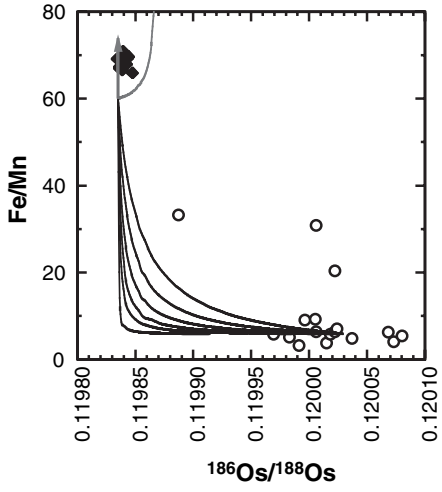

Fig. 2. Fe/Mn versus $^{186}Os/^{188}Os$ (*1*) for the Hawaiian picrites (black diamonds) compared with model predictions for mixing between recycled Mn-rich sediment (black curves), outer core (gray curves), and normal mantle. The Pt/Os ratios of the Troodos umbers (*7*) were used to calculate the $^{186}Os/^{188}Os$ ratios for these sedimentary compositions after 2 Ga of radiogenic ingrowth (circles). Mixing lines were calculated between average sediment [6.5% Mn, Fe/Mn = 5.8, Os = 230 parts per trillion (ppt) (*7*), $^{186}Os/^{188}Os$ = 0.12003], and peridotite [Mn = 0.1045%, Fe/Mn = 60 (*13*); Os = 3800 ppt, $^{186}Os/^{188}Os$ = 0.1198345 (*1*)] or picrite [Mn = 0.13%, Fe/Mn = 60, $^{186}Os/^{188}Os$ = 0.1198345 (*1*, *17*)] and are hyperbolic concave downward. The most hyperbolic curve is that for normal mantle, with successive picrite curves for 800, 400, 200, 100, and 50 ppt Os, respectively. Mixtures between mantle and outer core [parameters from (*9*, *13*)] are shown as gray curves. The Fe/Mn > 65 for Hawaiian picrites are compatible with a combination of FeO metasomatism (gray vertical arrow) and outer core admixture (gray hyperbola).

Table 1. Fe/Mn (weight ratio) corrected for olivine gain/loss, mole fraction of Fe, Mg#, and density anomaly, inferred in the source of Hawaiian volcanoes (*16*). δX_{Fe}, the anomaly in the mole fraction of Fe; PUM, primitive upper mantle.

	Fe/Mn	X_{Fe}	δX_{Fe}	Mg#	δρ/ρ (%)
Kilauea	67.4 ± 0.4	0.1189 ± 6	0.017	88.11 ± 0.06	+0.55 ± 0.06
Mauna Loa	65.8 ± 0.9	0.1164 ± 14	0.015	88.36 ± 0.14	+0.47 ± 0.07
Hualalai	66.4 ± 0.5	0.1173 ± 8	0.016	88.27 ± 0.08	+0.50 ± 0.06
Iceland	59.5 ± 1.5	0.1064 ± 24	0.005	89.36 ± 0.24	+0.15 ± 0.10
MORB	56.5 ± 1.1	0.1016 ± 18	≡0	89.84 ± 0.18	≡0
PUM (*13*)	60 ± 10	0.107 ± 16	0.006	89.3 ± 1.6	+0.18 ± 0.51

recycling/assimilation by peridotite, picrites, or basalts fail to increase the $^{186}Os/^{188}Os$ ratio without lowering the value of Fe/Mn (Fig. 2).

Three hypotheses may explain the elevated Fe/Mn value of Hawaiian lavas relative to MORB or Icelandic picrites: (i) partial melting of low-olivine mantle, (ii) pyroxenite melt contributions, and (iii) Fe flux across the CMB. To assess the effect of mineralogical control on the Fe/Mn ratio of mantle melts, Fig. 3A shows the partition coefficients (D) for Fe and Mn in major phases for experimental melts of garnet peridotite (*18*). Both D(Fe) and D(Mn) are <1 in all phases (i.e., both elements are mildly incompatible). Olivine exhibits D(Fe) > D(Mn), garnet and clinopyroxene exhibit the reverse effect, and orthopyroxene is intermediate in its Fe/Mn preference. Thus, melts derived from spinel and garnet peridotites exhibit an Fe/Mn value slightly lower than that of their source region (between 55 and 58 versus 61) (Fig. 3, B and C). The presence of olivine in the residual mantle counterbalances the effect of garnet and clinopyroxene on the Fe/Mn ratio of the melt such that no systematic large deviations of the Fe/Mn ratio for mantle-derived melts occur (Fig. 3A). The proportions of garnet and clinopyroxene are important in controlling the abundances of the rare earth elements and are well estimated in the Hawaiian source (*17*). But the ratio of olivine to orthopyroxene is not similarly constrained, so if the Hawaiian source were substantially more Si-rich (<25% olivine in the source), then the resulting partial melts could exhibit higher Fe/Mn ratios. However, no other evidence supports a Si-rich mantle, with the exception of Koolau (*17*).

Recycling of MORB crust (Fe/Mn ~ 55 to 58) should not increase the Fe/Mn value of the source, but could increase the Fe/Mn ratio of partial melts derived from pyroxenite veins due to mineralogical control by clinopyroxene and garnet. Experimental studies of the partial melting of MORB-composition pyroxenites (*19*, *20*) show that the Fe/Mn value of pyroxenite melts decreases as the degree of partial melting increases; melts formed by over 60% partial melting (MgO > 5%) show no deviation from their source composition (Fig. 3C). However, because peridotite melting only begins at temperatures at which such pyroxenites are over 60% melted (*19*), pyroxenite partial melts cannot contribute substantially to the high Fe/Mn ratio of the Hawaiian picrites. Silica-undersaturated pyroxenite melts (*21*) provide a more potent end-member. The addition of 25% of melt V162 (*21*) to basalt with Fe/Mn ~ 58 produces a liquid with Fe/Mn ~ 66. However, the amount of pyroxenite contribution to the sources of the various Hawaiian picrites was estimated from trace element abundances to be negligible for all but the Koolau lavas, in which it is <10% (*17*). No systematic difference of Fe/Mn between Koolau and other lavas can be discerned (fig. S2), indicating that the effect of pyroxenite melting on the Fe/Mn ratio is minor. It must be concluded that the high Fe/Mn value is a feature of the source composition and not of the melting process.

Oxygen (as FeO) is a likely candidate for the light element in the core (*22*). The exchange of FeO between the core and the lower mantle may occur during core formation processes as FeO-saturated melts percolate through the lower mantle (*4*), or FeO may exsolve from the outer core as the inner core grows (*5*, *23*), creating the seismic anomalies observed at the CMB (*11*, *24*). For the outer core, Fe/Mn > 170 (*13*). Thus, FeO exchange between the liquid outer core occurring either in the ancient Earth, or actively over time, would impart a high Fe/Mn to regions of the lower mantle. The Hawaiian plume may have entrained small amounts of a FeO-rich layer from the CMB (*25*) or entrained lower mantle with primordially high FeO contents (*4*, *10*). This raises an important question: Why is the Fe/Mn ratio not correlated with radiogenic $^{186}Os/^{188}Os$ ratios observed in the picrites?

Both modern liquid outer core and ancient percolating melts may be composed of an FeO-FeS-Fe liquid (*22*), which would react with the lower mantle mineralogy (Mg perovskite and ferropericlase). Reactions between a FeO-FeS-Fe liquid and ferropericlase can be written in a simplified form as

$$(\text{Fe-FeS-FeO})_{\text{liquid}} + (\text{Mg, Fe})\text{O}_{\text{solid}} \rightarrow (\text{Fe-FeS})_{\text{liquid}} + (\text{Mg, Fe}')\text{O}_{\text{solid}} \quad (1)$$

where the prime indicates a solid solution richer in FeO. Because oxygen is only

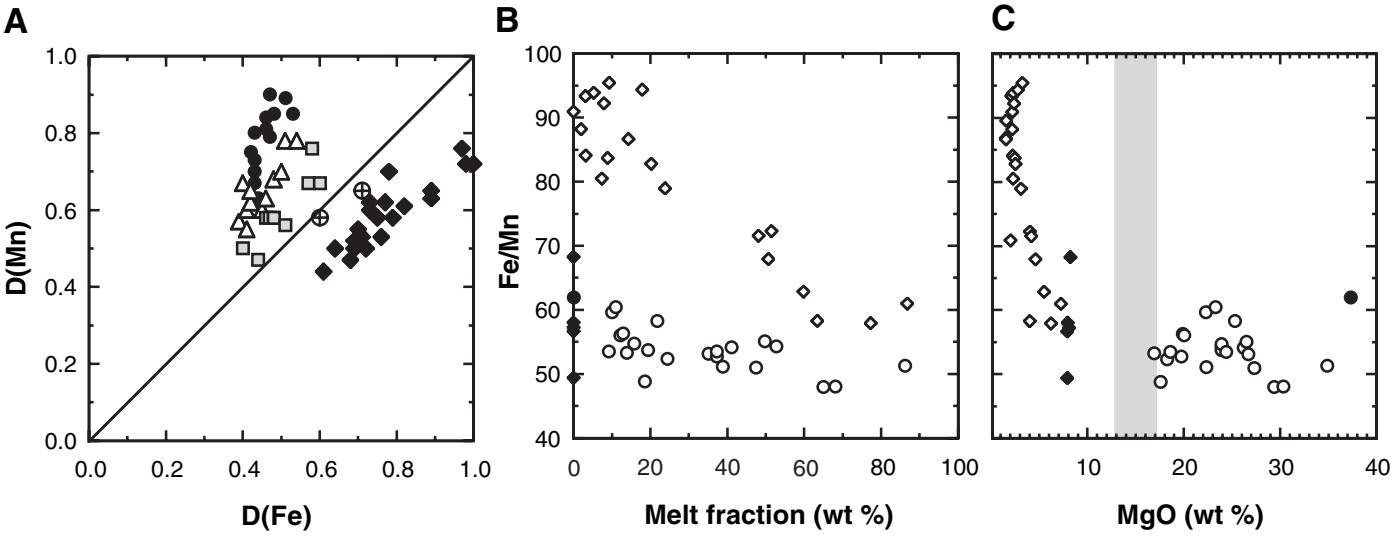

Fig. 3. (**A**) Partition coefficients for Fe versus Mn in olivine (diamonds), orthopyroxene (squares), clinopyroxene (triangles), and garnet (circles) from experimental melting of garnet peridotite (*18*). Bulk partitioning for peridotite compositions with 55% olivine, 25% orthopyroxene, 10% clinopyroxene, and 10% garnet is shown for two runs in which all four minerals and liquids were present (circled crosses). Note the Mn preference of garnet and clinopyroxene, the Fe preference of olivine, and the tendency of the bulk Ds to plot near the 1:1 line. (**B**) Fe/Mn of experimental partial melts versus melt fraction: garnet peridotite melts (open circles) and their starting composition (solid circle) (*18*), pyroxenite melts (open diamonds) and their starting compositions (solid diamonds) (*20*). (**C**) Fe/Mn for experimental partial melts versus MgO for garnet peridotite (*18*) and pyroxenite (*20*) [symbols as in (B)]. The shaded gray region is the MgO range estimated for primitive Hawaiian picrite melts (*17*). High-degree (>60%) pyroxenite partial melts and all peridotite partial melts exhibit Fe/Mn < 60.

slightly soluble in iron metal at the pressure of the CMB (*23*), Reaction 1 represents a net transfer of FeO to ferropericlase. The residual Fe-FeS liquid is probably immiscible with the lower mantle and either drains back to the core or crystallizes within the lower mantle as Fe-FeS veins. Thus, large regions of the lower mantle may be metasomatized by FeO-bearing liquids creating high Fe/Mn sources, with siderophile Os [and hence the outer core $^{186}Os/^{188}Os$ signature (*1*)] heterogeneously distributed within the source as veins. Because tungsten has a lower preference for solid metal than does Os (*26*), W and Os could be decoupled by fractional crystallization of the Fe-FeS melts. Thus, coupling between $^{182}W/^{184}W$, $^{186}Os/^{188}Os$, and Fe/Mn is not a prerequisite for evidence of core-mantle interaction.

Seismic studies indicate a correlation between ultralow-velocity zones (ULVZs) at the CMB, interpreted to be regions of partial melt, and the distribution of hot spots at the surface (*27*). There also appear to be rigid zones at the top of the core that correspond with ULVZs in the CMB region (*28*) that may be sites of FeO release from the core (*5*). Thus, the sources of mantle plumes originating from the CMB may have been affected by FeO metasomatism. This is the most tenable explanation at present for the observed excess of Fe/Mn in the Hawaiian lavas. Notably, Iceland neither is associated with a ULVZ (*29*) nor exhibits high Fe/Mn.

Table 1 shows that the observed Fe/Mn ratio in the Hawaiian lavas corresponds to a lower Mg# (88) than average upper mantle (Mg# = 89). This Mg# is within the 1σ range of measured Mg#'s of upper mantle peridotites [89 ± 2 (*13*)]. The higher FeO content implies a higher density, +0.5% relative to MORB mantle. This density contrast is about twice that estimated from seismic tomography models (*12*) but is sensitive to the choice of MORB Fe/Mn for normalization (Table 1). It is important to observe that our estimate of the density anomaly $\delta\rho/\rho$ does not include the effect of Fe enrichment due to recycling crust with a Fe/Mn ~ 60 because this contribution is not resolved by our technique. However, core-mantle interaction appears to have added enough FeO to the Hawaiian plume source to account for some (*10*) or all (*11*, *12*) of the geophysically observed density excess in the lower mantle. Thus, Fe/Mn analysis of hot spot lavas provides geochemical "ground truth" to geodynamical models of mantle circulation based on seismic tomography (*12*, *29*).

References and Notes

1. A. D. Brandon, M. D. Norman, R. J. Walker, J. W. Morgan, *Earth Planet. Sci. Lett.* **174**, 25 (1999).
2. E. Knittle, R. Jeanloz, *Science* **251**, 1438 (1991).
3. D. Walker, *Geochim. Cosmochim. Acta* **64**, 2897 (2000).
4. D. C. Rubie, C. K. Gessmann, D. J. Frost, *Nature* **429**, 58 (2004).
5. I. S. Puchtel, M. Humayun, *Geochim. Cosmochim. Acta* **64**, 4227 (2000).
6. B. Buffett, E. J. Garnero, R. Jeanloz, *Science* **290**, 1338 (2000).
7. A. Schersten, T. Elliott, C. Hawkesworth, M. Norman, *Nature* **427**, 234 (2004).
8. G. Ravizza, J. Blusztajn, H. M. Prichard, *Earth Planet. Sci. Lett.* **188**, 369 (2001).
9. A. D. Brandon *et al.*, *Earth Planet. Sci. Lett.* **206**, 411 (2003).
10. L. H. Kellogg, B. H. Hager, R. D. van der Hilst, *Science* **283**, 1881 (1999).
11. E. J. Garnero, *Annu. Rev. Earth Planet. Sci.* **28**, 509 (2000).
12. A. M. Forte, J. X. Mitrovica, *Nature* **410**, 1049 (2001).
13. W. F. McDonough, S.-s. Sun, *Chem. Geol.* **120**, 223 (1995).
14. C. H. Langmuir, G. N. Hanson, *Philos. Trans. R. Soc. London Ser. A* **297**, 383 (1980).
15. A. Ruzicka, G. A. Snyder, L. A. Taylor, *Geochim. Cosmochim. Acta* **65**, 979 (2001).
16. Materials and methods are available as supporting material on *Science* Online.
17. M. D. Norman, M. O. Garcia, *Earth Planet. Sci. Lett.* **168**, 27 (1999).
18. M. J. Walter, *J. Petrol.* **39**, 29 (1998).
19. M. Pertermann, M. M. Hirschmann, *J. Geophys. Res.* **108**, 2125, 10.1029/2000JB000118 (2003).
20. M. Pertermann, M. M. Hirschmann, *J. Petrol.* **44**, 2173 (2003).
21. T. Kogiso, M. M. Hirschmann, D. J. Frost, *Earth Planet. Sci. Lett.* **216**, 603 (2003).
22. J.-P. Poirier, *Phys. Earth Planet. Inter.* **85**, 319 (1994).
23. Experimental results of Rubie *et al.* (*4*) were extrapolated to 128 to 136 GPa and 2600 to 3000K with the use of their equation 2 to obtain the molar metal-silicate partition coefficient, $K_d \leq 6 \times 10^{-4}$. Setting $X_{Fe}^{metal} \sim 1$, $X_{FeO}^{Mg\text{–}wüstite} \sim 0.2$, where X represents the mole fraction, in their definition of K_d yields $X_O^{metal} \leq 1 \times 10^{-4}$. These experiments imply that metallic liquids in equilibrium with lower mantle mineralogy should be very low in oxygen content and that FeO should be released from the core to the mantle at the CMB, if oxygen is present in the outer core at 9 weight percent (wt %) (FeO = 40 wt %) (*22*).
24. T. Lay, Q. Williams, E. J. Garnero, *Nature* **392**, 461 (1998).
25. A. M. Jellinek, M. Manga, *Nature* **418**, 760 (2002).
26. N. L. Chabot, A. J. Campbell, J. H. Jones, M. Humayun, C. B. Agee, *Meteoritics Planet. Sci.* **38**, 181 (2003).
27. Q. Williams, J. Revenaugh, E. Garnero, *Science* **281**, 546 (1998).
28. S. Rost, J. Revenaugh, *Science* **294**, 1911 (2001).
29. A. M. Jellinek, M. Manga, *Rev. Geophysics*. **42**, RG3002, 10.1029/2003RG000144 (2004).

30. We thank S. Sorenson (Smithsonian Institution) and A. T. Anderson for providing samples; A. J. Campbell for support on the Element; and A. D. Brandon, B. Buffett, M. Hirschmann, and C. Langmuir for comments and discussions. Constructive reviews by C.-T. Lee and P. Reiners are gratefully acknowledged. NSF EAR-0309786 (M.H.) supported this work.

Supporting Online Material

www.sciencemag.org/cgi/content/full/306/5693/91/DC1
Materials and Methods
Figs. S1 and S2
Tables S1 and S2
References

3 June 2004; accepted 17 August 2004

Toroidal Triblock Copolymer Assemblies

Darrin J. Pochan,[1]* Zhiyun Chen,[2]† Honggang Cui,[1]† Kelly Hales,[1]† Kai Qi,[2]† Karen L. Wooley[2]*

A stable phase of toroidal, or ringlike, supramolecular assemblies was formed by combining dilute solution characteristics critical for both bundling of like-charged biopolymers and block copolymer micelle formation. The key to toroid versus classic cylinder micelle formation is the interaction of the negatively charged hydrophilic block of an amphiphilic triblock copolymer with a positively charged divalent organic counterion. This produces a self-attraction of cylindrical micelles that leads to toroid formation, a mechanism akin to the toroidal bundling of semiflexible charged biopolymers such as DNA. The toroids can be kinetically trapped or chemically cross-linked. Insight into the mechanism of toroid formation can be gained by observation of intermediate structures kinetically trapped during film casting.

Simple self-assembly methods can produce a broad range of intricate bioinspired nanostructures from synthetic block copolymers in dilute solution. For example, robust vesicles have been constructed from amphiphilic diblock copolymers (*1*–*3*). By using block copolymers instead of low–molecular weight lipid amphiphiles, direct control over the membrane thickness is achieved and the ultimate toughness of the vesicle is consequently enhanced (*1*, *4*). Similarly, cylindrical micelles exhibit stiffness behavior that is directly dependent on the core chemistry (*5*) or chain length (*6*). Such cylindrical structures have been designed to display specific coronal chemistry for biomimetic inorganic phase nucleation (*7*, *8*). Many examples of spherical micellar assemblies also exist in which the particle size and function can be controlled by means of block copolymer segment designs (*9*). In addition to the classic geometries of sphere, cylinder, and bilayer membrane, dilute block copolymers

[1]Materials Science and Engineering and Delaware Biotechnology Institute, University of Delaware, Newark, DE 19716, USA. [2]Center for Materials Innovation and Department of Chemistry, Washington University in Saint Louis, One Brookings Drive, CB 1134, Saint Louis, MO 63130, USA.

*To whom correspondence should be addressed.
†These authors contributed equally to this work.

can create a diverse catalog of geometries, including helices (*10*), cylindrical networks (*11*, *12*), nanotubes (*13*, *14*), the hollow hoop (*15*), and the bowl-shaped micelle (*16*). This complexity is prominent when the assembly occurs in solvent mixtures (*13*, *15*–*17*).

Nature produces complex intermolecular structure with biomolecules, namely peptides and nucleic acids, through the control of biomolecular primary, secondary, tertiary, and quaternary structure. The presence of electrostatic charge in biomolecular primary structure provides natural systems with a molecular-level tool to control intramolecular conformation (secondary and tertiary structure) and intermolecular aggregation (quaternary structure) over nanoscopic and microscopic dimensions. Charged biopolymer organization, such as DNA (*18*) or f-actin (*19*), is being studied in order to understand in vivo processes, including DNA compaction and storage in the chromosome, or to develop bioinspired vehicles for gene therapy delivery, such as DNA/lipid complexes (*20*, *21*). A key factor in controlling the final charged biopolymer assembly structure is counterion valency. In DNA, multivalent counterions, including heavy metal salts or oligoamines, can produce hexagonally close-packed DNA at almost crystalline DNA densities (*22*). Importantly, when the DNA is in the presence of multivalent counterions and is sufficiently dilute (in order to prevent lateral intermolecular association), chains close-pack locally but produce toroidal bundles on the length scale of one-hundred to several hundred nanometers. This toroidal bundle formation is due to the semiflexible nature of DNA; the large persistence length (~50 nm) prevents the complete collapse of the self-attractive molecules into a compact globule. The situation is slightly different in f-actin, a much stiffer chain that has a persistence length in excess of several micrometers. Counterion multivalency also produces attraction between like-charged, stiff f-actin chains. However, these attractive interactions primarily produce close-packed bundles of extended chains (*23*). In some cases, f-actin rings can be formed in the presence of multivalent counterions, but the rings are very large (diameters of more than several micrometers) relative to those formed by DNA. This is believed to be the consequence of the much higher bending stiffness of f-actin due to its much larger persistence length (*24*).

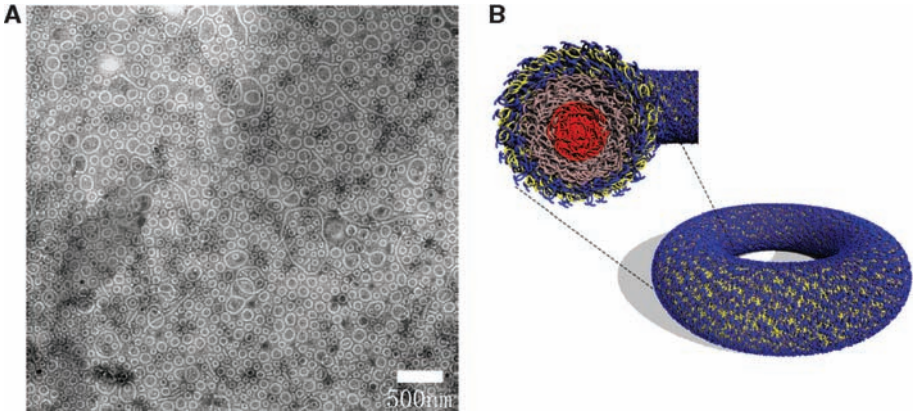

Fig. 1. (**A**) Low-magnification TEM image of toroidal micelle structure. This sample was cast from a solution with 0.1 wt % PAA_{99}-PMA_{73}-PS_{66} triblock copolymer, a THF:water volume ratio of 1:2, and an amine:acid molar ratio of 0.5:1 by addition of EDDA. The cast film was negatively stained with uranyl acetate. The toroidal micelles appear as light rings against a dark background. Although the micelle structure is overwhelmingly small rings (<200 nm in diameter), there exist a small minority of large rings, unclosed cylindrical micelles (appearing as white lines), and spherical micelles (appearing as light dots). (**B**) Cartoon schematic of toroidal micelle with cross section showing hydrophobic PS (red) and PMA (brown) core and hydrophilic PAA (yellow) corona with closely associated EDDA (blue).

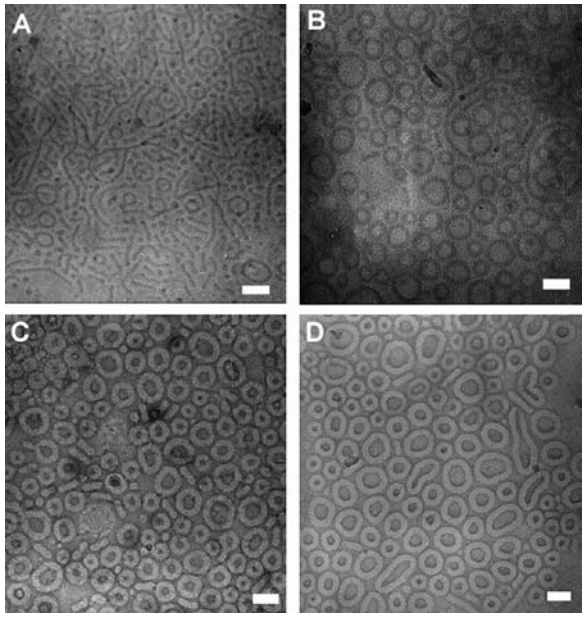

Fig. 2. TEM of PAA_{99}-PMA_{73}-PS_{66} micelles from 0.1 wt % triblock copolymer in solution of 1:2 by volume THF to water and 0.5:1 molar ratio of amine to acid. Scale bar, 100 nm. (**A**) CryoTEM of vitrified fresh solution showing mixture of cylindrical and spherical micelles with a small minority of toroids. The micelles appear dark against the vitrified solution background. (**B**) CryoTEM of the same solution as in (A) after allowing all of the THF to evaporate from the bulk solution showing predominantly a toroidal micelle structure. (**C**) Negatively stained TEM of a quickly cast film from solution in (A). Most of the micelles in (A) have transformed to toroidal micelles. (**D**) Negatively stained TEM of quickly cast film from solution in (B). The toroidal micelle structure is simply preserved on film casting.

We have combined synthetic block copolymer molecular design with solution conditions that favor self-attraction of charged semiflexible biopolymers to produce toroidal, or ring-shaped, micelles with a high degree of control and uniformity. The toroidal micelles are stable reproducible structures that are formed by the collapse of negatively charged cylindrical micelles, driven by interaction with a divalent organic cation. The assemblies are formed by a mixture of poly(acrylic acid–*b*–methyl acrylate–*b*-styrene) (PAA_{99}-PMA_{73}-PS_{66}) triblock copolymer amphiphile, water, tetrahydrofuran (THF), and 2,2′-(ethylenedioxy)diethylamine (EDDA). All four components are critical for toroid formation. Under optimized conditions, the toroidal phase is the predominant structure of the amphiphilic triblock copolymer, as seen from the low magnification transmission electron microscopy (TEM) micrograph of Fig. 1A, captured from a single layer of toroidal micelles drop cast from dilute suspension. Figure 1B illustrates the expected morphology that is generated in solutions composed predominantly of water; the hydrophobic PS and PMA are packaged within the core domain and are partially solvated by THF, and the hydrophilic PAA and hydrophilic but oppositely charged EDDA comprise the micelle corona.

A specific procedure was developed to produce the optimized conditions under which the toroids were formed and remained stable, ultimately in a mixture of water, THF, and EDDA. First, the triblock copolymer was allowed to dissolve in THF with a specific amount of EDDA that defined the molar ratio of amine:acid functionality between 0.5:1 and 1:1. Second, nanopure water was added dropwise to the solution with stirring

until the desired ratio of water to THF was reached. For eventual toroid formation, it was found that the water:THF volume ratio at this stage must be 1:1 < x < 4:1 and the polymer concentration should be dilute, with a value of <0.1 weight percent (wt %). The evaporation of THF from these solutions favored complete toroid formation and stability, but the THF was originally necessary for solvation of the core and transition between various assembly forms. The necessity for THF during supramolecular assembly transitions has been observed for vesicular fusion as well (*2*, *25*). Figure 2A contains cryoTEM data obtained from a solution with a volume ratio of water:THF = 2:1 and a molar ratio of amine:acid = 0.5:1. Under these conditions, a majority of cylinders were formed with only a minority of spherical and closed toroidal micelles. This low frequency of toroids has been observed in many cylindrical micelle systems (*11*, *26*, *27*). However, when the THF cosolvent was allowed to evaporate, a marked change in structure to predominantly toroids was observed. The THF was evaporated selectively by exposing the bulk solution to the laboratory atmosphere for several days, because THF has a considerably higher vapor pressure than that of water (129 mm Hg for pure THF versus 18 mm Hg for water at 20°C). CryoTEM data of the assemblies contained within the resulting aqueous suspension exhibited almost exclusively toroidal micelles (Fig. 2B). THF removal from the original suspension of Fig. 2A can be accelerated by casting a drop of micelle suspension directly onto a carbon-coated TEM sample grid. During drying over a period of 30 min, the THF again evaporated more rapidly than did the water. This allowed for reorganization of the assemblies into a thin film of overwhelmingly toroidal micelle structures (Fig. 2C). If a film of the suspension used for the cryogenic capture of the assemblies of Fig. 2B is cast directly onto a TEM grid and allowed to dry, then the toroid structure is preserved (Fig. 2D). Such stability suggests that the ring structure is kinetically trapped by the glassy state of the PS hydrophobic interior blocks of the toroids upon evaporation of the THF.

The mechanism of ring formation can be inferred by observing structures formed during the quick casting of films from water/THF suspensions (quickly going from the dominant cylindrical structure in Fig. 2A to the dominant toroidal structure in Fig. 2C). Although a majority of the structures formed by quick film casting are toroids, many intermediate structures (Fig. 3), rarely observed in cryoTEM experiments or in slowly evaporated solutions, are also formed. These structures include lariats, figure eights, dumbbells, and closed loops within the interior of cylindrical micelles, or combinations of these structures. In addition, cylinder ends that have come together but have not completely fused can be seen clearly because of the penetration of negative stain. These intermediates are dominated by trifunctional branch points as observed by Jain and Bates for nonionic diblock surfactants (*11*). However, unlike Jain and Bates, no network formation is observed, only toroidal micelles. The formation of intermediate structures and toroids appears to result from an identical mechanism, primarily the collapse of cylindrical micelles. This cylinder self-attraction is attributed to what can be considered the divalency of the oligodiamine EDDA [divalent cation at neutral pH in water resulting from primary amine p$K_a \approx 10$ (where K_a is the acid dissociation constant)] and the EDDA interaction with the carboxylates of the poly(acrylic acid) coronas (polyanionic at neutral pH in water with a p$K_a \approx 5$) of the cylindrical micelles. At amine:acid molar ratios of 0.5:1 to 1:1, the cylindrical micelles undergo a transition akin to the attractive toroidal bundling of DNA in the presence of multivalent counterions.

The cylinder collapse to rings cannot be exclusively end-to-end connection; this mechanism, predicted theoretically to form rings in cylindrical micelle suspensions with low critical micelle concentrations and high end-cap energies (*28*, *29*), has been only partially observed experimentally (*11–13*, *26*, *27*, *29*). End-to-end cylinder connection cannot be the exclusive ring-forming mechanism in the triblock system, primarily because the average toroid circumference is smaller than the contour length of the average cylindrical micelle (Fig. 2A). In addition, the existence of closed ring structures at the ends (Fig. 3, A, B, and G) and in the middle (Fig. 3, E, F, G, and I) of cylindrical micelles, along with lariat (Fig. 3, D, F, and H) and figure-eight structures (Fig. 3, C and J), is not possible through simple end-to-end connection of cylinders. Rather, these intermediates must be formed by the free end of a cylinder connecting to the midsection of a neighboring cylinder (or itself). Alternatively, severe cylinder buckling must occur to bring the body of the micelle in contact with itself in order to fuse together and form an internal ring structure. This is not to say that end-to-end connection of self-attractive cylinders does not take place. Indeed, the number of spherical micelles decreases as the solutions evaporate slowly (Figs. 1 and 2, B and D), suggesting that the spherical micelles are also attractive and fuse into cylinders that collapse into rings. In dilute polymer solution, the cylinder collapse is primarily from single cylindrical micelles leading to more regular ring structure. Quickly cast films result in an increased polymer concentration and more multicylinder collapse. The resulting multicylinder collapse may lead to single rings and the intermediate structures in Fig. 3.

The size and stability of the toroidal micelles can be influenced by the valency and concentration of organic counterion. For example, the valency of the organic counterion is critical in defining the ultimate structure formed. When PAA_{99}-*b*-PMA_{73}-*b*-PS_{66} suspensions were made with a 1:1 molar ratio of amine to acid with the use of a monoamine, 2-methoxyethylamine (essentially one-half of the EDDA unit), no closed ring structures were observed. Instead of a defined system of toroids with only a minority of remaining cylinders and spheres, small spherical micelles were formed (fig. S1A). Likewise, if the polymer was assembled in THF/water mixtures with little or no added divalent EDDA (<0.2:1 amine to acid), spherical micelles were also formed (fig. S1B). Therefore, the presence of an organic counterion and the valency of the counterion directly affect the geometry and the topology of micelles formed. In addition, the amine:acid functionality molar ratio can

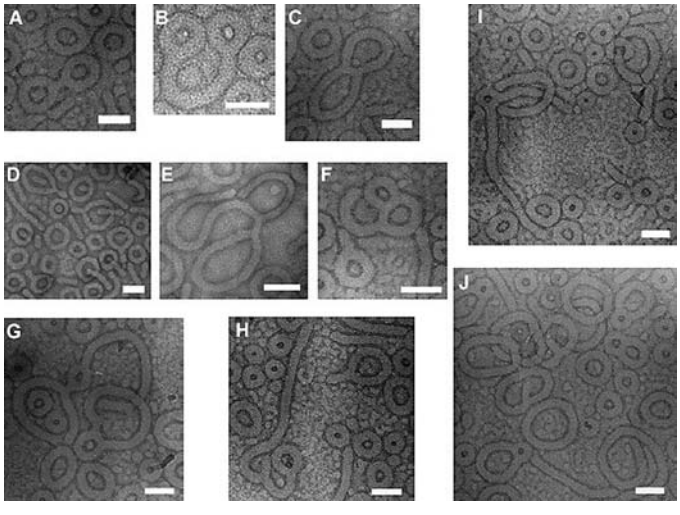

Fig. 3. (A to J) Negatively stained TEM data of intermediate structures formed by quick casting films from solutions containing 0.1 wt % PAA_{99}-PMA_{73}-PS_{66} triblock copolymer with a volume ratio of 1:2 THF to water and 0.5:1 molar ratio of amine to acid. Scale bar, 100 nm. Intermediate structures include dumbbells [(A), (B), and (G)], interior closed rings [(E), (F), (G), and (I)], lariats [(D), (F), and (H)], figure eights [(C) and (J)], and cylinders with ends connected but not fused together as indicated by the penetration of negative stain [(G) and (I)].

be altered to influence the ultimate size of the rings formed. As the relative ratio of amine to acid was increased from 0.5:1 to 1:1, the TEM images showed an increase in the average sizes of the ring micelles from a mean diameter for the overall structure of 98 to 126 nm, respectively (fig. S2). Images from either cryoTEM or negatively stained cast films revealed the same ring-size distribution, indicating that the toroids were formed in solution as a stable structure.

The toroidal micelles can be kinetically or chemically stabilized. During THF evaporation when self-attractive forces begin to dominate, sufficient THF swelling of the PS-PMA micelle cores exists to allow the formation of toroids through the fusion of cylindrical and spherical micelles. However, on complete THF evaporation (except for trace amounts contained in the micelle cores) the PS core resides below its glass transition, which, consequently, kinetically preserves the ring structure (compare Fig. 2, B and D). Alternatively, the toroids can be fixed chemically by means of cross-linking reactions on PAA coronal chains. In the presence of an activator, such as 1-[3′-(dimethylamino)propyl]-3-ethylcarbodiimide methiodide (DPEM), cross-linking occurs through the coupling of carboxylic acid moieties along the PAA backbone with N termini of the EDDA. Both chemical and physical toroid stabilization retain the average micelle size and distribution observed in solution (fig. S3).

Further evidence supporting like-charged attractive bundling as the mechanism for toroid formation can be found in the formation of another previously unrecognized structure observed in solutions with a low volume ratio of water to THF (<1:1 water to THF) and a 1:1 molar ratio of amine to acid. The cryoTEM in Fig. 4A reveals a suspension of flexible cylinders and spheres, presumably highly swollen with THF, exhibiting a low frequency of ring formation. However, upon slow casting of a film of this suspension, the cylinders and spheres collapse into close-packed bundles of cylinders (Fig. 4, B and C). Hexagonal symmetry can be observed in end-on projections of the cylinder bundles, whereas projections primarily perpendicular to the cylinder axes reveal the highly bent flexible nature of the cylindrical micelles during collapse (Fig. 4C) (*30*). During sample casting and THF evaporation, a critical solvent composition is attained in which attractive interactions between diamine and acid dominate, thus forming cylindrical micelles that collapse upon themselves. Importantly, the cylinders are flexible because they have hydrophobic cores that are swollen by THF. This flexibility allows the cylinders to collapse into dense bundles as shown in Fig. 4. This is in contrast with previously discussed toroid-forming solutions that begin with higher relative volume ratios of water to THF (>1:1 water to THF). These larger water:THF ratios produce PS and PMA cores that are relatively less swollen with THF, resulting in stiffer, semiflexible cylinders that cannot completely bundle on themselves during film casting. Rather, because of their higher bending stiffness, these micelles curl and fuse into toroidal micelles.

By combining parameters critical for (i) like-charged attraction bundling of biopolymers and (ii) block copolymer micelle formation in dilute solution, we produced a stable phase of toroidal micelles. The micelles are formed by a combination of cylindrical micelle curling and end-to-end collapse of cylindrical and spherical micelles. The size of the toroidal micelles can be influenced with the concentration of diamine counterion. The toroids can be kinetically trapped by ridding the system of organic solvent, thus taking the PS core block below its glass transition, or by chemically cross-linking the acid corona functionality.

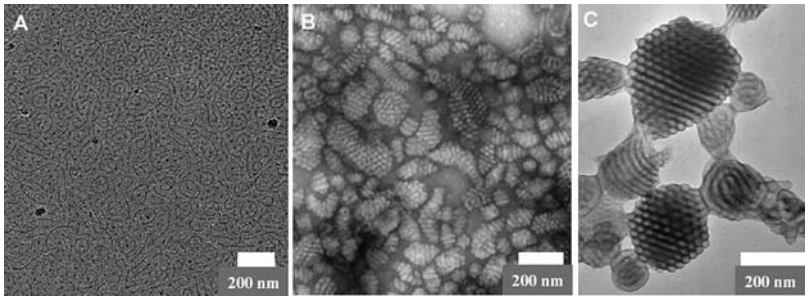

Fig. 4. TEM of PAA_{99}-PMA_{73}-PS_{66} micelles from 0.1 wt % triblock copolymer in 1:1 volume ratio of water to THF and 1:1 molar ratio amine to acid solution. (**A**) CryoTEM image of a cylindrical and spherical micelle mixture. (**B**) Negatively stained image of close-packed cylinder bundles formed during the casting of the solution from (A). (**C**) Higher magnification image of close-packed bundles. The electron imaging contrast between cylinders within the bundles is due to the penetration of the uranyl acetate negative stain between close-packed cylinders. The hexagonal symmetry from projections primarily parallel with the cylinder axes is clearly observed, as are projections more perpendicular to the cylinder axes appearing as a layered structure.

References and Notes

1. B. M. Discher *et al.*, *Science* **284**, 1143 (1999).
2. D. M. Vriezema *et al.*, *Angew. Chem. Int. Ed. Engl.* **42**, 772 (2003).
3. L. F. Zhang, A. Eisenberg, *Science* **268**, 1728 (1995).
4. H. Bermudez, A. K. Brannan, D. A. Hammer, F. S. Bates, D. E. Discher, *Macromolecules* **35**, 8203 (2002).
5. Y. Y. Won, H. T. Davis, F. S. Bates, *Science* **283**, 960 (1999).
6. P. Dalhaimer, H. Bermudez, D. E. Discher, *J. Polym. Sci. Part B Polym. Phys.* **42**, 168 (2004).
7. J. D. Hartgerink, E. Beniash, S. I. Stupp, *Science* **294**, 1684 (2001).
8. G. A. Silva *et al.*, *Science* **303**, 1352 (2004).
9. K. Prochazka, T. J. Martin, P. Munk, S. E. Webber, *Macromolecules* **29**, 6518 (1996).
10. J. Cornelissen, M. Fischer, N. Sommerdijk, R. J. M. Nolte, *Science* **280**, 1427 (1998).
11. S. Jain, F. S. Bates, *Science* **300**, 460 (2003).
12. S. Jain, F. S. Bates, *Macromolecules* **37**, 1511 (2004).
13. K. Yu, L. F. Zhang, A. Eisenberg, *Langmuir* **12**, 5980 (1996).
14. J. Raez, I. Manners, M. A. Winnik, *J. Am. Chem. Soc.* **124**, 10381 (2002).
15. L. F. Zhang, C. Bartels, Y. S. Yu, H. W. Shen, A. Eisenberg, *Phys. Rev. Lett.* **79**, 5034 (1997).
16. I. C. Riegel, A. Eisenberg, C. L. Petzhold, D. Samios, *Langmuir* **18**, 3358 (2002).
17. L. F. Zhang, A. Eisenberg, *J. Am. Chem. Soc.* **118**, 3168 (1996).
18. C. Bottcher, C. Endisch, J. H. Fuhrhop, C. Catterall, M. Eaton, *J. Am. Chem. Soc.* **120**, 12 (1998).
19. G. C. L. Wong *et al.*, *Science* **288**, 2035 (2000).
20. I. Koltover, T. Salditt, J. O. Radler, C. R. Safinya, *Science* **281**, 78 (1998).
21. K. Ewert *et al.*, *Curr. Med. Chem.* **11**, 133 (2004).
22. V. A. Bloomfield, *Biopolymers* **44**, 269 (1997).
23. J. X. Tang, P. A. Janmey, *J. Biol. Chem.* **271**, 8556 (1996).
24. J. X. Tang, J. A. Kas, J. V. Shah, P. A. Janmey, *Eur. Biophys. J Biophys. Lett.* **30**, 477 (2001).
25. D. M. Vriezema *et al.*, *Macromolecules* **37**, 4736 (2004).
26. A. Bernheim-Groswasser, R. Zana, Y. Talmon, *J. Phys. Chem. B* **104**, 4005 (2000).
27. J. T. Zhu, Y. G. Liao, W. Jiang, *Langmuir* **20**, 3809 (2004).
28. P. van der Schoot, J. P. Wittmer, *Macromol. Theor. Sim.* **8**, 428 (1999).
29. M. In, O. Aguerre-Chariol, R. Zana, *J. Phys. Chem. B* **103**, 7747 (1999).
30. The bundled cylinder particles are distinct from the hexagonal hollow hoop (HHH) structure observed by Zhang *et al.* (*15*). The interior structure of the HHH particles is actually similar to a bulk cylindrical phase in which cylinders of one block of a diblock polymer are locally hexagonally packed within a matrix of the other block. (However, the closed-hoop nature of the cylinder phase is unique to the HHH phase and is not observed in bulk cylindrical phases.) In contrast, the collapsed cylinders presented here are cylindrical micelles with a THF swollen PS/PMA core surrounded by a PAA corona complexed with diamine. The hexagonal packing does not arise from bulklike phase separation but from the intimate close-packing of the flexible cylindrical micelles.
31. We thank NSF for funding, specifically the Nanoscale Interdisciplinary Research Teams program under grant DMR-0210247. Any opinions, findings, conclusions, or recommendations expressed in this material are those of the authors and do not necessarily reflect the views of NSF. We thank J. L. Turner for creation of the toroid schematic in Fig. 1B. We also thank the W. M. Keck College of Engineering electron microscopy lab at the University of Delaware, nuclear magnetic resonance facilities of the Department of Chemistry and TEM facilities of Department of Physics at Washington University in Saint Louis.

Supporting Online Material

www.sciencemag.org/cgi/content/full/306/5693/94/DC1
Materials and Methods
Figs. S1 to S3
References

16 July 2004; accepted 7 September 2004

Multicompartment Micelles from ABC Miktoarm Stars in Water

Zhibo Li,[1] Ellina Kesselman,[3] Yeshayahu Talmon,[3] Marc A. Hillmyer,[1]* Timothy P. Lodge[1,2]*

By combining three mutually immiscible polymeric components in a mixed-arm star block terpolymer architecture, we have observed the formation of a previously unknown class of multicompartment micelles in dilute aqueous solution. Connection of water-soluble poly(ethylene oxide) and two hydrophobic but immiscible components (a polymeric hydrocarbon and a perfluorinated polyether) at a common junction leads to molecular frustration when dispersed in aqueous solution. The incompatible hydrophobic blocks form cores that are protected from the water by the poly(ethylene oxide) blocks, but both are forced to make contact with the poly(ethylene oxide) by virtue of the chain architecture. The structures that emerge depend on the relative lengths of the blocks and can be tuned from discrete multicompartment micelles to extended wormlike structures with segmented cores.

The spontaneous self-assembly of amphiphilic molecules into discrete supramolecular assemblies and two- and three-dimensional macrolattices has been used in the development of many new nanotechnological applications, including nanolithography (*1*), biomineralization (*2*), and drug delivery (*3*). Indeed, such free energy–driven processes have been touted as the exemplar of bottom-up engineering (*4*). Block copolymers, which consist of macromolecules formed by covalent end-linking of two or more disparate polymeric blocks, represent a particularly appealing template material. They potentially combine traditional attributes of polymeric materials with sophisticated functions (e.g., luminescence, conductivity, and storage and release of active molecules) (*5*–*7*). As a design platform, they offer a host of control variables through which structure may be tuned, including block length, polymer architecture, choice of monomers, and selection of interaction strengths. The ability of two-monomer diblock (AB) copolymers to form micelles is well documented (*5*, *8*, *9*). As with their lower-molar-mass surfactant and lipid analogs, the predominant micellar morphologies formed are spheres, cylinders, and vesicles, the last corresponding to nearly flat bilayer sheets curved around to form a sealed container.

The structures available with AB copolymers are all limited to partitioning of space into an "inside" and an "outside." In contrast, the possibilities inherent in multicompartment micellar structures have recently been recognized (*10*). A biological analogy is apt: Prokaryotic systems such as bacteria have a single lipid bilayer dividing space and thus are analogous to vesicular assemblies in AB copolymers, whereas eukaryotic cells, with multiple functional units (nucleus, organelles, etc.) contained within one overall membrane, are the paradigm for a multicompartment system (*11*). For example, copolymer micelles and vesicles are being extensively investigated for drug delivery applications (*3*, *12*). A multicompartment system could deliver simultaneously two or more active but incompatible agents in precise stoichiometric proportions. Some progress toward multicompartment micelles has been reported (*13*–*15*); examples using linear ABC triblocks include core-shell-corona spheres (*16*) and disks (*17*). In these cases, the subdivision of the micellar interior is limited to two concentric nanodomains.

There are several design criteria to consider in developing suitable ABC terpolymers. Clearly one key feature is a strong effective repulsion between each pair of blocks, such that A, B, and C segregate into distinct nanodomains. The segregation strength in polymers is quantified by the dimensionless product χN, where χ is the monomer-monomer interaction parameter and N is the degree of polymerization (*18*). However, limited solubility, kinetics of structural equilibration, and synthetic convenience all favor relatively modest molecular weights (small N), requiring that the three pairwise χ parameters be very large. The chosen monomers must also be amenable to controlled polymerization schemes in order to prepare blocks of well-defined length. To this end, we selected a water-soluble poly(ethylene oxide) (O) block, a saturated hydrocarbon polyethylethylene (E) block, and a hydrophobic, lipophobic poly(perfluoropropylene oxide) (F) block. The hydrophilic O block has the largest N, to enhance water solubility. The final design feature is the chain architecture; for example, ABC, ACB, and BAC triblocks can adopt quite different bulk morphologies, even if the block lengths remain constant, due to the competition between "desirable" interfaces (those between the blocks with the smallest χ) and "mandatory" interfaces (those between covalently linked blocks) (*19*–*21*). With this in mind, we have targeted miktoarm star ABC terpolymers (Fig. 1) (*22*), whereby the threefold connector enforces a one-dimensional locus of terpolymer junctions along which the three nanodomains must intersect (*23*). This strategy in particular suppresses formation of core-shell-corona structures in favor of multicompartment micelles. Furthermore, this architecture combines the rather short E and F blocks to impose appealingly small (<10 nm) elementary compartments.

The structure of the ABC miktoarm star block terpolymers is given in Fig. 1. The details of the synthetic protocol will be presented elsewhere (*24*). Briefly, butadiene is polymerized anionically and terminated with a heterobifunctional protected initiator. The resulting hydroxyl end-functionalized polybutadiene is hydrogenated to polyethylethylene. This end-functionalized E block serves as a macroinitiator for anionic polymerization of ethylene oxide, yielding the O block. After capping the O block with ethylbromide and deprotection of a hydroxyl group located at the juncture of the E and O blocks, acid chloride end-functionalized F blocks are coupled with this hydroxyl group. The resulting miktoarm stars are designated μ-EOF(x-y-z), where x, y, and z represent the E, O, and F block molecular weights, respectively, in kD (table S1). This overall protocol is conveniently modular, in that a given batch of E may be used to prepare a series of EO diblocks of varying O content,

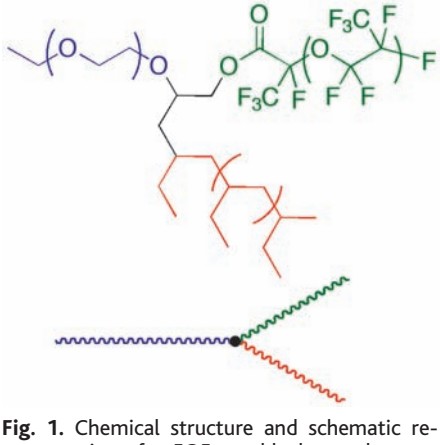

Fig. 1. Chemical structure and schematic representation of μ-EOF star block terpolymers.

[1]Department of Chemistry, [2]Department of Chemical Engineering and Materials Science, University of Minnesota, Minneapolis, MN 55455, USA. [3]Department of Chemical Engineering, Technion-Israel Institute of Technology, Haifa 32000, Israel.

*To whom correspondence should be addressed. E-mail: lodge@chem.umn.edu (T.P.L.); hillmyer@chem.umn.edu (M.A.H.)

and these diblocks in turn may be conjugated to a series of F blocks. A series of μ-EOF polymers were prepared, and in all cases the molecular weight distributions were narrow (polydispersity indices range from 1.1 to 1.3).

We have used a variety of experimental techniques to characterize micellar structures formed in dilute aqueous solutions (*25*), but, in situations where rather complicated, irregular, and polydisperse aggregates are anticipated, direct imaging by cryo-transmission electron microscopy (cryo-TEM) is the method of choice. Samples are prepared by suspending 100- to 200-nm-thick menisci of 1 weight percent aqueous solutions on a lacy carbon film, which is then rapidly immersed in liquid ethane at its freezing point. The resulting vitreous water preserves the possibly delicate self-assembled structures, which are then imaged without staining, in transmission, at about –175°C, by using very low electron exposures. Further details of the cryo-TEM technique may be found elsewhere (*26*, *27*).

Typical cryo-TEM images from 1 wt % solutions of μ-EOF(2-13-2) and μ-EOF(2-13-3) are shown in Fig. 2, A to D (also figs. S1 and S2). Figure 2A reveals a preponderance of distinct micellar cores with sizes of about 12 ± 2 nm, each of which contains irregular small dark regions (*28*). The dark regions (highest electron density) are attributable to the F nanodomains because they minimize contact with the surrounding aqueous phase, with the remainder of the core (gray regions) made up of the E blocks. The O coronas are not directly visible because they are well solvated, but their presence and spatial extent is indicated by the typical separation distances between neighboring cores. The apparent order in the micrographs is the result of specimen preparation. In some instances, the F domains are larger and more distinct (Fig. 2, B to D). Here, fascinating three-lobe and four-lobe micellar cores can be discerned, with the lighter gray E domains more spherical and the darker F domains filling the interstitial spaces.

The results in Fig. 2 reflect the stars with the largest hydrophilic (O) block. Images for stars with shorter O blocks are shown in Fig. 3, A to D. In these cases, elongated, wormlike structures are obtained, and furthermore the worms are layered or segmented along the long axis. Specifically, in Fig. 3A (also fig. S3) μ-EOF(2-7-2) exhibits long "strings" of dark cores in addition to discrete micelles. These results imply an attractive interaction between micelles, which is initially surprising given the steric repulsion arising from the O corona. In addition, the attraction is apparently uniaxial, leading exclusively to strings of micelles. We propose that the individual micellar elements contain an oblate disk-like F core, surrounded top and bottom by an E shell (Fig. 4A). Because the O blocks must emanate from the E-F interface and curl around the top and bottom of the micelle to screen the hydrophobic core, a natural explanation for the uniaxial attraction emerges. As two micelles approach one another, any fluctuation in O concentration in the corona can expose the hydrophobic core components. In forming a string, the different cores are able to share their O coronas, thus protecting them from the highly unfavorable exposure to water.

"Segmented worm" micelles formed by μ-EOF(2-9-2), μ-EOF(2-9-3), and μ-EOF(2-9-5) are shown in Fig. 3, B to D, respectively (also figs. S4 to S6). In this series of molecules with increasing F block compositions, a variety of overall micellar shapes and sizes are evident, and a consistent local packing motif persists, namely alternating flat disks of dark (F) and gray (E), each about 5 to 7 nm in thickness. As in the previous case, the O coronas are shared, forming cylindrical structures; the difference from Fig. 3A lies in the flatness of the E and F domains. The proposed chain packing in the segmented worms is illustrated in Fig. 4B. The O coronas are anchored around circles formed at the intersection of each E and F disk. Within the disks, the E and F chains are almost fully extended. For example, the apparent radii of the segmented worms are about 6 to 7 nm, 7 to 8 nm, and 9 to 10 nm in the μ-EOF(2-9-2), μ-EOF(2-9-3), and μ-EOF(2-9-5) samples, respectively. The fully extended F block in each case would be about 5, 7.5, and 11.5 nm, respectively, consistent with the proposed chain packing motif in Fig. 4B. The fully extended E block would be about 8 nm in all cases. The thickness of each segment combined with the known densities of E and F indicates an aggregation number of 350 to 450 for each repeat unit of the segmented worm.

Although a rich variety of multicompartment micellar structures are revealed in Figs. 2 and 3, they can be understood at least qualitatively through the interplay of a few factors. First, the three components (E, F, and O plus water) are strongly incompatible, leading to the formation of distinct domains. In fact, this system probably lies in the so-called superstrong segregation regime (SSSR) (*29*, *30*), in which the interfacial energies overwhelm the entropic penalties for stretching the shorter blocks. One consequence of the SSSR is that flat interfaces are preferred. Also, the E and F domain sizes are limited by chain length; they cannot stretch beyond the fully extended block size. Second, although the extremely large interfacial ten-

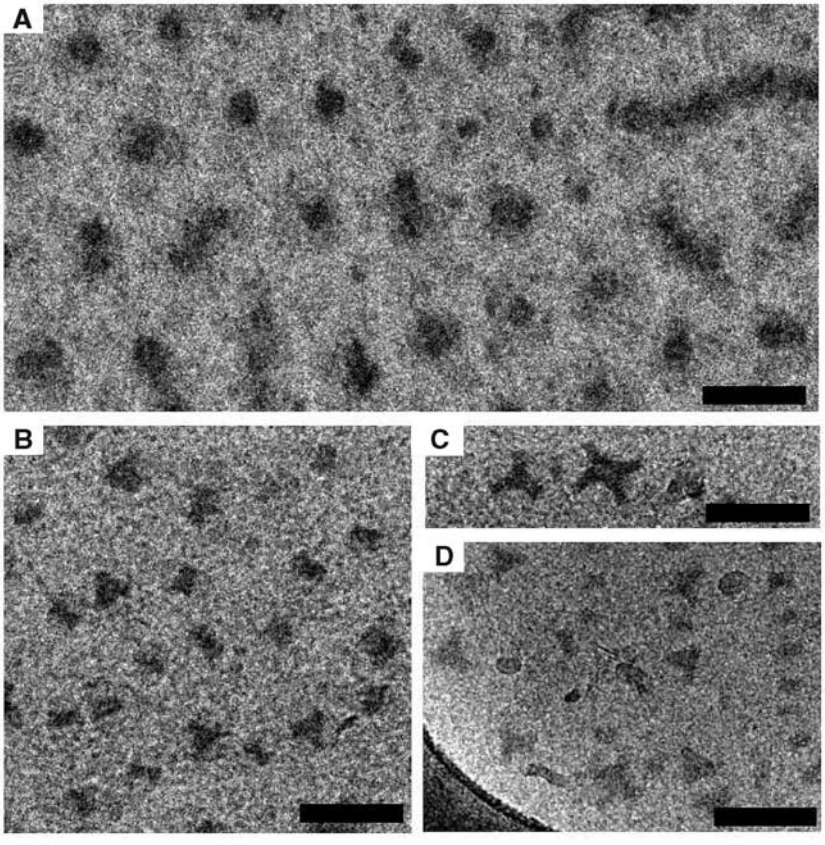

Fig. 2. Cryo-TEM images of 1 wt % aqueous solutions of μ-EOF(2-13-2) (**A**) and μ-EOF(2-13-3) (**B** to **D**); scale bars indicate 50 nm.

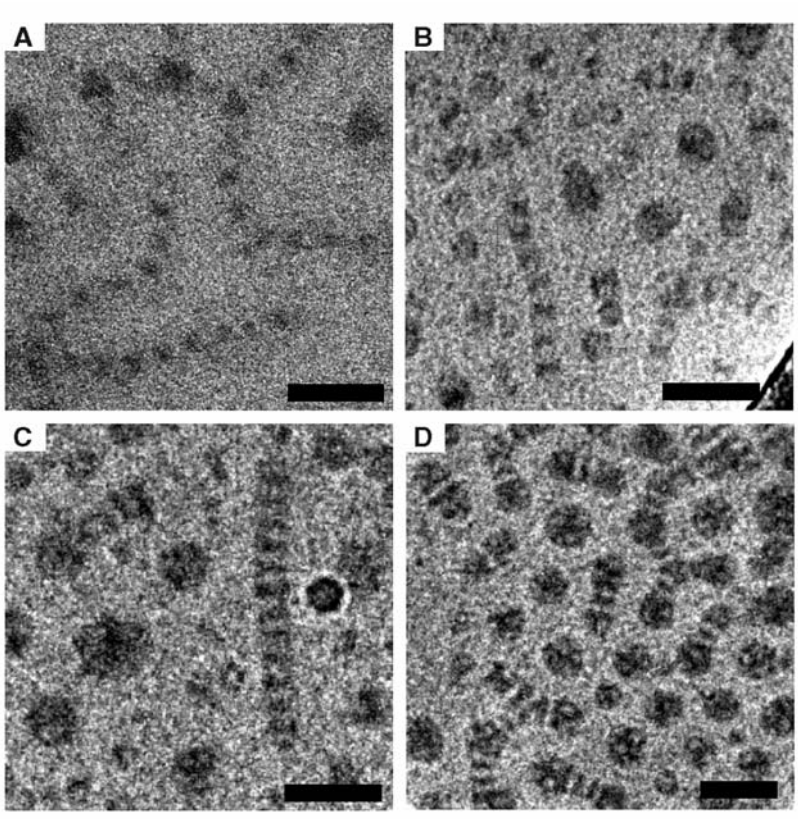

Fig. 3. Cryo-TEM images of 1 wt % aqueous solutions of (**A**) μ-EOF(2-7-2), (**B**) μ-EOF(2-9-2), (**C**) μ-EOF(2-9-3), and (**D**) μ-EOF(2-9-5); scale bars indicate 50 nm.

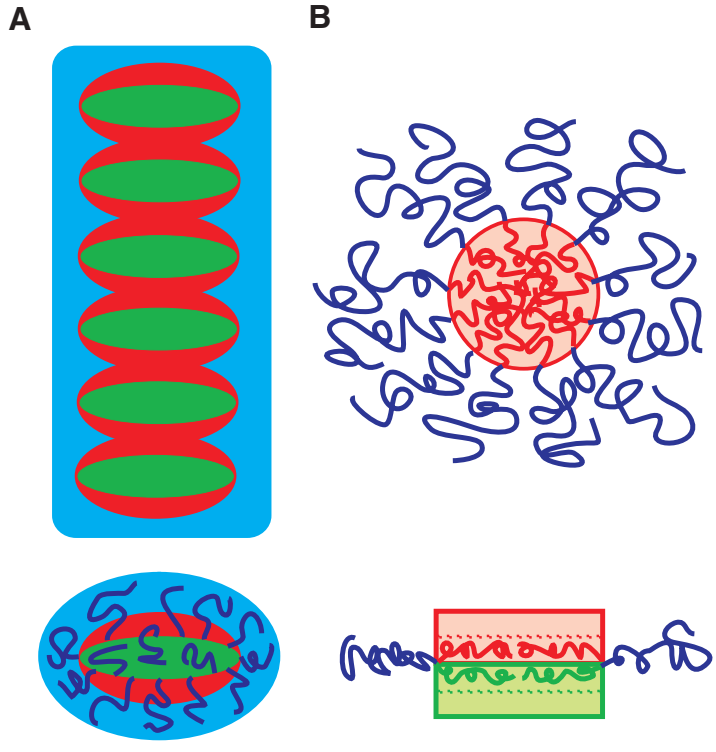

Fig. 4. Schematic drawing of (**A**) an individual μ-EOF(2-7-2) micelle and the stacking into a string as in Fig. 3A; (**B**) side and end-on views of proposed chain packing for μ-EOF segmented worms in Fig. 3, B to D.

sions favor flat interfaces, this comes into conflict with the terpolymer composition, in which the longer and well-solvated O blocks favor high interfacial curvature. Because the O-F interfacial tension should be even greater than the (still large) O-E and E-F interfacial tensions, the chains pack as best they can to shield F from O. However, by virtue of the covalent connectivity of F and O in the star architecture (Fig. 1), some contact between F and O is inevitable. This, in turn, imposes constraints on the dimensions of the core compartments. Lastly, for each terpolymer a distribution of micellar aggregates is observed. This is indicative of a nonergodic system, as has already been documented in aqueous diblocks (*31*); the system is unable to find the global free energy minimum, because the exchange of chains between micelles is prohibitively slow. Nevertheless, the various local minima share a small number of common packing motifs, because chains within a given aggregate are able to adjust their packing and conformation.

With these considerations in mind, the discrete micelles favored by μ-EOF(2-13-2) and μ-EOF(2-13-3) (Fig. 2) can be attributed to the longest O blocks dictating a high interfacial curvature. Within each core, the F blocks segregate into one or more domains; the smaller the domain, the greater the opportunity for the anchors of the O blocks to be dispersed uniformly across the surfaces of the core. Nevertheless, these terpolymers also form the three- and four-lobe cores illustrated in Fig. 2, B to D; here, the E-F interfaces are flatter, and the F blocks are generally shielded from O by the E domains. Similarly, the segmented worms that are observed for the terpolymers with shorter O blocks have flatter O-F and O-E interfaces, indicating the smaller role of corona crowding. The segmented worm and micellar strings shown in Fig. 3, A to D, are all formed by terpolymers with shorter O blocks. The immediate consequence of this is the prevalence of extended structures, whereby the core surface area per O chain is reduced and the E-F interfaces are flatter. The numerical considerations given above also confirm that the individual hydrophobic blocks adopt nearly fully extended conformations, consistent with the SSSR.

These results demonstrate a strategy for forming multicompartment micelles. Although there is a large parameter space to explore (e.g., block lengths, choice of monomers, and chain architecture), these results already give indications of the relative block lengths needed to favor discrete, multidomain cores [i.e., μ-EOF(2-13-2) and μ-EOF(2-13-3)] or extended, segmented worm structures. The choice of fluorocarbon and hydrocarbon blocks allows access to the SSSR, even for relatively modest molecular weights, and the miktoarm star architecture is remarkably

successful in promoting formation of multicompartment cores (*32*).

References and Notes

1. M. Park, C. Harrison, P. M. Chaikin, R. A. Register, D. H. Adamson, *Science* **276**, 1401 (1997).
2. J. H. Collier, P. B. Messersmith, *Annu. Rev. Mater. Res.* **31**, 237 (2001).
3. R. Savic, L. Luo, A. Eisenberg, D. Maysinger, *Science* **300**, 615 (2003).
4. M. Shimomura, T. Sawadaishi, *Curr. Opin. Colloids Interface Sci.* **6**, 11 (2001).
5. I. W. Hamley, *The Physics of Block Copolymers* (Oxford Univ. Press, New York, 1998).
6. C. Park, J. Yoon, E. L. Thomas, *Polymer* **44**, 6725 (2003).
7. T. P. Lodge, *Macromol. Chem. Phys.* **204**, 265 (2003).
8. G. Riess, *Prog. Polymer Sci.* **28**, 1107 (2003).
9. A. Halperin, M. Tirrell, T. P. Lodge, *Adv. Polym. Sci.* **100**, 31 (1991).
10. A. Laschewsky, *Curr. Opin. Colloids Interface Sci.* **8**, 274 (2003).
11. E. T. Kisak, B. Coldren, C. A. Evans, C. Boyer, J. A. Zasadzinski, *Curr. Med. Chem.* **11**, 199 (2004).
12. D. E. Discher, A. Eisenberg, *Science* **297**, 967 (2002).
13. A. Kotzev, A. Laschewsky, P. Adriaensens, J. Gelan, *Macromolecules* **35**, 1091 (2002).
14. K. Stähler, J. Selb, F. Candau, *Langmuir* **15**, 7565 (1999).
15. R. Weberskirch, J. Preuschen, H. W. Spiess, O. Nuyken, *Macromol. Chem. Phys.* **201**, 995 (2000).
16. J.-F. Gohy, N. Willet, S. Varshney, J.-X. Zhang, R. Jérôme, *Angew. Chem. Int. Ed. Engl.* **40**, 3214 (2001).
17. Z. Zhou, Z. Li, Y. Ren, M. A. Hillmyer, T. P. Lodge, *J. Am. Chem. Soc.* **125**, 10182 (2003).
18. F. S. Bates, *Science* **251**, 898 (1991).
19. A. Balsamo *et al.*, *Macromolecules* **36**, 4515 (2003).
20. T. S. Bailey, C. M. Hardy, T. H. Epps, F. S. Bates, *Macromolecules* **35**, 7007 (2002).
21. T. Goldacker, V. Abetz, R. Stadler, I. Erukhimovich, L. Leibler, *Nature* **398**, 137 (1999).
22. N. Hadjichristidis, *J. Polym. Sci. Polym. Chem.* **37**, 857 (1999).
23. S. Sioula, N. Hadjichristidis, E. L. Thomas, *Macromolecules* **31**, 8429 (1998).
24. Z. Li, M. A. Hillmyer, T. P. Lodge, unpublished results.
25. Dynamic light scattering (DLS) data on dilute aqueous solutions of the μ-EOF samples were consistent with the cryo-TEM images. Namely, we typically observed a rather narrow distribution of relatively small micelles with hydrodyamic radii, in agreement with discrete micellar-like aggregates (Fig. 2), as well as a population of larger hydrodynamic particles consistent with the strings shown in Fig. 3. A description of the DLS technique and representative data (fig. S7) are given in (*26*).
26. Details of the cryo-TEM measurements and representative images of μ-EOF solutions with large fields of view are given on *Science* Online.
27. D. Danino, A. Bernheim-Groswasser, Y. Talmon, *Colloid Surf. A Physicochem. Eng.* **183**, 113 (2001).
28. E. E. Dormidontova, A. R. Khokhlov, *Macromolecules* **30**, 1890 (1997).
29. A. N. Semenov, I. A. Nyrkova, A. R. Khokhlov, *Macromolecules* **28**, 7491 (1995).
30. T. P. Lodge, M. A. Hillmyer, Z. Zhou, Y. Talmon, *Macromolecules* **37**, 6680 (2004).
31. S. Jain, F. S. Bates, *Science* **300**, 460 (2003).

32. This work was supported primarily by the Materials Research Science and Engineering Center program of NSF under award no. DMR-0212302.

Supporting Online Material

www.sciencemag.org/cgi/content/full/306/5693/98/DC1
Materials and Methods
Figs. S1 to S7
Table S1
References

28 July 2004; accepted 20 August 2004

Cope's Rule, Hypercarnivory, and Extinction in North American Canids

Blaire Van Valkenburgh,[1]* Xiaoming Wang,[2] John Damuth[3]

Over the past 50 million years, successive clades of large carnivorous mammals diversified and then declined to extinction. In most instances, the cause of the decline remains a puzzle. Here we argue that energetic constraints and pervasive selection for larger size (Cope's rule) in carnivores lead to dietary specialization (hypercarnivory) and increased vulnerability to extinction. In two major clades of extinct North American canids, the evolution of large size was associated with a dietary shift to hypercarnivory and a decline in species durations. Thus, selection for attributes that promoted individual success resulted in progressive evolutionary failure of their clades.

The history of large (>7 kg) predatory mammals is one of repeated ecological replacement (*1*). The various ecomorphological roles of cat-like, wolf-like, and hyena-like predator have been filled by representatives of distinct families at different times. In general, a single subfamily or family diversified and dominated a given ecomorphological role for about 10 million years and then declined, only to be replaced by a new clade. The expansion phase is often explained as a result of key adaptations and/or ecological opportunity, but it has been more difficult to understand the decline to extinction of a formerly successful group. Here we use the recently documented and exceptionally rich fossil record of North American canids (*2*, *3*) as a test case for studying the dynamics of extinction.

The dog family Canidae has three subfamilies: the extant Caninae, the extinct Hesperocyoninae [40 to 15 million years ago (Ma)], and the Borophaginae (34 to 2 Ma) (*4*). Both extinct subfamilies were endemic to North America and were very diverse in the Miocene, reaching a peak of 25 contemporaneous species approximately 30 Ma (Fig. 1A). The fossil record of these canids is impressive and well studied, with at least 28 species of hesperocyoninines and 68 species of borophagines described (*2*, *3*, *5*). In dental specialization and inferred diets, hesperocyonines ranged from relatively unspecialized mesocarnivores (inferred diet of small prey and plant matter) to more specialized hypercarnivores (inferred diet of large prey) characterized by enhanced shearing blades on their molar teeth (*2*). The more diverse borophagines included both of these types, as well as hypocarnivores (inferred diet of more plant matter than mesocarnivores) with reduced shearing blades and enlarged grinding areas on their molars (*3*).

To examine trends in body size and dietary specialization in fossil canids, we relied on inferences from dental morphology. Based on the established correlation between lower carnassial tooth [first molar (M_1)] length and body mass in living canids, we used M_1 length as a surrogate for body mass (*6*, *7*). To estimate dietary adaptations, we relied on previous studies of the correspondence between morphology and diet in canids (*8*, *9*). A discriminant analysis of 30 craniodental measurements on 27 species of modern canids easily separated hypercarnivores as having relatively deep jaws, large canine and incisor teeth, reduced molar grinding areas, and longer shearing blades on their lower carnassials (*9*). Because fossil species are rarely represented by complete specimens, we focused on three shape indices (six measurements) that together are highly informative about canid diets, independent of body mass. These are jaw depth relative to length, the proportion of the lower carnassial devoted to shearing rather than grinding function, and the proportion of the upper carnassial and molars devoted to grinding rather than shearing (*10*). Relative to hypo- and mesocarnivores, hypercarnivores tend to have deeper jaws to withstand loads imposed by killing and feeding on large prey, as well as long shearing blades and reduced molar grinding areas.

In both subfamilies, mean body mass increased substantially with time (Fig. 1, B and C) and within-lineage transitions to larger size significantly exceeded those to smaller

[1]Department of Ecology and Evolutionary Biology, University of California at Los Angeles, Los Angeles, CA 90095–1606, USA. [2]Department of Vertebrate Paleontology, Natural History Museum of Los Angeles County, 900 Exposition Boulevard, Los Angeles, CA 90007, USA. [3]Department of Ecology, Evolution, and Marine Biology, University of California at Santa Barbara, Santa Barbara, CA 93106, USA.

*To whom correspondence should be addressed. E-mail: bvanval@ucla.edu

size (*11*). In the Hesperocyoninae, M_1 length underwent a 400% expansion over 25 million years, and it increased by 600% over 35 million years in the Borophaginae. Increase in body size was accompanied by a disappearance of small species in both groups. The role of small canid-like carnivore was then filled by the earliest members of the Caninae (*3*), as well as perhaps a few species of procyonids (raccoon-like carnivores) (*12*).

A principal components analysis (PCA) of the three morphometric indices for 16 species of hesperocyonines for which the indices could be measured displays a diversity of forms and implies that the first principal component (PC1) can be used to infer hypercarnivorous adaptation (Table 1 and Fig. 2A). Species with the relatively deepest jaws, largest carnassial blades, and most reduced grinding areas have low, negative scores on this component, whereas those with less hypercarnivorous features have high positive scores. The second component further distinguishes species with deep jaws and reduced grinding area as having a very positive score on this axis. Within-lineage trends toward hypercarnivory are apparent within *Osbornodon* (N → P, Fig. 2A), as well as in the hypothesized lineage from *Mesocyon* to *Sunhunketanka* to *Enhydrocyon* (*2*) [H → G → (M and K), Fig. 2A].

The same analysis was run for 26 species of borophagines for which the three morphometric indices could be measured. Results largely parallel that for the hesperocyonines: PC1 defined an axis of hypercarnivory (Table 1 and Fig. 2A). Specialized hypercarnivores had low negative scores on this axis and positive scores on the second. As was true of the hesperocyonines, there were within-lineage trends toward hypercarnivory. For example, the proposed evolutionary sequence of *Paratomarctus* to *Carpocyon* to *Protepicyon* to *Epicyon* to *Borophagus* (*3*) can be traced across the PCA plot, moving from right to left on PC1 and then upward on PC2, as the lineage becomes increasingly specialized for hypercarnivory [s → v → (w and x) → y → z, Fig. 2A].

We used PC1 score as an index of specialization for hypercarnivory and plotted it against estimated body size for each species by subfamily. The pattern is unambiguous: Larger species are more specialized for hypercarnivory as defined by their position on PC1 (Fig. 2B). Moreover, there are no small species with adaptations for hypercarnivory as extreme as those seen in the larger species, nor are there large species with more mesocarnivorous or hypocarnivorous morphology. As mean body size increased, species evolved into specialized hypercarnivores.

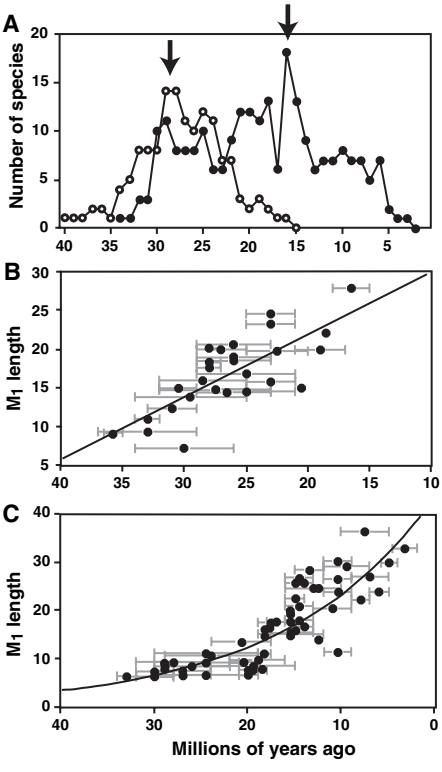

Fig. 1. Trends in species diversity and body size in extinct canids. (**A**) Changes in species diversity with time in hesperocyonines (open symbols) and borophagines (solid symbols). Arrows indicate the first appearance of species with hypercarnivorous adaptations as defined by a PCA of craniodental morphology. Body size (lower first molar length in millimeters) is plotted against time, from oldest to youngest, for species of (**B**) Hesperocyoninae ($n = 27$, $r^2 = 0.57$, $P < 0.001$) and (**C**) Borophaginae ($n = 60$, $r^2 = 0.74$, $P < 0.001$). Each bar spans the known species duration in the fossil record, with the symbol positioned at the midpoint. Diversity data are modified from (*2, 3*).

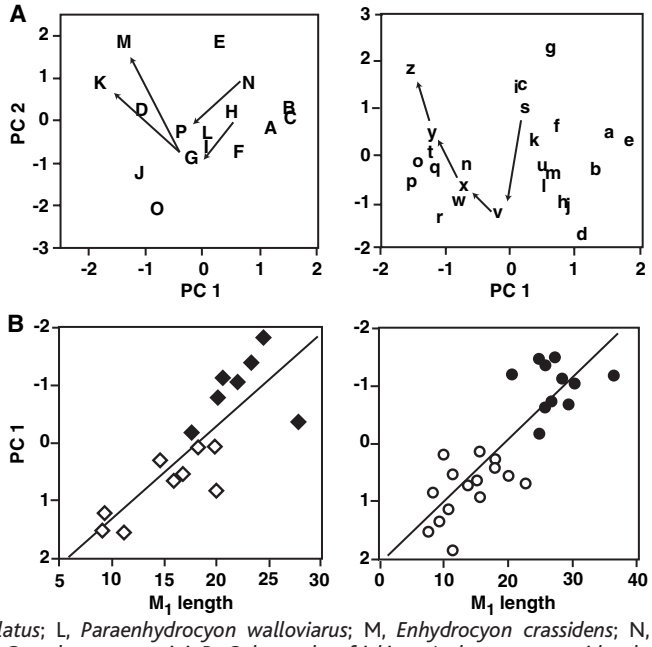

Fig. 2. Dietary specialization and its association with body size increase in hesperocyonines (left) and borophagines (right). (**A**) Plot of the first two PCs of a PCA of craniodental indices. Species with negative values on PC1 are predicted to have been hypercarnivorous to varying degrees. Arrows link species within a proposed evolutionary series. Species labels are as follows: A, *Hesperocyon gregarious*; B, *Prohesperocyon wilsoni*; C, *Hesperocyon coloradensis*; D, *Ectopocynus* sp.; E, *Paraenhydrocyon josephi*; F, *Cynodesmus thoides*; G, *Sunkahetanka geringensis*; H, *Mesocyon coryphaeus*; I, *Philotrox condoni*; J, *Enhydrocyon pahinsintewakpa*; K, *E. basilatus*; L, *Paraenhydrocyon walloviarus*; M, *Enhydrocyon crassidens*; N, *Osbornodon iamonensis*; O, *Cynodesmus martini*; P, *Osbornodon fricki*; a, *Archaeocyon pavidus*; b, *Rhizocyon oregonensis*; c, *Phlaocyon leucosteus*; d, *Cormocyon haydeni*; e, *C. copei*; f, *Desmocyon thomsoni*; g, *D. matthewi*; h, *Cynarctus galushai*; i, *Psalidocyon mariae*; j, *Microtomarctus conferta*; k, *Prototomarctus optatus*; l, *Tomarctus hippophagus*; m, *T. brevirostris*; n, *Aeleurodon aesthenostylus*; o, *A. mcgrewi*; p, *A. stirtoni*; q, *A. ferox*; r, *A. taxoides*; s, *Paratomarctus temerius*; t, *P. euthos*; u, *Carpocyon compressus*; v, *C. webbi*; w, *Protepicyon raki*; x, *Epicyon saveus*; y, *E. haydeni*; z, *Borophagus secundus*. (**B**) Degree of hypercarnivorous specialization (PC1 score in PCA analysis) plotted against body size (M_1 length in millimeters) (hesperyocyonines, $n = 16$, $r^2 = 0.67$, $P < 0.001$; borophagines, $n = 26$, $r^2 = 0.71$, $P < 0.001$). Note that values on PC1 are reversed. Putative hypercarnivores with PC1 score < 0 are indicated by solid symbols; hypo- and mesocarnivores (PC1 > 0) are indicated by open symbols. For analyses of body size trends, all species in (*2*, *3*) for which lower first molar length was available were included.

Table 1. Variable loadings and variance explained for the first two PCs.

	Hesperocyoninae		Borophaginae	
Variables	PC1	PC2	PC1	PC2
Relative blade length	–0.947	–0.171	–0.929	–0.247
Relative grinding area	0.812	–0.581	0.936	0.186
Relative jaw depth	–0.911	–0.34	–0.891	0.453
Percent variance explained	80%	16%	84.5%	10%

Did this result in an increased susceptibility to extinction? A plot of the index of hypercarnivory (PC1 score) against estimated species durations (Fig. 3A) indicates that none of the hypercarnivorous species (solid symbols) persisted for more than six million years, whereas some more omnivorous species (open symbols) endured for as much as 11 million years. Thus, the large hypercarnivores appear to have been limited in duration relative to other species, suggesting a greater vulnerability to extinction.

The shorter species longevities of large hypercarnivores might reflect a decreased probability of fossil preservation. Because they were large and carnivorous, their population densities are expected to have been reduced relative to those of smaller species (*13*–*15*), making them less likely to be recovered as fossils. Conversely, their greater body size, more massive bones and teeth, and presumed large geographic ranges favor fossil preservation (*16*, *17*). The mean frequency of borophagine species in individual fossil localities (194 occurrences) is approximately 0.02, and that of hesperocyonines (39 occurrences) is approximately 0.03 (*18*). Relative abundance in a fossil sample is uncorrelated with observed species duration or body size in both subfamilies (Fig. 3B). Based on these observed frequencies and calculating binomial probabilities (*19*), it would require a total fossil sample of 500 to 2000 specimens to be 99% or more certain of recovering at least one specimen of each canid species, if present. Thus, we can regard the observed endpoints of species ranges as being accurate indicators of the true stratigraphic ranges when samples approach or exceed these sizes for the interval above and below a given observed endpoint interval. At the temporal resolution we used, the known fossil record is sufficiently rich in each of the major regions that this condition is easily met at most levels throughout the Oligocene and Miocene. Given this, we do not believe that the observed differences in species durations result from artifacts of sampling.

Because hypercarnivory and increased body size evolved in tandem within our sampled canids, it is unclear which is most responsible for the drop in species durations. Both are associated with reduced population densities, a pivotal factor in modern species extinctions (*20*). Examination of the histories of each subfamily reveals that the first appearance of hypercarnivores (here defined as PC1 score < 0) occurs at the diversity peak in each subfamily (Fig. 1A). Subsequently, each subfamily declines to extinction over the next 14 to 16 million years. In both, new species continue to appear after the diversity peak, but extinction outpaces origination and species durations are shortened, leading to progressive declines in species richness.

Cope's rule, or the evolutionary trend toward larger body size, is common among mammals (*21*). Large size enhances the ability to avoid predators and capture prey, enhances reproductive success, and improves thermal efficiency (*22*, *23*). Moreover, in large carnivores, interspecific competition for food tends to be relatively intense, and bigger species tend to dominate and kill smaller competitors (*24*, *25*). Progenitors of hypercarnivorous lineages may have started as relatively small-bodied scavengers of large carcasses, similar to foxes and coyotes, with selection favoring both larger size and enhanced craniodental adaptations for meat eating. Moreover, the evolution of predator size is likely to be influenced by changes in prey size, and a significant trend toward larger size has been documented for large North American mammals, including both herbivores and carnivores, in the Cenozoic (*21*). After 30 Ma, large (>100 kg) prey species were always present and tended over time to become an increasingly significant resource (*26*).

Among living meat eaters, almost all species larger than about 21 kg prey on species as large or larger than themselves, whereas smaller carnivores can subsist on much smaller prey (such as invertebrates and rodents) (*27*). This transition to taking larger prey seems to reflect energetic constraints imposed by tradeoffs between foraging effort and food acquired. For species > ~21 kg, energy spent acquiring small prey is not likely to be balanced by nutrition gained (*27*). Thus, as moderately carnivorous hesperocyonines and borophagines became larger, they crossed the threshold where taking big prey was favored. Based on the relation between M_1 length and body mass in living canids (*6*, *7*), this threshold would have been crossed at an M_1 length of 18 to 25 mm. In both subfamilies, this transition was coincident with the first appearance of species with negative PC1 scores (Fig. 2B), which our analysis suggests were hypercarnivores. To be an effective predator of large prey required additional morphological specializations such as deeper jaws, reduced dental grinding areas, and enlarged dental shearing blades. Once species reached this elevated position in the trophic chain, their vulnerability to extinction increased. Reversals to a more generalized morphology and diet were rare in these two extinct canid subfamilies (*2*, *3*). Consequently, selection for larger size and hypercarnivory acted as a macroevolutionary ratchet, locking them into a trend of increasingly specialized forms that resulted ultimately in clade extinction. Similar trends toward larger size and hypercarnivory have been suggested in other extinct predatory taxa, such as Permian therapsids (*28*), creodonts, amphicyonids, and hyaenids (*1*), and these clades may have succumbed to the same macroevolutionary ratchet. Evolution may progress in a direction that favors individual fitness but ultimately

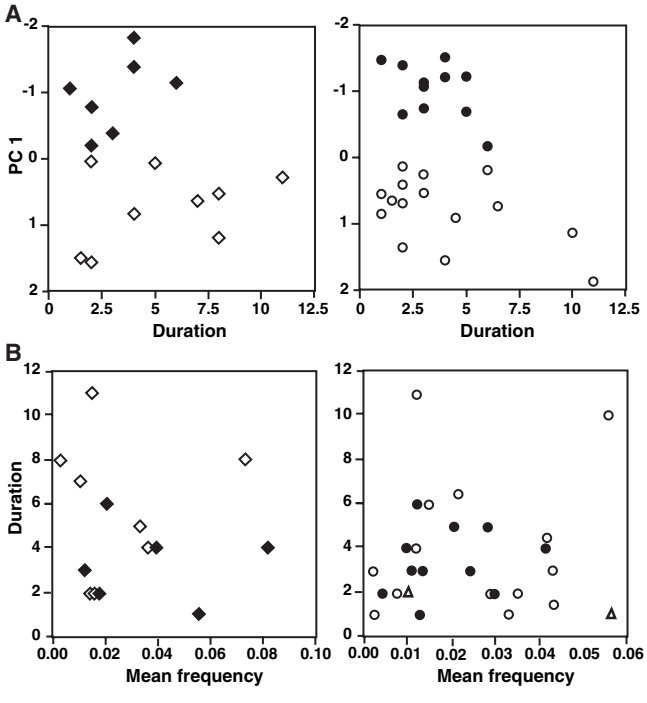

Fig. 3. Dietary specialization, species duration, and frequency in collections in hesperocyonines (left) and borophagines (right). Solid symbols, putative hypercarnivores with PC1 score < 0; open symbols, hypo- and mesocarnivores (PC1 > 0); open triangles, species not included in PC analysis because of insufficient data. Species durations were determined from published data (*2*, *3*) on stratigraphic range and are minima, given that the fossil record is unlikely to preserve either the first or last representative of a species. (**A**) PC1 score plotted against species durations (hesperocyonines, $n = 16$, $r^2 = 0.03$, $P = 0.55$; borophagines, $n = 26$, $r^2 = 0.1$, $P = 0.12$). Note that values on PC1 are reversed. (**B**) Species durations plotted against mean frequency in individual fossil collections. (hesperocyonines, $n = 14$, $r^2 = 0.01$; $P = 0.73$; borophagines, $n = 27$, $r^2 = 0.004$, $P = 0.74$). M_1 length is also not correlated with mean frequency (analysis not shown; hesperocyonines, $n = 14$, $r^2 = 0.004$; $P = 0.82$; borophagines, $n = 26$, $r^2 = 0.007$, $P = 0.69$).

results in a lineage that is less likely to persist (*29*). The risk of extinction will rise if the evolutionary trend is associated with a decline in population density and/or increased trophic specialization (given that reversals are uncommon). The same or a similar ratchet might be responsible for the decline to extinction of many formerly successful groups of organisms, especially in mammals, where Cope's rule is often observed and species turnover rates tend to be high (*21*, *29*).

References and Notes

1. B. Van Valkenburgh, *Annu. Rev. Earth Planet. Sci.* **27**, 463 (1999).
2. X. Wang, *Bull. Am. Mus. Nat. Hist.* **221**, 1 (1994).
3. X. Wang, R. H. Tedford, B. Taylor, *Bull. Am. Mus. Nat. Hist.* **243**, 1 (1999).
4. R. H. Tedford, in *Nutrition and Management of Dogs and Cats* (Ralston Purina, St. Louis, MO, 1978), chap. M23.
5. B. Van Valkenburgh, T. Sacco, X. Wang, *Bull. Am. Mus. Nat. Hist.* **278**, 147 (2003).
6. B. Van Valkenburgh, in *Body Size in Mammalian Paleobiology*, J. Damuth, B. MacFadden, Eds. (Cambridge Univ. Press, Cambridge, 1990), pp. 181–205.
7. To predict the body mass of the extinct canids, we used the allometric relation established for living canid species [$\log_{10}$ $Mass_{kg}$ = 1.82($\log_{10}$ $M_1Length_{mm}$) – 1.22; n = 27, r = 0.87]. Using this equation, the smallest hesperocyonine in our sample weighed about 2 kg and the largest 26 kg. The same values for the borophaginae are 2 kg and 42 kg.
8. B. Van Valkenburgh, *Paleobiology* **17**, 340 (1991).
9. B. Van Valkenburgh, K. Koepfli, *Symp. Zool. Soc. London* **65**, 15 (1993).
10. These measurements are as follows: jaw length, distance between posterior margin of mandibular condyle and anterior margin of canine tooth; jaw depth, maximum dorsoventral depth of dentary measured at junction of M_1 and M_2; lower carnassial length, maximum mesiodistal length of lower M_1; lower carnassial blade length, maximum mesiodistal length of the M_1 trigonid; upper carnassial length, maximum mesiodistal length of upper fourth premolar; upper molar grinding area, the sum of the products of width and length of upper M^1 and M^2. Morphometric indices are as follows: relative jaw depth = jaw depth/jaw length; relative blade length = lower M_1 trigonid length/lower M_1 length; relative grinding area = square root of upper molar grinding area/upper carnassial length. All measurements were made with calipers by X.W.
11. Current researchers often define Cope's rule as a net tendency toward size increase throughout a clade's entire history and across all of its lineages (*21*, *30*). Our conclusions do not depend on the satisfaction of this strict definition, only on whether canid clades were dominated by species of large body size and hypercarnivorous diets relatively late in their histories. Nevertheless, based on the sample of phylogenetically independent ancestor/descendant size transitions implied by the full phylogenies for each clade (*2*, *3*), in both subfamilies, numbers and magnitudes of size increases significantly exceeded size decreases [hesperocyonines, 11+, 2–, P = 0.02 (sign test), P = 0.01 (Wilcoxon signed rank test); borophagines, 16+, 6–, P = 0.05 (sign test), P = 0.04 (Wilcoxon signed rank test); species sizes are based on the average length of the first lower molar; Wilcoxon tests are based on log (base 10)–transformed data].
12. J. A. Baskin, in *Evolution of Tertiary Mammals of North America*, C. M. Janis, K. M. Scott, L. L. Jacobs, Eds. (Cambridge Univ. Press, Cambridge, 1998), pp. 144–151.
13. J. Damuth, *Nature* **290**, 699 (1981).
14. J. Damuth, *Biol. J. Linn. Soc* **31**, 193 (1987).
15. J. Damuth, *Nature* **365**, 748 (1993).
16. A. K. Behrensmeyer, D. Western, D. E. Dechant Boaz, *Paleobiology* **5**, 12 (1979).
17. J. Damuth, *Paleobiology* **8**, 434 (1982).
18. The mean frequency of each canid species in individual fossil collections where it occurs was based on the number of canid specimens reported, by locality (*3*, *4*), for those species used in the PCA. These values were divided by the total number of specimens collected from the respective localities, when available. Only collections totaling ≥15 specimens were used. Sources for total specimen numbers included some literature compilations (*31*, *32*), direct counts of museum specimens, and numbers of specimens reported in online museum catalogs (Univ. of California Museum of Paleontology, Berkeley, CA; Field Museum of Natural History, Chicago, IL; American Museum of Natural History, New York; Yale Peabody Museum, New Haven, CT). The catalog sources likely sometimes inflate the canid frequencies by not including uncataloged material, but in cases where comparisons could be made, the values derived from the three sources were in rough agreement. The mean for each species is based on from 1 to 24 collections (average, 5.3) and represents a total of 233 species occurrences.
19. J. C. Barry *et al.*, *Paleobiology* **28** (suppl.), 1 (2002).
20. A. Purvis, J. L. Gittleman, G. Cowlishaw, G. M. Mace, *Proc. R. Soc. London Ser. B* **267**, 1947 (2000).
21. J. Alroy, *Science* **280**, 731 (1998).
22. M. L. McKinney, in *Evolutionary Trends*, K. J. McNamara, Ed. (Univ. of Arizona Press, Tucson, AZ, 1990), pp. 75–120.
23. S. Stanley, *Evolution* **27**, 1 (1973).
24. F. Palomares, T. M. Caro, *Am. Nat.* **153**, 492 (1999).
25. B. Van Valkenburgh, in *Meat-Eating and Human Evolution*, C. Stanford, H. T. Bunn, Eds. (Oxford Univ. Press, Oxford, 2001), pp. 101–121.
26. C. M. Janis, K. M. Scott, L. L. Jacobs, Eds., *Evolution of Tertiary Mammals of North America* (Cambridge Univ. Press, Cambridge, 1998).
27. C. Carbone, G. M. Mace, S. C. Roberts, D. W. Macdonald, *Nature* **402**, 286 (1999).
28. B. Van Valkenburgh, I. Jenkins, in *The Fossil Record of Predation*, M. Kowalewski, P. H. Kelley, Eds. (The Paleontological Society Papers, The Paleontological Society, Washington, DC, 2002), vol. 8, pp. 267–288.
29. S. Stanley, *Macroevolution: Pattern and Process*. (Freeman, San Francisco, CA, 1979).
30. D. Jablonski, *Nature* **385**, 250 (1997).
31. M. F. Skinner, F. W. Johnson, *Bull. Am. Mus. Nat. Hist.* **178**, 215 (1984).
32. M. R. Voorhies, "Vertebrate paleontology of the proposed Norden Reservoir area, Brown, Cherry, and Keya Paha Counties, Nebraska: Lincoln, Nebraska" (Technical Report 82-09, Univ. of Nebraska, prepared for the U.S. Bureau of Reclamation, 1990).

33. For helpful comments on the manuscript, we thank P. Adam, A. R. Friscia, J. Meachan, J. Samuels, R. H. Tedford, R. K. Wayne, M. Webster, participants in the UCLA Paleobiology journal club, and two anonymous reviewers.

7 July 2004; accepted 26 August 2004

Basis for Structural Diversity in Homologous RNAs

Andrey S. Krasilnikov,[1] Yinghua Xiao,[1] Tao Pan,[2] Alfonso Mondragón[1]*

Large RNA molecules, such as ribozymes, fold with well-defined tertiary structures that are important for their activity. There are many instances of ribozymes with identical function but differences in their secondary structures, suggesting alternative tertiary folds. Here, we report a crystal structure of the 161-nucleotide specificity domain of an A-type ribonuclease P that differs in secondary and tertiary structure from the specificity domain of a B-type molecule. Despite the differences, the cores of the domains have similar three-dimensional structure. Remarkably, the similar geometry of the cores is stabilized by a different set of interactions involving distinct auxiliary elements.

Ribonuclease (RNase) P is one of only two known ribozymes conserved in all taxonomic kingdoms and is responsible for maturation of the 5′ end of tRNA (*1*, *2*). It is a multiple-turnover endonuclease that contains an RNA subunit and protein components. In bacteria, the RNA subunit is capable of cleaving pre-tRNA without its protein partner in vitro (*3*, *4*). Most of the bacterial RNase Ps can be classified into two major distinct types—A and B—on the basis of the sequence of the RNA component. In both types of bacterial RNase P, the RNA consists of two independently folding domains: a specificity domain and a catalytic domain. The specificity (S) domain is responsible for substrate recognition and binding (*5*, *6*).

Although the RNA components of all bacterial RNase P types share many secondary-structural features throughout the molecule, there are noticeable differences (*3*, *4*). In particular, the S domains of the two major bacterial types exhibit differences in secondary structure that might affect the tertiary fold (Fig. 1). Most noticeably, in the A-type RNase P, the P10.1 stem is absent and the J12/11 internal loop is interrupted by the insertion of the P13 and P14 stems, which are not present in the B type. Because the major tertiary interactions in the S domain of B-type RNase P involve the P10.1 stem (*7*), a substantially different fold for the A-type RNase P could be anticipated. However, biochemical data indicate that substrate recognition involves equivalent nucleotides in both types (*8*, *9*), suggesting similar structures for the pre-tRNA recognition region.

[1]Department of Biochemistry, Molecular Biology, and Cell Biology, Northwestern University, Evanston, IL 60208, USA. [2]Department of Biochemistry and Molecular Biology, University of Chicago, 920 East 58th Street, Chicago, IL 60637, USA.

*To whom correspondence should be addressed. E-mail: a-mondragon@northwestern.edu

The S domain of *Thermus thermophilus* RNase P (nucleotides 75 to 235) was crystallized as described (*10*). The crystal structure was solved to 2.9 Å resolution from a single-wavelength anomalous diffraction experiment with the use of Ba^{+2} as the anomalous scatterer (*10*, *11*). A second crystal form was also solved and the structures proved to be identical (*12*).

The crystal structure of the S domain of the A-type *T. thermophilus* RNase P is shown in Fig. 1A. The general features of the structure match the predictions based on sequence and phylogenetic analysis very well (*13*, *14*) and agree with available biochemical data (*9*, *10*, *14*). The central feature of the structure is a large nonhelical module formed by the J11/12 and J12/11 internal loops that sits atop a four-way junction formed by stems P7 to P11 (Fig. 1). Stem P12 joins the J11/12 and J12/11 internal loops, and stems P13 and P14, which are unique to the A-type molecules, branch out of this nonhelical module and stabilize the molecule by forming tertiary interactions with P12 and P8, respectively.

The fold of the domain differs substantially from the previously reported S domain of the B-type *Bacillus subtilis* RNase P (*7*) (Fig. 1B). The fold of the P7–P11 four-way junction is similar in A- and B-type S domains (*7*): Stems P8 and P9 and stems P7, P10, and P11 form two semicontinuous stacks, as predicted (*13*) (Fig. 2A). The angle between stems P8 and P9 and stems P7, P10, and P11, however, differs by about 20° in the two structures. This difference likely reflects the inherent flexibility of the four-way junction and is consistent with

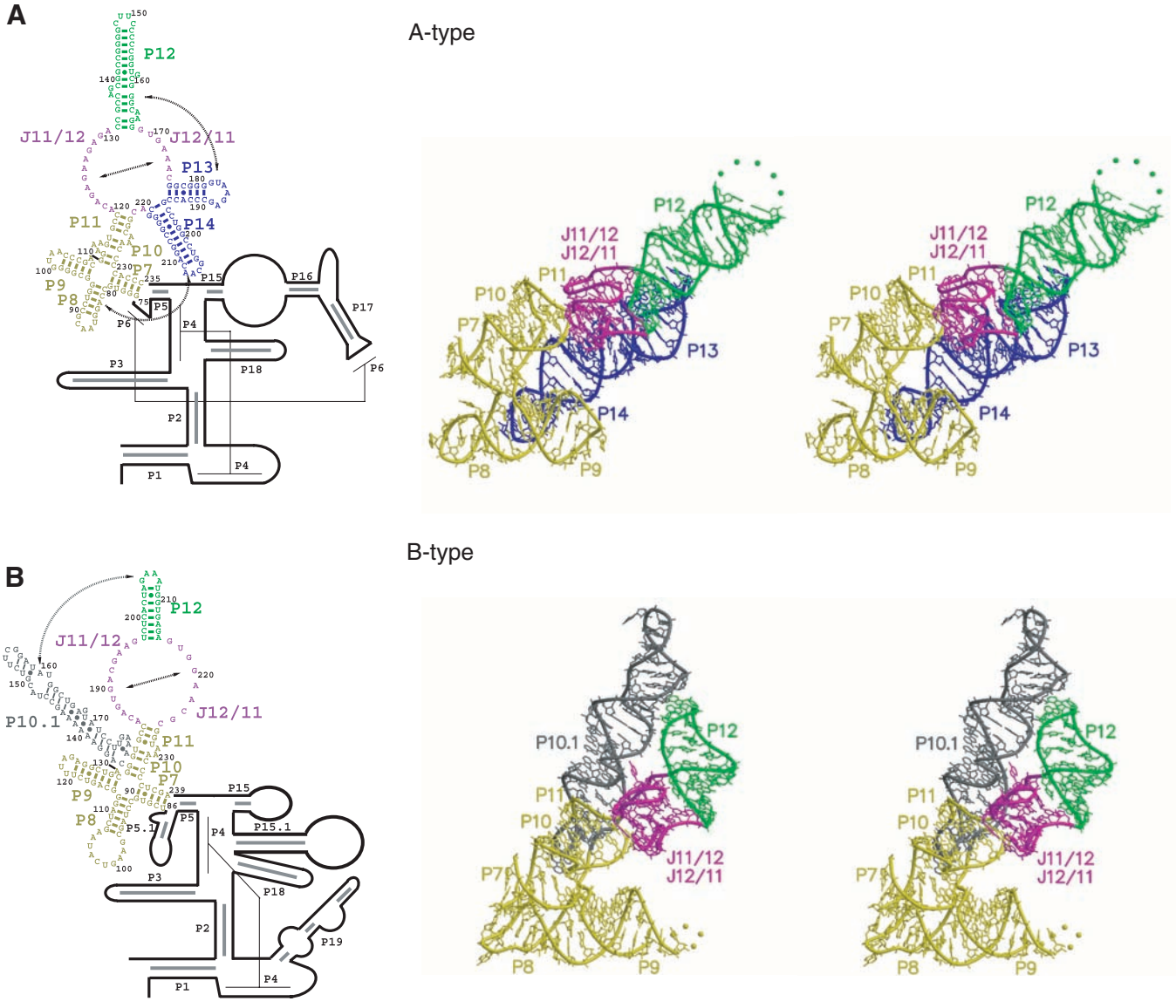

Fig. 1. Secondary-structure diagrams and structures of the specificity domain of A- and B-type bacterial RNase P. The two major bacterial RNase P types are defined by sequence characteristics of their RNAs. In both cases, the RNA component consists of two independently folded structural domains: a specificity domain (shown in colors) and a catalytic domain (shown in black). Major tertiary interactions in the specificity domain are shown with dotted arrows. The nomenclature and the catalytic domain secondary structure are according to (*25*). The specificity domain secondary-structure diagrams are based on the structural information. In all cases, the four-way junction formed by stems P7 to P11 is shown in yellow, the nonhelical module J11/12-J12/11 in magenta, the P12 stem in green, the P13 and P14 stems in blue, and the P10.1 stem in gray. (**A**) A-type bacterial RNase P. The left panel shows the secondary-structure diagram and the right panel shows a stereodiagram of the crystal structure of the *T. thermophilus* specificity domain. The putative path of a disordered tetraloop closing the P12 stem is shown with a dotted line. (**B**) B-type bacterial RNase P. The left panel shows the secondary-structure diagram and the right panel shows a stereodiagram of the crystal structure of the *B. subtilis* specificity domain (*7*). The putative path of a disordered tetraloop closing the P9 stem is shown with a dotted line. Of the two molecules in the asymmetric unit in the crystal structure (*7*), the more complete molecule is shown here and below.

the flexibility observed in the B-type RNase P, in which the angle differed by about 10° when the two molecules in the asymmetric unit were compared (*7*). The helical geometry of the P10 and P11 stems is substantially distorted by the presence of unpaired nucleotides A(225) to A(226) and a trinucleotide loop A(112) to A(114). B-type molecules do not have an analog of the A(112) to A(114) loop but instead have the P10.1 stem inserted at that position (*7*). Nevertheless, the P10 and P11 stems are similar in both types [root mean square deviation (RMSD) = 1.6 Å], as previously suggested (*7*). The helical distortion of the P10 and P11 stems seems to be a necessary feature of the S domains and is accomplished in two distinct ways (Fig. 2A).

The large nonhelical module formed by J11/12 and J12/11 contains nucleotides that are highly conserved across all species and is a universal feature of all RNase Ps (*3*). Furthermore, this module is directly involved in substrate interactions (*8*, *9*). In both major bacterial RNase P types, the nonhelical module is stabilized by an intricate network of stacking interactions and hydrogen bonds but does not contain any Watson-Crick base pairs (Fig. 2B). The module contains two interleaving pentaloops [A(122) to A(126) and U(170) to A(174) in *T. thermophilus*], each of which is folded into a T-loop motif (*15*, *16*) and is followed by a dinucleotide platform (*17*, *18*) [A(126) to A(127) and A(174) to C(175)]. In the structures of both S-domain types, this region has a very similar fold (Fig. 2B), but the presence of P13 and P14 and differences in P12 cause changes in J11/12 and J12/11 away from the pentaloops. For example, in *T. thermophilus* RNase P, nucleotides G(128) to A(131) fold differently as a result of the stacking of A(131) on A(165) from the P12 stem. Surprisingly, the insertion of the P13 and P14 stems into the J12/11 loop is accommodated with little distortion (Fig. 2B). P13 and P14 form a continuous stack, as predicted (*13*), with the bulged base G(218) involved in a base stack with G(188) from the loop of P13.

Although the P12 stem is present in both types of bacterial RNase P, it is positioned differently (Fig. 1). In B-type RNase P, the top of the P12 stem forms a tetraloop that interacts with a tetraloop receptor in the P10.1 helix. This interaction is impossible in A-type RNase Ps because they lack the P10.1 stem. Instead, adenosines A(184) and A(185) in the U-turn (*18*) at the top of the P13 stem [U(183) to A(185)] form A-minor or ribose-zipper (*19*, *20*) interactions with the base pairs C(135)-G(163) and C(136)-G(162) from the P12 stem, and the 2′-OH group of G(186) forms a hydrogen bond with the 2′-OH of C(164) (Fig. 3). In addition, a distortion in the P12 stem results in a stacking interaction between A(184) in the P13 loop and G(138) in the P12 stem (Fig. 3). At the other end of the P13 and P14 stack, a tetraloop [G(205) to A(208)] interacts with the P8 stem, and the two adenosines from the loop enter the minor groove of P8 to form A-minor or ribose-zipper (*19*, *20*) interactions with the C(80)-G(94) and C(81)-G(93) pairs. Interactions between the P12 stem and the P13 loop and between the P14 loop and the P8 stem had been suggested previously (*2*, *13*, *14*).

Despite the different overall fold of the S domains in the two bacterial types, they share a major common feature: an opening formed by stems P9, P10 and P11, and the

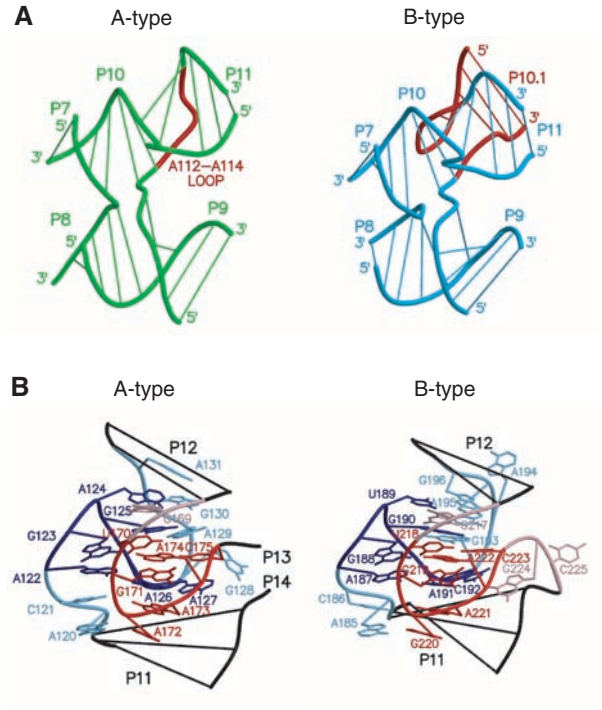

Fig. 2. The differences in the two types of the specificity domain are accommodated without substantial distortions in the functionally important four-way junction and J11/12-J12/11 nonhelical module. The base pairs are shown as thin lines connecting the phosphate backbones. (**A**) Structures of the four-way junctions in the A and B types of RNase P. In the A type (shown in green on the left), the A(112) to A(114) loop (red) compensates for the absence of the P10.1 stem found in the B type (shown on the right in blue with P10.1 in red). In both types, the four-way junction is formed in a similar manner with equivalent local interactions: The bases of A(226), from stem P11, and A(108), from stem P9, form a stack and A(225), from stem P11, intercalates between G(111) and A(112), from stem P10, whereas A(112) forms a triple base with the U(116)-A(227) base pair (the numbering is for *T. thermophilus*; the bases are not shown for clarity). (**B**) Structures of the J11/12-J12/11 nonhelical modules in the A and B types of RNase P (on the left and right, respectively). In the A type, the P13 and P14 stems interrupt the J12/11 loop. In spite of different sequences and the insertion of the P13 and P14 stems in the A-type molecules, the region formed by the interleaving pentaloops is structurally conserved (with RMSD of 0.84 Å when the two pairs of the pentaloops are compared), whereas the 3′-termini of the J11/12 loops are folded differently. The RMSD between the two assemblies of conserved parts of J11/12-J12/11 and P11 is 1.6 Å. The structural conservation of the interleaving pentaloops is expected to extend to RNase Ps from all kingdoms of life. The internal loops J11/12 and J12/11 are shown in blue and pink, respectively. The interleaving pentaloops, each folded into a T-loop motif (*15, 16*) followed by a dinucleotide platform, are highlighted in dark blue and red.

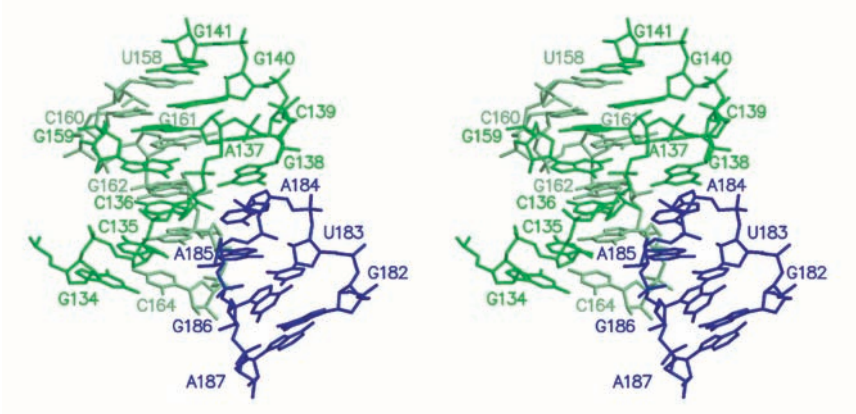

Fig. 3. The P12 and P13 stems interact in A-type RNase P. The stereopair illustrates the interactions between the P12 stem (green) and the terminal loop of P13 (blue) in the specificity domain of A-type RNase P. Adenosines A(184) to A(185) from the U(183) to A(185) U-turn (*18*) in the P13 stem enter the minor groove of the P12 helix, forming A-minor or ribose-zipper interactions (*19*, *20*) involving base pairs G(162)-C(136) and G(163)-C(135). In addition, the 2′-OH of G(186) forms a hydrogen bond with the 2′-OH of C(164). Distortions in the P12 stem allow the formation of a base stack between A(184) and G(138).

nonhelical module J11/12-J12/11 (Fig. 4). In both cases, nucleotides that were shown to be involved in direct interactions with the substrate [the equivalent of A(108) from P9, A(226) from P11, and A(172) from J12/11 in *T. thermophilus*] (*8*, *9*) face this opening and expose their bases to the solvent. The shape of this opening is defined by both the structural elements that form it and their relative orientation. The global architecture of the elements involved differs in the two S domains: The B type contains the P10.1 stem rather than the A(112) to A(114) loop, the A type contains the P13 and P14 stems in J12/11, and both exhibit different folds in the 3′ regions of J11/12 as well as distinct orientations and interactions of the P12 stem. In spite of these large differences, however, the local positions of the nucleotides involved in forming the opening are remarkably similar. In A-type RNase P, the A(112) to A(114) loop compensates for the absence of the P10.1 stem, and the insertion of the P13 and P14 stems is arranged in a way that does not affect the local folding of the J12/11 internal loop (Fig. 2). Moreover, to maintain the shape of the opening, the nonhelical module J11/12-J12/11 must be in a particular orientation relative to the P9, P10, and P11 stems. In the two types of S domain, the same relative orientation is stabilized in two different ways: by a tetraloop-tetraloop receptor interaction (*18*, *20*) between stems P12 and P10.1 and an A-minor or ribose-zipper interaction (*19*, *20*) between the P10.1 pentaloop and the P10 stem in the B type (*7*) and by A-minor or ribose-zipper interactions between stems P14 and P8 and between stems P13 and P12 in the A type. This notable structural conservation in the pre-tRNA recognition region likely extends across all three kingdoms of life, given that the J11/12-J12/11 module and the P7–P10 (or P7–P11) four-way junction are universally conserved (*3*).

Several nucleotides in the nonhelical module formed by J11/12-J12/11 are conserved in all RNase Ps of known sequence in all kingdoms of life (*3*). The two S-domain structures show remarkable structural conservation within this region, and phylogenetically conserved nucleotides map to the T-loop motifs of the interleaving pentaloops. Sequence analysis shows that the consensus for the two pentaloops satisfies the sequence requirements for the T-loop motif (*16*), making it plausible that the sequence conservation arises from strong structural constraints.

The high degree of structural conservation and the size of the opening formed by the nonhelical module J11/12-J12/11 and the P9, P10, and P11 stems (Fig. 4), combined with the presence of the nucleotides directly involved in interaction with the substrate, strongly suggest that this region accommodates the pre-tRNA and orients it for interaction with the catalytic domain. Additionally, the geometry of the opening in the A- and B-type S domains, taken together with the available biochemical data on RNase P interaction with the substrate (*8*, *9*), suggests that the substrate lies partially immersed in the opening, with the long axis of the T-stem of pre-tRNA across the opening and the Tψ-loop of the pre-tRNA molecules facing the U(170) to A(174) (*T. thermophilus*) pentaloop in J12/11. This positions the nucleotides at the T-stem in close proximity to the bulged A(108) and A(226) bases (*T. thermophilus*) from the P9 and the P10 and P11 stems.

The specificity domains from A- and B-type RNase P represent two different large RNA molecules with identical function. Their structural comparison demonstrates that functionally important core regions are structurally preserved at the local level, whereas the overall fold of the molecules differs as a result of variability in auxiliary elements that serve to stabilize this invariant three-dimensional core. The richness of the variety of possible intramolecular interactions within RNA molecules allows for the formation of similar local folds in different global environments, thus contributing to the great structural variety of RNAs.

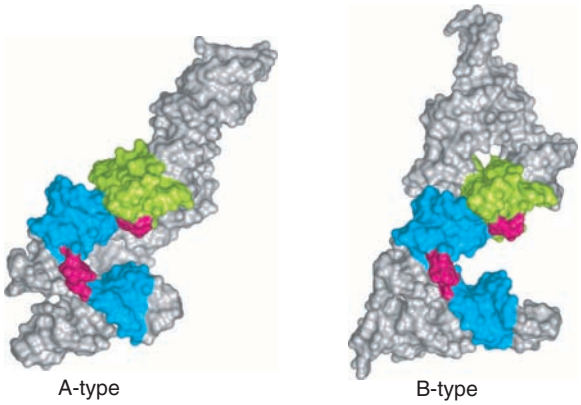

Fig. 4. Structural conservation of the pre-tRNA recognition region. The opening formed by nonhelical region J11/12-J12/11 (green) and stems P9, P10, and P11 (blue) contains nucleotides involved in pre-tRNA binding (red). The structure of this region is conserved despite the differences in the overall fold of the specificity domains in the two RNase P types. The nucleotides directly involved in interactions with the pre-tRNA substrate (*8*, *9*) [A(108), A(172), and A(226) in *T. thermophilus* and A(130), G(220), and A(230) in *B. subtilis*] are located in similar positions. In the two RNase P types, the pre-tRNA recognition regions adopt the same geometry but are stabilized differently.

References and Notes

1. S. Altman, L. A. Kirsebom, in *The RNA World*, R. F. Gesteland, T. R. Cech, J. F. Atkins, Eds. (Cold Spring Harbor Laboratory Press, Cold Spring Harbor, NY, 1999), pp. 351–380.
2. D. N. Frank, N. R. Pace, *Annu. Rev. Biochem.* **67**, 153 (1998).
3. J.-L. Chen, N. R. Pace, *RNA* **3**, 557 (1997).
4. J. W. Brown, E. S. Haas, D. G. Gilbert, N. R. Pace, *Nucleic Acids Res.* **22**, 3660 (1994).
5. A. Loria, T. Pan, *RNA* **2**, 551 (1996).
6. T. Pan, *Biochemistry* **34**, 902 (1995).
7. A. S. Krasilnikov, X. Yang, T. Pan, A. Mondragón, *Nature* **421**, 760 (2003).
8. L. Odell, V. Huang, M. Jakacka, T. Pan, *Nucleic Acids Res.* **26**, 3717 (1998).
9. T. E. LaGrandeur, A. Huttenhofer, H. F. Noller, N. R. Pace, *EMBO J.* **13**, 3945 (1994).
10. Materials and methods are available as supporting material on *Science* Online.
11. The phase ambiguity in single-wavelength anomalous diffraction phasing was partially resolved using OASIS (*21*) and solvent flattening as implemented in SHARP (*22*). Cycles of model building with O (*23*), refinement with CNS (*24*), and phasing with SHARP allowed the tracing of the molecule. The final R_{factor} and R_{free} are 24.1% and 27.5%, respectively. The RMSDs for bond lengths and angles are 0.005 Å and 1.27°, and the mean *B* factor is 87 Å^2. The model contains 21 Ba^{+2} ions as well as all RNA atoms except for disordered nucleotides 75, 148 to 151, and 235.
12. The specificity domain also crystallized in an alternative crystal form. The structure of the second form (solved to 3.2 Å resolution by molecular replacement) was shown to be practically identical to the original one and was not refined further.
13. C. Massire, L. Jaeger, E. Westhof, *J. Mol. Biol.* **279**, 773 (1998).
14. J. L. Chen, J. M. Nolan, M. E. Harris, N. R. Pace, *EMBO J.* **17**, 1515 (1998).
15. U. Nagaswamy, G. E. Fox, *RNA* **8**, 1112 (2002).
16. A. S. Krasilnikov, A. Mondragon, *RNA* **9**, 640 (2003).
17. J. H. Cate *et al.*, *Science* **273**, 1696 (1996).
18. P. B. Moore, *Annu. Rev. Biochem.* **68**, 287 (1999).
19. P. Nissen, J. A. Ippolito, N. Ban, P. B. Moore, T. A. Steitz, *Proc. Natl. Acad. Sci. U.S.A.* **98**, 4899 (2001).
20. J. H. Cate *et al.*, *Science* **273**, 1678 (1996).
21. Collaborative Computational Project Number 4, *Acta Crystallogr.* **D50**, 760 (1994).
22. E. delaFortelle, G. Bricogne, *Methods Enzymol.* **276**, 472 (1997).
23. T. A. Jones, J. Y. Zou, S. W. Cowan, M. Kjeldgaard, *Acta Crystallogr.* **A47**, 110 (1991).
24. A. T. Brunger *et al.*, *Acta Crystallogr.* **D54**, 905 (1998).
25. E. S. Haas, A. B. Banta, J. K. Harris, N. R. Pace, J. W. Brown, *Nucleic Acids Res.* **24**, 4775 (1996).
26. We thank C. Correll, E. Sontheimer, A. Torres, O. Uhlenbeck, J. Wedekind, and B. Wurzburg for comments and suggestions. We thank members of DuPont-Northwestern-Dow Collaborative Access Team (DND-CAT) for help with data collection. Research was supported by NIH (A.M.) and an NIH National Research Service Award Fellowship (A.K.). We acknowledge support from the R.H. Lurie Cancer Center of Northwestern University to the Structural Biology Center. Portions of this work were performed at the DND-CAT Synchrotron Research Center at the Advanced Photon Source (APS). DND-CAT is supported by DuPont, Dow, and NSF and use of the APS is supported by the U.S. Department of Energy. Coordinates and structure factors have been deposited in the Protein Data Bank under the accession code 1U9S.

Supporting Online Material

www.sciencemag.org/cgi/content/full/306/5693/104/DC1
Materials and Methods
Figs. S1 to S3
Tables S1 and S2
References

15 June 2004; accepted 20 August 2004

Interstitial Collagenase Is a Brownian Ratchet Driven by Proteolysis of Collagen

Saveez Saffarian,[1] Ivan E. Collier,[2] Barry L. Marmer,[2] Elliot L. Elson,[1] Gregory Goldberg[1,2]*

We show that activated collagenase (MMP-1) moves processively on the collagen fibril. The mechanism of movement is a biased diffusion with the bias component dependent on the proteolysis of its substrate, not adenosine triphosphate (ATP) hydrolysis. Inactivation of the enzyme by a single amino acid residue substitution in the active center eliminates the bias without noticeable effect on rate of diffusion. Monte Carlo simulations using a model similar to a "burnt bridge" Brownian ratchet accurately describe our experimental results and previous observations on kinetics of collagen digestion. The biological implications of MMP-1 acting as a molecular ratchet tethered to the cell surface suggest new mechanisms for its role in tissue remodeling and cell-matrix interaction.

The extracellular matrix (ECM) of vertebrates is a three-dimensional scaffold consisting of highly organized macromolecular assemblies that vary in structure and composition to define and maintain the shapes and mechanical properties of tissues. Many physiological and pathophysiological processes from morphogenesis to wound healing, tumor progression, and metastatic invasion are characterized by intensified tissue remodeling that begins with degradation of the existing ECM (*1*, *2*).

Collagen is the most abundant component of the ECM. Monomers of fibrillar collagens have a unique triple-helical structure that self-assembles to produce tightly packed periodic fibrils (*3*). Fibrils can be up to 500 nm in diameter and are highly resistant to proteolytic degradation. Resident cells of tissues can secrete a specialized group of enzymes, matrix metalloproteases (MMPs), that degrade ECM macromolecules including collagens (*4*). Interstitial collagenase, MMP-1 (*5*, *6*), cleaves all three α chains of the collagen monomer at a single site. The assembled collagen fibril contains multiple cleavage sites spaced 300 nm apart. Here, we demonstrate that the digestion of a collagen fibril occurs when the bound MMP-1 undergoes biased diffusion along the fibril and encounters cleavage sites without noticeable dissociation. The MMP-1 transport mechanism is akin to a Brownian ratchet with biased diffusion independent of ATP hydrolysis but coupled to collagen proteolysis instead.

[1]Department of Biochemistry and Molecular Biophysics and [2]Division of Dermatology, Washington University School of Medicine, St. Louis, MO 63110, USA.

*To whom correspondence should be addressed. E-mail: goldberg@medicine.wustl.edu

Feynman showed (*7*) that particles diffusing in an anisotropic environment cannot produce work in an isothermal system, but a thermal gradient applied to the same system can bias the diffusion. This makes microscopic machines plausible. There are now several models of biased diffusion that do not require a system-wide gradient or field (*8*), among them Brownian ratchets (*9*–*12*). In a "burnt bridge" model of a Brownian ratchet (*13*), the diffusion bias is created because the moving particle destroys weak places on its track, so its ability to diffuse back is inhibited. A slight modification of the burnt bridge model explains our observation of MMP-1 activity.

We used two-photon excitation fluorescence correlation spectroscopy (FCS) to observe the interaction of MMP-1 molecules with collagen fibrils in their most native state in a hydrated collagen gel. Under these conditions, the substrate is resistant to other nonspecific proteases. Collagen gels with oriented fibrils were produced by polymerizing acid-soluble rat-tail collagen in a magnetic field of 8 T (*14*) and were decorated with fluorescent dye (Alexa 488)–labeled enzyme (*15*). A selected individual fibril was centered under the 5-mW laser beam and illuminated for 120 s to achieve a constant average fluorescence, indicating a steady state. The initial exposure was immediately followed by collection of primary fluorescence data for 300 s with a bin time of 400 μs (Fig. 1, A.1). We obtained the control record from undecorated fibrils by using collagen luminescence for imaging. The primary fluorescence data from both the experiment and the control were dominated by shot noise. Increasing the bin time of the primary 400-μs record to 80 ms (Fig. 1, A.2) revealed large spikes of fluorescence present in the record obtained from MMP-1–decorated fibrils but not in the control record. The appearance of these spikes was completely suppressed when the bound Alexa 488–labeled enzyme was immobilized by cross-linking to the fibrils before observation. The intensity of the spikes was well within the limits expected for a single molecule of labeled enzyme [Fig. 1, A.3, and (*15*)]. Because contribution of enzyme readsorption to the appearance of the spikes is insignificant (*15*), we conclude that the spikes of fluorescence intensity observed in FCS experiments on an individual MMP-1–decorated fibril represent single molecules of the collagen-bound enzyme passing through the laser beam (*15*).

To isolate the spikes from the background [see Spatial Background Filter (*15*)], we scanned the 80-ms bin time record (Fig. 1, A.2) with a 2-s window. The fluorescence above the threshold set to five times the standard deviation of the average signal in each window was counted as a spike, and its position was recorded. This information was then used to suppress the background contribution and to calculate a correlation function (Fig. 1B) using the 400-μs binned fluorescence record (*15*, *16*). A particle diffusing freely in one dimension has a finite probability of returning to a point that it visited previously. Therefore, the correlation function characteristic of one-dimensional (1D) diffusion has an elongated tail. The experimental correlation function for the active enzyme (Fig. 1B) deviates from the free diffusion model (*15*) but fits well to a 1D diffusion plus flow model (*17*) in which particles exhibit diffusive behavior at fast time scales but have zero probability of return at longer times, owing to the directional flow. The local diffusion coefficient $D = 8 \pm 1.5 \times 10^{-9}$ cm^2 s^{-1} and the transport velocity $V = 4.5 \pm 0.36$ μm s^{-1} were determined from the fit of the correlation function obtained from the wild-type activated MMP-1.

Biased diffusion is a characteristic of a molecular motor and requires energy dissipation. For classical molecular motors, energy comes from ATP hydrolysis (*18*–*20*). In the absence of ATP, we hypothesized that energy may come from coupling to proteolysis. To investigate this possibility, we inactivated the enzyme by a single point mutation, glutamic acid at position 219 to glutamine (E219Q), in its active center (*15*). The mutation specifically eliminates the catalytic activity of the enzyme with little or no effect on enzyme structure or binding to collagen (*21*, *22*). FCS measurements on the inactive MMP-1 mutant gave experimental correlation functions with an elongated tail consistent with 1D diffusion with no directional bias (Fig. 1B). The diffusion coefficient $D = 6.7 \pm 1.5 \times 10^9$ cm^2 s^{-1}

was similar to the diffusion coefficient of the active enzyme; this finding suggests that the inactivation of the enzyme has little effect on the diffusion properties of MMP-1 on the collagen fibrils and that the transport mechanism depends on the catalytic activity of the enzyme. The values of the diffusion coefficient obtained for wild-type and mutant MMP-1 on collagen fibril are in good agreement with those for MMP-2 proenzyme on a gelatin layer that we determined earlier (*23*).

To verify these results and to determine whether the biased component dominates the transport process on a macroscopic scale, we measured the flux of single MMP-1 molecules around a "no-transport" block created on a collagen fibril (Fig. 2). When MMP-1–decorated collagen fibrils are photobleached with a laser beam intensity below 50 mW, the fluorescence recovers after termination of the bleach pulse owing to diffusion of fresh MMP-1 molecules into the bleached region (*24*). Raising the laser intensity to 80 to 90 mW prevents the fluorescence recovery, which indicates a blockage of the enzyme transport across the bleached area because of damage to the fibril. A flux difference between the upstream and downstream regions would indicate directional transport of the MMP-1 on the fibril (Fig. 2). An asymmetry ratio is defined as the difference between the upstream and downstream fluxes divided by the total flux, so that a value of 1 indicates perfect asymmetry (flow dominates diffusion) and a value of 0, a completely symmetric diffusion. Flux is highly asymmetric for the wild-type active enzyme, whereas the inactive mutant shows complete symmetry (Fig. 2). Intermediate results were observed when proteolysis was inhibited in the presence of the metalloprotease inhibitor, Galardin, or the collagen fibrils were immersed in heavy water (*25*). Thus, the active MMP-1 bound to a collagen fibril undergoes proteolysis-dependent directional transport, with the degree of asymmetry in the flux depending on the efficiency of proteolysis.

What is the mechanism that rectifies symmetric diffusive motion to induce biased transport of the active enzyme along the fibril? We considered a theoretical model similar to a recently formalized burnt bridges Brownian ratchet (*13*), with two assumptions (Fig. 3): First, at recognition sites, a cleavage occurs with a probability P_C and the enzyme always ends up on a specific side of the cleaved peptide bond. Second, the molecules are not allowed to cross the cleaved collagen helix from either side but are allowed to

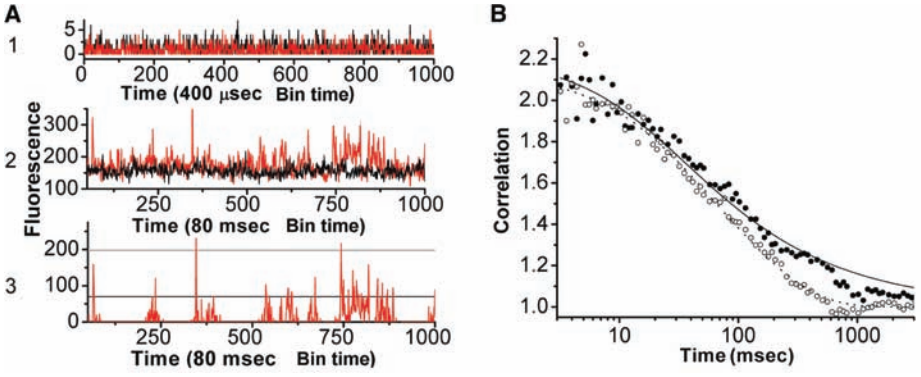

Fig. 1. Mobility of MMP-1 bound to a collagen fibril. (**A**) An individual collagen fibril was positioned under the laser beam by using a nano positioning stage. A constant average fluorescence indicating a steady state was achieved in the first 120 s, after which fluorescent signal was collected for 300 s with a 400-μs bin time. (**A.1**) Primary fluorescent record of an MMP-1–decorated (red) and an untreated collagen fibril (black) recorded at a 400-μs bin time and plotted as the number of collected photons versus the bin number. One thousand bins out of the entire 300-s experiment are shown. Both records are dominated by shot noise. (**A.2**) Primary fluorescent count record as in A.1 displayed with the bin time increased to 80 ms. Spikes of fluorescent counts are observed in the experiments performed on MMP-1–decorated fibrils. Background fluorescence from untreated collagen fibrils shows no spikes in the record. (**A.3**) The 80-ms binned record from A.2 was used for finding the position of the spikes (*15*). Isolated from the background, the spikes of fluorescence intensity represent single molecules of MMP-1 passing through the laser beam. The single-molecule fluorescence was measured in FCS experiments with Alexa 488–labeled MMP-1 in solution. The average value of 870 Hz (black line) and a maximum of 2.4 kHz (gray line) were calculated either by averaging the fluorescence over the entire observation volume or by assuming that the molecule traveled through the center of the 300-nm waist beam, respectively. The intensity of spikes is within the expected range for a single-molecule intensity. (**B**) The normalized experimental correlation functions were calculated by using the 400-μs binned records from six independent experiments. The background was suppressed using the spatial background filter (*15*). The correlation function obtained from collagen fibrils decorated with either wild-type activated MMP-1 (open circles) or its inactive mutant (filled circles). The experimental correlation function for wild-type activated enzyme was fitted (gray line) to a flow plus diffusion model (*17*)

$$G(t)=1+exp\left[-\left(t/\tau_f\right)^2\frac{1}{1+t/\tau_D}\right]\frac{1}{\left(1+t/\tau_D\right)^{0.5}}$$

where $\tau_D = w^2/4D$ is the diffusion time, $\tau_f = w/V$ is the flow time, w is the beam waist, D is the diffusion coefficient and V is the flow velocity. The shown fit of the wild-type MMP-1 data has a diffusion coefficient of $8 \pm 1.5 \times 10^{-9}$ cm^2 s^{-1} and a transport velocity of 4.5 ± 0.36 μm s^{-1}. The correlation function of the inactive mutant exhibits a long tail characteristic of an unbiased 1-D diffusion $G(\tau) = 1 + [1/(1 + t/\tau_D)^{0.5}]$, with a local diffusion coefficient of $6.7 \pm 1.5 \times 10^{-9}$ cm^2 s^{-1}.

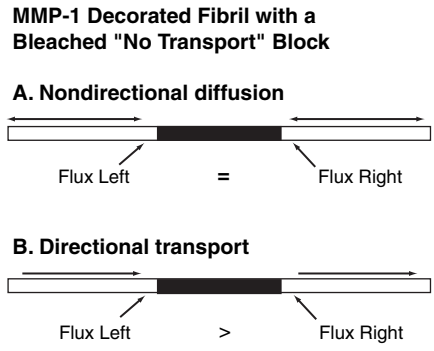

C. Average Number of Molecules in:

	Left Flux	Right Flux	Ratio
Activated WT	44.5	5.5	0.81±0.1
Inactivated mutant	50.6	42.3	0.1 ±0.06
Heavy water	34.5	14.5	0.39±0.08
Galardin	77.6	32	0.44±0.08

Fig. 2. The unequal flux of MMP-1 molecules around a no-transport block on the collagen fibril. (**A** and **B**) Photobleaching of MMP-1–decorated collagen fibrils (white bar) with a laser beam intensity below 50 mW results in the recovery of fluorescence after termination of beam exposure (*24*). Raising the laser intensity to 80 to 90 mW prevents recovery after photobleaching, which indicates a blockage of the enzyme transport across the bleached area (solid bar) due to a damage of the fibril. (**C**) The average number of single enzyme molecules passing through the laser beam in the left $\langle C_L \rangle$ and right $\langle C_R \rangle$ flanks of the no-transport block are calculated by counting the number of spikes in the fluorescence record and are averaged from three independent experiments for each form of the enzyme. The differences are expressed as the asymmetry ratio calculated as $\langle C_L - C_R/C_L + C_R \rangle$, which is then averaged over all three experiments so that 1 indicates a perfect asymmetry and 0 a completely symmetric experiment. The arrows indicate the direction of enzyme transport.

jump to a neighboring triple-helical track with a small probability P_J. This mechanism produces a net transport (*13*), with velocity V that depends on the diffusion coefficient, the probability P_C, and the spatial distribution of the cleavage sites along the tracks (300 nm apart for a collagen fibril).

The analytical solution of this model for an enzyme molecule moving on a single track with an equidistant distribution of sites and low P_C is given in (*13*). To model the behavior of an ensemble of the enzyme molecules diffusing on a fibril, we have constructed Monte Carlo simulations as described in [Fig. 3B and (*15*)]. The simulations (Fig. 4) demonstrate that both correlation functions and asymmetry ratios are dependent on P_C, whereas the rate of jumping to a neighboring triple-helical track P_J = 1/200 s remains constant (fig. S2). With the experimentally determined diffusion coefficient ($D = 8 \pm 1.5 \times 10^{-9}$ cm^2 s^{-1}) and a Gaussian laser profile with a waist of 300 nm, simulations of correlation functions and the asymmetry ratios (Fig. 4) reproduced those obtained experimentally for the active enzyme when P_C = 10%. Similarly, change of a value of a single parameter, $P_C = 2 \times 10^{-5}$, in simulations reproduced experimental data for the mutant enzyme (*15*). The asymmetry ratio has an exponential dependence on the probability of cleavage P_C so that a 50% decline in the asymmetry ratio corresponds to a two orders of magnitude drop in the cleavage probability. Because correlation functions and the asymmetry ratios are experimentally independent, it is notable that Monte Carlo simulations accurately predict both for active and inhibited enzymes, depending on the value of a single parameter P_C.

Because cleavage of a triple-helical track by a passing enzyme acts as a roadblock for molecules following on the same track, the model predicts the accumulation of enzyme molecules confined to a free diffusion between cleaved sites, which create a traffic jam. Relief of the traffic jam is achieved by the transfer of the trapped enzyme to new tracks with probability P_J. In the computer simulations where P_J = 1/200 s^{-1} and P_C = 10%, the traffic jam is seen as peaks of the enzyme concentration along the fibril that disappear when P_C = 0 (Fig. 4A, inset). In our experiments, the trapped enzyme is bleached during the first 120 s of beam exposure. The traffic jam phenomenon also explains certain peculiarities of the collagen digestion kinetics observed earlier (*26*). In these experiments, the overall speed of collagen digestion increased linearly with the enzyme concentration. However, at a nonsaturating concentration of MMP-1, the enzyme activity rose substantially with an increase of collagen substrate concentration. Under conditions of the traffic jam, presenting more substrate reduces the average concentration of the trapped enzyme, which causes an increase in overall digestion rate.

Thermodynamic measurements support this interpretation. At a constant substrate concentration, the acquisition of the new tracks

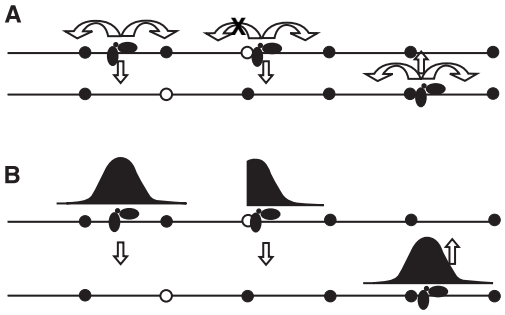

Fig. 3. Burnt bridges mechanism of MMP-1 transport on a collagen fibril. (**A**) The rules of the road. The enzyme molecules perform a random walk (curved open arrows) in one-dimension along a collagen fibril. Once they reach a cleavage recognition site (circles), a successful cleavage (open circles) occurs with a set probability P_C, and the enzyme molecule responsible for the cleavage always ends up on one specific side of the cleaved peptide bond. The molecules are not allowed to cross the cleaved triple helix from either side but are allowed to jump to a neighboring triple-helical track with a small probability P_J (vertical arrows). This mechanism, akin to a Brownian ratchet, produces a net transport with velocity V, which depends on a diffusion coefficient, the probabilities defined above and the spatial distribution of the cleavage sites. (**B**) Monte Carlo simulations of the interaction of MMP-1 with a collagen fibril. To construct a Monte Carlo simulation of MMP-1 motion on collagen, we monitored 10 enzyme molecules on a 30-μm-long fibril with a cross section of 100 triple helixes of collagen and cleavage sites 0.3 μm apart. In the beginning of an experiment, MMP-1 molecules were positioned randomly on a fibril and were allowed to diffuse according to the rules described above. The value of P_J was set at 1/200 s, and the diffusion coefficient was as determined experimentally. Once molecules exited the monitored 30-μm region they were put back on the opposite end of the fibril to approximate the conditions on a long fibril. The random walk steps have a Gaussian size distribution and walkers encounter a reflective boundary condition at each of the burnt bridges (open circles). In each case, the results of three Monte Carlo simulation runs with different seeds were averaged.

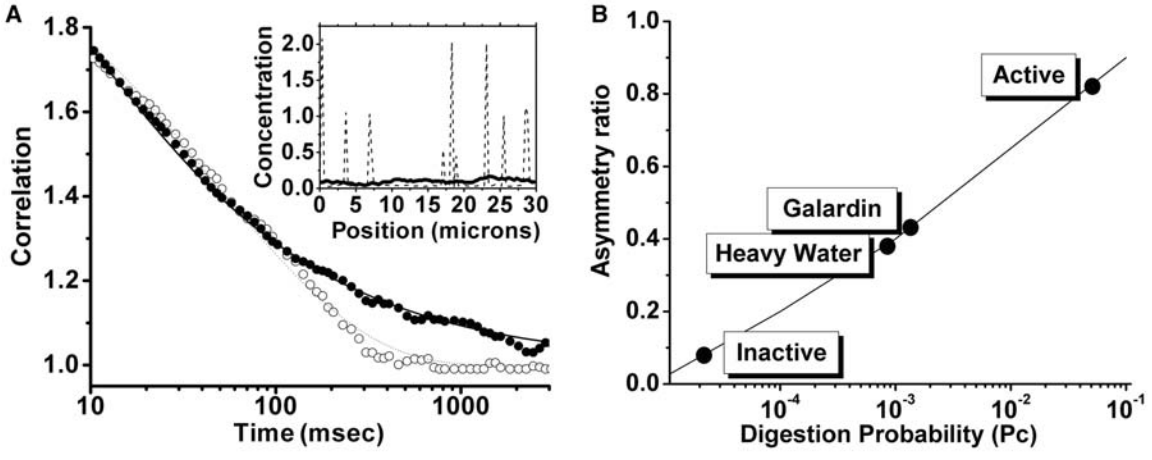

Fig. 4. Monte Carlo simulations of the experimental correlation functions and the asymmetry ratio. (**A**) Monte Carlo simulations were performed as in Fig. 3B. Two simulated correlation functions for P_C = 10% (open circles) and P_C = 0 (filled circles), each an average of three Monte Carlo simulation runs with different seeds, were fitted as in Fig. 1 with either 1D diffusion plus flow or 1D diffusion models, respectively. They are in good agreement with experimental functions obtained for WT and inactive mutant enzymes. (A, inset) The simulated concentration profiles of WT (dashed line) and inactive mutant (solid line) enzymes on a collagen fibril. The simulation was composed as described above. The concentration profile was summed over 24 s of the simulation. (**B**) Monte Carlo simulations were performed as in Fig. 3B with a reflective boundary condition set in the middle of the fibril representing the no-transport block. The number of molecules on each side of the block was recorded to calculate the asymmetry ratios as in Fig. 2. The simulations demonstrate that the asymmetry ratio is highly dependent on the value of P_C. The asymmetry ratios obtained experimentally with active MMP-1, its inactive mutant, and MMP-1 inhibited by the protease inhibitor Galardin, or heavy water, are indicated.

depends on unfolding of a collagen fibril that can become rate-limiting. The activation energy for fibril digestion (101 kcal mol^{-1}) was found to be 4 times that of a helical collagen monomer (*26*). The high energy of activation for collagenolysis is in good agreement, however, with the apparent energy of activation for collagen fibril unfolding (124 kcal mol^{-1}) measured more recently (*27*).

We thus conclude that the MMP-1–collagen system is a Brownian ratchet that is able to rectify Brownian forces into a propulsion mechanism by coupling to collagen proteolysis. The minimum power of 1.7×10^{-19} W per molecule of MMP-1 is required to propel the enzyme along the collagen fibril with the velocity $V = 4.5 \pm 0.36$ μm s^{-1}, which was calculated from the diffusion coefficient measured experimentally (*15*). A maximum power input for the directional transport of MMP-1 at room temperature (P_C = 10%) of 1.1×10^{-18} W per molecule of MMP-1 was calculated from the assumption of 5 kcal/mol of free energy for a cleaved peptide bond (*15*). The efficiency of the motor at room temperature can then be calculated as the ratio of power output over input to be 15% (*28*). These numbers are expected to change as the value of P_C increases with rise of the temperature.

The biological consequences of the collagenase motor activity are of great interest. We hypothesize that the collagenase ratchet can serve as a clutch mechanism, assisting cell locomotion on collagen matrices and contraction of collagen gels in three-dimensional cultures. Association of the enzyme with cell membranes via interaction with tissue-specific integrins can couple the extracellular proteolysis with the forces exerted by the cytoskeleton to direct membrane protrusions along a "no-skid" surface generated by the digestion of collagen fibrils. Membrane-type MMPs (*29*, *30*) can potentially act in a similar fashion. Experimental observations that clearly demonstrate the requirement of MMP-1–dependent collagenolysis for migration of keratinocytes on collagen support this hypothesis (*31*).

References and Notes

1. T. Vu, Z. Werb, *Genes Dev.* **14**, 2123 (2000).
2. M. Egeblad, Z. Werb, *Nature Rev. Cancer* **2**, 161 (2002).
3. K. E. Kadler, D. F. Holmes, J. A. Trotter, J. A. Chapman, *Biochem. J.* **316**, 1 (1996).
4. R. Visse, H. Nagase, *Circ. Res.* **92**, 827 (2003).
5. G. I. Goldberg *et al.*, *J. Biol. Chem.* **261**, 6600 (1986).
6. G. Fields, H. Van Wart, H. Birkedal-Hansen, *J. Biol. Chem.* **262**, 6221 (1987).
7. R. P. Feynman, R. B. Leighton, M. Sands, *The Feynman Lectures on Physics* (Addison-Wesley. Reading, MA, 1966), vol. 1.
8. R. D. Astumian, *Science* **276**, 917 (1997).
9. F. Jülicher, A. Ajdari, J. Prost, *Rev. Mod. Phys.* **69**, 1269 (1997).
10. C. Peskin, G. Odell, G. Oster, *Biophys. J.* **65**, 316 (1993).
11. J. Prost, J. F. Chauwin, L. Peliti, A. Ajdari, *Phys. Rev. Lett.* **72**, 2652 (1994).
12. R. F. Fox, *Phys. Rev. E* **57**, 2177 (1998).
13. J. Mai, I. M. Sokolov, A. Blumen, *Phys. Rev. E.* **64**, 011102 (2001).
14. J. Torbet, M. Ronziere, *Biochem. J.* **219**, 1057 (1984).
15. Materials and methods are available as supporting material on *Science* Online.
16. S. Saffarian, E. L. Elson, *Biophys. J.* **84**, 2030 (2003).
17. D. Magde, E. L. Elson, W. W. Webb, *Biopolymers* **17**, 361 (1978).
18. M. Schliwa, G. Woehlke, *Nature* **422**, 759 (2003).
19. R. D. Vale, R. A. Milligan, *Science* **288**, 88 (2000).
20. H. Qian, *Biophys. Chem.* **83**, 35 (2000).
21. L. J. Windsor, M. K. Bodden, B. Birkedal-Hansen, J. A. Engler, H. Birkedal-Hansen, *J. Biol. Chem.* **269**, 26201 (1994).
22. D. L. Steele *et al.*, *Protein Eng.* **13**, 397 (2000).
23. I. E. Collier, S. Saffarian, B. L. Marmer, E. L. Elson, G. Goldberg, *Biophys. J.* **81**, 2370 (2001).
24. S. Saffarian, I. E. Collier, B. L. Marmer, E. L. Elson, G. Goldberg, unpublished observations.
25. J. J. Jeffrey, H. G. Welgus, R. Burgeson, A. Eisen, *J. Biol. Chem.* **258**, 11123 (1983).
26. H. Welgus, J. Jeffrey, G. Stricklin, W. Roswit, A. Eisen, *J. Biol. Chem.* **255**, 6806 (1980).
27. E. Leikina, M. V. Mertts, N. Kuznetsova, S. Leikin, *Proc. Natl. Acad. Sci. U.S.A.* **99**, 1314 (2002).
28. I. Derényi, M. Bier, R. D. Astumian, *Phys. Rev. Lett.* **83**, 903 (1999).
29. T. Shimada *et al.*, *Eur. J. Biochem.* **262**, 907 (1999).
30. E. Ohuchi *et al.*, *J. Biol. Chem.* **272**, 2446 (1997).
31. B. K. Pilcher *et al.*, *J. Cell Biol.* **137**, 1445 (1997).

32. The authors would like to thank M. S. Conrady for the use of the superconducting magnet. We also thank H. Qian and A. Eisen for reading the manuscript and helpful discussions. This work was supported in part by NIH grants GM-38838 to E.L.E., AR40618, AR39472 to G.I.G. and Washington University-Pfizer Inc. agreement.

Supporting Online Material

www.sciencemag.org/cgi/content/full/306/5693/108/DC1
Materials and Methods
SOM Text
Figs. S1 and S2
Tables S1 to S3
References and Notes

15 April 2004; accepted 5 August 2004

Life History Trade-Offs Assemble Ecological Guilds

Michael B. Bonsall,[1]*† Vincent A. A. Jansen,[2]* Michael P. Hassell[1]

Ecological theory predicts that competition for a limiting resource will lead to the exclusion of species unless the within-species effects outweigh the between-species effects. Understanding how multiple competitors might coexist on a single resource has focused on the prescriptive formalism of a necessary niche width and limiting similarity. Here, we show how continuously varying life histories and trade-offs in these characteristics can allow multiple competitors to coexist, and we reveal how limiting similarity emerges and is shaped by the ecological and evolutionary characteristics of competitors. In this way, we illustrate how the interplay of ecological and evolutionary processes acts to shape ecological communities in a unique way. This leads us to argue that evolutionary processes (life-history trait trade-offs) are fundamental to the understanding of the structure of ecological communities.

Ecological theory predicts that species in ecological communities can coexist only if there are differences in their responses to limiting resources (*1*, *2*). Evolutionary processes underpin this coexistence: Differences between species arise through the combined effects of selection and life-history trade-offs. Trade-offs in life histories (*3*, *4*) prevent species from evolving as Darwinian "demons" (species that develop rapidly, reproduce continuously, and do not age). Sanctioning investment in life-history characteristics against ecological competitive ability has the potential to allow multiple species to coexist by reducing the probability that any one species is demonic in an assemblage (*5*–*9*). Reducing the dominance of any one species in an assemblage and fostering equivalence among species has the potential to allow ecological diversity to be promoted (*10*, *11*).

Here, we explore the hypothesis that communities are assembled or shaped through evolutionary processes and that diversity is maintained and generated through species equivalence. Using a continuously varying strategy set, we evaluate the role of assembly and trade-offs as mechanisms for the formation of complex predator-prey assemblages. We consider a generic interaction between a class of natural enemies (parasitoids) competing for a limiting host resource (*12*, *13*). We assume that n types of consumer can attack particular juvenile (larval) stages of the host and that there is no a priori partitioning of this resource class. We describe the interaction between competing parasitoids within a generation with a system of differential equations. Solutions to these equations provide a description of the population dynamics of the system from which (ecological) difference equations (*14*) can be derived. Finally, the invasion and replacement

[1]Department of Biological Sciences, Imperial College London, Silwood Park Campus, Ascot, Berkshire SL5 7PY, UK. [2]School of Biological Sciences, Royal Holloway University of London, Egham, Surrey TW20 0EX, UK.

*These authors contributed equally to this work.
†To whom correspondence should be addressed. E-mail: m.bonsall@imperial.ac.uk

(evolutionary) dynamics can be explored from knowledge of both the competitive interaction and population dynamics.

We partition the host population into three classes: susceptible host larvae, singly parasitized larvae susceptible to further attack, and parasitized larvae not susceptible to further attack. We do this for n different strains of competing parasitoids. Parasitoids are time-limited with a finite amount of time to locate hosts, and per unit of time each parasitoid of type i discovers a host larva and lays an egg on or in it with a rate of α_i per host. Once oviposition has occurred, the parasitized host passes through a phase in which it is susceptible to further attack either by conspecifics (superparasitism events) or heterospecifics (multiparasitism events). This period of susceptibility lasts on average μ time units. This second egg will hatch and win in competition within the host with probability π_{ij}, where i denotes the type of the first parasitoid and j the type of the second. Obviously, if the same type superparasitizes a host, a parasitoid of that type will emerge. The model gives rise to a system of equations that can be solved to give the number of hosts that are parasitized and the number of consumers that arise at the beginning of the next season (*15*).

We assume that there is a trade-off between competitive ability and a life-history characteristic (*3*, *4*), in particular parasitoid attack rate (α) or parasitoid longevity ($1/c$). A parasitoid that is better at discovering new hosts (higher α) is worse at outcompeting or defending a host that is attacked (by a heterospecific) (*16*). When we use this trade-off, we assume that parasitoid death rates are the same for all parasitoids ($c_i = c$). The second trade-off that we consider is between parasitoid longevity and competitive ability (*5*, *9*). With this trade-off, it is the longer lived species that are inferior competitors. When we use this trade-off function, we assume that the potential for parasitoids to discover hosts is equivalent for all species ($\alpha_i = \alpha$). Competitive ability is always a function of the resident and invading parasitoid life-history strategies and is a characteristic determined by the ecological and evolutionary dynamics of the assemblage.

The population dynamics of the host and parasitoids (H', P'_i) over the seasons can be described by the following system of difference equations:

$$H' = f[H, x(T)] \quad (1)$$

$$P'_i = H[y_i(T) + z_i(T)] \quad (2)$$

Here, $f[H, x(T)]$ is the function relating hosts in the current season to those at the start of the next season, and within this function $x(T)$ is the probability that hosts survive parasitism. For simplicity, host density (H) is kept constant from season to season [but see (*15*) for results using variable host densities]. The functions $y_i(T)$ and $z_i(T)$ are the respective probabilities of a host being singly and doubly parasitized and producing a parasitoid of type i (*15*).

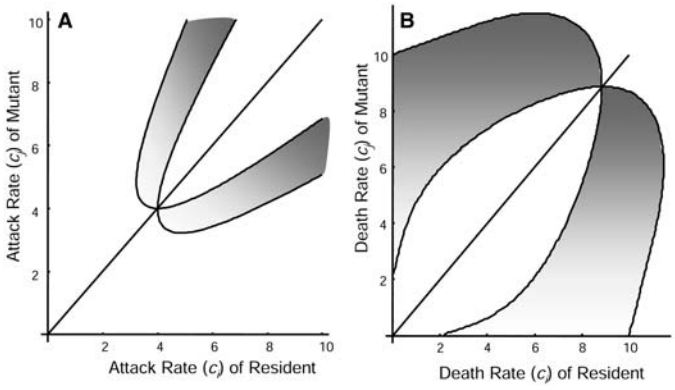

Fig. 1. Regions of coexistence (shaded areas) for the parasitoid competition model for trade-offs in (**A**) fecundity (H = 10, μ = 1.0, c = 0.5, and T = 10) and (**B**) longevity (death rate) (H = 10, μ = 1.0, α = 1.0, and T = 10). Coexistence is promoted if the mutant strategy has a higher fecundity or lower death rate compared with that of the resident. The more dissimilar two strategies are, the more likely coexistence is between competing parasitoids. These plots can also be used to infer the replacement dynamics of different strains. If the region under the diagonal is negative and the opposite region above the diagonal is positive, this will result in a strain with a marginally higher value of trait replacing the resident. If the sign pattern is opposite, then a strain with a marginally lower value of the trait will invade and outcompete the resident. Repeated appearance of slightly different strains (mutants) will result in an evolutionary change of the trait. The invasion boundaries were evaluated using a root-solving algorithm and numerical integration of the model (*15*).

To understand how different life-history characteristics affect the coexistence of competing parasitoids, we derive a set of invasion conditions. That is, for successful invasion of a second parasitoid P_j (characterized by its death rate c_j or attack rate α_j) into a population in which a parasitoid P_i (characterized by c_i or α_i) is already present, we evaluate whether P_j can invade, when rare, a population consisting of only P_i at equilibrium. The precise conditions for invasion can be derived from the rate that a rare parasitoid invades a persistent resident host–parasitoid interaction. The invasibility conditions (*15*, *17*) can be illustrated graphically in a pairwise invasibility plot (*18*, *19*) and can be analyzed using tools from game theory and adaptive dynamics. Here, rather than focusing solely on this type of dynamic, we examine what factors influence the assembly of parasitoids into guilds [closely related species that share similar life-history characteristics (*20*, *21*)] and under what conditions these guilds cannot be invaded by further species (*7*, *22*).

Mutual invasibility and coexistence of natural enemies is possible if there are differences in searching efficiency such that the inferior competitor has the higher attack rate (Fig. 1A). Similarly, Fig. 1B shows combinations of resident and invader parasitoid death rates (c) that permit coexistence under fixed host densities. Mutual invasibility and hence coexistence of parasitoids can occur only if there are distinct differences in life histories (fecundity or longevity); for example, as an inferior larval competitor, the invading parasitoid must have a lower adult death rate (or live longer) than the resident parasitoid (Fig. 1B). However, transient coexistence is possible if invading parasitoids are almost identical to the residents, because the fitness differences will be very small and the effects of competition will be almost neutral.

It is important to note from Fig. 1 (see also fig. S1) that any two combinations of strategies taken from the shaded area can coexist. However, subsequent episodes of invasion and replacement will impose a particular dynamic on the coexisting pair, and this could either result in the eventual loss of one of the strategies or introduce additional species to the assemblage. We used numerical simulations to study the dynamics of the assemblage and find its stable composition. This final assemblage is not just the assemblage in which the largest number of species can coexist. In all of the cases, the number of species in the final assemblage is larger than one but is always less than the number of species that could potentially coexist.

Numerical exploration illustrates that the invasion and dynamics of multiple parasitoids on a single limiting host resource gives rise to multiple coexisting species. However, this prediction is dependent on the abundance of the host. When host abundance is low, a dimorphism arises and two parasitoid strategies coexist (Fig. 2A). When host abundance is high, a polymorphism arises and multiple parasitoid strategies coexist (Fig. 2B). Throughout, it is assumed that new strategies are similar to existing residents, as would be the case if new variants are created through mutation in a polygenic trait. Evolutionary branching leads to a number of coexisting distinct types. Within each broad group, several closely related parasitoid types compete intensely for dominance and assemble into clades. These assemblages arise as a result of the interplay between evolutionary and ecological processes: This is not encountered in conventional studies, which solely concentrate on the ecological processes of coexistence (*8*, *23*–*26*). For instance, the oc-

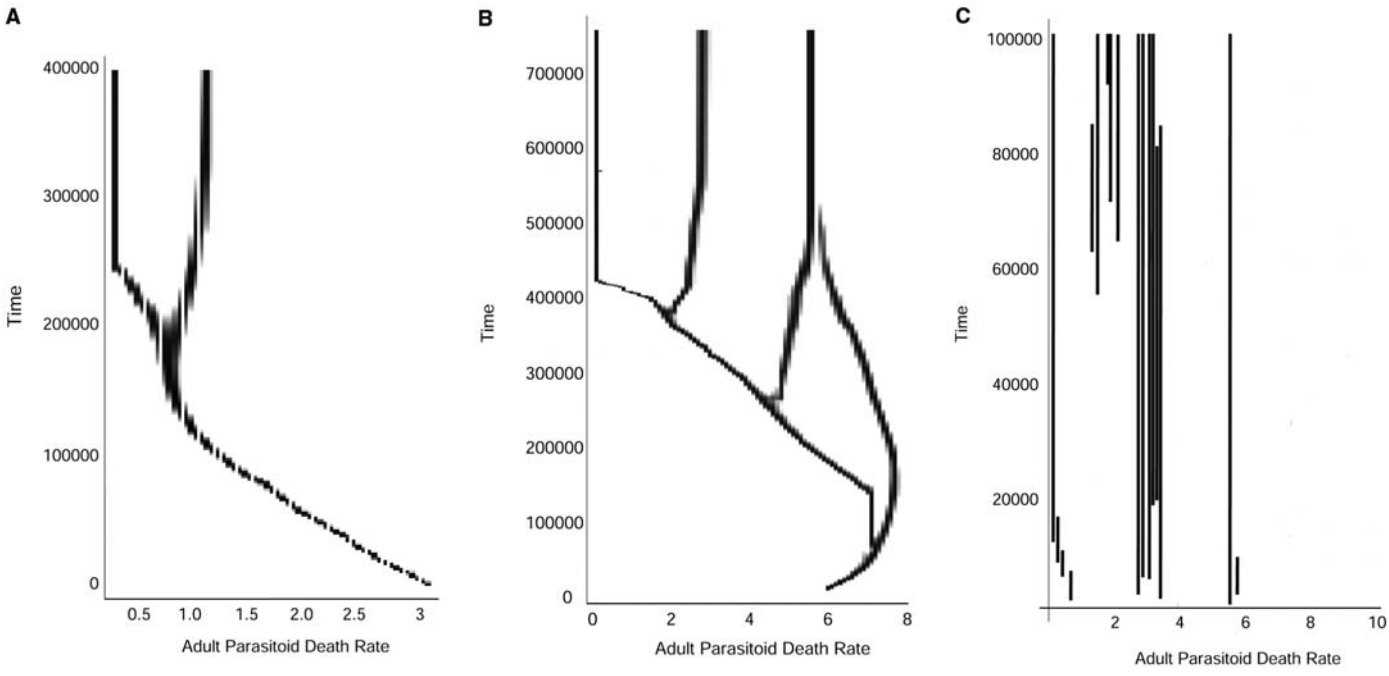

Fig. 2. Branching pattern and community assembly under (**A**) a fixed initial strategy under low host density ($H = 4$, $\mu = 1.0$, $\alpha = 1.0$, and $T = 10$), (**B**) a fixed strategy under high host density ($H = 10$, $\mu = 1.0$, $\alpha = 1.0$, and $T = 10$), and (**C**) a variety of initial strategies under trade-offs in longevity (death rate) and competitive ability ($H = 10$, $\mu = 1.0$, $\alpha = 1.0$, and $T = 10$). Limiting similarity between groups [in (A) and (B)] arises as a consequence of the population and evolutionary dynamics among competing species. In (C), transitory dynamics underpinned the interaction between similar species. Between the groups, competition is skewed, with longer lived species experiencing severe interspecific effects.

currence of this type of polymorphism can lead to reproductive isolation and speciation through sympatric mechanisms (*27*, *28*).

However, the formation of clades through evolution need not necessarily be the only mechanism by which species assembly occurs. When guilds are formed through random assembly, we find the same qualitative patterns of niche differentiation. This is demonstrated in Fig. 2C, in which new immigrants arrive as migrants from a species pool. Although guilds assembled this way converge to the same final assemblage as in Fig. 2B, there are some notable differences. In particular, the coexistence of many types is manifest. However, there are numerous unsuccessful invasions. A striking phenomenon in the assembly of species guilds is that invading strategies may persist as transients at low abundance for very long periods of time. Note that the number of different types that can coexist ecologically exceeds the number observed in the final evolutionary stable assemblage. The coexistence of multiple strategies gives rise to a form of limiting similarity with a minimum distance between each group (Fig. 2C). The competition between different types is highly asymmetric, such that long-lived strategies are subjected to greater effects of interspecific competition than are short-lived strategies or that higher fecund strategies are subjected to stronger interspecific competition than are less fecund strategies; then, the observed evolutionary stable coexistence arises as a result of distinct differences in life history. The degree of competition between similar species is intense and almost symmetric.

Unlike earlier theoretical studies (*1–2*, *29–31*), this limiting similarity between strategy sets arises as a consequence of the population and evolutionary dynamics of the trophic interaction rather than as a result of a prescriptive statistical relationship derived from the shape of the competition function (*1*, *2*). It is expected that locally coexisting species should be less similar than one would expect by chance alone. However, across similar life-history strategies a number of species contest for dominance through intense interspecific competition. Given that over appropriate time scales species are observed to coexist, we conjecture that coexisting species may be more similar than one would expect by chance alone and that their distribution falls into a number of distinct life-history class clusters. Difference in resource use will depend on species demographic and life-history characteristics.

These properties (the emergence of niche structures, limiting similarity, and transient coexistence) are likely to hold for a large class of competitive interactions (*15*) (fig. S2). Our generic result that is not limited to predator-prey interactions is that ecological and evolutionary dynamics of resource-consumer interactions shape the structure of species assemblages (*15*). In contrast to conventional theory on trade-offs and community assembly (*32*), which predict no limit to diversity (because any species can occupy any point in trait space), we show that species life-history trade-offs can generate a limiting similarity that promotes ecological diversity. Evolutionary and ecological dynamical processes drive niche partitioning and limiting similarity, and at the same time generate diversity within a niche. While the total size of different niches is determined by competition for a set of limited resources, the relative abundance of strains within a niche is determined predominantly by chance (*33*). Our approach reconciles two conflicting views about the organization of ecological communities: organization dominated by niche structure (*29–31*) and organization through chance and neutral processes (*10*, *11*). These two views are not mutually exclusive. Both processes operate simultaneously to generate and maintain diversity in ecological communities.

References and Notes

1. R. H. MacArthur, R. Levins, *Am. Nat.* **101**, 377 (1967).
2. R. M. May, *Stability and Complexity in Model Ecosystems* (Princeton Univ. Press, Princeton, NJ, 1974).
3. S. C. Stearns, *The Evolution of Life Histories* (Oxford Univ. Press, Oxford, 1992).
4. D. A. Roff, *The Evolution of Life Histories: Theory and Analysis* (Chapman & Hall, New York, 1992).
5. R. Levins, D. Culver, *Proc. Natl. Acad. Sci. U.S.A.* **68**, 1246 (1971).
6. D. Tilman, *Ecology* **75**, 2 (1994).
7. V. A. A. Jansen, G. S. E. E. Mulder, *Ecol. Lett.* **2**, 379 (1999).
8. M. B. Bonsall, M. P. Hassell, G. Asefa, *Ecology* **83**, 925 (2002).
9. M. B. Bonsall, M. Mangel, *Proc. R. Soc. Lond. B. Biol. Sci.* **271**, 1143 (2004).
10. G. Bell, *Am. Nat.* **155**, 606 (2000).
11. S. P. Hubbell, *The Unified Theory of Biodiversity and Biogeography* (Princeton Univ. Press, Princeton, NJ, 2001).
12. M. P. Hassell, *The Dynamics of Arthropod Predator-Prey Systems* (Princeton Univ. Press, Princeton, NJ, 1978).

13. M. P. Hassell, *The Temporal and Spatial Dynamics of Host-Parasitoid Associations* (Oxford Univ. Press, Oxford, 2000).
14. A. J. Nicholson, V. A. Bailey, *Proc. Zoo. Soc. Lond.* **3**, 551 (1935).
15. Materials and methods are available as supporting material on *Science* Online.
16. R. M. May, M. P. Hassell, *Am. Nat.* **117**, 234 (1981).
17. R. A. Armstrong, R. McGehee, *Am. Nat.* **115**, 151 (1980).
18. J. A. J. Metz, R. M. Nisbet, S. A. H. Geritz, *Trends Ecol. Evol.* **7**, 198 (1992).
19. S. A. H. Geritz, E. Kisdi, G. Meszena, J. A. J. Metz, *Evol. Ecol.* **12**, 35 (1998).
20. R. B. Root, *Ecol. Monogr.* **37**, 317 (1967).
21. P. Morin, *Community Ecology* (Blackwell Science, Oxford, 1999).
22. U. Dieckmann, *Trends Ecol. Evol.* **12**, 128 (1997).
23. B. R. Levin, *Evolution* **25**, 249 (1971).
24. J. Haigh, J. Maynard-Smith, *Theor. Popul. Biol.* **3**, 290 (1972).
25. F. M. Stewart, B. R. Levin, *Am. Nat.* **107**, 171 (1973).
26. C. J. Briggs, *Am. Nat.* **141**, 372 (1993).
27. U. Dieckmann, M. Doebeli, *Nature* **400**, 354 (1999).
28. M. Doebeli, U. Dieckmann, *Nature* **421**, 259 (2003).
29. G. E. Hutchinson, *Am. Nat.* **93**, 145 (1959).
30. P. A. Abrams, *Theor. Popul. Biol.* **8**, 356 (1975).
31. D. Lack, *Darwin's Finches* (Cambridge University Press, Cambridge, 1947).
32. D. Tilman, *Resource Competition and Community Structure* (Princeton Univ. Press, Princeton, NJ, 1982).
33. D. Tilman, *Proc. Natl. Acad. Sci. U.S.A.* **101**, 10854 (2004).
34. M.B.B. is a Royal Society University Research Fellow.

Supporting Online Material
www.sciencemag.org/cgi/content/full/306/5693/111/DC1
SOM Text
Figs. S1 and S2
References

25 May 2004; accepted 11 August 2004

Zebrafish Dpr2 Inhibits Mesoderm Induction by Promoting Degradation of Nodal Receptors

Lixia Zhang,[1]* Hu Zhou,[2]* Ying Su,[1]* Zhihui Sun,[1] Haiwen Zhang,[1] Long Zhang,[2] Yu Zhang,[1] Yuanheng Ning,[2] Ye-Guang Chen,[2]† Anming Meng[1]†

Nodal proteins, members of the transforming growth factor–β (TGFβ) superfamily, have been identified as key endogenous mesoderm inducers in vertebrates. Precise control of Nodal signaling is essential for normal development of embryos. Here, we report that zebrafish *dapper2* (*dpr2*) is expressed in mesoderm precursors during early embryogenesis and is positively regulated by Nodal signals. In vivo functional studies in zebrafish suggest that Dpr2 suppresses mesoderm induction activities of Nodal signaling. Dpr2 is localized in late endosomes, binds to the TGFβ receptors ALK5 and ALK4, and accelerates lysosomal degradation of these receptors.

Genetic studies have revealed that Nodal proteins are essential for mesoderm induction in vertebrates (*1*–*4*). So far, few factors have been found to inhibit Nodal signaling during early embryogenesis. Lefty proteins inhibit Nodal activity by competing for binding to their common receptors (*5*–*8*). An extracellular protein, Cerberus, binds to Nodal and blocks its activity (*9*). Tomoregulin-1, a transmembrane protein, blocks Nodal signaling by interacting with the Nodal coreceptor Cripto (*10*). Drap1 interacts with and inhibits DNA binding of FoxH1, a transcription factor that mediates Nodal signaling (*11*). Here, we demonstrate that Dpr2 inhibits Nodal signaling in zebrafish embryos, targeting Nodal receptors for lysosomal degradation.

Zebrafish *dpr2* was identified by a whole-mount in situ hybridization screen for tissue-specific genes. The putative Dpr2 protein, 837 residues long, has overall sequence identity of 30 and 36% to the putative human DAPPER1 and DAPPER2 proteins (*12*), respectively, with higher similarity in several domains (fig. S1). Several *dpr2* ESTs have been mapped adjacent to the *oprm1* and *smoc2* loci in the zebrafish linkage group 13 (LG13), a region syntenic to the human *DAPPER2* locus, which suggests that zebrafish *dpr2* is an ortholog of human *DAPPER2*. Although *Xenopus* Dapper and Frodo are almost identical, Dapper is apparently a general Dishevelled antagonist (*13*), whereas Frodo is a positive regulator of Wnt signaling (*14*).

Whole-mount in situ hybridization revealed a specific expression pattern of *dpr2* during zebrafish embryogenesis (fig. S2). It was first expressed on the dorsal blastoderm at the sphere stage, about 4 hours postfertilization (hpf). At the onset of gastrulation, *dpr2* expression was restricted to the whole germ ring where mesoderm precursors reside, with the highest expression in the embryonic shield. The *dpr2*-positive cells then involute and converge during gastrulation and thus contribute to the formation of epiblast and hypoblast. When segmentation starts, *dpr2* is expressed in the dorsal trunk neural tube, the lateral plate mesoderm, and the tail bud. At 24 hpf, *dpr2* expression is restricted to blood progenitors and the tail bud. This expression pattern of *dpr2* suggests a role in early mesoderm induction.

To study the function of *dpr2*, endogenous expression of *dpr2* was knocked down by injecting a mix of two specific and equally effective antisense morpholinos (dpr2-MOs) (fig. S3). The injected embryos generally showed a thicker, curled down trunk at 24 hpf (fig. S3), a phenotype also observed with a *lefty1* morpholino (lft1-MO) (*15*). The majority (53 to 95%) of morpholino-injected embryos showed increased expression of the organizer-specific marker *gsc* (Fig. 1A), the lateral mesodermal marker *snail1* (Fig. 1B), and the axial mesodermal markers *no tail* (*ntl*) (Fig. 1C) and *shh* (Fig. 1D). Mutations of the *oep* locus, which encodes a coreceptor for the Nodal ligands *squint* (*sqt*) and *cyclops* (*cyc*) in zebrafish, give rise to reduced Nodal activity (*4*, *16*). Overexpression of *dpr2* caused partial or complete fusion of the eyes (Fig. 1F), resembling the *oep* (Fig. 1G) and *cyc* phenotypes, which also result from insufficient Nodal signaling (*16*, *17*). Overexpression also caused partial loss of the notochord and tail reduction in about one-third of the embryos at 24 hpf. Injection of *dpr2* mRNA also led to reduction or elimination of *shh* expression at 24 hpf (Fig. 1H), as well as decreased *ntl* expression at the bud stage (fig. S3). These data suggest that *dpr2* functions to inhibit mesoderm formation.

Because *dpr2* overexpression phenocopied *oep* mutants and because *dpr2* knockdown resulted in morphological changes that resembled *lefty1* knockdown, there may be genetic interactions between Dpr2 and Nodal signaling. We found that 55% (38 out of 69) of embryos coinjected with dpr2-MOs and 0.1 pg *sqt* mRNA had a much wider notochord, an effect not seen in embryos injected with *sqt* mRNA alone (fig. S4). This notochord effect showed that knockdown of *dpr2* can enhance the phenotypes caused by elevated Nodal activity. In addition, 91% (n = 135) of embryos coinjected with 4 ng dpr2-MOs and 1.25 ng lft1-MO underwent arrest of development or died at 24 hpf, whereas this percentage was usually below 10% for single injections. Like *lft1* knockdown (Fig. 1E, right), *dpr2* knockdown rescued *shh* expression in the ventral midbrain and in the floor plate (Fig. 1E, middle) in 22 out of 23 zygotic oep^{tz257} mutants. However, *dpr2* knockdown in *MZoep* mutants,

[1]Laboratory of Developmental Biology, [2]Laboratory of Molecular Cell Biology, State Key Laboratory of Biomembrane and Membrane Biotechnology, Protein Sciences Laboratory of the Ministry of Education (MOE), Department of Biological Sciences and Biotechnology, Tsinghua University, Beijing 100084, China.

*These authors contributed equally to this work.
†To whom correspondence should be addressed. E-mail: mengam@mail.tsinghua.edu.cn (A.M.) and ygchen@mail.tsinghua.edu.cn (Y.-G.C.)

which completely lack Nodal signaling (*4*, *18*), failed to rescue *shh* expression (*19*), which suggests that Dpr2 function depends on the availability of Nodal signals. Furthermore, *dpr2* knockdown counteracted *lft1* overexpression, and *dpr2* overexpression compromised the effect of *lft1* knockdown (fig. S4).

We also examined the possible involvement of Dpr2 in other signaling pathways prominent in early embryogenesis. Overexpression of *dpr2* and *bmp7* had similar influences on expression of certain marker genes, and this ectopic *bmp7* effect was inhibited by *dpr2* knockdown (fig. S4), which suggests that Dpr2 could not inhibit the ventralizing BMP signals. Also, Dpr2 may not be an antagonist of either FGF or Wnt signals, because *dpr2* knockdown led to phenotypes different from those caused by ectopic expression of *fgf8* and *wnt8*; also, increased FGF or Wnt signaling failed to rescue *shh* expression in *oep* mutant embryos (figs. S5 and S6).

The inhibitory effect of Dpr2 on Nodal-related signaling was next tested in mammalian cells with a transforming growth factor–β (TGFβ)–induced luciferase activity with an activin-responsive element–containing luciferase reporter, ARE-luciferase. The expression of this reporter was stimulated by constitutively active ALK5/TβRI, a TGFβ receptor, in Hep3B cells. This stimulation was attenuated by coexpressing fish *dpr2* (Fig. 2A), whereas human DAPPER1 (hDpr1) did not interfere with TGFβ signaling (*19*). Unlike hDpr1, Dpr2 had little effect on Wnt signaling (Fig. 2B). Furthermore, *dpr2* overexpression inhibited the receptor-mediated phosphorylation of Smad2, as well as the formation of Smad2-Smad4 and Smad3-Smad4 complexes (fig. S7). Together, these data indicate that Dpr2 specifically antagonizes TGFβ signaling in mammalian cells.

To determine the mechanism of Dpr2 action on TGFβ signaling, we next tested whether Dpr2 associates with TGFβ receptors. Dpr2 bound to overexpressed ALK5 in HEK293T cells and interacted with the active forms of ALK5 with high affinity (Fig. 2C), which indicates that Dpr2 preferentially associates with the activated receptors. This notion is supported by the observation that Dpr2 associated with endogenous ALK5 upon TGFβ stimulation (Fig. 2D). In contrast, Dpr2 associated with ALK6 (BMPR-IB) and TβRII weakly, if at all, and not at all with ActRII (*19*).

Immunofluorescence analysis indicated a punctate subcellular localization of Dpr2 (Fig. 2E), which overlapped with the late-endosomal marker Rab7 (Fig. 2F and 2G), but not with the early-endosomal markers EEA1 (fig. S8), Rab5 and transferrin (*19*), the lysosomal marker LAMP3 (fig. S8), or the caveolae marker Caveolin (fig. S8). TGFβ receptors are internalized into the cell via clathrin-coated pits or lipid rafts and/or

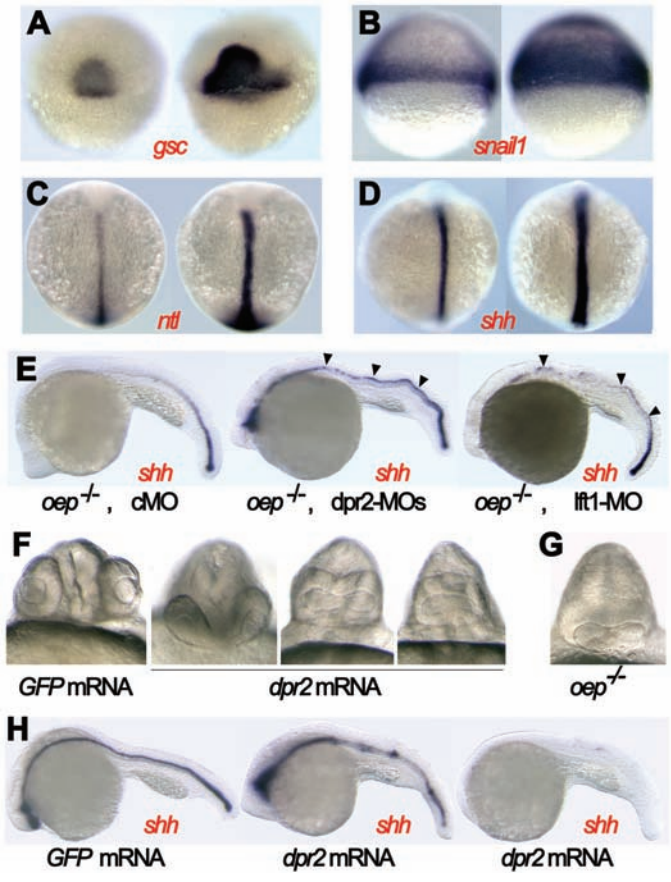

Fig. 1. Effects of *dpr2* knockdown and overexpression in zebrafish embryos. Whole-mount in situ hybridization reveals that morpholino-mediated knockdown of *dpr2* resulted in increase of *gsc* (**A**) and *snail1* (**B**) at the shield stage, *ntl* (**C**) at the 5-somite stage, and *shh* (**D**) at the 8-somite stage. In each panel, the left embryo was injected with 8 ng control morpholino (cMO) and the right one with 8 ng dpr2-MOs. (A, C, and D) Dorsal views. (B) Lateral view. (**E**) Injection of dpr2-MOs (middle) or lft1-MO (right), but not cMO (left), led to recovery of *shh* expression in the floor plate (arrowheads) of oep^{tz257} mutant embryos at 24 hpf. (**F**) Injection of wild-type embryos with 200 pg *dpr2* mRNA caused partial or complete fusion of eyes in the 24-hpf embryo, which then resembled the phenotype of oep^{tz257} embryo (**G**). (F and G) Head ventral views of live embryos. (**H**) *dpr2* overexpression reduces (middle) or eliminates (right) *shh* expression in the 24-hpf embryo. Embryos injected with the same amount of *GFP* mRNA were served as controls in (F) and (H).

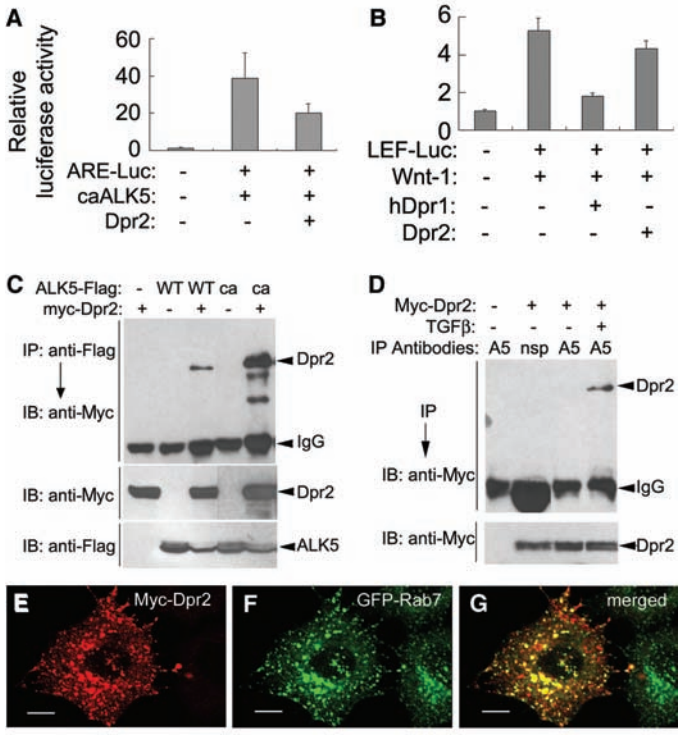

Fig. 2. (**A**) Dpr2 inhibits its TGFβ receptor ALK5-mediated expression of the ARE-luciferase reporter in human hepatoma Hep3B cells. (**B**) Human Dpr1 (hDpr1) attenuates Wnt signaling, whereas Dpr2 does not. Data were from three independent experiments and were expressed as mean with standard deviations. (**C**) Dpr2 binds to ALK5 in HEK293T cells, as revealed by immunoprecipitation (IP) and immunoblotting (IB). Note that stronger binding was detected for the constitutively active (ca) ALK5. (**D**) Dpr2 binds to endogenous ALK5. A5, anti-ALK5 antibody; nsp, nonspecific IgG. (**E** to **G**) Dpr2 colocalizes with the late endosomal marker Rab7 in HeLa cells. Scale bars, 10 μm.

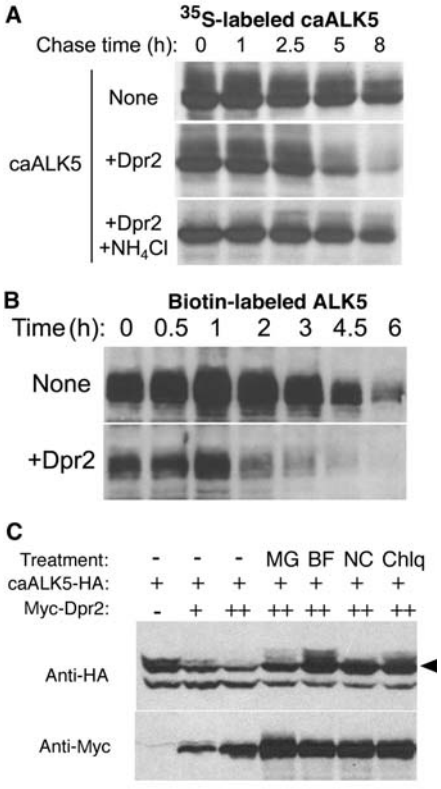

Fig. 3. Dpr2 targets ALK5 for lysosomal degradation. (**A**) Degradation of active ALK5, pulse-labeled with ^{35}S-Met/Cys for 2 hours, was accelerated by *dpr2* overexpression, and this degradation was attenuated by NH_4Cl. (**B**) Dpr2 promotes the turnover of biotinylated cell surface ALK5 molecules. (**C**) Dpr2-mediated ALK5 degradation is sensitive to the lysosomal inhibitors bafilomycin A1 (BF), NH_4Cl (NC), and chloroquine (Chlq), but not to the proteasome inhibitor MG-132 (MG). The arrowhead indicates the position of the ALK5 receptor. The amount of myc-Dpr2 was indicated as + (0.1 μg) or ++ (0.2 μg).

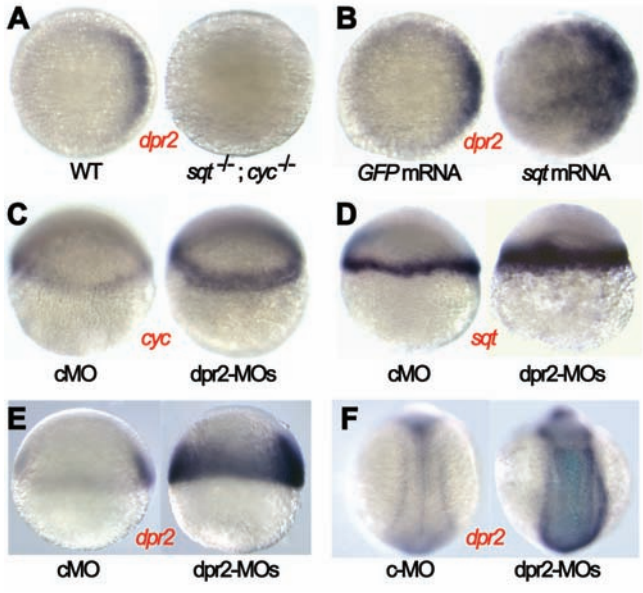

Fig. 4. Reciprocal regulation of *dpr2*, *sqt*, and *cyc* expression. (**A**) *dpr2* expression is not detectable in the $sqt^{L235};cyc^{m294}$ double mutants. (**B**) Injection with 0.1 pg *sqt* mRNA induces ectopic expression of *dpr2*. (**C** and **D**) *dpr2* knockdown increases expression of *cyc* (C) and *sqt* (D). (**E** and **F**) *dpr2* knockdown also enhances expression of *dpr2* itself. The injected embryos were examined by whole-mount in situ hybridization for expression of the marker genes. In each panel, the control is on the left. (A to B) Animal-pole views at the 30% epiboly stage, dorsal to the right. (C and D) Lateral views at the 30% epiboly stage. (E) Lateral view at the shield stage. (F) Dorsal view at the 6-somite stage.

caveolae (*20*–*23*), and are down-regulated by Smad7-Smurf or by β-arrestin-2 (*21*, *24*). The localization of Dpr2 in late endosomes suggests that it may play a role in sorting endocytosed receptors into late endosomes and/or facilitating their transport to lysosomes.

Overexpression of *dpr2* led to reduction of receptor protein levels (Fig. 2C, bottom). Pulse-chase analysis confirmed that Dpr2 overexpression accelerated the degradation of ALK5 in HEK293T cells (Fig. 3A and fig. S9). Furthermore, fewer cell surface receptors, owing to a shorter half-life, were detected in the Dpr2-expressing cells (Fig. 3B and fig. S9), which suggests that Dpr2 facilitates degradation of receptors internalized from the cell surface. In addition, Dpr2-induced ALK5 degradation was inhibited by the lysosomal inhibitors bafilomycin A_1, NH_4Cl, or chloroquine, but not by the proteasome inhibitor MG132 (Fig. 3C). These results suggest that Dpr2 promotes lysosomal degradation of endocytosed receptors.

Similar experiments with ALK4/ActRIB, an activin and Nodal receptor, revealed that Dpr2 was able to bind to ALK4, and Dpr2 overexpression inhibited active ALK4-mediated reporter expression and promoted degradation of ALK4 through lysosomal pathway (fig. S10). Analysis of the functional regions of Dpr2 demonstrated that the first 361 amino acids could bind to ALK5, and binding of this segment was sufficient to attenuate the reporter gene activation (fig. S11).

During embryogenesis, transcripts of *dpr2* were not detected in *sqt;cyc* double mutants (Fig. 4A), and overexpression of *sqt* induced ectopic expression of *dpr2* (Fig. 4B), which demonstrated an essential role of Nodal signaling in activating *dpr2* expression. Knockdown of *dpr2* led to a higher expression level of *cyc* (Fig. 4C) and *sqt* (Fig. 4D), consistent with a positive activation loop for Nodal signals (*25*). It was noteworthy that *dpr2* knockdown increased its own transcription (Fig. 4, E and F), which implies that intracellular level of Dpr2 is precisely perceived and negatively autoregulated.

In summary, our results indicate that Dpr2 functions as an antagonist of Nodal signaling during embryonic development, although we cannot fully exclude minor roles of Dpr2 in other signaling pathways. Our data suggest that Dpr2 binds to endocytosed TGFβ/Nodal receptors and facilitates their transport to lysosomes for degradation. Compared with phenotypes caused by *lefty1* overexpression, however, phenotypes of *dpr2* overexpression are mild. This may be attributed to divergent mechanisms by which Dpr2 and Lefty1 function. Dpr2 acts at late trafficking stages of internalized Nodal receptors, after the extracellular signals have passed to the downstream effectors, the Smad proteins. Thus, Dpr2 overexpression should never completely block initial transduction of Nodal signals. In contrast, Lefty proteins are able to completely shut off initial transduction of Nodal signals as they compete with the ligands for the signaling receptors.

References and Notes

1. X. Zhou, H. Sasaki, L. Lowe, B. L. Hogan, M. R. Kuehn, *Nature* **361**, 543 (1993).
2. B. Feldman *et al.*, *Nature* **395**, 181 (1998).
3. A. F. Schier, M. M. Shen, *Nature* **403**, 385 (2000).
4. K. Gritsman *et al.*, *Cell* **97**, 121 (1999).
5. C. Meno *et al.*, *Mol. Cell* **4**, 287 (1999).
6. C. Thisse, B. Thisse, *Development* **126**, 229 (1999).
7. R. Sakuma *et al.*, *Genes Cells* **7**, 401 (2002).
8. Y. Chen, A. F. Schier, *Curr. Biol.* **12**, 2124 (2002).
9. S. Piccolo *et al.*, *Nature* **397**, 707 (1999).
10. P. W. Harms, C. Chang, *Genes Dev.* **17**, 2624 (2003).
11. R. Iratni *et al.*, *Science* **298**, 1996 (2002).
12. M. Katoh, *Int. J. Oncol.* **22**, 907 (2003).
13. B. N. Cheyette *et al.*, *Dev. Cell* **2**, 449 (2002).
14. J. Gloy, H. Hikasa, S. Y. Sokol, *Nature Cell Biol.* **4**, 351 (2002).
15. A. Agathon, B. Thisse, C. Thisse, *Genesis* **30**, 178 (2001).
16. A. F. Schier, S. C. Neuhauss, K. A. Helde, W. S. Talbot, W. Driever, *Development* **124**, 327 (1997).
17. K. Hatta, C. B. Kimmel, R. K. Ho, C. Walker, *Nature* **350**, 339 (1991).
18. J. Zhang, W. S. Talbot, A. F. Schier, *Cell* **92**, 241 (1998).
19. L. X. Zhang *et al.*, unpublished observations.
20. Z. Lu *et al.*, *J. Biol. Chem.* **277**, 29363 (2002).
21. G. M. Di Guglielmo, C. Le Roy, A. F. Goodfellow, J. L. Wrana, *Nature Cell Biol.* **5**, 410 (2003).
22. S. G. Penheiter *et al.*, *Mol. Cell. Biol.* **22**, 4750 (2002).
23. S. Hayes, A. Chawla, S. Corvera, *J. Cell Biol.* **158**, 1239 (2002).
24. W. Chen *et al.*, *Science* **301**, 1394 (2003).
25. S. I. Osada *et al.*, *Development* **127**, 2503 (2000).
26. We thank S. Lin, J. Massague, X. H. Feng, J. S. Eisen, B. Van Deurs, D. Meyer, Z. J. Chang, and B. Thisse for providing plasmids and fish; X. Li for technical support; and M. Cusick for proofreading. This work was supported by grants from the National Natural Science Foundation of China to A.M. and Y.-G.C., from the "863" Program and from the Teaching and Research Award Program for Outstanding Young

Teachers in Higher Education Institutions of the MOE to A.M., and from the Bugher Foundation and from the Specialized Research Fund for the Doctoral Program of Higher Education of the MOE to Y.-G.C.

Supporting Online Material
www.sciencemag.org/cgi/content/full/306/5693/114/DC1
Materials and Methods
Figs. S1 to S11
References and Notes

21 May 2004; accepted 17 August 2004

Ubistatins Inhibit Proteasome-Dependent Degradation by Binding the Ubiquitin Chain

Rati Verma,[1] Noel R. Peters,[2] Mariapina D'Onofrio,[3] Gregory P. Tochtrop,[2] Kathleen M. Sakamoto,[1,4] Ranjani Varadan,[3] Mingsheng Zhang,[5] Philip Coffino,[5] David Fushman,[3] Raymond J. Deshaies,[1] Randall W. King[2]*

To identify previously unknown small molecules that inhibit cell cycle machinery, we performed a chemical genetic screen in *Xenopus* extracts. One class of inhibitors, termed ubistatins, blocked cell cycle progression by inhibiting cyclin B proteolysis and inhibited degradation of ubiquitinated Sic1 by purified proteasomes. Ubistatins blocked the binding of ubiquitinated substrates to the proteasome by targeting the ubiquitin-ubiquitin interface of Lys[48]-linked chains. The same interface is recognized by ubiquitin-chain receptors of the proteasome, indicating that ubistatins act by disrupting a critical protein-protein interaction in the ubiquitin-proteasome system.

Unbiased chemical genetic screens can identify small molecules that target unknown proteins or act through unexpected mechanisms (*1*). To identify previously unknown components or potential drug targets required for cell division, we screened for small molecules that stabilize cyclin B in *Xenopus* cell cycle extracts. Cyclin B degradation regulates exit from mitosis and requires activation of an E3 ubiquitin ligase called the anaphase-promoting complex/cyclosome (APC/C) (*2*). Because APC/C activation requires mitotic entry, we anticipated that this screen would identify compounds that stabilized cyclin B indirectly by blocking mitotic entry as well as compounds that directly inhibited the cyclin proteolysis machinery. To monitor APC/C activation, we fused the destruction-box domain of *Xenopus* cyclin B1 to luciferase (*3*) and found that the reporter protein was degraded in mitotic but not interphase extracts (fig. S1). Proteolysis was sensitive to inhibitors of cyclin-dependent kinases and the ubiquitin-proteasome system but not affected by inhibitors of DNA replication or spindle assembly, as expected in egg extracts lacking exogenous nuclei (*4*, *5*) (fig. S2).

We developed a miniaturized assay system (*6*) and screened 109,113 compounds to identify 22 inhibitors (Table 1). To distinguish compounds that blocked mitotic entry from direct inhibitors of proteolysis, we arrested extracts in mitosis before addition of the compound and the reporter protein. Sixteen compounds lost inhibitory activity under these conditions (class I, fig. S3), whereas six compounds (class II, fig. S4) remained inhibitory. We next activated proteolysis directly in interphase extracts by adding the APC/C activator Cdh1 (Cdc20 homolog 1) (*7*). Again we found that only class II compounds re-

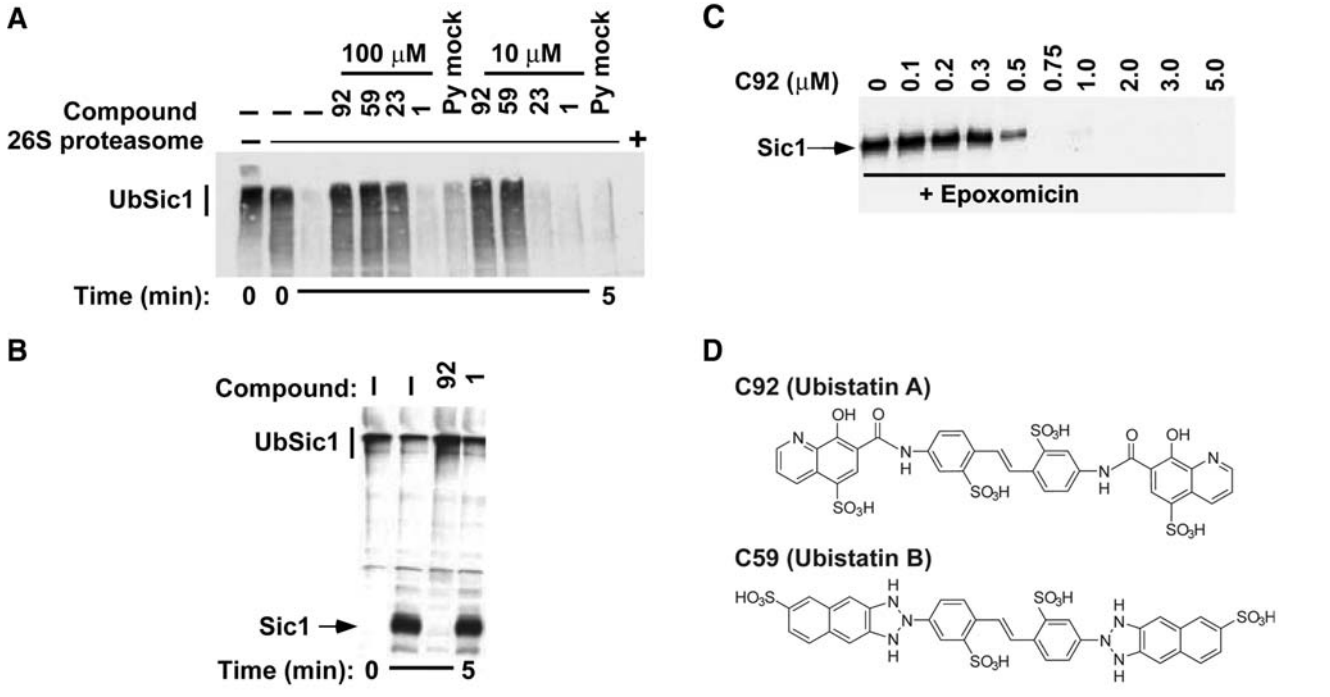

Fig. 1. Class IIB compounds inhibit degradation and deubiquitination of UbSic1 by purified 26S proteasomes. (**A**) Purified 26S proteasomes were preincubated in the presence or absence of test compounds. UbSic1 was then added and assayed for degradation by immunoblotting for Sic1 (*3*). Py mock refers to pyridine in which C23 was dissolved. (**B**) Purified 26S proteasomes were preincubated with 100 μM epoxomicin in the presence or absence of 100 μM test compound. UbSic1 was then added and deubiquitination monitored by immunoblotting for Sic1 (*3*). (**C**) Titration of C92 in deubiquitination assay. (**D**) Structures of C92 and C59 (ubistatins A and B).

tained inhibitory activity. We concluded that class I compounds blocked entry into mitosis or APC/C activation, whereas class II compounds directly blocked components of the cyclin degradation machinery. We next examined whether the inhibitors could block turnover of a β-catenin reporter protein (*8*), a substrate of the SKP1/cullin/F-box protein ($SCF^{\beta\text{-}TRCP}$, where β-TRCP is β-transduction repeat–containing protein) ubiquitin ligase (Table 1). Three class II compounds (class IIB) were inhibitory, suggesting these compounds inhibited a protein required for the degradation of both APC/C and $SCF^{\beta\text{-}TRCP}$ substrates. Class IIB compounds did not block cyclin B ubiquitination or 20S peptidase activity (*9*), indicating they did not inhibit E1 or act as conventional proteasome inhibitors.

To understand how class IIB compounds inhibited proteolysis, we turned to a reconstituted system using purified 26S proteasomes and ubiquitinated Sic1 (UbSic1) (*10*). Degradation of Sic1 requires its ubiquitination by the ligase SCF^{Cdc4} (*11*, *12*), after which UbSic1 is docked to the 19S regulatory particle by a multi-Ub chain receptor (*13*). Proteolysis of UbSic1 requires removal of the multi-Ub chain, catalyzed by the metalloisopeptidase Rpn11 (*14*, *15*). The deubiquitinated substrate is concomitantly translocated into the 20S core particle, where it is degraded. Two class IIB molecules, C92 and C59 (Fig. 1D), strongly inhibited UbSic1 turnover in the reconstituted system (Fig. 1A). To address whether these

Table 1. Characterization of compounds in *Xenopus* extract assays. Results are reported as percent inhibition (percent stimulation). Compounds (200 μM, except C10 and C92, tested at 100 μM) and cyclin-luciferase (cyc-luc) were added to interphase extracts and then induced to enter mitosis by addition of nondegradable cyclin B, or extracts were pretreated with nondegradable cyclin B to allow entry into mitosis before addition of test compound and cyc-luc. Cdh1 was added to interphase extracts before addition of compound and cyc-luc. Interphase extracts were treated with recombinant axin to induce turnover of β-catenin-luciferase. Parentheses indicate those values where stimulation, rather than inhibition, was observed by addition of compound to the reaction.

Compound	Addition before mitotic entry	Addition after mitotic entry	Cdh1-activated interphase extract	β-catenin reporter protein
		Class IA		
C77	100	4	(12)	0
C58	100	5	(8)	2
C82	100	0	0	0
C34	100	0	(8)	6
C62	84	0	(8)	0
C61	77	8	(8)	2
C13	75	0	(9)	0
C18	73	4	(7)	0
C25	66	3	(6)	0
C54	54	3	(6)	0
C67	53	3	(8)	3
C40	42	0	(6)	3
		Class IB		
C39	100	9	(7)	67
C57	100	4	0	60
C51	100	0	0	30
C10	33	0	(4)	21
		Class IIA		
C1	100	100	35	6
C2	80	50	100	0
C8	70	63	20	0
		Class IIB		
C23	100	100	100	27
C59	97	100	100	70
C92	60	22	65	21

[1]Department of Biology, Howard Hughes Medical Institute (HHMI), California Institute of Technology, Pasadena, CA 91125, USA. [2]Institute of Chemistry and Cell Biology and Department of Cell Biology, Harvard Medical School, 240 Longwood Avenue, Boston, MA 02115, USA. [3]Department of Chemistry and Biochemistry, Center for Biomolecular Structure and Organization, University of Maryland, College Park, MD 20742, USA. [4]Division of Hematology-Oncology, Mattel Children's Hospital, Jonsson Comprehensive Cancer Center, David Geffen School of Medicine at University of California at Los Angeles (UCLA), 10833 Le Conte Avenue, Los Angeles, CA 90095, USA. [5]Department of Microbiology and Immunology, University of California, San Francisco, 513 Parnassus Avenue, San Francisco, CA 94143–0414, USA.

*To whom correspondence should be addressed. E-mail: randy_king@hms.harvard.edu

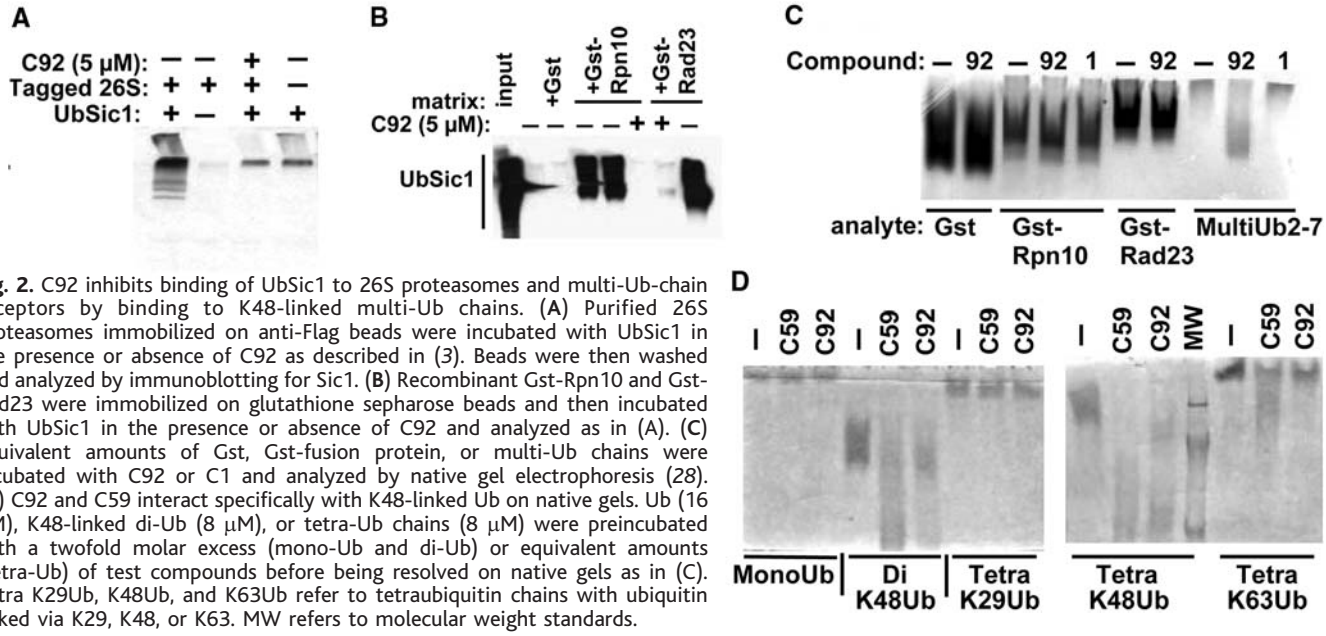

Fig. 2. C92 inhibits binding of UbSic1 to 26S proteasomes and multi-Ub-chain receptors by binding to K48-linked multi-Ub chains. (**A**) Purified 26S proteasomes immobilized on anti-Flag beads were incubated with UbSic1 in the presence or absence of C92 as described in (*3*). Beads were then washed and analyzed by immunoblotting for Sic1. (**B**) Recombinant Gst-Rpn10 and Gst-Rad23 were immobilized on glutathione sepharose beads and then incubated with UbSic1 in the presence or absence of C92 and analyzed as in (A). (**C**) Equivalent amounts of Gst, Gst-fusion protein, or multi-Ub chains were incubated with C92 or C1 and analyzed by native gel electrophoresis (*28*). (**D**) C92 and C59 interact specifically with K48-linked Ub on native gels. Ub (16 μM), K48-linked di-Ub (8 μM), or tetra-Ub chains (8 μM) were preincubated with a twofold molar excess (mono-Ub and di-Ub) or equivalent amounts (tetra-Ub) of test compounds before being resolved on native gels as in (C). Tetra K29Ub, K48Ub, and K63Ub refer to tetraubiquitin chains with ubiquitin linked via K29, K48, or K63. MW refers to molecular weight standards.

compounds acted upstream or downstream of Rpn11 isopeptidase, we treated proteasomes with the 20S inhibitor epoxomicin, which results in Rpn11-dependent substrate deubiquitination (*14*, *16*) and accumulation of deubiquitinated Sic1 within the 20S chamber (*13*). This reaction was completely blocked by C92 (Fig. 1B), with a median inhibitory concentration (IC_{50}) of about 400 nM (Fig. 1C). C59, which is structurally related to C92, also inhibited deubiquitination of UbSic1 (IC_{50} = 1 μM), whereas C23 inhibited marginally (fig. S5). Thus C92 and C59 potently blocked proteolysis at or upstream of the essential isopeptidase-dependent step.

Selective recognition of the multi-Ub chain by the 26S proteasome is the first step in UbSic1 degradation (*13*). C92 strongly inhibited binding of UbSic1 to purified 26S proteasomes (Fig. 2A), suggesting that it inhibited UbSic1 turnover by blocking the first step in the degradation process. The multi-Ub chain receptors Rad23 and Rpn10 serve a redundant role in targeting UbSic1 to the proteasome and sustaining its degradation (*13*). In the absence of the Ub-binding activities of Rpn10 and Rad23, UbSic1 is not recruited, deubiquitinated, or degraded by purified 26S proteasomes. We thus tested whether C92 could interfere with binding of UbSic1 to recombinant Rpn10 and Rad23. C92 abolished binding of UbSic1 to both proteins (Fig. 2B), even though these receptors use distinct domains [the Ub-interaction motif (UIM) and the Ub-associated (UBA) domain, respectively] to bind ubiquitin chains (*17*). C59 also abrogated binding of UbSic1 to Rpn10, whereas other compounds were without effect (fig. S5).

To distinguish whether C92 inhibited proteolysis by binding to proteasome receptor proteins or to the Ub chain on Sic1, we exploited the negative charge of C92 to determine whether compound binding induced a mobility shift of the target proteins upon fractionation on a native polyacrylamide gel. C92 was preincubated with recombinant Rpn10, Rad23, or a mixture of Ub chains containing two to seven Ub molecules. The mobility of the multi-Ub chains, but not Gst-Rpn10 or Gst-Rad23, was altered by incubation with C92, suggesting that C92 bound Ub chains (Fig. 2C). Ubiquitin molecules can be linked to each other in vivo through different internal lysines, including K29, K48, and K63 (*18*). The K48-linked chain is the principal targeting signal in proteolysis, whereas K63-linked chains are implicated in enzyme regulation (*19*). Whereas C92 and C59 efficiently shifted the native gel mobility of K48-linked ubiquitin chains, they had little or no effect on K29- or K63-linked chains (Fig. 2D). Because C92 and C59 bind to ubiquitin chains and block interactions with proteasome-associated receptors without affecting 26S assembly or peptidase activity (fig. S6), we refer to these compounds as ubistatin A and B, respectively.

We next tested the ability of ubistatins to block proteolysis of ornithine decarboxylase (ODC), whose degradation does not require ubiquitin (*20*). Whereas a 30-fold molar excess of ubistatin A over the substrate strongly inhibited UbSic1 degradation by purified yeast proteasomes (Fig. 1A), a 100-fold molar excess of ubistatin A over the substrate had no effect on degradation of radiolabeled ODC by purified rat proteasomes (fig. S7). Ubistatin B marginally inhibited ODC turnover at this concentration (12%). In contrast, a 20-fold molar excess of cold ODC inhibited degradation of labeled ODC by 43% under the same conditions. These data indicate that ubistatins at low concentrations preferentially inhibit the degradation of ubiquitin-dependent substrates. Inhibition of ODC turnover by high concentrations of ubistatins, especially ubistatin B (fig. S7), may reflect either nonspecific activity or specific inhibition of a targeting mechanism shared by ubiquitin-dependent and ubiquitin-independent substrates of the proteasome (*20*).

On the basis of the selectivity of ubistatin A for binding K48-linked chains and inhibiting the ubiquitin-dependent turnover of Sic1 but not the ubiquitin-independent turnover of ODC, we tested the effect of ubistatin A on protein degradation within intact mammalian cells. Because the negative charge on ubistatin A precluded efficient membrane permeation, we introduced the compound into cells by microinjection and monitored degradation of an androgen receptor–green fluorescent protein (AR-GFP) fusion protein by fluorescence microscopy. Microinjection of a synthetic compound (protac, proteolysis-targeting chimeric molecule), which recruits AR-GFP to $SCF^{\beta\text{-}TRCP}$, induces rapid proteasome-dependent turnover of AR-GFP (*21*). Microinjection of 100 nM ubistatin A into mammalian cells inhibited the Protac-induced degradation of AR-GFP as efficiently as 100 nM epoxomicin (fig. S8), demonstrating that ubistatin A is an effective

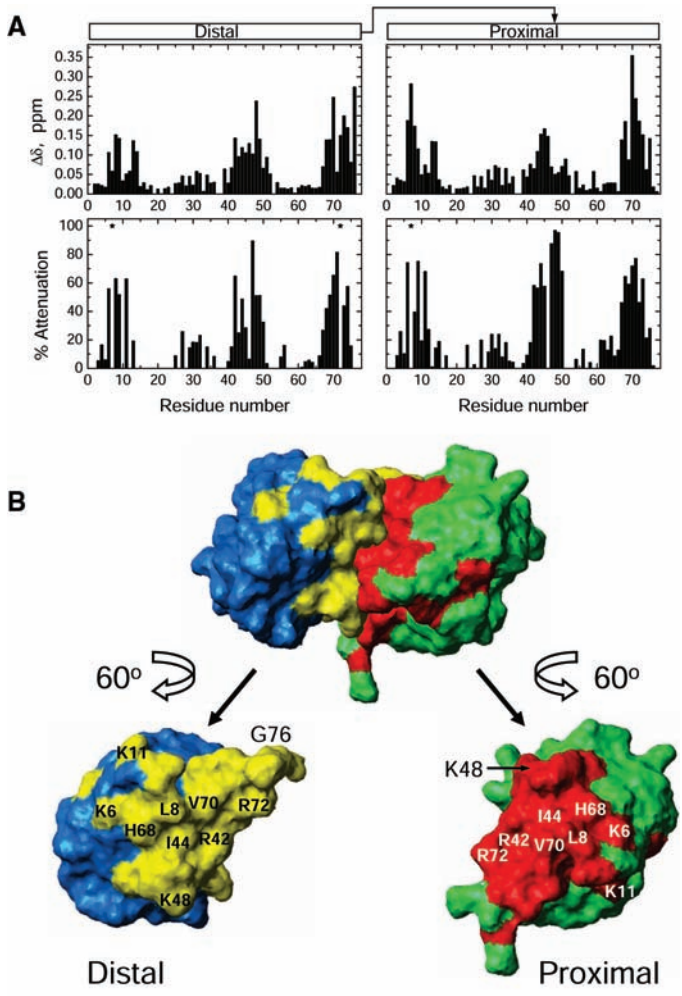

Fig. 3. Ubistatin A binding to K48-linked di-Ub induces site-specific perturbations in NMR spectra for both Ub domains. (**A**) Backbone NH chemical shift perturbation, Δδ, and percent signal attenuation caused by ubistatin A binding as a function of residue number for the distal (left) and the proximal (right) domains. Ub units are called "distal" and "proximal" to reflect their location in the chain relative to the free C terminus. The diagram (top) depicts the location of the G76-K48 isopeptide bond between the two Ub domains. Asterisks indicate residues that showed significant signal attenuation that could not be accurately quantified because of signal overlap. (**B**) Mapping of the perturbed sites on the surface of di-Ub. The distal and proximal domains are shown in surface representation and colored blue and green, respectively; the perturbed sites on these domains are colored yellow and red and correspond to residues with Δδ > 0.075 parts per million and/or signal attenuation greater than 50%. Numbers indicate surface location of the hydrophobic patch and some basic residues along with G76 (distal) and the side chain of K48 (proximal).

inhibitor of ubiquitin-dependent degradation in multiple experimental settings.

The specificity of ubistatin A for K48-linked ubiquitin chains suggested that it might bind at the Ub-Ub interface, which is well defined in K48-linked chains but is not present in K63-linked di-ubiquitin (Ub_2) (*22*). We performed nuclear magnetic resonance (NMR) titration studies of K48-linked Ub_2 by using a segmental labeling strategy (*23*). Well-defined site-specific perturbations were observed in the resonances of the backbone amides of both Ub units in Ub_2 (Fig. 3), indicating that the hydrophobic patch residues L8, I44, V70 (*24*), and neighboring sites (including basic residues K6, K11, R42, H68, and R72) experienced alterations in their molecular environment upon binding of ubistatin A. The same hydrophobic patch is involved in the formation of the interdomain interface in Ub_2 (*23*, *25*) and mediates the binding of ubiquitin to multiple proteins containing CUE (coupling of ubiquitin conjugation to ER degradation), UBA, and UIM domains (*17*). At the high concentrations of compound used in the NMR titration experiments, ubistatin A induced a similar pattern of chemical shift perturbations in monomeric ubiquitin, suggesting that the effect of ubistatin A on Ub_2 arises from its direct binding to the hydrophobic patch and the basic residues around it. The same sites are perturbed when ubistatin A binds tetra-Ub chains (*26*).

Although there is intense interest in developing drugs for defined molecular targets, it is often difficult to know a priori which proteins can be most effectively targeted with small molecules. Our study demonstrates that chemical genetic screens in complex biochemical systems such as *Xenopus* extracts can identify small-molecule inhibitors that act through unexpected mechanisms. Although target identification remains challenging, our work highlights the value of reconstituted biochemical systems to illuminate the mechanism of action of inhibitors discovered in unbiased screens. The recent approval of the 20S proteasome inhibitor Velcade (Millenium Pharmaceuticals, Cambridge, MA) for treatment of relapsed multiple myeloma (*27*) has suggested that the ubiquitin-proteasome system is an attractive target for cancer drug development. The identification of ubistatins indicates that the ubiquitin chain itself provides another potential opportunity for pharmacological intervention in this important pathway.

References and Notes

1. T. U. Mayer, *Trends Cell Biol.* **13**, 270 (2003).
2. J. M. Peters, *Mol. Cell* **9**, 931 (2002).
3. Materials and methods are available as supporting material on *Science* Online.
4. M. Dasso, J. W. Newport, *Cell* **61**, 811 (1990).
5. J. Minshull, H. Sun, N. K. Tonks, A. W. Murray, *Cell* **79**, 475 (1994).
6. L. A. Walling, N. R. Peters, E. J. Horn, R. W. King, *J. Cell. Biochem.* **S37**, 7 (2001).
7. C. M. Pfleger, M. W. Kirschner, *Genes Dev.* **14**, 655 (2000).
8. A. Salic, E. Lee, L. Mayer, M. W. Kirschner, *Mol. Cell* **5**, 523 (2000).
9. N. Peters, R. W. King, unpublished data.
10. R. Verma, H. McDonald, J. R. Yates 3rd, R. J. Deshaies, *Mol. Cell* **8**, 439 (2001).
11. D. Skowyra *et al.*, *Science* **284**, 662 (1999).
12. J. H. Seol *et al.*, *Genes Dev.* **13**, 1614 (1999).
13. R. Verma, R. Oania, J. Graumann, R. J. Deshaies, *Cell* **118**, 99 (2004).
14. R. Verma *et al.*, *Science* **298**, 611 (2002); published online 15 August 2002; 10.1126/science.1075898.
15. T. Yao, R. E. Cohen, *Nature* **419**, 403 (2002).
16. L. Meng *et al.*, *Proc. Natl. Acad. Sci. U.S.A.* **96**, 10403 (1999).
17. R. Hartmann-Petersen, M. Seeger, C. Gordon, *Trends Biochem. Sci.* **28**, 26 (2003).
18. J. Peng *et al.*, *Nat. Biotechnol.* **21**, 921 (2003).
19. C. M. Pickart, *Cell* **116**, 181 (2004).
20. M. Zhang, C. M. Pickart, P. Coffino, *EMBO J.* **22**, 1488 (2003).
21. K. M. Sakamoto *et al.*, *Mol. Cell. Proteomics* **2**, 1350 (2003).
22. R. Varadan *et al.*, *J. Biol. Chem.* **279**, 7055 (2004).
23. R. Varadan, O. Walker, C. Pickart, D. Fushman, *J. Mol. Biol.* **324**, 637 (2002).
24. Single-letter abbreviations for the amino acid residues are as follows: H, His; I, Ile; K, Lys; L, Leu; R, Arg; and V, Val.
25. W. J. Cook, L. C. Jeffrey, M. Carson, Z. Chen, C. M. Pickart, *J. Biol. Chem.* **267**, 16467 (1992).
26. D. Fushman, unpublished data.
27. J. Adams, *Nat. Rev. Cancer* **4**, 349 (2004).
28. R. Verma *et al.*, *Mol. Biol. Cell* **11**, 3425 (2000).

29. We thank the Developmental Therapeutics Program, National Cancer Institute, for providing access to compound collections, C. Pickart for tetraubiquitin chains of defined linkages, A. Salic for recombinant Axin and β-catenin-luciferase, and C. Sawyers for AR-GFP. G.T. is supported by NIH National Research Service Award GM068276. K.M.S. is supported by a UCLA Specialized Programs of Research Excellence in Prostate Cancer Development Research Seed Grant (P50 CA92131), U.S. Department of Defense (DAMD17-03-1-0220), and NIH (R21CA108545). P.C. is supported by NIH R01 GM-45335. D.F. is supported by NIH grant GM65334. R.J.D. is supported by HHMI and the Susan G. Komen Breast Cancer Foundation (DISS0201703). R.W.K. is supported by the NIH (CA78048 and GM66492), the McKenzie Family Foundation, and the Harvard-Armenise Foundation and is a Damon Runyon Scholar. Screening facilities at the Harvard Institute of Chemistry and Cell Biology were supported by grants from the Keck Foundation, Merck and Company, and Merck KGaA. R.J.D. is a founder and paid consultant of Proteolix, which is negotiating with Caltech and Harvard to license a patent related to ubistatin. Molecular interaction data have been deposited in the Biomolecular Interaction Network Database with accession codes 151787 to 151791.

Supporting Online Material

www.sciencemag.org/cgi/content/full/306/5693/117/DC1
Materials and Methods
Figs. S1 to S8
Table S1

1 June 2004; accepted 6 August 2004

Regulation of Cytokine Receptors by Golgi N-Glycan Processing and Endocytosis

Emily A. Partridge,[1,3] Christine Le Roy,[1] Gianni M. Di Guglielmo,[1] Judy Pawling,[1] Pam Cheung,[1,2] Maria Granovsky,[1,2] Ivan R. Nabi,[4] Jeffrey L. Wrana,[1,2] James W. Dennis[1,2,3]*

The Golgi enzyme β1,6 N-acetylglucosaminyltransferase V (Mgat5) is upregulated in carcinomas and promotes the substitution of N-glycan with poly N-acetyllactosamine, the preferred ligand for galectin-3 (Gal-3). Here, we report that expression of Mgat5 sensitized mouse cells to multiple cytokines. Gal-3 cross-linked Mgat5-modified N-glycans on epidermal growth factor and transforming growth factor–β receptors at the cell surface and delayed their removal by constitutive endocytosis. Mgat5 expression in mammary carcinoma was rate limiting for cytokine signaling and consequently for epithelial-mesenchymal transition, cell motility, and tumor metastasis. Mgat5 also promoted cytokine-mediated leukocyte signaling, phagocytosis, and extravasation in vivo. Thus, conditional regulation of N-glycan processing drives synchronous modification of cytokine receptors, which balances their surface retention against loss via endocytosis.

Co-translational modification of proteins in the endoplasmic reticulum by N-glycosylation facilitates their folding and is essential in single-cell eukaryotes. Metazoans have additional Golgi enzymes that trim and remodel the N-glycans, producing complex-type N-glycans on glycoproteins destined for the cell surface. Mammalian development requires complex-type N-glycans containing N-acetyllactosamine antennae, because their complete absence in Mgat1-deficient embryos is lethal (*1*, *2*). Deficiencies in N-acetylglucosaminyltransferase II and V (Mgat2 and Mgat5) acting downstream of Mgat1 reduce the content of N-acetyllactosamine, and mutations in these loci result in viable mice with a number of tissue defects (*3*, *4*). N-glycan processing generates ligands for various mammalian lectins, but the consequences of these interactions are poorly understood. The galectin family of N-acetyllactosamine-binding lectins has been implicated in cell

growth, endothelial cell morphogenesis, angiogenesis (*5*), cell adhesion (*6*), and cancer metastasis (*7*). Galectins are expressed widely in metazoan tissues, located in the cytosol and nucleus, and secreted by a nonclassical pathway to the cell surface (*8*).

Galectin-3 (Gal-3) binds to poly-N-acetyllactosamine (i.e., a polymer of Galβ1,4GlcNAcβ1,3) with higher affinity than to the more ubiquitous N-acetyllactosamine antennae (*9*), and Mgat5 controls production of these larger polymers by producing the preferred intermediate for their addition (fig. S1A) (*10*). The nonlectin N-terminal domain of Gal-3 mediates pentamer formation in the presence of multivalent ligands, thereby cross-linking glycoproteins in proportion to ligand concentrations (*11*). The resulting superstructure of galectins and glycoproteins at the cell surface generates a molecular lattice. Mgat5-modified N-glycans on T cell receptors bind Gal-3, which opposes antigen-dependent clustering and suppresses autoimmune disease (*12*). Here, we examine the possibility that Mgat5-modified N-glycans on cytokine receptors oppose constitutive endocytosis by retaining surface receptors where membrane remodeling is active, notably in tumor cells and monocytes (model in fig. S1B).

The Mgat5-deficient background suppresses the oncogenic potency of a polyomavirus middle T oncogene (PyMT) transgene in mice (*4*). The PyMT protein is a cytosolic scaffold that promotes Src, phosphatidylinositol (PI) 3-kinase, and Shc/Ras activation (*13*), but activation of these intracellular pathways remains partially dependent on host cell responses to extracellular stimuli and to Mgat5-modified N-

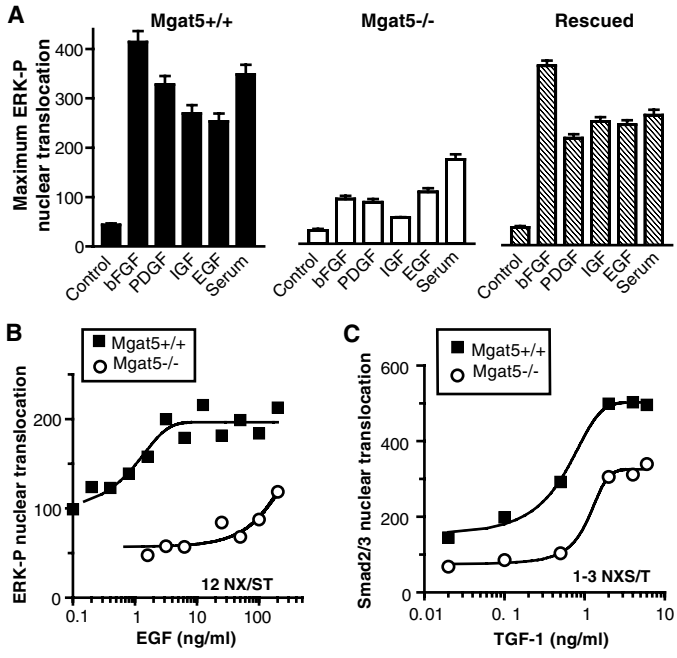

Fig. 1. Mgat5-modified N-glycans promote cytokine signaling. (**A**) Nuclear translocation of Erk-P 10 min after stimulation with cytokines (100 ng/ml) or 5% fetal calf serum, measured by scan array immunofluorescence imaging (ArrayScan, Cellomics, Incorporated, Pittsburgh, PA). (**B**) Erk-P nuclear translocation 10 min after stimulation with EGF. (**C**) Smad2 and 3 nuclear translocation 45 min after stimulation with TGF-β1.

[1]Samuel Lunenfeld Research Institute, Mount Sinai Hospital, 600 University Avenue, Toronto, ON M5G 1X5, Canada. [2]Department of Medical Genetics and Microbiology, University of Toronto, Toronto, ON M5S 1A8, Canada. [3]Department of Laboratory Medicine and Pathology, [4]Department of Anatomy, Cell Biology, and Physiology, University of British Columbia, Vancouver, BC V6T 1Z3, Canada.

*To whom correspondence should be addressed. E-mail: Dennis@mshri.on.ca

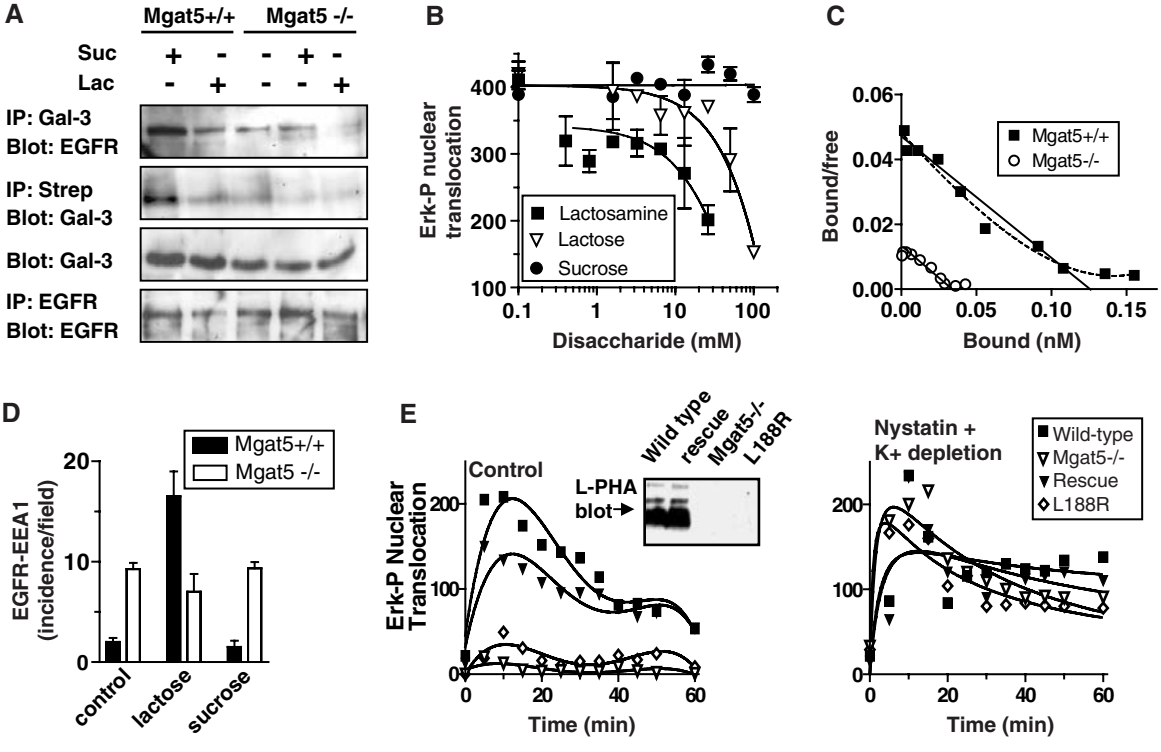

Fig. 2. Cell-surface EGFR binds to Gal-3 in an Mgat5-dependent manner. (**A**) Mgat5$^{+/+}$ and Mgat5$^{-/-}$ cells were pretreated as indicated, then subjected to DTSSP (dithio-bis-suffosuccinimydyl propionate) cross-linking and biotinylation of surface proteins. Biotinylated proteins were captured on streptoavidin-agarose beads. Sucrose and untreated cells were identical, and data shown are representative of three independent experiments. (**B**) EGF stimulated Erk-P nuclear translocation after a 24-hour pretreatment with lactose, N-acetyllactosamine, or sucrose in Mgat5$^{+/+}$ cells. (**C**) Scatchard plot of EGFR ^{125}I-EGF binding to Mgat5$^{+/+}$ and Mgat5$^{-/-}$ cells revealed 14,000 and 2500 binding sites per cell, with affinities of 2.7 and 2.5 nM, respectively. (**D**) Co-localization of EGFR with the endosome protein EEA-1 by immunofluorescence. (**E**) Erk-P nuclear translocation in cells pretreated with buffer (left) or nystatin plus K$^+$ depletion (right) before addition of EGF (100 ng/ml). Mgat5$^{-/-}$ cells were infected with retrovirus vectors for expression of either Mgat5 (rescued) or a mutant form of Mgat5 (L188R). (Inset) A blot of cell lysates probed with L-PHA lectin to reveal Mgat5-modified N-glycans.

glycans (*4*). To explore this interaction, we isolated mammary epithelial tumor cells lines from PyMT transgenic mice on Mgat5$^{-/-}$ and Mgat5$^{+/+}$backgrounds and compared their responsiveness to growth factors by measuring phosphorylation and nuclear translocation of extracellular signal–regulated kinase (Erk) (Fig. 1A and fig. S2). Mgat5$^{-/-}$ tumor cells were less responsive than Mgat5$^{+/+}$ cells to epidermal growth factor (EGF), insulin-like growth factor (IGF), platelet-derived growth factor (PDGF), basic fibroblast growth factor (bFGF), and fetal calf serum, but infection of the cells with a retroviral vector encoding Mgat5 restored responsiveness (Fig. 1B and fig. S3). These cytokine receptors are all highly N-glycosylated with 8 to 16 N-glycosylation sites (N-X-S/T). Characterization of EGF receptors (EGFR) in carcinoma cells has revealed 10 to 12 occupied sites, and a subset of the N-glycans are Mgat5-modified and extended with poly-N-acetyllactosamine (*14*). The transforming growth factor–β (TGF-β) receptors TβRI and TβRII have only one and three N-X-S/T consensus sites, respectively. Mgat5$^{-/-}$ cells displayed a two- to threefold decrease in sensitivity to TGF-β compared with the ~100-fold decrease in sensitivity to EGF, PDGF, IGF-1, and FGF, supporting the notion that both Golgi processing (i.e., Mgat5 and poly-N-acetyllactosamine) and the number of N-glycans per receptor are important (Fig. 1, B and C, and fig. S3).

Next we probed the cell surface with a chemical cross-linker, which revealed that EGFR was associated with Gal-3 on the surface of Mgat5$^{+/+}$ cells whereas this interaction was greatly reduced on Mgat5$^{-/-}$ cells (Fig. 2A). Pretreatment of Mgat5$^{+/+}$ tumor cells with lactose, a competitive inhibitor of Gal-3 binding, blocked EGFR–Gal-3 cross-linking, confirming that the carbohydrate-reactive domain of Gal-3 is required. Lactose pretreatment also depleted surface Gal-3 on Mgat5$^{+/+}$ cells, producing a phenocopy of the Mgat5$^{-/-}$ cells. Furthermore, lactose and, with greater effect, N-acetyllactosamine dampened EGF-dependent activation of Erk in Mgat5$^{+/+}$ cells (Fig. 2B). Thus, surface residency of both Gal-3 and glycoprotein receptors displays a dependency on Mgat5 modification of the receptor N-glycans.

Receptor density at the cell surface is influenced by rates of de novo production, endocytosis, recycling, and degradation (*15*). Scatchard analysis revealed sixfold fewer EGFRs at the cell surface in mutant cells (Fig. 2C), although total EGFR amounts were not different between Mgat5$^{+/+}$ and Mgat5$^{-/-}$ cell lysates (Fig. 2A). The affinity of EGF binding (2 to 3 nM) was the same in Mgat5$^{+/+}$ and Mgat5$^{-/-}$ cells, consistent with previous observations that ligand affinity is not markedly altered by variations in N-glycan processing (*16*). Mgat5$^{-/-}$ cells displayed fourfold greater co-localization of EGFR with EEA-1, an early endosomal marker (Fig. 2D and fig. S6A). Pretreatment of Mgat5$^{+/+}$ cells with lactose but not sucrose promoted receptor accumulation in the endosomes, mimicking the distribution observed in untreated Mgat5$^{-/-}$ cells and providing further evidence that receptors are anchored at the cell surface by the lattice. In the absence of the lattice, receptor amounts increase in the early endosomes, possibly because of reduced trafficking downstream of receptor tyrosine kinase signaling (*17*). Lastly, the Mgat5$^{-/-}$ signaling deficiency could be rescued by K^+ depletion and nystatin treatment, agents that inhibit endocytosis (Fig. 2E and figs. S2C and S4). This chemical rescue of signaling was comparable to a genetic rescue using Mgat5, whereas a mutated Mgat5 [Lys^{188} → Arg^{188} (L188R)] that could not enter the Golgi failed to rescue signaling (Fig. 2E).

Ligand binding and autophosphorylation of EGFR stimulates clathrin-dependent EGFR endocytosis, where signaling is briefly amplified and then followed by transit of receptors

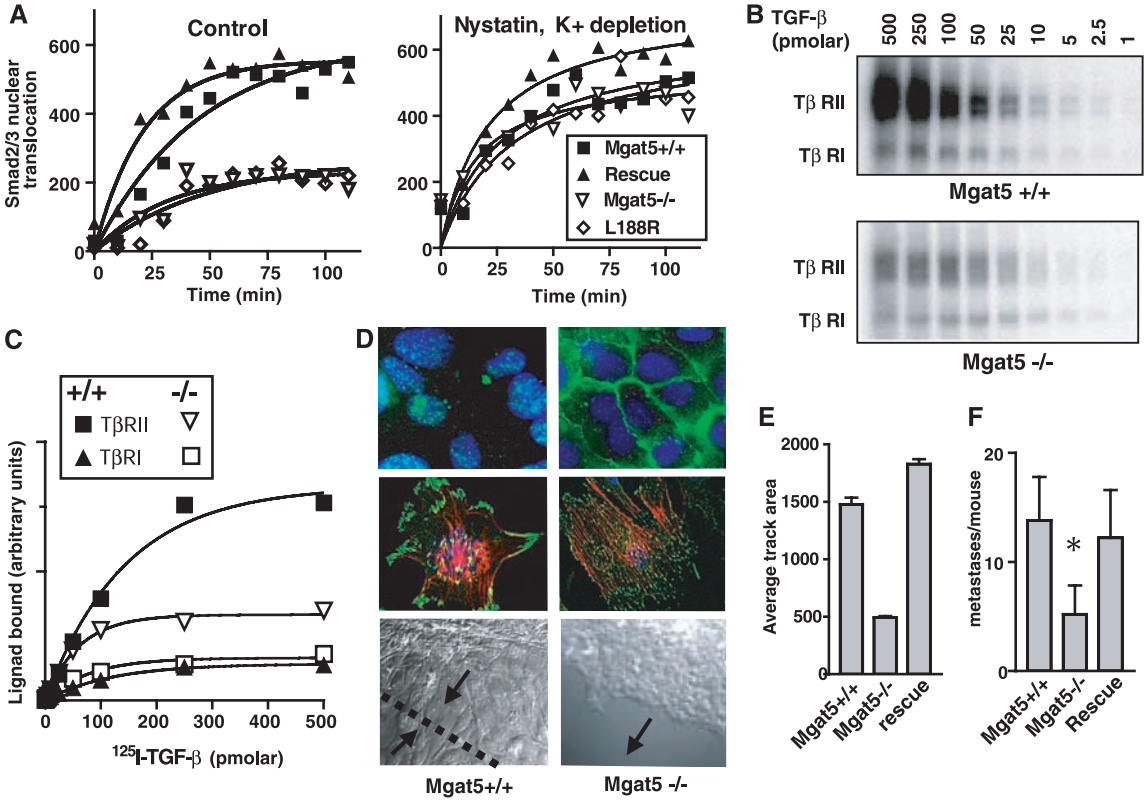

Fig. 3. EMT and the malignant phenotype are dependent on Mgat5. (**A**) Smad2 and 3 nuclear translocation in cells pretreated with buffer (left) or nystatin plus K^+ depletion (right) before addition of TGF-β (5 ng/ml). Mgat5$^{+/+}$, Mgat5$^{-/-}$, and mutant cells were infected with Mgat5 retroviral vectors. (**B**) Autoradiograph showing ^{125}I-TGF-β1 binding to cell-surface TβR. The identities of TβRI and TβRII were confirmed by immunoprecipitation. (**C**) ^{125}I-TGF-β1 bound to TGF-β receptors was quantified by densitometry. (**D**) E-cadherin (green) in tight junctions of Mgat5$^{+/+}$ and Mgat5$^{-/-}$ tumor cell monolayers revealed by immunofluorescence. Nuclear DNA is revealed by Hoechst staining. Cells plated at low density in second row are stained for actin microfilaments with rhodamine-phalloidin (red) and antibodies against vinculin (green). In the third row, contact inhibition is assessed by scratch-wounding confluent cell monolayers. The arrow indicates direction of cell movement, showing closure of the wound at 24 hours by Mgat5$^{+/+}$ but not by Mgat5$^{-/-}$ cells. (**E**) Cell motility on fibronectin-coated wells measured by scan array microbead clearance over 18 hours and expressed as mean ± SE for 100 cell tracks. (**F**) Spontaneous lung metastases (mean ± SE, $n = 6$) in wild-type mice (*$P < 0.01$).

to recycling or proteolytic compartments (*18*). In contrast, TβRII internalization is ligand-independent and occurs via both clathrin- and caveolae-dependent pathways (*19*). In spite of the differences between TβR and EGFR receptor dynamics, their regulation by the lattice was qualitatively similar. TβRII receptors associate with Gal-3 in an Mgat5-dependent manner, and the interaction could be blocked by lactose (fig. S6A). TGF-β signaling in mutant cells was restored by infection with the Mgat5 retroviral vector and by blocking endocytosis with the use of K^+ depletion and nystatin (Fig. 3A and fig. S5B). Total TβRII amounts were similar in mutant and wild-type cells, but more were localized to endosomes and less were at the surface in mutant cells (figs. S5C and S6B). Binding of ^{125}I-labeled TGF-β1 to surface TβRII was reduced 2.3-fold, whereas binding to TβRI was unchanged, an effect consistent with the number of N-X-S/T sites per receptor (i.e., three and one, respectively) (Fig. 3, B and C). We conclude that cytokine receptors are cleared from the surface of Mgat5$^{-/-}$ cells more rapidly but are delayed in the early endosomes compared to Mgat5^{++} cells.

Epithelial-mesenchymal transition (EMT) in epithelial cancers is characterized by the loss of adhesion junctions, increased membrane remodeling, and metastasis (*20*). The Mgat5$^{+/+}$ tumor cells displayed EMT with loss-of-adhesion junctions, a fibroblastic morphology with lamelipodia containing active signaling, and reduced contact inhibition in a scratch-wound assay (Fig. 3D). In contrast, Mgat5$^{-/-}$ tumor cells retained an epithelial morphology characterized by E-cadherin localization in cell adhesion junctions, cortical actin stress fibers, small focal adhesions, and strong contact inhibition of growth. EMT could be induced in Mgat5$^{-/-}$ by infecting the cells with a retroviral vector for expression of Mgat5. In vitro, wild-type and Mgat5-rescued mutant cells displayed greater cell motility (Fig. 3E), and in vivo these cells produced significantly greater numbers of lung tumor metastases, than Mgat5$^{-/-}$ cells (Fig. 3F). We conclude that Mgat5 is necessary for EMT and supplies positive feedback through cytokine receptors to Ras, PI3 kinase, and Smad2 and 3 signaling (*20*). The Ras-Raf-Ets pathway positively regulates Mgat5 transcription (*21*). TGF-β signaling also stimulates Mgat5 expression in mesenchymal cells (*22*), and we confirmed that TGF-β increased the surface expression of Mgat5-modified N-glycans (fig. S5E). TGF-β induces its own gene expression as well as that of other cytokines, and, cumulatively, these sources of positive feedback appear to maintain the EMT-invasive phenotype. Suppressors of constitutive endocytosis other than the lattice described here may promote tumor progression. In this regard, the metastasis suppressor protein Nm23-H1 is a nucleotide diphosphate kinase that supplies guanine triphosphate (GTP) to the small guanine triphosphatase (GTPase) dynamin required for membrane invagination (*23*).

These observations suggest that a transformation-associated increase in membrane remodeling and endocytosis may require the lattice to protect receptors at the surface. We found that nontransformed Chinese hamster ovary (CHO) cells and the lectin-resistant cell lines Lec1 and Lec8 all displayed similar responses to TGF-β, suggesting the lattice was not required (fig. S7A). The Lec1 and Lec8 cell lines are deficient in Mgat1 and Golgi uridine 5′diphosphate–Gal transporter activity, respectively, and consequently depleted for poly-N-acetyllactosamine and presumably the lattice. However, when these cell lines were transformed with polyomavirus large T (designated CHOP), signaling was significantly greater in the wild-type cells compared to the transformed Lec mutants (fig. S7B). To explore this with other cell lines, we treated transformed and nontransformed cells with swainsonine, a Golgi α-mannosidase II inhibitor that blocks processing upstream of Mgat5. Swainsonine reduced TGF-β responsiveness in B16F10 murine melanoma cells and SW620 human colorectal cancer cells but not in nontransformed murine epithelial NMuMG cells (fig. S7, C to F).

The motile and highly endocytic phenotype of activated macrophages is similar in this regard to tumor cells and may require the lattice to retain surface cytokine receptors. We examined this possibility by using lipopolysaccharide (LPS)-elicited peritoneal macrophages and determined that endogenous phospho-Smad2 and -Erk2 and 3, as well as acute responses to TGF-β and serum, were suppressed in Mgat5$^{-/-}$ cells (Fig. 4, A and B). Furthermore, binding of ^{125}I-labeled TGF-β1 to surface receptors was reduced in Mgat5$^{-/-}$ macrophages, characteristic of the Mgat5-deficient phenotype observed in tumor cells (fig. S5F). Early in the injury response, cytokines stimulate leukocyte migration, and subsequently TGF-β attains amounts that suppress the inflammatory process (*24*). Consistent with this chronology, we observed that skin inflammation induced by either arachidonic acid or phorbol ester was delayed in both its onset and its resolution phases in Mgat5$^{-/-}$ mice (Fig. 4C). Similarly, the initial rate of leukocyte extravasation into the peritoneal cavity in response to an injection of thioglycollate was impaired in Mgat5$^{-/-}$ mice (Fig. 4D), demonstrating that Mgat5 regulates leukocytes motility. Phagocytosis of latex beads by Mgat5$^{-/-}$ macrophages was reduced. The PI3 kinase inhibitor wortmannin reduced phagocytosis in wild-type macrophages but did not suppress further in Mgat5$^{-/-}$ cells (Fig. 4E). Thus, the lattice promotes responsiveness to extracellular cytokines in this example of a nontransformed but endocytic cell type. Mgat5 modification of N-glycans on integrins and other adhesion receptors may also influence membrane remodeling and extracellular matrix assembly (*25*).

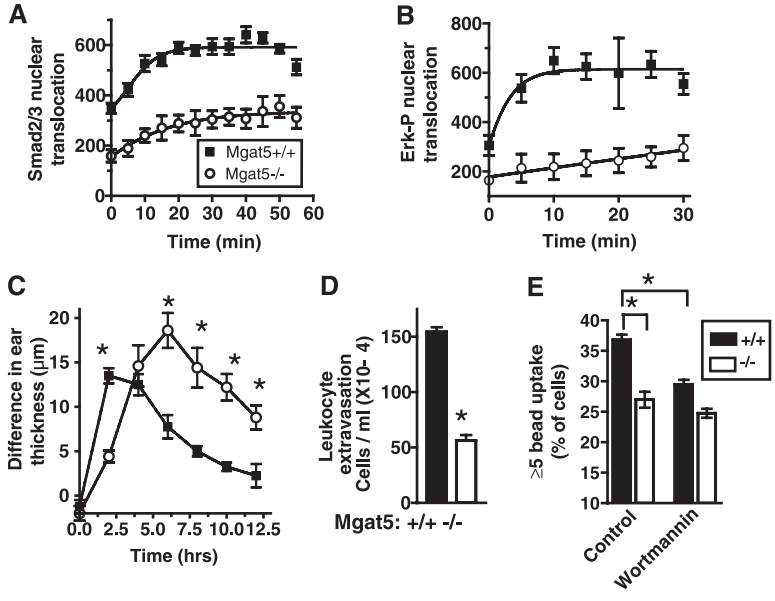

Fig. 4. Macrophage signaling, migration, and phagocytosis are dependent on Mgat5. (**A**) Smad2 and 3 and (**B**) Erk-P nuclear translocation in LPS-elicited peritoneal macrophages from Mgat5$^{+/+}$ and Mgat5$^{-/-}$ mice stimulated TGF-β1 (2 ng/ml) and 5% FCS, respectively. (**C**) Ear swelling induced by topical application of arachidonic acid in Mgat5$^{-/-}$ (○) and Mgat5$^{+/+}$ (+) mice (*$P < 0.001$). (**D**) Leukocytes recruitment into the peritoneal cavity 3 hours after an injection of thioglycolate (*$P < 0.001$). (**E**) Phagocytosis of five or more fluorescent latex beads by thioglycolate-elicited macrophages, either untreated or treated with wortmannin (100 nM) for 1 hour ex vivo during bead phagocytosis (*$P < 0.01$). Values are mean ± SE for five mice per genotype.

Lattice-dependent regulation of receptors occurs primarily at the cell surface, is dependent on Golgi enzyme activities and the number of N-glycans per receptor, and opposes receptor loss to endocytosis (fig. S1B). Receptor tyrosine kinases activate Rab5, a small GTPase required for endocytosis (*17*), thereby promoting receptor loss, whereas our results show that positive feedback from signaling to the Golgi pathway strengthens the lattice, thereby maintaining cytokine responsiveness. Lastly, we speculate that genetic and environmental factors that regulate the integrity of the lattice should influence the decline in surface cytokine receptors known to occur with aging (*26*, *27*) and thereby progenitor cell and tissue renewal.

References and Notes

1. E. Ioffe, P. Stanley, *Proc. Natl. Acad. Sci. U.S.A.* **91**, 728 (1994).
2. M. Metzler *et al.*, *EMBO J.* **13**, 2056 (1994).
3. Y. Wang *et al.*, *Glycobiology* **11**, 1051 (2001).
4. M. Granovsky *et al.*, *Nat. Med.* **6**, 306 (2000).
5. P. Nangia-Makker *et al.*, *Am. J. Pathol.* **156**, 899 (2000).
6. Y. Levy, D. Ronen, A. D. Bershadsky, Y. Zick, *J. Biol. Chem.* **278**, 14533 (2003).
7. H. C. Gong *et al.*, *Cancer Res.* **59**, 6239 (1999).
8. R. C. Hughes, *Biochim. Biophys. Acta* **1473**, 172 (1999).
9. J. Hirabayashi *et al.*, *Biochim. Biophys. Acta* **1572**, 232 (2002).
10. S. Yousefi *et al.*, *J. Biol. Chem.* **266**, 1772 (1991).
11. N. Ahmad *et al.*, *J. Biol. Chem.* **279**, 10841 (2003).
12. M. Demetriou, M. Granovsky, S. Quaggin, J. W. Dennis, *Nature* **409**, 733 (2001).
13. M. A. Webster *et al.*, *Mol. Cell. Biol.* **18**, 2344 (1998).
14. C. J. Stroop *et al.*, *Glycobiology* **10**, 901 (2000).
15. H. S. Wiley, S. Y. Shvartsman, D. A. Lauffenburger, *Trends Cell Biol.* **13**, 43 (2003).
16. T. C. Elleman *et al.*, *Biochem. J.* **347**, 771 (2000).
17. L. Lanzetti, A. Palamidessi, L. Areces, G. Scita, P. P. Di Fiore, *Nature* **429**, 309 (2004).
18. P. Soubeyran, K. Kowanetz, I. Szymkiewicz, W. Y. Langdon, I. Dikic, *Nature* **416**, 183 (2002).
19. G. M. Di Guglielmo, C. Le Roy, A. F. Goodfellow, J. L. Wrana, *Nature Cell Biol.* **5**, 410 (2003).
20. M. Oft, R. J. Akhurst, A. Balmain, *Nature Cell Biol.* **4**, 487 (2002).
21. L. Chen, W. Zhang, N. Fregien, M. Pierce, *Oncogene* **17**, 2087 (1998).
22. E. Miyoshi *et al.*, *J. Biol. Chem.* **270**, 6216 (1995).
23. F. Palacios, J. K. Schweitzer, R. L. Boshans, C. D'Souza-Schorey, *Nature Cell Biol.* **4**, 929 (2002).
24. M. J. Crowe, T. Doetschman, D. G. Greenhalgh, *J. Invest. Dermatol.* **115**, 3 (2000).
25. M. Demetriou, I. R. Nabi, M. Coppolino, S. Dedhar, J. W. Dennis, *J. Cell Biol.* **130**, 383 (1995).
26. S. C. Park, *Mech. Ageing Dev.* **123**, 917 (2002).
27. H. Shiraha, K. Gupta, K. Drabik, A. Wells, *J. Biol. Chem.* **275**, 19343 (2000).

28. This research was supported by grants from the Canadian Institute for Health Research (CIHR) and a U.S. Army Breast Cancer Research grant to J.W.D. and a CIHR studentship to E.P. The authors thank A. Raz for Gal-3 antibodies and J. Hudson and C. Swallow for helpful discussion.

Supporting Online Material

www.sciencemag.org/cgi/content/full/306/5693/120/DC1
Materials and Methods
SOM Text
Figs. S1 to S7
Table S1

29 June 2004; accepted 13 August 2004

Src Mediates a Switch from Microtubule- to Actin-Based Motility of Vaccinia Virus

Timothy P. Newsome, Niki Scaplehorn, Michael Way*

The cascade of events that leads to vaccinia-induced actin polymerization requires Src-dependent tyrosine phosphorylation of the viral membrane protein A36R. We found that a localized outside-in signaling cascade induced by the viral membrane protein B5R is required to potently activate Src and induce A36R phosphorylation at the plasma membrane. In addition, Src-mediated phosphorylation of A36R regulated the ability of virus particles to recruit and release conventional kinesin. Thus, Src activity regulates the transition between cytoplasmic microtubule transport and actin-based motility at the plasma membrane.

The microtubule cytoskeleton provides many viruses with an efficient way to reach their site of replication, as well as a means for newly assembled viruses to leave their unwilling host (*1*, *2*). In the case of vaccinia virus, recruitment of conventional kinesin by intracellular enveloped virus (IEV) particles results in their microtubule-dependent transport from perinuclear assembly sites to the cell periphery (*3*–*7*). Upon reaching the plasma membrane, vaccinia induces localized actin polymerization that acts to enhance cell-to-cell spread of the virus (*4*, *5*, *7*–*9*). Vaccinia actin tail formation, which occurs beneath the extracellular cell-associated enveloped virus (CEV) at the plasma membrane (*4*, *5*, *10*), appears to mimic receptor kinase signaling at the leading edge of motile cells (*11*–*14*). Src-dependent phosphorylation of Tyr^{112} and Tyr^{132} of A36R results in the generation of binding sites for the SH2 (Src homology 2) domains of the adapter proteins Nck and Grb2, respectively (*11*, *14*). Nck is recruited to the virus as a complex with WASP interacting protein (WIP) and N-WASP; this complex is stabilized by additional interactions with Grb2 (*11*, *12*, *14*–*16*). Ultimately, recruitment of N-WASP leads to stimulation of the actin-nucleating activity of the Arp2/3 complex and actin tail formation (*13*).

To address how the microtubule and actin phases of virus transport are coordinated at the plasma membrane, we examined the regulation of A36R phosphorylation, which is the most upstream event of actin tail formation. Src activity is required for actin tail formation (*11*), but it is not clear whether A36R is a Src substrate. In in vitro kinase assays using purified components, Src was able to phosphorylate Tyr^{112} of A36R (residues 24 to 118) directly, and this led to the binding of Nck (Fig. 1A) (*17*). Neither Src-mediated phosphorylation of A36R (residues 24 to 118) nor the subsequent binding of Nck disrupted its interaction with conventional kinesin in vitro (*18*) (Fig. 1A). Endogenous Src kinase was localized beneath CEV particles that were promoting actin polymerization. Src kinase recruited to CEV was also phosphorylated at Tyr^{418}, indicating the active conformation of the kinase (Fig. 1B). Activated Src was not detected on kinesin-positive IEV or in cells that lack Src (Figs. 1C and 2A) (*17*). To determine whether A36R phosphorylation was restricted to the plasma membrane in response to Src recruitment, we raised antibodies against a phosphopeptide corresponding to Tyr^{132} of A36R (anti–A36R-$Y132PO_4$) (*17*). Anti–A36R-$Y132PO_4$ detected a signal beneath actin tail–inducing CEV at the plasma membrane, but not on A36R-Y132F virus (Fig. 1, D and E). No signal was observed with anti–A36R-$Y132PO_4$ on kinesin-positive IEV in the cytoplasm (Fig. 2C). The pattern of A36R phosphorylation reflected a subset of the total distribution of A36R, which was also observed on the perinuclear trans-Golgi network as well as on IEV being transported to the plasma membrane on microtubules (Figs. 1D and 2C). The absence of a signal on kinesin-positive IEV suggests that Src-mediated phosphorylation of A36R occurred only when the virus reached the plasma membrane, and not before.

To confirm that Src recruitment and activation occur upstream of A36R phosphorylation, we looked for evidence of the presence of the kinase on A36R-YdF virus particles that cannot induce actin tails because Tyr^{112} and Tyr^{132} of A36R have been mutated to Phe (*5*). A36R-YdF virus particles recruited active Src, indicating that its activation was independent of interactions

Cell Motility Laboratory, Room 529, Cancer Research UK, London Research Institute, Lincoln's Inn Fields Laboratories, 44 Lincoln's Inn Fields, London WC2A 3PX, UK.

*To whom correspondence should be addressed. E-mail: michael.way@cancer.org.uk

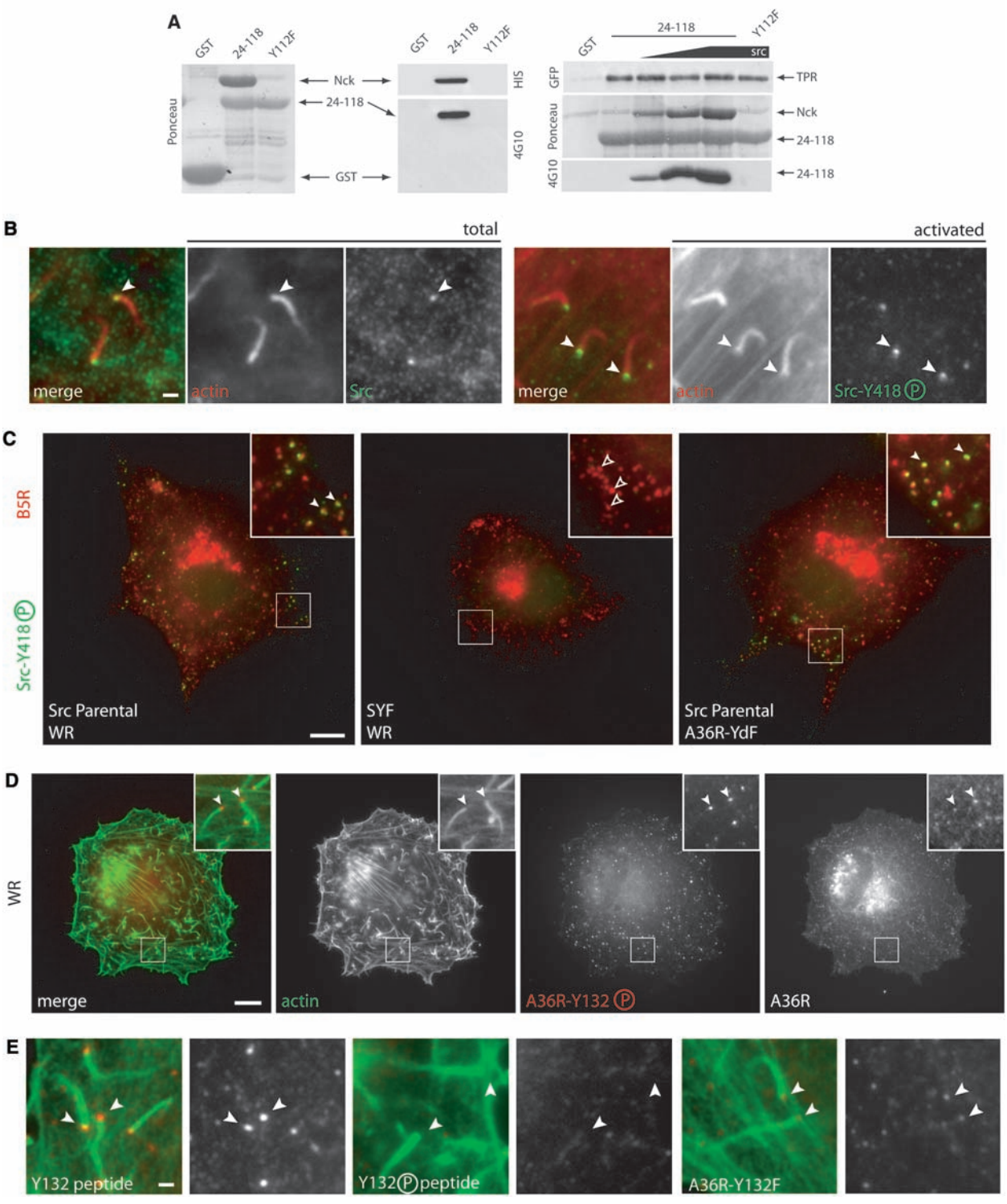

Fig. 1. Src phosphorylates A36R at the plasma membrane. (**A**) Immunoblot of in vitro phosphorylated GST-A36R. Recombinant Src directly phosphorylated A36R (residues 24 to 118) at Tyr^{112}, which was sufficient to mediate binding to Nck (left and center panels). A36R phosphorylation was detected by mAb 4G10 to phosphotyrosine. The interaction between A36R (residues 24 to 118) and GFP-TPR was independent of A36R phosphorylation and Nck binding (right panel). The degree of A36R phosphorylation and Nck binding was proportional to the amount of Src added (0.0, 0.4, 1.2, and 3.6 units in right panel). (**B**) Src kinase (detected by mAb 3-27) was locally recruited and activated (detected by anti–Src-Y418PO_4) at the plasma membrane beneath actin tail–inducing CEV in WR-infected cells. (**C**) Activated Src was observed on B5R-positive (detected by mAb 19C2) WR and A36R-YdF virus particles in infected Src parental cells (solid arrowheads) but not in SYF cells, which lack Src, Yes, and Fyn kinases (open arrowheads). (**D**) Tyrosine-phosphorylated A36R was restricted to the growing tips of actin tails (arrowheads). (**E**) Preincubation of anti–A36R-Y132PO_4 with the phosphorylated but not the unphosphorylated Tyr^{132} peptide abrogated the signal. Anti–A36R-Y132PO_4 did not label CEV in cells infected with A36R-Y132F virus. Scale bars, 1 μm [(B) and (E)], 10 μm [(C) and (D)].

with cellular components in the vaccinia actin tail–promoting complex (Figs. 1C and 2A). In contrast to WR (the wild-type Western Reserve strain), kinesin was still present beneath CEV particles that had recruited Src in A36R-YdF–infected cells (Fig. 2A). However, both WR and A36R-YdF viruses were potent stimulators of Src activation, as judged by the increase in phosphorylation of Tyr^{418} by immunoblot analysis (Fig. 2B) (*17*). Consistent with elevated Src activity, we found a substantial increase in tyrosine phosphorylation of cortactin in WR-infected cells (Fig. 2B). Cortactin is a Src substrate that is recruited to sites of dynamic actin polymerization, including pathogen-induced actin tails (*13*). In contrast, cortactin phosphorylation in A36R-YdF–infected cells was not increased, which suggests that Src-mediated phosphorylation of cortactin requires the prior recruitment of the vaccinia actin tail–nucleating complex (Fig. 2B). Thus, the localized recruitment and activation of Src at the plasma membrane, and subsequent phosphorylation of A36R, determines the site of vaccinia actin tail formation.

Our observations in vitro suggested that phosphorylation of A36R and binding of Nck did not affect its ability to interact with the kinesin light chain (Fig. 1A). In WR-infected cells, however, the presence of activated Src and phosphorylated A36R beneath CEV particles was always mutually exclusive with that of conventional kinesin (Fig. 2, A and C). The exception to this was the A36R-YdF virus, which accumulated active Src in addition to conventional kinesin (Fig. 2A). One possible explanation would be that phosphorylation of A36R by Src defines a switch required to regulate conventional kinesin release at the plasma membrane, before the initiation of actin polymerization. Consistent with this idea, kinesin was not released when the virus reached the plasma membrane in HeLa cells when Src activity was inhibited by a Src kinase inhibitor (PP2) or in the absence of Src in SYF cells (*19*).

We examined the effects of overexpression of Src-GFP (chicken Src fused to green fluorescent protein) on the ability of IEV to recruit kinesin. In cells expressing Src-GFP, A36R was ectopically phosphorylated at the site of IEV assembly, and virus particles were concentrated in the perinuclear region, having failed to recruit kinesin and be transported to the cell surface (Fig. 3, A and B) (*17*). Premature phosphorylation of A36R severely inhibited microtubule-dependent transport of virus particles to the cell periphery by blocking their ability to recruit conventional kinesin (Fig. 3D). In contrast, overexpression of Src-GFP did not affect the ability of the A36R-YdF virus to recruit kinesin and disperse to the cell periphery. Furthermore, the motor was not released when the A36R-YdF virus reached the plasma membrane (Figs. 2C and 3A). Thus, the phosphorylation of A36R, and not conventional kinesin or the recruitment of Src to IEV, inhibits microtubule-dependent movement of virus particles to the cell periphery. Consistent with this idea, dominant-negative Src, which inhibits actin tail formation (*11*), was recruited to the site of IEV assembly in WR-infected cells but did not block their transport to the cell periphery (Fig. 3, C and D). Thus, in the absence of Src-mediated phosphorylation of A36R, conventional kinesin remains bound to virus particles, which then accumulate in the cell periphery. Conversely, pre-

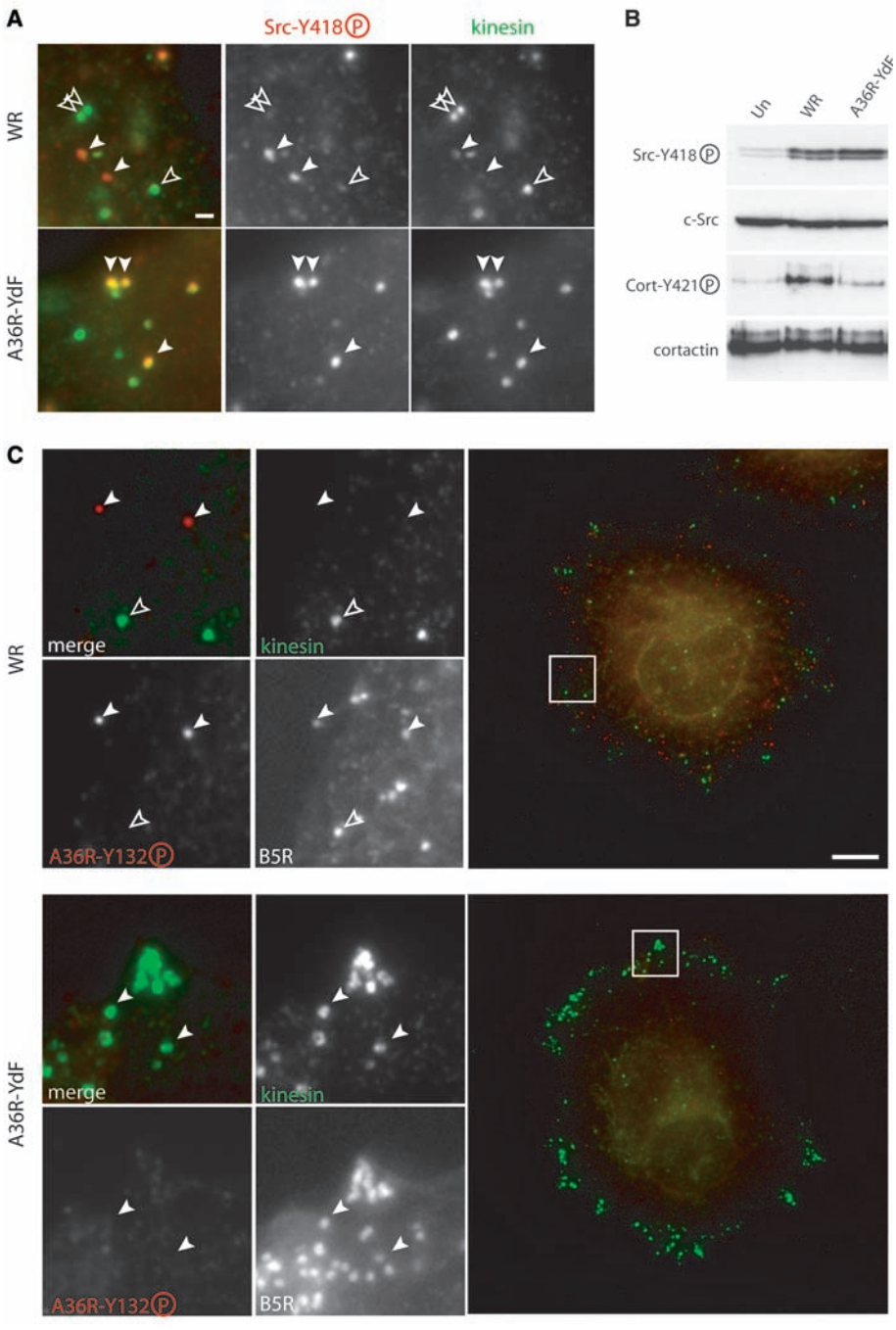

Fig. 2. Vaccinia activates Src upstream of actin tail formation. (**A**) Conventional kinesin and phospho-Src recruitment to virus particles was mutually exclusive in WR-infected but not A36R-YdF–infected cells. (**B**) WR-infected whole-cell extracts displayed a marked increase in phosphorylation of Src and cortactin. In contrast, A36R-YdF stimulated activation of Src without corresponding cortactin phosphorylation. (**C**) The presence of phospho-A36R (solid arrowheads) on B5R-positive virus particles was mutually exclusive to conventional kinesin (open arrowhead). In A36R-YdF–infected cells, kinesin-positive virus particles accumulated at the cell periphery. Scale bars, 1 μm (A), 10 μm (B).

mature phosphorylation of A36R blocks kinesin recruitment and IEV egress.

Src-mediated phosphorylation of A36R at the plasma membrane is essential in vivo to achieve release of conventional kinesin and the subsequent switch to actin-based motility. However, in vitro phosphorylation of A36R did not affect its direct binding to the kinesin light chain (Fig. 1A). It is thus possible that phosphorylation of A36R also modulates its interaction with additional proteins. The binding site for kinesin on A36R (residues 81 to 111) overlaps with that of the integral viral membrane protein A33R (residues 91 to 111 of A36R) (*18*, *20*). Moreover, the interaction of A33R with A36R is mutually exclusive with that of kinesin (*18*). It is possible that Src-mediated phosphorylation of A36R promotes or modulates its interaction with A33R, resulting in release of kinesin.

One possible explanation for vaccinia-induced activation of Src at the plasma membrane is that extracellular CEV induces a localized outside-in signaling cascade. If this were the case, we would predict that the viral protein responsible is present on the surface of CEV. The lumenal tails of only four integral viral membrane proteins—A33R, A34R, A56R and B5R—are exposed on the surface of CEV (*21*). Previous studies suggest that

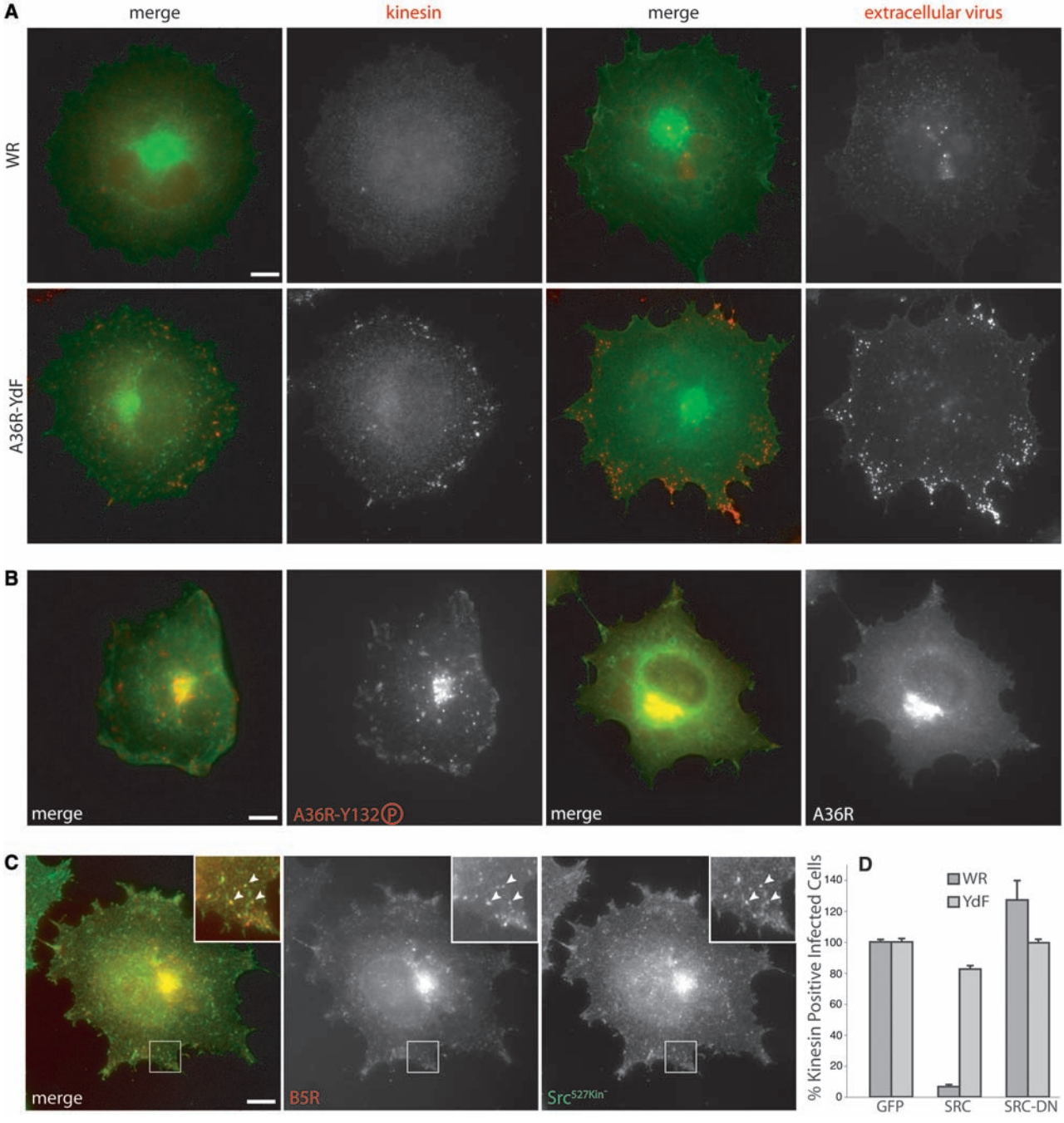

Fig. 3. Src regulates vaccinia recruitment and release of conventional kinesin. (**A**) Overexpression of Src-GFP inhibited kinesin recruitment and IEV dispersal to the cell periphery in WR-infected but not A36R-YdF–infected cells. (**B**) Src-GFP was recruited to the perinuclear trans-Golgi network in WR-infected cells and induced premature tyrosine phosphorylation of A36R. (**C**) Dominant-negative Src 527Kin$^-$ was recruited to IEV particles and their site of assembly but did not inhibit their dispersal to the cell periphery. (**D**) Quantification of microtubule-dependent viral egress in cells expressing GFP, GFP-Src, or Src 527Kin$^-$ (Src-DN). Bars represent the percentage of cells with at least a single kinesin-positive virus particle for each condition at 8 hours after infection. Error bars represent SD of the mean from three experiments. Scale bars, 10 μm.

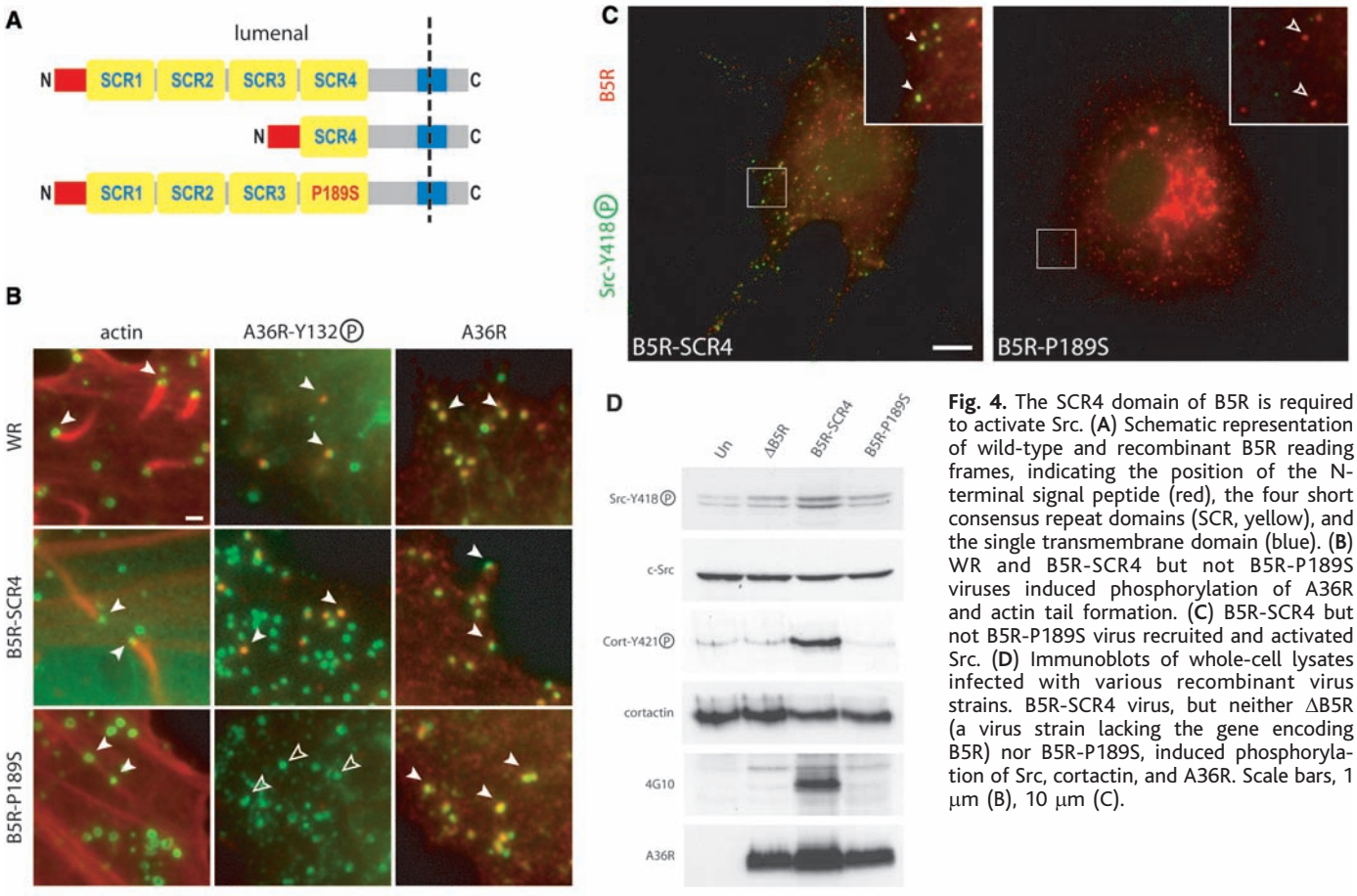

Fig. 4. The SCR4 domain of B5R is required to activate Src. (**A**) Schematic representation of wild-type and recombinant B5R reading frames, indicating the position of the N-terminal signal peptide (red), the four short consensus repeat domains (SCR, yellow), and the single transmembrane domain (blue). (**B**) WR and B5R-SCR4 but not B5R-P189S viruses induced phosphorylation of A36R and actin tail formation. (**C**) B5R-SCR4 but not B5R-P189S virus recruited and activated Src. (**D**) Immunoblots of whole-cell lysates infected with various recombinant virus strains. B5R-SCR4 virus, but neither ΔB5R (a virus strain lacking the gene encoding B5R) nor B5R-P189S, induced phosphorylation of Src, cortactin, and A36R. Scale bars, 1 μm (B), 10 μm (C).

B5R is the best candidate to induce outside-in signaling, because deletion of its lumenal domain, which consists of four short consensus repeats (SCRs), does not inhibit the ability of the virus to reach the plasma membrane but does result in a loss of actin tail formation (*22*, *23*). Furthermore, a recombinant virus expressing SCR domains 1 to 3 of B5R is not able to promote actin tail formation, even though the virus is able to reach the plasma membrane (*23*). We constructed two recombinant viruses, B5R-SCR4 and B5R-P189S, to test the role of the SCR4 domain in vaccinia actin tail formation (Fig. 4A) (*17*). In cells infected with the B5R-SCR4 virus, which lacks the first three SCR domains, CEV induced actin tails with associated phospho-A36R and Src (Fig. 4, B and C). Immunoblot analysis revealed that the B5R-SCR4 virus also activated Src and induced tyrosine phosphorylation of A36R and cortactin (Fig. 4D). In contrast, the B5R-P189S virus (*24*), which contains a $Pro^{189} \rightarrow Ser$ amino acid substitution in the structural fold of the SCR4 domain, did not induce increased activation of Src, A36R phosphorylation, or actin tail formation (Fig. 4, B to D). Thus, the SCR4 domain of B5R exposed on the surface of extracellular CEV was required to activate Src at the plasma membrane.

The coordinated regulation of multiple motors on the same cargo, including membrane-bound organelles, plays an important role in ensuring their delivery to the correct destination (*25*, *26*). However, understanding the molecular basis by which microtubule motors recognize and bind their correct cargo will also be required to unravel the mechanisms that ensure their delivery to the right cellular location. Phosphorylation of components in motor complexes modulates their ability to bind cargoes (*25*, *26*). Our results show that tyrosine phosphorylation of a cargo component can also be an important determinant regulating intracellular transport.

In addition, localized recruitment and activation of Src play an important role in regulating the switch between intracellular microtubule transport and actin-based motility at the plasma membrane (fig. S1). In uninfected cells, we envisage that local activation of Src, in addition to regulating turnover of focal adhesions, ensures coordinated microtubule-based delivery of membranes and their associated cargoes to areas of active actin polymerization at the leading edge of migrating cells.

References and Notes

1. B. Sodeik, *Trends Microbiol.* **8**, 465 (2000).
2. G. A. Smith, L. W. Enquist, *Annu. Rev. Cell Dev. Biol.* **18**, 135 (2002).
3. M. M. Geada, I. Galindo, M. M. Lorenzo, B. Perdiguero, R. Blasco, *J. Gen. Virol.* **82**, 2747 (2001).
4. M. Hollinshead *et al.*, *J. Cell Biol.* **154**, 389 (2001).
5. J. Rietdorf *et al.*, *Nature Cell Biol.* **3**, 992 (2001).
6. B. M. Ward, B. Moss, *J. Virol.* **75**, 4802 (2001).
7. B. M. Ward, B. Moss, *J. Virol.* **75**, 11651 (2001).
8. S. Cudmore, P. Cossart, G. Griffiths, M. Way, *Nature* **378**, 636 (1995).
9. S. Cudmore, I. Reckmann, G. Griffiths, M. Way, *J. Cell Sci.* **109**, 1739 (1996).
10. H. van Eijl, M. Hollinshead, G. L. Smith, *Virology* **271**, 26 (2000).
11. F. Frischknecht *et al.*, *Nature* **401**, 926 (1999).
12. V. Moreau *et al.*, *Nature Cell Biol.* **2**, 441 (2000).
13. F. Frischknecht, M. Way, *Trends Cell Biol.* **11**, 30 (2001).
14. N. Scaplehorn *et al.*, *Curr. Biol.* **12**, 740 (2002).
15. S. B. Snapper *et al.*, *Nature Cell Biol.* **3**, 897 (2001).
16. M. Zettl, M. Way, *Curr. Biol.* **12**, 1617 (2002).
17. See supporting data on *Science* Online.
18. B. M. Ward, B. Moss, *J. Virol.* **78**, 2486 (2004).
19. T. P. Newsome, N. Scaplehorn, M. Way, data not shown.
20. B. M. Ward, A. S. Weisberg, B. Moss, *J. Virol.* **77**, 4113 (2003).
21. G. L. Smith, A. Vanderplasschen, M. Law, *J. Gen. Virol.* **83**, 2915 (2002).
22. E. Herrera, M. del Mar Lorenzo, R. Blasco, S. N. Isaacs, *J. Virol.* **72**, 294 (1998).
23. E. Mathew, C. M. Sanderson, M. Hollinshead, G. L. Smith, *J. Virol.* **72**, 2439 (1998).
24. E. Katz, B. M. Ward, A. S. Weisberg, B. Moss, *J. Virol.* **77**, 12266 (2003).
25. R. L. Karcher, S. W. Deacon, V. I. Gelfand, *Trends Cell Biol.* **12**, 21 (2002).
26. R. D. Vale, *Cell* **112**, 467 (2003).

27. We thank G. Superti-Furga and J. Krijnse-Locker for providing monoclonal antibody (mAb) 3-27, Src-GFP, and mAb 19C2; G. Smith for the ΔB5R virus; and the Way lab, N. Hogg, G. Schiavo, and K. Dorey for helpful comments. Supported by the Human Frontier Science Program (T.P.N.). Molecular interaction data have been deposited in the Biomolecular Interaction Network Database with accession codes 151863 and 151864.

Supporting Online Material
www.sciencemag.org/cgi/content/full/1101509/DC1
Materials and Methods
Fig. S1
References

16 June 2004; accepted 23 July 2004
Published online 5 August 2004;
10.1126/science.1101509
Include this information when citing this paper.

Nonvisual Photoreception in the Chick Iris

Daniel C. Tu,[1] Matthew L. Batten,[3] Krzysztof Palczewski,[3,4] Russell N. Van Gelder[1,2]*

The embryonic chicken iris constricts to light ex vivo, but with characteristics atypical of visual phototransduction. The chick iris was most sensitive to short-wavelength light, demonstrating an action spectrum consistent with cryptochrome rather than with opsin pigments. Pupillary responses did not attenuate after saturating light exposure, but showed paradoxical potentiation. Iris photosensitivity was not affected by retinoid depletion or inhibitors of visual phototransduction. Knockdown of cryptochrome expression, but not of melanopsin expression, decreased iris photosensitivity. These data characterize a non-opsin photoreception mechanism in a vertebrate eye and suggest a conserved photoreceptive role for cryptochromes in vertebrates.

The ability to sense ambient light without forming an image (nonvisual photoreception) is widespread among vertebrates. Nonvisual photosensitive tissues in vertebrates include brain and parietal eye photoreceptors in lizards (*1*, *2*), pineal and iris photoreceptors in avians (*3*, *4*), iris and dermal photoreceptors in amphibians (*5*, *6*), and retinal ganglion cell photoreceptors in mammals (*7*). These photoreceptors regulate diverse nonvisual functions, including the entrainment of circadian rhythms to the light-dark cycle, pupillary constriction, and hormone secretion. The mechanisms underlying murine retinal ganglion cell photoreception have recently been investigated with targeted mutations in genes that encode potential photopigment. The opsin family member melanopsin has been found to be essential to inner retinal photoreception (*8*, *9*), whereas the potential flavin photopigments cryptochrome 1 and 2 contribute to the amplitude of nonvisual light responses (*10*, *11*).

Despite being recognized for more than 150 years (*12*), little is known about the mechanisms underlying the intrinsic pupillary light response (PLR) of some vertebrate irises. In the chick, intrinsic iris photosensitivity is present during a brief developmental window [embryonic days (E) 14 to 18)] (*4*). Infrared pupillometry of E15 iris maintained ex vivo showed strong constriction and dilation to sequential light and dark exposure (Fig. 1A and movies S1 and S2). Light-induced constriction was preserved after removal of the pigmentary epithelium layer, indicating that nonpigmented tissue contains functional photopigment (fig. S1). The kinetics of response to subsaturating light exposure showed an initial peak constriction preceding a slightly lower steady state (Fig. 1B). Prolonged exposure to heat-filtered, bright white light induced sustained maximal constriction (Fig. 1C), which could be maintained for at least 3 hours under continuous illumination. Quantitatively identical PLRs were observed after subsequent stimulation for more than 10 hours, and the preparation maintained robust photoresponsiveness for at least 48 hours (*13*).

To characterize the photopigment(s) mediating this light response, action spectra were constructed from irradiance-response relations with 10-nm half-bandwidth filtered light from 350 to 590 nm (fig. S1). The action spectrum showed preferential sensitivity to ultraviolet-blue light, with a local secondary peak at 430 nm (Fig. 1D and fig. S2), qualitatively similar to the absorption spectra of cryptochrome purified from *Vibrio cholera* (*14*) (Fig.1E) and of heterologously expressed human cryptochrome (*15*) (Fig. 1F), but not to that of any opsin photopigment.

Opsin-based photopigments bleach after saturating white light exposure because of *cis/trans*-retinaldehyde photoisomerization, leading to pigment desensitization. However, rather than desensitizing after saturating stimulation, the isolated chick iris PLR demonstrated increased sensitivity to subsequent dim light pulses (Fig. 2). We have termed this phenomenon photopotentiation. Photopotentiation was wavelength-dependent: It could be elicited after exposure to bright monochromatic blue light, but did not result from exposure to bright green light of equivalent irradiance (*13*). Because the same color of light can both maximally stimulate the PLR and induce its photopotentiation, this is unlikely to represent behavior of a bistable opsin (*16*). Bright light–induced photopotentiation showed logarithmic decay with a half-life of ~2.8 min (Fig. 2 and fig. S3).

All known opsin-based photopigments use specific retinoids as their chromophore. To test whether the chick iris photopigment(s) require retinoids, irises were depleted of endogenous retinoids by exposure to 312-nm ultraviolet (UV) light, a treatment that irreversibly degrades all retinoids to nonfunctional products (*17*). A 20-min exposure to 312-nm UV light (8 mW/cm^2) fully depleted control solutions of all-*trans*-retinol (Fig. 3A). From 57 embryos, irises from one eye received 20 min of 312-nm light, while irises from the other eye underwent mock exposure. A subset of both groups was tested for PLR to 450-nm light of varying irradiance. Endogenous iris retinoids were extracted and subjected to high-pressure liquid chromatography (HPLC) separation and quantitation. In the mock-exposed group of irises, very low amounts of retinoids were detected, mostly in the form of all-*trans*-retinyl esters (~0.2 pmol per iris) and all-*trans*-retinol (~0.1 pmol per iris) (Fig. 3B). No 11-*cis*-retinoids were detected. After UV light exposure, no retinoids could be detected in the irises (Fig. 3C), demonstrating complete depletion to the limit of HPLC detection (1.53 pmol for all-*trans*-retinyl ester, or 0.027 pmol per iris, and 1.8 pmol for all-*trans*-retinol, or 0.03 pmol per iris). Sensitivity of the PLR to blue light was not different between UV-depleted and mock-treated irises (Fig. 3D). The same result was obtained in irises lacking their pigment layer, demonstrating that the UV resistance of the light response is not due to shielding by iris pigment (fig. S4). These data suggest that the chick iris PLR uses a photopigment that does not require a retinoid-based chromophore.

Specific pharmacologic agents were used to dissect the signal transduction pathway of the iris-based photoreceptor (table S1). All known visual phototransduction cascades use specific G proteins in signaling. Neither cholera toxin (G_s inhibitor) nor pertussis toxin (G_i inhibitor) affected the PLR sensitivity.

[1]Department of Ophthalmology and Visual Sciences, [2]Department of Molecular Biology and Pharmacology, Washington University Medical School, St. Louis, MO 63110 USA. [3]Department of Ophthalmology, [4]Departments of Pharmacology and Chemistry, University of Washington, Seattle, WA 98195 USA.

*To whom correspondence should be addressed. E-mail: Vangelder@vision.wustl.edu

Invertebrate photoreception relies on the G protein G_q, which signals through inositol triphosphate and phospholipase C (PLC). Administration of two different PLC inhibitors (U-73122 and neomycin) had no effect on PLR sensitivity. Drugs that decreased PLR sensitivity included thapsigargin, forskolin, and staurosporine (fig. S5). Thapsigargin inhibits the PLR by depleting intracellular Ca^{2+} stores (*18*); thapsigargin also blocked acetylcholine (ACh)–induced pupillary constriction. Staurosporine, a pan-kinase inhibitor, equivalently blocked light-, ACh-, and K^+-mediated constriction (*19*). Staurosporine has been shown to block myosin light-chain phosphorylation, which may account for its effects on iris muscle (*20*). Forskolin, an adenylyl cyclase activator, increases cyclic adenosine monophosphate levels and is a smooth muscle relaxant (*21*); however, forskolin was a more potent blocker of light-induced than of ACh-induced constriction.

We performed reverse transcription–polymerase chain reaction (RT-PCR) to determine the expression of candidate photopigments in the embryonic iris (Fig. 4A). Melanopsin and cryptochromes 1 and 2 are three candidate blue-light photopigment proteins currently implicated in mammalian inner retinal nonvisual photoreception. mRNA for each was identified in embryonic chick iris, although (as assayed by quantitative RT-PCR) melanopsin mRNA was expressed at much lower levels (<0.5%) than either cryptochrome. A third cryptochrome (*gCry4*) has been cloned from chickens (GenBank accession no. AY102068), but we could not detect this transcript in chick iris by RT-PCR.

To determine whether melanopsin or cryptochromes contribute to the intrinsic PLR, irises were transfected with heterogeneous small interfering RNA (siRNA) to knock down melanopsin, cryptochrome 1, cryptochrome 2, or β-galactosidase (*LacZ*) mRNA (Fig. 4B). Thirty hours after transfection, expression of melanopsin, cryptochrome 1, and cryptochrome 2 mRNAs (as measured by quantitative RT-PCR) was reduced by 44%, 65%, and 50%, respectively, relative to transcript levels found in *LacZ* siRNA-transfected controls. *LacZ* siRNA had no effect on transcript levels of either cryptochrome or melanopsin. Although there was partial cross-suppression of *Cry2* siRNA on *Cry1* transcript levels (chicken cryptochromes 1 and 2 showed 76% nucleotide identity in their coding sequences), cryptochrome siRNA did not affect melanopsin mRNA expression, nor did melanopsin siRNA suppress cryptochrome mRNA expression. The PLR sensitivity of irises transfected with either cryptochrome 1 or 2 siRNAs was reduced by ~40% relative to *LacZ* siRNA-transfected control irises (Fig. 4C). When irises were transfected with siRNAs targeting both cryptochromes 1 and 2, the PLR sensitivity was reduced by 58%. Melanopsin siRNA-transfected irises showed PLR sensitivity indistinguishable from paired *LacZ* siRNA-transfected controls. Qualitatively identical results were also obtained 45 to 48 hours after transfection with phosphothiorate antisense oligonucleotides to mediate knockdown of cryptochromes or melanopsin (fig. S6). These data suggest that cryptochromes 1 and 2 are additive in their contributions to the sensitivity of the intrinsic light response, whereas melanopsin may not be required.

The isolated embryonic chicken iris is a very robust and readily available photosensitive ocular tissue for the study of nonvisual photoreception in a vertebrate. Five lines of evidence support the hypothesis that this nonvisual photoreceptive phenomenon is not opsin-based: (i) The action spectrum is not consistent with an opsin template (but shows univariance consistent with a single pigment); (ii) the photoreceptor is not bleached by bright light exposure (as are most opsins), but rather shows paradoxical photopotentiation to supersaturating stimulus; (iii) substantial retinoid depletion does not alter the sensitivity of the photoreceptor; (iv) pharmacologic blockade of vertebrate and inverte-

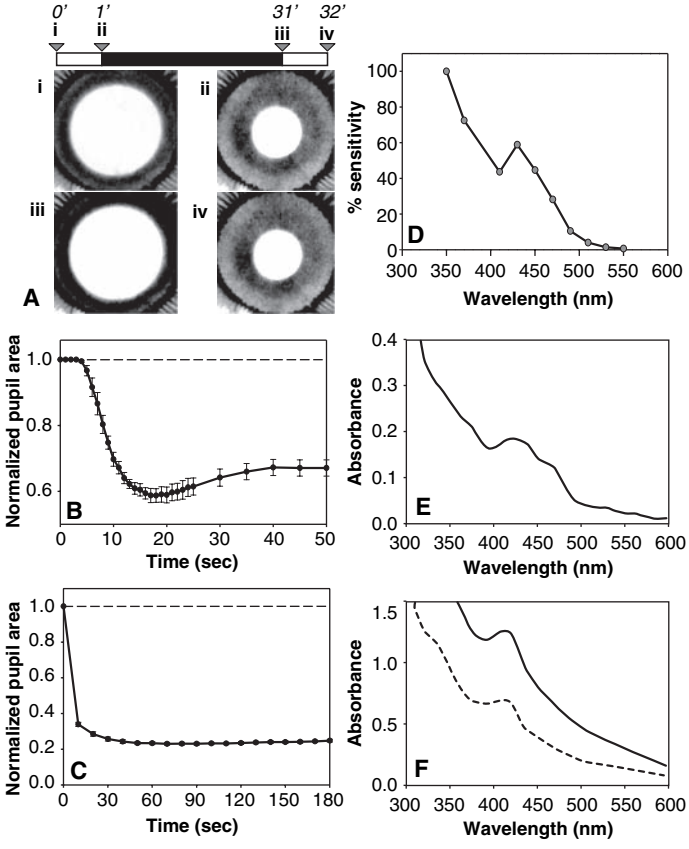

Fig. 1. Isolated embryonic chicken iris sphincter muscle constricts in response to light. (**A**) Two sequential light-induced pupillary constrictions. Images were captured at the time points indicated above and depict the same iris muscle in the following states: (i) dark-adapted, (ii) after a 1-min white light exposure (350 W/m^2), (iii) after 30 min in the dark, and (iv) after a second 1-min white light exposure (350 W/m^2). (**B**) PLR to subsaturating blue light (430 nm, 11.44 W/m^2, n = 5 irises). (**C**) PLR to bright broad-spectrum light (180 s of white light, 350 W/m^2). Normalized pupil area was calculated as pupil area/dark-adapted pupil area (mean ± SEM; n = 5 irises). (**D**) Action spectrum of depigmented embryonic chick iris PLR (steady-state PLR measurements). (**E**) *V. cholerae* cryptochrome absorption spectrum (*14*). [Modified and reprinted with permission from (*14*), © 2003 American Society for Biochemistry and Molecular Biology]. (**F**) Absorption spectrum for heterologously expressed human *Cry1* (solid line) and *Cry2* (dashed line) (*15*). [Modified and reprinted with permission from (*15*), © 1996 American Chemical Society].

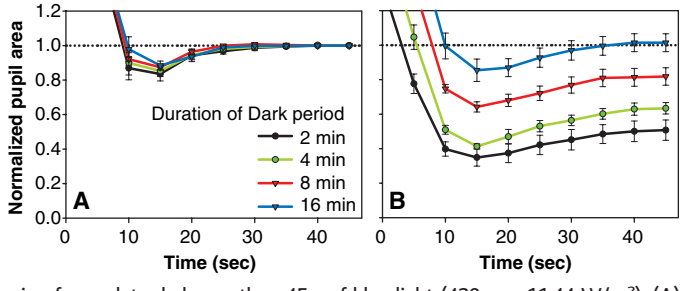

Fig. 2. Bright white light exposure potentiates subsequent pupillary responses. Dark-adapted irises were exposed to four sequential periods of illumination or darkness in the following order: 45 s of blue light (430 nm, 11.44 W/m^2), 1 min of bright white light (400 W/m^2), 2 to 16 min of complete darkness, then 45 s of blue light (430 nm, 11.44 W/m^2). (**A**) Time series of pupillary constriction to the first 45-s pulse of blue light (mean ± SEM; n = 6 to 8 irises). (**B**) Time series of pupillary constriction to the second 45-s pulse of blue light (mean ± SEM; n = 6 to 8 irises).

brate opsin-mediated signal transduction pathways does not affect the PLR sensitivity; and (v) genetic knock-down of mRNA for melanopsin does not decrease the PLR sensitivity. This last experiment must be qualified: Because antibodies for detection of melanopsin are not presently available, it is not known to what extent mRNA knockdown is reflected in decreased protein levels. However, the action spectrum is qualitatively similar to the absorption spectrum of purified *V. cholerae* and human cryptochrome, and knockdown of cryptochrome 1 and 2 mRNA decreases PLR sensitivity. These lines of evidence also suggest the involvement of cryptochrome-based photopigments in the chick PLR. Invertebrate and plant cryptochromes are believed to be bona fide photopigments (*22*), whereas in vertebrates it has been unclear if cryptochromes serve a photoreceptive function separate from their role in circadian rhythms (*10*). The ultimate demonstration of vertebrate cryptochrome photopigment function will require elucidation of its photocycle (*23*).

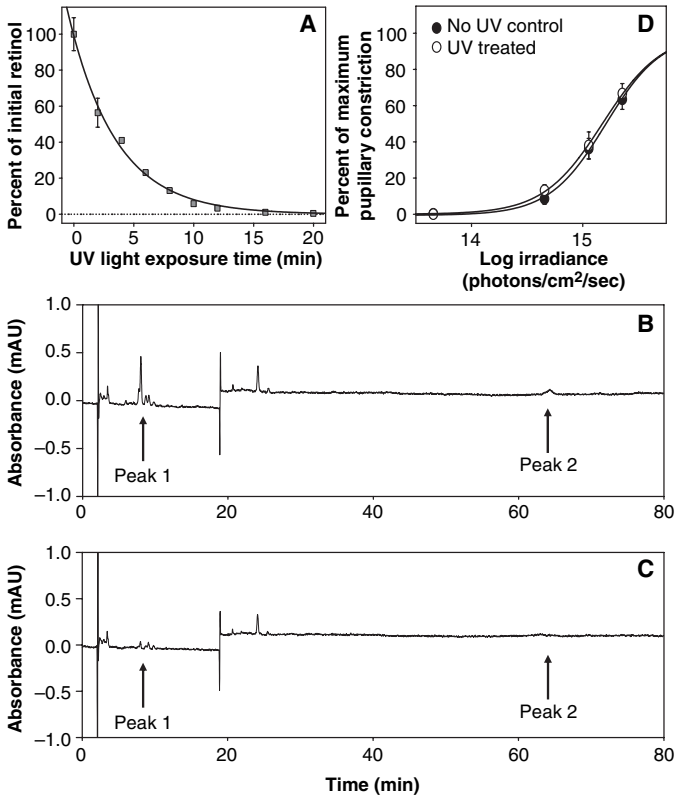

Fig. 3. UV light depletion of endogenous retinoids does not alter photic sensitivity of the pupillary light response. (**A**) UV light (312 nm) depletion of all-*trans*-retinol in methanol (mean ± SEM). (**B**) HPLC separation of retinoids from a pooled sample of 57 chick irises mock-exposed to UV light. Very low levels of all-*trans*-retinyl ester (peak 1, ~0.2 pmol per iris) and all-*trans*-retinol (peak 2, ~0.1 pmol per iris) were detected. (**C**) HPLC from a matching set of 57 irises after a 20-min exposure to 312-nm UV light (8 mW/cm^2) with loss of all-*trans*-retinyl ester and all-*trans*-retinol peaks. (**D**) Irradiance-response relationship of PLR to 450-nm light with and without UV light pretreatment (mean ± SEM; n = 4 irises).

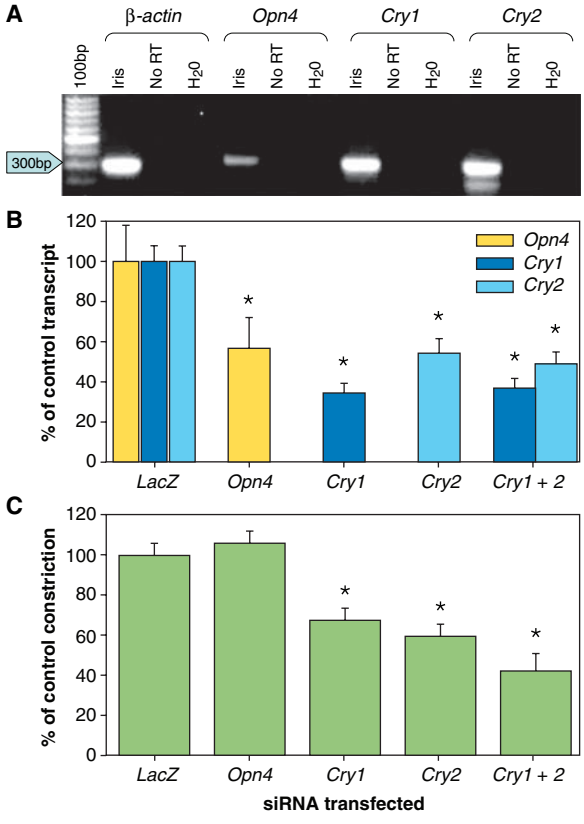

Fig. 4. Knockdown of candidate photopigment genes expressed in embryonic chicken iris. (**A**) RT-PCR of chicken β-*actin*, *Cry1*, *Cry2*, and *Opn4* (melanopsin) in E15 embryonic chick iris tissue. PCR reactions used 35 cycles of amplification. "No RT" lanes represent RT-PCR reactions performed without reverse transcriptase. "H_2O" lanes contained no template mRNA. bp, base pairs. (**B**) Quantitative RT-PCR of total RNA collected from the irises tested in (C), showing the amount of *Opn4*, *Cry1*, or *Cry2* transcript (normalized to β-*actin* levels) relative to that measured in the *LacZ* siRNA-transfected control irises (mean ± SEM; *Cry1* and *Cry2*, n = 16 to 18 irises; *Opn4*, n = 9 irises). Asterisks indicate statistically significant differences ($P < 0.05$, unpaired two-tailed t test) between experimental and control groups. (**C**) Percent pupillary constriction for irises transfected with siRNAs targeting regions of *LacZ*, *Opn4*, *Cry1*, *Cry2*, or *Cry1* and *Cry2*, relative to the control irises transfected with *LacZ* siRNAs (mean ± SEM; n = 7 to 8 irises). Asterisks indicate statistically significant differences ($P < 0.05$, unpaired two-tailed t test) between experimental and control groups.

References and Notes

1. M. Pasqualetti *et al.*, *Eur. J. Neurosci.* **18**, 364 (2003).
2. E. Solessio, G. A. Engbretson, *Nature* **364**, 442 (1993).
3. T. Deguchi, *Nature* **290**, 706 (1981).
4. G. Pilar, R. Nunez, I. S. McLennan, S. D. Meriney, *J. Neurosci.* **7**, 3813 (1987).
5. L. Barr, M. Alpern, *J. Gen. Physiol.* **46**, 1249 (1963).
6. T. Moriya *et al.*, *J. Exp. Zool.* **276**, 11 (1996).
7. D. M. Berson, F. A. Dunn, M. Takao, *Science* **295**, 1070 (2002).
8. S. Panda *et al.*, *Science* **301**, 525 (2003).
9. S. Hattar *et al.*, *Nature* **424**, 76 (2003).
10. C. P. Selby, C. Thompson, T. M. Schmitz, R. N. Van Gelder, A. Sancar, *Proc. Natl. Acad. Sci. U.S.A.* **97**, 14697 (2000).
11. R. N. Van Gelder, R. Wee, J. A. Lee, D. C. Tu, *Science* **299**, 222 (2003).
12. E. Brown-Sequard, *Compt. Rend. Acad. Sc.* **25**, 482 (1847).
13. D. C. Tu, R. N. Van Gelder, unpublished data.
14. E. N. Worthington *et al.*, *J. Biol. Chem.* **278**, 39143 (2003).
15. D. S. Hsu *et al.*, *Biochemistry* **35**, 13871 (1996).
16. M. Koyanagi *et al.*, *Proc. Natl. Acad. Sci. U.S.A.* **101**, 6687 (2004).
17. J. K. McBee, J. P. Van Hooser, G. F. Jang, K. Palczewski, *J. Biol. Chem.* **276**, 48483 (2001).
18. O. Thastrup *et al.*, *Agents Actions* **27**, 17 (1989).
19. U. T. Ruegg, G. M. Burgess, *Trends Pharmacol. Sci.* **10**, 218 (1989).
20. Y. Kureishi *et al.*, *Eur. J. Pharmacol.* **376**, 315 (1999).
21. A. A. Abdel-Latif, *Exp. Biol. Med.* **226**, 153 (2001).
22. A. R. Cashmore, *Cell* **114**, 537 (2003).
23. A. Sancar, *Chem. Rev.* **103**, 2203 (2003).

24. We thank S. Bassnett, A. C. Pira, and P. M. Boone for assistance, and I. Provencio, V. Cassone, and M. Iuvone for cDNA plasmids. Supported by grants from the National Eye Institute of the NIH (R.V.G. and K.P.), Research to Prevent Blindness (RPB) (R.V.G., K.P., and D.C.T.), the Medical Scientist Training Program of Washington University (D.C.T.), the Culpeper Physician Scientist Award of the Rockefeller Brothers Foundation (R.V.G.), the Becker/Association of University Professors of Ophthalmology PB Physician Scientist Award (R.V.G.), and a grant from the E. K. Bishop Foundation (K.P.). R.V.G. is the recipient of a RPB career development award, and K.P. is a RPB Senior Investigator.

Supporting Online Material

www.sciencemag.org/cgi/content/full/306/5693/129/DC1
Materials and Methods
SOM Text
Figs. S1 to S6
Table S1
References and Notes
Movies S1 and S2

15 June 2004; accepted 11 August 2004

New Products

Genetix
For more information
877-436-3849
www.genetix.com
www.scienceproductlink.org

Protein Portfolio Platform

The Protein Portfolio Platform is a powerful combination of proven automation, on-board intelligent imaging, and information tracking tools that delivers performance and confidence in data fidelity, helping accelerate work flows and cut costs in drug discovery and basic protein research. The new platforms ensure that protein applications previously hampered by lack of appropriate instrumentation and data tracking can now be performed without errors and in a more efficient way. Protein Portfolio workstations are available optimized for a growing series of protein applications, including phage display, library management, enzyme evolution, protein–protein interactions and pathways, and automated DNA cloning with regional colony picking.

Ariadne Genomics and Integrated Genomics
For more information
847-644-1557
www.ariadnegenomics.com
www.scienceproductlink.org

Microbial Metabolic Pathway Database

Metabolic Vision is an advanced microbial metabolic pathway database that can be incorporated into Ariadne's PathwayAssist software suite. Metabolic Vision combines PathwayAssist's pathway analysis and visualization tools with Integrated Genomics' extensive ERGO database of more than 600 curated genomes to allow researchers to explore and manage microbial metabolic pathways easily, with outstanding depth and specificity. The Metabolic Vision module is available to PathwaysAssist customers as a downloadable database. There are several packages available for researchers investigating microbial metabolism, including specific packages for bacterial pathogens, antibiotic production, and fungal metabolism.

Molecular Probes
For more information
541-335-0338
www.probes.com
www.scienceproductlink.org

Biomolecule Quantitation Kits

Four new kits are available for the fluorescence-based quantitation of DNA, RNA, and protein in solution. All Quant-iT Assay Kits offer high sensitivity and selectivity, using the same "mix-and-read" format. Results are obtained in minutes: The user simply dilutes the dye with the included buffer, adds sample, and reads the fluorescence. The Quant-iT assays are more sensitive than ultraviolet absorbance readings, and require only 1–20 μL of sample per assay. The assays are highly selective for the target compounds; assay accuracy is not affected by common contaminants. The dyes provided in the Quant-iT kits match common fluorescence excitation and emission filter sets, making the assays equally useful for high-throughput platforms and routine sample analysis.

Vector Laboratories
For more information
650-697-3600
www.vectorlabs.com
www.scienceproductlink.org

Immunohistochemistry Reagents

The ImmPress polymerized reporter enzyme staining system is based on a new method of polymerizing enzymes and attaching these polymers to antibodies. The ImmPress reagents provide high sensitivity with low background staining in immunohistochemical applications. The novel approach employed to form enzyme "micro-polymers" avoids the inherent shortcomings of using large dextrans or other macromolecules as a backbone. Attaching an enzyme "micro-polymer" with a greater density of highly active enzymes to a secondary antibody provides a reagent that has increased accessibility to its target, resulting in less background and enhanced signal intensity. In addition, fewer steps are required so staining times can be significantly shortened.

Photometrics
For more information
520-889-9933
www.photomet.com
www.scienceproductlink.org

Live-Cell Microscopy Camera

The Cascade:128 charge-coupled device (CCD) camera can collect more than 500 full frames of true 16-bit data per second. Faster frame rates are achievable via subregion readout or binning. The back-illuminated CCD with "on-chip multiplication gain" provides extra sensitivity for low-light-level, live-cell microscopy applications. This combination of speed and sensitivity makes the Cascade:128 suitable for neuroscience applications and single-molecule fluorescence imaging. The instrument's low-noise, impact-ionization signal-boosting process enables multiplication of photon-generated charges right on the CCD.

Amresco
For more information
800-448-4442
www.amresco-inc.com
www.scienceproductlink.org

Electrophoresis System

The NEXT (New Electrophoresis X'-Press Technology) Gel PAGE System is a continuous gel electrophoresis system designed for superior protein separation. NEXT Gel offers full range resolution, similar to a gradient gel, of a wide range of proteins in a simple-to-use continuous gel electrophoresis format. The NEXT Gel will resolve 14.2 kDa and 14.4 kDa on a mini-gel, as well as separate 3.5 kDa and 212 kDa on the same gel. These ready-to-use solutions are stable for six months and can be stored right on the benchtop at room temperature. It is easy to pour with no stacking gel required.

Turner BioSystems
For more information
408-212-4015
www.turnerbiosystems.com
www.scienceproductlink.org

Luminometer

The 20/20n Tube Luminometer is a sensitive, versatile, and easy-to-use instrument designed to measure all bioluminescent and chemiluminescent assays. The touchscreen-based graphical user interface provides comprehensive instrument control and data collection. Optional automatic injectors enable the user to measure flash reactions. A fluorescent module is also available.

Newly offered instrumentation, apparatus, and laboratory materials of interest to researchers in all disciplines in academic, industrial, and government organizations are featured in this space. Emphasis is given to purpose, chief characteristics, and availability of products and materials. Endorsement by *Science* or AAAS of any products or materials mentioned is not implied. Additional information may be obtained from the manufacturer or supplier by visiting www.scienceproductlink.org on the Web, where you can request that the information be sent to you by e-mail, fax, mail, or telephone.